Search for dark matter produced in association with a Z boson
in the ATLAS detector at the Large Hadron Collider

by

Kayla Dawn McLean
B.Sc., University of Victoria, 2014

A Dissertation Submitted in Partial Fulfillment of the
Requirements for the Degree of

DOCTOR OF PHILOSOPHY

in the Department of Physics and Astronomy

Search for dark matter produced in association with a Z boson
in the ATLAS detector at the Large Hadron Collider

by

Kayla Dawn McLean
B.Sc., University of Victoria, 2014

Supervisory Committee

Dr. M. Lefebvre, Supervisor
(Department of Physics and Astronomy)

Dr. R. Kowalewski, Departmental Member
(Department of Physics and Astronomy)

Dr. D. Harrington, Outside Member
(Department of Chemistry)

Abstract

This dissertation presents a search for dark matter particles produced in association with a Z boson in proton-proton collisions. The dataset consists of 139 fb^{-1} of collision events with centre-of-mass energy of 13 TeV, and was collected by the ATLAS detector from 2015-2018 at the Large Hadron Collider. Signal region events are required to contain a Z boson that decays leptonically to either e^+e^- or $\mu^+\mu^-$, and a significant amount of missing transverse momentum, which indicates the presence of undetected particles. Two types of dark matter models are studied: (1) simplified models with an s-channel axial-vector or vector mediator that couples to dark matter Dirac fermions, and (2) two-Higgs-doublet models with an additional pseudo-scalar that couples to dark matter Dirac fermions. The main Standard Model background sources are ZZ, WZ, non-resonant $\ell^+\ell^-$, and Z+jets processes, which are estimated using a combination of data and/or simulation. A new reweighting technique is developed for estimating the Z+jets background using γ+jets events in data; the resulting estimate significantly improves on the statistical and systematic errors compared to the estimate obtained from simulation. The observed data in the signal region are compared to Standard Model prediction using a transverse mass discriminant distribution. No significant excess in data is observed for the simplified models and two-Higgs-doublet models studied. A statistical analysis is performed and several exclusion limits are set on the parameters of the dark matter models. Results are compared to direct detection experiments, the CMS experiment, and other ATLAS searches. Prospects and improvements for future iterations of the search are also presented.

Contents

List of Tables

List of Figures

Acknowledgements

I would like to thank:

My parents, Paul and Kathy McLean, if I didn't have such amazing parents I don't know where I would be. You've always believed in me and never told me who I should be; you let me carve my own path and always provided me with unwavering support. I will never be able to thank you enough.

Nick Lange, you wear kindness on your sleeve. When we first met we bonded over our physics homework; since then you've patiently helped me with so many more things, but more than anything you've taught me about myself, and helped me to grow as a person. Thank you for everything.

Michel Lefebvre, you have shown me endless enthusiasm, patience, and encouragement. As my professor you inspired me to love particle physics, as my supervisor you taught me to be confident, and as my friend we enjoyed many barbecues and movie nights together. I am thankful to have worked with you for so many years; I will miss them but always remember them fondly. Thank you for taking me on this spectacular journey.

Kenji Hamano, your patience and expertise were invaluable to our UVic group. Thank you for all of your help with the analysis. **Chris Anelli,** thank you for all of your efforts in our group. We were able to achieve so much thanks to your determination and hard work.

Sophie Behenna and Erin Laplante, my two rocks. Your friendship means everything to me. Thank you both for believing in me, and being there for me no matter what. I couldn't have made it this far without you.

Kate Taylor, thank you for for fiercely believing in me and always having my back. You're amazing. **Tony Kwan,** you're such a great friend, I know I can always count on you. Thank you for listening to me over the years. **Alison Elliot,** I couldn't have asked for a better mentor. I would not have survived this Ph.D. without you. Thank you

for everything. **Justin Chiu,** thank you for being there with me through undergrad and grad school. We've been through a lot together, and I'm glad to have you as a friend. **Savino Longo,** thank you for our random chats and for keeping office morale high. I'll never forget our Green Lake trips together. **Megan Tannock,** we survived undergrad together, what more can I say? Together we realized that we are capable women in science. Thank you for inspiring me. **Jaymie Kopelow,** thank you for keeping me sane during undergrad; you brought us all together with the social events that you organized. And thank you to the other **grad students** who pulled me out of my shell and made my time at UVic so memorable.

Jesse McLean, for keeping my heart young and filled with nostalgia. Thank you for distracting me from physics with D&D and video games.

Alex van Netten, for inspiring me, a first year biology student, to pursue physics instead. Your lectures were magical and your love for physics was captivating. Thank you for showing me the way.

Mark Laidlaw, for being there to listen. I remember the beginning of my physics career was filled with worry and self doubt. You took the time to share your own anecdotes and reassure me that I was in the right place. Thank you.

Jeremy Tatum, I learned more about how to write proper sentences in your undergraduate physics courses than any English class I ever had. You taught me that I was capable and to take pride in my work. I still have the article clipping that you gave to me after class one day, titled "A woman's place should be in the lab and at the cutting edge." When I started grad school I pinned it on the board above my desk, and it's been there ever since. Thank you for giving me the confidence I needed to do physics.

Richard Keeler, as my undergrad honours project supervisor you taught me how to design and test my own experiment from the ground up, something I never thought I could do. You continued to support me as a grad student. I really appreciated those moments when you'd poke your head into my office to check in. Thank you for looking out for me.

Bob Kowalewski and **David Harrington,** thank you both for being on my committee and helping to guide me along the way.

The cosmos is within us. We are made of star-stuff.
We are a way for the cosmos to know itself.
– Carl Sagan

Dedication

For Mom, Dad, and Nick.

Declaration

The ATLAS collaboration is divided into several physics analysis groups. This search is part of the HZZ subgroup, which is a part of the Higgs working group. The HZZ subgroup is a collection of analyses that primarily study the Higgs boson decaying into two Z bosons. Although this analysis is a search for dark matter, it shares strategies and background estimates with an invisible Higgs search with the same final state. The analysis team itself consists of about a dozen active analysts in addition to supervisors and analysis coordinators. This declaration explicitly lists the author's personal contributions to the analysis. Contributions to detector performance and operations are also listed.

Analysis contributions

- Primary analyzer for the mono-Z dark matter search. With the exceptions of the signal region optimization and the ZZ, WZ, non-resonant $\ell\ell$, and $ttV(V)/VVV$ background estimates, which are provided by others, all work related to the mono-Z search is completed by the author.
- Complete development of a novel reweighting technique to estimate the Z+jets background using γ+jets events in data for m_{T}^{ZZ} and $E_{\mathrm{T}}^{\mathrm{miss}}$ discriminants.
- Validation and implementation of dark matter signal sample emulation.
- Evaluation of experimental and theoretical systematic uncertainties on dark matter signals.
- Statistical analysis and limit setting for dark matter models.
- Binning optimization for m_{T}^{ZZ} and $E_{\mathrm{T}}^{\mathrm{miss}}$ discriminant distributions.
- Acceptance and shape studies of dark matter signal distributions.
- Sensitivity studies for t-channel dark matter simplified models.

- Studies of the impact of ZZ background uncertainties on dark matter limits.
- Provided frequent consistency checks with other analyzers (e.g. cutflow and limit comparisons, orthogonality cross checks with other searches).
- Comparison studies of AntiKt4EMTopo and AntiKt4EMPFlow jets.
- Signal significance studies for various jet p_{T} thresholds.
- Developer and primary maintainer of main analysis software and generator-level analysis software.
- Editor for supporting internal documentation.
- Analysis liaison to Common Dark Matter (CDM) working group.
- Analyzer for the mono-Z search with the early Run 2 dataset of 36.1 fb^{-1}, including dark matter limit setting, performing the Z+jets background estimate using the ABCD method, and support note editing.

Detector and operations contributions

- ATLAS authorship qualification task on jet calibration and truth-matching studies (see Appendix F).
- ATLAS control room shifts (calorimeter and forward detectors) during 2017 data-taking.

Chapter 1

Introduction

The Standard Model (SM) is currently the most complete theory that describes elementary particles and their interactions. While many of its predictions have been validated with remarkable success, it also has several well-known limitations: the SM cannot explain the matter-antimatter asymmetry observed in the universe, it contains no description of dark energy to explain the expansion of the universe, and it fails to describe the existence of *dark matter* (DM), the focus of this dissertation. There is strong evidence from astronomical measurements that there is a significant excess of matter in the universe that appears to interact only gravitationally. Galactic measurements have shown that luminous objects at the edges of galaxies rotate around the galactic centre much faster than predicted by Kepler's laws based on luminous matter alone. For a galaxy with most of the mass at the centre, the velocity should fall off with radius as $v \propto 1/\sqrt{r}$. Instead, the velocity is observed to be relatively independent of r in regions away from the galactic centre, suggesting that there is a halo of dark matter contained in the galaxy. Gravitational lensing observations, which measure gravitational deflections of light, suggest that there can be significant clouds of DM existing between galaxy clusters. There is also evidence to support that dark matter has been a part of our universe since its beginning; immediately after the Big Bang, the universe consisted of a primordial plasma that was so hot and dense that stable atoms could not form. Because of this, photons could not travel long distances before interacting with free electrons. After approximately 379,000 years, the temperature was cool enough to allow recombination to occur, and electrons and protons combined to form neutral hydrogen atoms. This allowed photons to decouple from matter and propagate freely; these photons are collectively known as Cosmic Microwave Background (CMB) radiation. If DM was present in the early

universe and decayed into secondary particles with significant energy, then it could heat the primordial plasma and affect the temperature fluctuations of the CMB. By measuring the angular power spectrum of the CMB, these temperature anisotropies can be determined and the ratio of normal matter to dark matter present in the universe can be obtained. The latest results from the Planck experiment show that the energy density of the universe is composed of 5% ordinary (baryonic) matter, 26% dark matter, and 69% dark energy [1]. Thus, there is substantial evidence for the existence of dark matter.

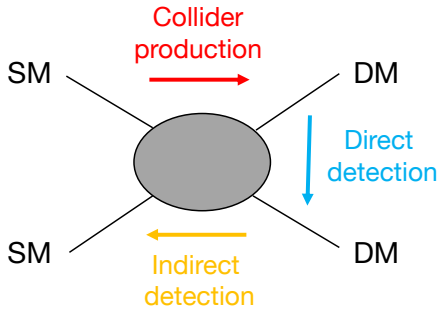

Figure 1.1: The three main categories of dark matter search experiments.

Although there has been evidence for the existence of dark matter for over 100 years [2], most of its properties are still largely unknown. Today there are many experiments that attempt to measure particle DM. In general they fall into three categories, as illustrated in Figure 1.1. *Direct detection* experiments consist of highly sensitive detectors, often large, that are usually located underground to reduce cosmic ray backgrounds. The detector material is specialized to produce a signal (via a combination of scintillation, ionization, and/or phonons) when dark matter scatters off the nuclei of the material; commonly used technologies are cryogenic crystals, bubble chambers, and noble liquids. Some of the most competitive experiments currently include XENON1T [3], PICO-60 C_3F_8 [4], PandaX-II [5], and DarkSide-50 [6]. While direct detection experiments search for DM passing through the Earth, *indirect detection* experiments search for DM annihilating or decaying into detectable particles in space. Indirect detection experiments come in several varieties and are optimized to detect different particles in specific energy ranges. For example, the Fermi-LAT telescope detects γ-rays with energies of 100 MeV to 1 TeV, whereas the giant IceCube detector at the South Pole specializes in detecting highly energetic neutrinos from 100 GeV up to more than a PeV in energy. Indirect detection experiments are

specialized to observe a specific source, such as the galactic centre of the Milky Way, galactic halos, or galaxy clusters. In contrast to direct and indirect detection experiments, *collider* experiments attempt to produce dark matter particles directly via the collision of Standard Model particles. For example, B-factories such as the Belle II experiment search for DM production in e^+e^- collisions. These types of experiments are most sensitive at low DM masses, typically less than 10 GeV. They also excel at precision measurements due to the clean signatures and low backgrounds produced in e^+e^- collisions. However, accelerating electrons radially causes large amounts of energy to be lost in the form of synchrotron radiation. There is no such issue for hadron colliders, which search for dark matter production in hadron collisions. The Large Hadron Collider (LHC) collides protons with protons. Although the products of proton-proton collisions are much more complicated to analyze compared to e^+e^- collisions, protons are much heavier than electrons and so produce far less synchrotron radiation when accelerated. Because of this, proton collisions have been achieved at very high energies, on the order of several TeV.

The ATLAS and CMS detectors are the two multipurpose detectors at the LHC. The two experiments have similar research programmes. One of the original goals of the ATLAS experiment was to discover the Higgs boson. Since its joint discovery by the ATLAS and CMS collaborations in 2012, the focus has shifted more towards searches for dark matter and other Beyond the Standard Model (BSM) physics. There are many dark matter theories and so there are many potential signatures to investigate. One such search, the focus of this dissertation, is the ATLAS mono-Z dark matter search, which looks for events containing DM and a Z boson decaying into two leptons.

The layout of the dissertation is as follows. The theory of the Standard Model and a selection of relevant DM models is introduced in Chapter 2. An overview of the LHC, the ATLAS detector, and the Run 2 dataset is presented in Chapter 3. Chapter 4 introduces the details of the mono-Z analysis, including an overview of the analysis strategy, object and event selections, and simulation samples. Chapter 5 discusses the systematic uncertainties of the analysis and the details of the signal and background estimation methods. The data-driven estimation of the Z+jets background using γ+jets reweighting is described in Chapter 6. Results and dark matter interpretations are discussed in Chapter 7, with final conclusions in Chapter 8.

Chapter 2

Theory

2.1 The Standard Model

Until the discovery of the electron by J. J. Thomson in 1897, it was believed that atoms were the fundamental building blocks of nature. His discovery is said to have marked the beginning of the era of modern physics, and since then our understanding of elementary particles has culminated into what is known as the Standard Model of particle physics. The SM is a theoretical model that describes elementary particles and their interactions; it is a quantum field theory that describes the electromagnetic, weak, and strong fundamental forces. Gravity has yet to be (fully) described by a quantum theory, and is currently best understood separately using Einstein's theory of general relativity.

The Standard Model describes particles as quanta of excitation of continuous fields. Specifically, the SM is a chiral gauge theory. It is composed of charged chiral (Weyl) fermion fields and is *gauge invariant*, meaning that the Lagrangian is invariant under *local* phase transformations. Gauge invariance implies automatic *global* phase invariance; this is significant because Noether's theorem [7] demonstrates that a global symmetry corresponds directly to a global conserved quantity that constrains the dynamics (e.g. energy, momentum, electric charge). Gauge transformations are local (vary with space and time, x) and describe physically indistinguishable field configurations. For a fermionic matter field $\psi_j(x)$ (a column vector with j components) that undergoes a local phase transformation, e.g.

$$\psi_j(x) \to e^{i\theta_k(x)T_k}\psi_j(x), \tag{2.1}$$

the Lagrangian is invariant when the transformation belongs to a specific *Lie group*. θ_k are real functions, and T_k are known as the *generators* of the group, which can be represented by matrices.[1] The Standard Model is fully described by three continuous Lie groups: $SU(3)_C \times SU(2)_L \times U(1)_Y$. $SU(3)_C$ is the quantum chromodynamics (QCD) gauge group, and $SU(2)_L \times U(1)_Y$ collectively describes the electroweak (EW) gauge group developed by Glashow, Salam, and Weinberg in the 1960's [8, 9, 10]. Colour charge, weak isospin, and weak hypercharge are the corresponding fundamental conserved quantities. Except for coupling strength parameters, mixing angles, and masses, all particles and their interactions are determined from these symmetries.

2.1.1 Fundamental particles

The particles of the Standard Model are categorized into *bosons* and *fermions*. Demanding gauge invariance of the fermion fields requires the addition of the gauge bosons. Bosons have integer spin and obey Bose-Einstein statistics. The gauge bosons are the force carriers of the SM. A summary of the SM bosons is presented in Table 2.1 [11]. The photon, γ, is massless, electrically neutral, and mediates electromagnetic interactions between charged particles. The gluons, g, are also massless and electrically neutral but contain colour charge, and therefore mediate the strong force between quarks. The $W^{\pm}$ and Z bosons are the weak gauge bosons; the Z boson is massive and is similar to the photon in that it mediates interactions without changing the charge. The $W^{\pm}$ bosons are the only charged bosons and therefore mediate charged current interactions.

Table 2.1: Summary of the Standard Model elementary bosons. Masses from the Particle Data Group [11].

Particle	Type	Force	Mass (GeV/c^2)	Charge	Spin
γ	Gauge	Electromagnetic	0	0	1
$g_1, \ldots g_8$		Strong	0	0	1
Z		Weak	91.1876 ± 0.0021	0	1
$W^{\pm}$		Weak	80.379 ± 0.012	± 1	1
h	Scalar	—	125.18 ± 0.16	0	0

The Higgs boson, h, is the most recently discovered particle that was predicted

[1] The $SU(N)$ Lie group is the special unitary group of degree N. The fundamental representation of the group consists of $N \times N$ unitary matrices with $N^2 - 1$ generators.

by the Standard Model. It is not a typical force carrier, and instead is associated with the mechanism responsible for giving mass to the $W^{\pm}$ and Z bosons and to all fundamental fermions. The fields corresponding to the $SU(2)_L \times U(1)_Y$ symmetry are massless bosons, but in reality the physical bosons are measured to be massive (except for the γ). The Higgs mechanism was introduced ad hoc to the SM to explain this phenomenon by Brout, Englert, and Higgs in 1964. The Brout-Englert-Higgs mechanism [12] introduces a Higgs doublet and self-interacting potential to the Standard Model Lagrangian, and the potential is allowed to have a minimum where the field does not vanish, i.e. a non-zero vacuum expectation value (VEV). After electroweak symmetry "hiding", the four degrees of freedom of the Higgs doublet are rearranged to produce the massive $W^{\pm}$ and Z bosons, in addition to a self-interacting Higgs boson, while preserving the gauge invariance of the theory. This symmetry hiding corresponds to the $SU(2)_L \times U(1)_Y$ symmetry rearranging into $U(1)_{\mathrm{EM}}$. In other words, rewriting the Lagrangian in terms of the reparameterized Higgs field with a non-zero VEV ($v = 246$ GeV) generates the mass terms for the bosons. For the fermion masses, gauge invariant Yukawa interaction terms between the Higgs and fermion fields are added to the Lagrangian, which then generate the fermion masses after symmetry hiding.

Table 2.2: Summary of the Standard Model leptons. Adapted from [13] with updates from the Particle Data Group [11].

Generation	Particle	Mass (MeV/c^2)	Charge (Q/e)	L_e	L_μ	L_τ
1	e^-	0.511	-1	1	0	0
	ν_e	$< 2 \times 10^{-6}$	0	1	0	0
2	μ^-	105.658	-1	0	1	0
	ν_μ	< 0.19	0	0	1	0
3	τ^-	1776.86 ± 0.12	-1	0	0	1
	ν_τ	< 18.2	0	0	0	1

The Standard Model fermions have spin 1/2 and obey Fermi-Dirac statistics. The interactions between fermions are mediated by the gauge bosons. Fermions are classified as either leptons or quarks. Table 2.2 [11] summarizes the leptons that occur in the SM. Leptons are organized into three generations. These generations are determined by the electron, muon, and tau flavours L_e, L_μ, and L_τ, which are conserved except for in the weak interaction. Electrons, muons, and tau leptons have negative charge and interact via the electromagnetic and weak forces. The

Table 2.3: Summary of the Standard Model quarks. Adapted from [13] with updates from the Particle Data Group [11].

Generation	Particle	Mass (MeV/c^2)	Charge (Q/e)	U	D	C	S	T	B'
1	u_r, u_b, u_g	$2.2^{+0.5}_{-0.4}$	$+2/3$	1	0	0	0	0	0
	d_r, d_b, d_g	$4.7^{+0.5}_{-0.3}$	$-1/3$	0	-1	0	0	0	0
2	c_r, c_b, c_g	$1.275^{+0.025}_{-0.035} \times 10^3$	$+2/3$	0	0	1	0	0	0
	s_r, s_b, s_g	95^{+9}_{-3}	$-1/3$	0	0	0	-1	0	0
3	t_r, t_b, t_g	$173.0 \pm 0.4 \times 10^3$	$+2/3$	0	0	0	0	1	0
	b_r, b_b, b_g	$4.18^{+0.04}_{-0.03} \times 10^3$	$-1/3$	0	0	0	0	0	-1

corresponding electron, muon, and tau neutrinos are neutral and only interact via the weak force. Although neutrinos are postulated to be massless in the SM, they are known to be massive due to the experimental observation of neutrino oscillations. Corresponding upper limits have been set on their masses. Table 2.3 [11] lists the quarks of the SM. Quarks have fractional electric charge and a broad range of masses, with the top quark being the heaviest known particle in the Standard Model. The quarks are also categorized into three generations. u, c, and t quarks have positive weak isospin and are known as up-type quarks; d, s, and b have negative weak isospin and are known as down-type quarks. The (u, d), (c, s), and (t, b) weak doublets define the three generations. Quarks can interact by the electromagnetic, strong, and weak interactions. Each has a flavour quantum number of U, D, C, S, T, or B', which, similarly to lepton flavour, is conserved except for in the weak interaction.[2] Interactions between quarks and gluons are governed by the strong force. Quarks have colour charge of red, blue, or green, and gluons carry simultaneous colour and anti-colour (anti-red, anti-blue, or anti-green). Quarks are found in colour-singlet combinations and cannot exist on their own due to *colour confinement*, a dynamic consequence of $SU(3)_C$.[3] In addition, all charged fermions have a corresponding anti-particle with opposite charge, while neutrinos have corresponding neutral anti-neutrinos (unless the neutrino is a Majorana particle and therefore is its own anti-particle). Anti-quarks also carry anti-colour.

[2] B is commonly used as a label for baryon number, therefore B' is used to identify the beauty/bottom flavour quantum number.

[3] Quarks can exist on their own, but only at very high temperatures in quark-gluon plasma.

2.1.2 Fundamental interactions

Quantum electrodynamics (QED) is governed by the interaction vertex shown in Figure 2.1. Photons mediate electromagnetic interactions between charged fermions. Charged fermions can radiate photons, fermion/anti-fermion pairs can annihilate to produce a photon, and a fermion/anti-fermion pair can be produced from photon pair production. Fermions can also scatter off one another by exchanging a photon. The strength of this interaction grows with α, the fine structure constant, which is proportional to the square of the electric charge. The interaction strength between two charged particles changes with distance and energy; this is due to charge screening produced by polarization of the vacuum (involving virtual electron-positron pairs). Hence the coupling constant is not actually constant and "runs"; $\alpha \approx 1/137$ at m_e, and $\alpha \approx 1/127$ at m_Z.

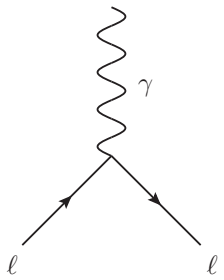

Figure 2.1: Fundamental vertex of QED.

The fundamental weak interaction vertices are illustrated in Figures 2.2 and 2.3. The Z boson mediates neutral current interactions between fermions. This is similar to the photon, but the Z also interacts with neutral fermions (i.e. neutrinos). In these processes there is no net charge flow. In contrast, the W boson is responsible for charged current interactions. The central diagram represents a flavour-conserving interaction (ℓ and ν_ℓ are of the same generation/flavour). The vertex on the right represents an interaction that is not flavour-conserving (e.g. q is an up-type quark and q' is a down-type quark). The probability for a given quark to change generation is governed by the CKM matrix. The strength of these diagrams is proportional to the weak coupling constant, $\alpha_w \approx 1/30$ [14].[4]

[4] α_w is larger than α despite being denoted as "weak." The strength of the weak force depends on the propagator $1/|q^2 - m^2c^2|$, where q is the momentum transfer of the interaction and $m \approx m_W$ or m_Z. The force is weak when the difference between q^2 and m_W^2 is large. At the LHC it is typical to have $q^2 > m_W^2 c^2$, but electroweak corrections remain important.

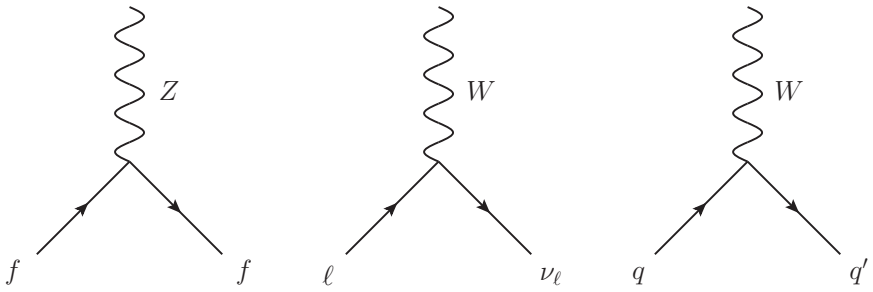

Figure 2.2: Fundamental weak vertices including fermions.

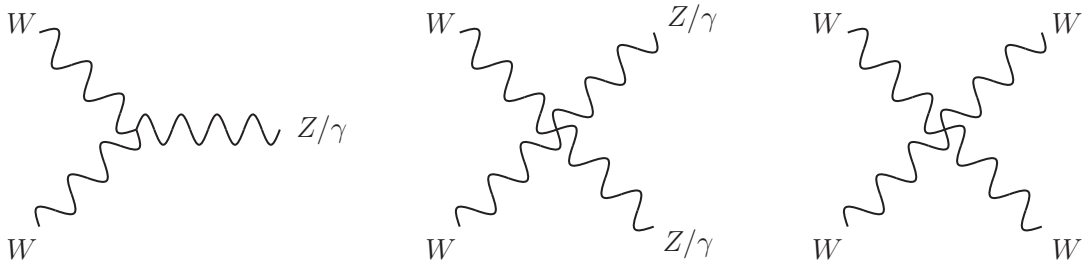

Figure 2.3: Fundamental weak vertices including gauge bosons only.

The fundamental QCD vertices are shown in Figure 2.4. Gluons mediate the strong interaction between quarks and also interact with each other. As for electric charge, charge screening also occurs for colour charge. However, gluons also carry colour (unlike the electrically neutral photon), so not only do quark/anti-quark pairs polarize the vacuum, but so do gluons via self-interactions; as a consequence of this, the strong force between two quarks becomes stronger with distance. In other words, α_s also runs, but unlike α it becomes large at low energies and larger distances. $\alpha_s \approx 1$

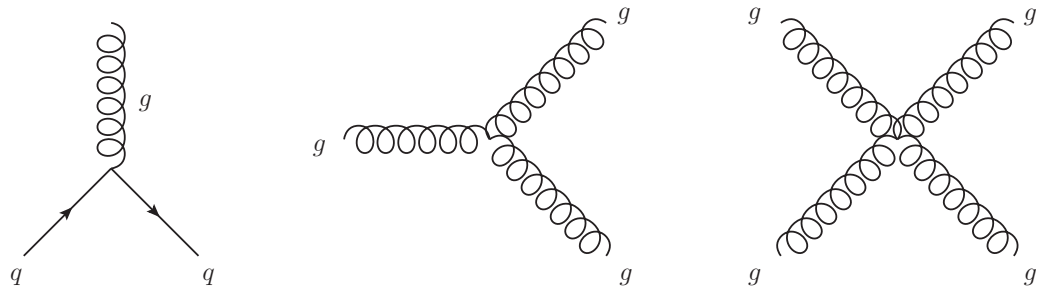

Figure 2.4: Fundamental vertices of QCD.

at energies near hadronic mass scales, and the theory becomes non-perturbative. As the energy increases α_s becomes increasingly weak, and in the limit as the energy approaches infinity, $\alpha_s = 0$; this is known as *asymptotic freedom* [15], [16].

Colour confinement has staggering implications in hadronic collisions. Hadrons are colourless bound states of quarks. During a collision, if two quarks become separated by a large enough distance, it becomes energetically favourable to produce more quarks and/or gluons from the vacuum. Because of this, quarks cannot exist in isolation, and will instead produce showers of quarks and gluons known as jets. Furthermore, the three *valence* quarks that make up the hadron do not simply exist on their own, but are surrounded by *sea* quark/anti-quarks and gluons, which can also interact during a collision. The valence quarks, sea quarks, and gluons that make up hadrons are collectively known as partons. Because of colour confinement, cross sections for QCD interactions between initial-state hadrons cannot be computed directly. Instead, the hadron structure functions are approximated using parton distribution functions (PDFs) [18]; these functions represent the probability density for a parton to carry fractional momentum x of the hadron at a given energy scale Q^2. Examples of MMHT14 PDF sets are shown in Figure 2.5 [17]. The contribution from gluons (g) and sea quarks (q and $\bar{q}$) becomes large at low momentum fraction x, whereas the valence quarks (q_V) have definite peaks. PDFs are obtained empirically from deep inelastic scattering and hard scatter measurements in an energy regime

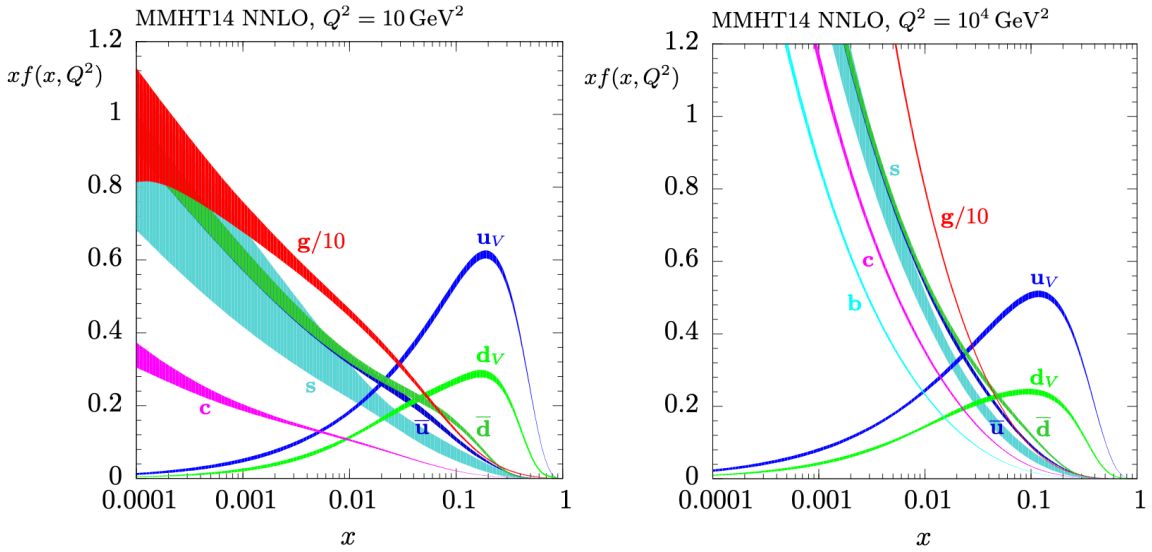

Figure 2.5: MMHT14 parton distribution function of the proton for momentum transfer $Q^2 = 10$ GeV^2 (left) and 10^4 GeV^2 (right) [17].

where α_s is small, and are then evolved to other energies using the DGLAP equations [19, 20, 21]. PDFs are essential for computing cross sections and simulating parton showers at hadron collider experiments.

2.2 Beyond the Standard Model: Dark matter

2.2.1 Overview

While the nature of dark matter is unknown, experimental observations provide some insight into its behaviour. From CMB measurements it is known that DM makes up 84% of all matter in the universe [1]. It is non-baryonic and has mass, and hence interacts gravitationally. It is also electrically neutral and stable over the lifetime of the universe. Depending on its mass, dark matter can be described as cold, warm, or hot. The ΛCDM model of cosmology generally favours cold, slow-moving dark matter; however, there is not enough small-scale structure observed to fully support cold DM models, suggesting that DM might instead be warm [22]. Models for relativistic, hot dark matter, e.g. neutrinos, are generally disfavoured.

There are many theories that attempt to explain what dark matter is. Some theories predict that DM can be explained by macroscopic objects, such as massive astrophysical compact halo objects (MACHOs), or by the modification of the theory of gravity (e.g. modified Newtonian dynamics or MOND); however, theories such as these do not consistently describe all observed properties of DM [23, 18]. In general most theories predict that dark matter is a particle.

Many potential dark matter candidates have been proposed in order to explain other BSM physics, not necessarily DM. For example, the QCD axion was originally theorized by Peccei and Quinn to explain the lack of charge-parity (CP) violation in QCD [24]; their theory introduces a new global $U(1)$ symmetry that is spontaneously broken to produce a new particle, the axion. A more general class of particles known as axion-like particles (ALPs) has also been theorized. The properties of axions and ALPs qualify them as good dark matter candidates. Sterile neutrinos are another proposition; since the SM has been shown experimentally to only contain left-handed chiral neutrinos, an extension that includes inert right-handed chiral neutrinos is not theoretically forbidden; in addition, the existence of heavy sterile neutrinos could explain the smallness of the neutrino masses via the seesaw mechanism [25]. Another potential candidate is the dark photon, which is is theorized to interact weakly with

charged particles and the SM photon, hence providing a "portal" into a dark sector of particles that could be equally as complex as the SM [26].

There are many astronomical constraints on the properties of the dark matter particle, which depend on the assumed model and the physics of the measurement. For example, one analysis of the CMB anisotropies obtained a lower limit on the DM mass of $m > 70$ eV [27]. A stronger constraint is obtained from measurements of the Lyman-α forest; the spectra produced by distant quasars are affected by Lyman-α absorption lines produced by clouds of intergalactic neutral hydrogen atoms. The frequency of the absorption lines varies depending on the redshift of the hydrogen clouds, producing a "forest" of lines. Measuring these lines allows for the study of the matter power spectrum between galaxies. These measurements require $m > 3.3$ keV [28]. Finally, the Bullet cluster is used to place constraints on the DM self-interaction cross section. The two colliding galaxies are studied using X-ray spectroscopy and gravitational lensing; by analysing the collision of the visible matter compared to the dark matter, the amount of DM mass loss can be measured. This sets a constraint on the self-interaction at $\sigma/m < 1$ cm^{2}g^{-1} [29]. For a particle with a mass of 100 GeV, this sets an upper limit on the cross section of $\sigma \leq 10^{-23}$ cm$^2 = 10$ b.

2.2.2 The case for WIMP dark matter

Several theories hypothesize the existence of dark matter as a *weakly interacting massive particle* (WIMP). The primary motivation for the WIMP comes from the *relic abundance* of dark matter that exists today [30]. From the CMB it is known that DM existed since the early universe, so it is assumed that DM particles were at some point in thermal equilibrium with SM particles, meaning that the dark matter number density was constant (annihilation rate = production rate). However, as the universe expanded, inflation caused a disruption to this equilibrium; the dependence of the number density on the Hubble expansion rate is described using the Boltzmann equation. When the DM annihilation rate becomes less than the expansion rate, then the number density of DM in the universe freezes out. This relic density can be approximated in terms of a hypothetical particle mass and coupling strength parameter. For a coupling with the same order of magnitude as the weak scale and $m \sim 100$ GeV, the observed relic density in the universe is obtained. This is the so-called "WIMP miracle," and is motivation to search for dark matter that interacts at the weak-scale.

Many theories predict the existence of a WIMP. Perhaps the most famous such theory is supersymmetry (SUSY) at the weak scale, a theory that was proposed in part to solve the hierarchy problem in the Standard Model; in the Minimal Supersymmetric Standard Model (MSSM), the lightest supersymmetric particle is stable and neutral, and is a candidate for WIMP dark matter. However, since its proposal in the 1970's, there has been no evidence yet to support the existence of SUSY. As a consequence, the study of simpler theories has become a priority in dark matter searches at the LHC.

2.2.3 Simplified models

During Run 1 data-taking from 2010-2012 at 7 and 8 TeV, effective field theories (EFTs) were used successfully to study dark matter signatures in a relatively model-independent way. In these models, the Standard Model is minimally modified to allow for a contact interaction between quarks and DM particles. The model adds non-renormalizable operators to the Lagrangian that depend on the DM particle mass and an effective scale Λ. Such a theory is desirable because of its simplicity, but for momentum transfers $q^2 \gg \Lambda^2$ the perturbativity of EFT models breaks down. For Run 2 LHC energies that are capable of producing DM particles with mass $\mathcal{O}$(TeV), EFTs are in general not reliable.

The recommendations for LHC dark matter searches are coordinated by the LHC Dark Matter Working Group. In their Run 2 recommendations [31], *simplified models* are the prioritized model for the ATLAS and CMS collaborations to study. In this type of model, the Standard Model is extended to include a $U(1)$ gauge symmetry under which the DM particle (a Dirac fermion, denoted χ with anti-particle $\bar{\chi}$) is charged. The SM quarks are also charged under the new group. A mediator particle, Z', governs the interactions between quarks and DM. Of particular interest to LHC searches are models involving spin-1 mediators that have either -1 parity (vector) or $+1$ parity (axial-vector). Models with spin-0 mediators are also relevant but are not yet considered in the analysis because their cross sections are $\sim 10^4$-10^6 times smaller than spin-1 models with otherwise identical parameters. In addition, the analysis focuses on s-channel simplified models, where DM is produced via $q\bar{q} \to Z' \to \chi\bar{\chi}$. t-channel simplified models [32] with a coloured scalar mediator were investigated, but the analysis was shown to have exclusion power only for a small mass range, so these models were not pursued further (see Appendix A for more details).

The SM Lagrangian is modified to include dark matter interactions. The respective vector and axial-vector interaction terms are given as

$$\mathcal{L}_{\text{vector}} = -g_q \sum_q \left({Z'}_\mu \bar{q} \gamma^\mu q + g_\chi {Z'}_\mu \bar{\chi} \gamma^\mu \chi \right) \tag{2.2}$$

$$\mathcal{L}_{\text{axial-vector}} = -g_q \sum_q \left({Z'}_\mu \bar{q} \gamma^\mu \gamma^5 q + g_\chi {Z'}_\mu \bar{\chi} \gamma^\mu \gamma^5 \chi \right) \tag{2.3}$$

where q is any flavour quark, g_q is the Z'-q coupling (universal for all quarks), g_χ is the Z'-χ coupling, and γ^μ and γ^5 are the Dirac matrices. Overall the model introduces five additional parameters to the SM:

$$\{m_\chi, m_{\text{med}}, \Gamma_{\text{med}}, g_\chi, g_q\} \tag{2.4}$$

m_χ is the DM mass, m_{med} is the mass of the vector or axial-vector mediator, Γ_{med} is the width of the mediator, and g_χ and g_q are the couplings as mentioned. The mediator width is not considered to be a free parameter of the model, as it can be calculated using the other four parameters ("minimal width" Equations 2.3 and 2.4 in [31]). In addition, the recommended coupling values are $g_\chi = 1.0$ and $g_q = 0.25$. This leaves m_χ and m_{med} as the two main parameters to study. If no evidence of dark matter is found, one of the final results of the analysis is a 2D m_χ-m_{med} limit identifying the mass parameter space that is excluded by the search. In addition, the results are transformed into limits on the DM-nucleon scattering cross section, the standard result from direct detection experiments.

Simplified models produce dark matter via $q\bar{q} \to Z' \to \chi\bar{\chi}$.[5] As will be discussed in more detail, the $\chi\bar{\chi}$ final state is invisible to the ATLAS detector. In order to measure such a signature, searches of this type require the use of a SM particle, referred to generically as X, that is used to identify potential DM events. X is usually emitted in the initial state by one of the quarks, and recoils against the invisible $\chi\bar{\chi}$ pair. This is called a "mono-X" signature. The mono-Z signature is relevant to this dissertation; some contributions are illustrated in Figure 2.6. The simplified models studied include next-to-leading order (NLO) diagrams in QCD (calculated up to order α_s^2). Furthermore, the analysis studies mono-Z signatures where the Z

[5] Resonance searches look for simplified model DM in signatures where the mediator decays back into Standard Model particles. For example, the di-jet search looks for a DM mediator produced via $q\bar{q} \to Z' \to q\bar{q}$.

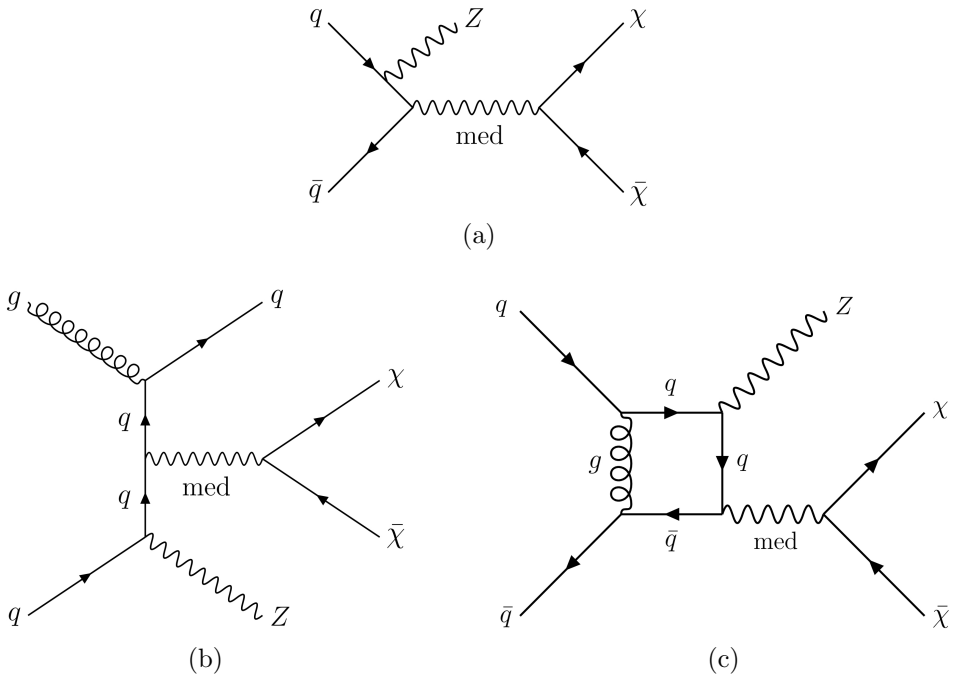

Figure 2.6: Simplified model Feynman diagrams that produce mono-Z signatures. The leading-order (LO) diagram is shown in (a), while (b) and (c) show example NLO diagrams.

decays leptonically to either e^+e^- or $\mu^+\mu^-$.[6]

While simplified models improve on the major theoretical issues of EFTs, they are not without their own problems. For example, for axial-vector s-channel models, at high energies the coupling between fermions and the longitudinal mode of the mediator is enhanced by the ratio m_χ/m_{med}. When considering self-scattering of DM particles, the model is only perturbative when [33]

$$m_\chi \lesssim \sqrt{\frac{\pi}{2}}\frac{m_{\text{med}}}{g_q}. \tag{2.5}$$

Even so, the model still breaks unitarity for other processes where the longitudinal component of the mediator is an external line. Hence the model is only valid in specific energy regimes and is therefore not UV complete. In addition, vector and axial-vector models allow for the mediator to couple differently to up- and down-type quarks, rather than coupling to the left-handed quark doublet. This means that in general

[6]While the Z also decays into $\tau\bar{\tau}$ with equal probability, the τ is unstable because of its mass and decays most often into final states including pions and neutrinos. Analysis of hadronic final states requires different strategies compared to leptonic final states, and the presence of a final-state neutrino means that the mass of the Z cannot be reliably determined.

they are not gauge invariant under the full SM group $SU(3)_C \times SU(2)_L \times U(1)_Y$ [34]. Because of limitations such as these, there is motivation to study more theoretically complete models in addition to simplified models.

2.2.4 2HDM+a models

The LHC Dark Matter Working Group also recommends the study of *two-Higgs-doublet models* (2HDMs) that include an additional pseudo-scalar mediator, a [35]. 2HDMs are UV complete and allow for a wide variety of phenomenologies. As suggested by the name, this type of model introduces a second SU(2) weak isospin doublet to the Standard Model. The presence of a second Higgs doublet is necessary for many well-motivated BSM theories. For example, two Higgs doublets are required in the MSSM and in QCD axion theories. Furthermore, a second Higgs doublet could also explain the large matter-antimatter asymmetry observed in the universe [36]. One of the Sakharov conditions necessary to explain how baryogenesis could produce matter and antimatter at different rates is that CP must be violated. CP violation is already present in the CKM matrix of the SM, but it is not large enough to account for the dominance of matter that is observed. With a second scalar Higgs, it is possible to include additional sources of CP violation large enough to explain such a significant dominance of matter over antimatter [37].

In 2HDMs, the Standard Model is modified to include fermion couplings to the two doublets H_1 and H_2 [35]:

$$\mathcal{L}_Y = -\sum_{i=1,2} \left(\bar{Q} Y_u^i \tilde{H}_i u_R + \bar{Q} Y_d^i H_i d_R + \bar{L} Y_\ell^i \tilde{H}_i \ell_R + \text{h.c.} \right) \tag{2.6}$$

Q and L are the left-handed quark and lepton doublets, u_R, d_R, and ℓ_R are the right-handed up-type quark, down-type quark, and lepton singlets, and Y_f^i are the Yukawa couplings. In 2HDM+a models, the $U(1)$ pseudo-scalar singlet P is also added and couples directly with the DM particle via [35]

$$\mathcal{L}_\chi = -i g_\chi P \bar{\chi} \gamma_5 \chi, \tag{2.7}$$

where g_χ is the coupling strength between the pseudo-scalar and dark matter particle.

There are several categories of 2HDMs; the ones studied here are of type-II, meaning that the Yukawa interactions are such that up-type and down-type quarks couple to different doublets, and the leptons couple to the same doublet as the down-type

quarks. This is equivalent to setting $Y_u^1 = Y_d^2 = Y_\ell^2 = 0$ in Equation 2.6. This type of 2HDM is flavour-conserving.[7] The doublets H_1 and H_2 can be parameterized in terms of six field components and two real, positive VEVs, totalling eight degrees of freedom, plus one more for the additional pseudo-scalar. After spontaneous symmetry breaking, these nine degrees of freedom are rearranged to form the $W^\pm$ and Z bosons, the dark pseudo-scalar mediator a, and five new Higgs CP eigenstates: two neutral scalars h and H, an additional pseudo-scalar A, and two charged scalars $H^\pm$. h and H are CP-even mass eigenstates. A and a are CP-odd mass eigenstates, and both couple to $\chi\bar{\chi}$.

The main 2HDM+a Feynman diagrams relevant to the mono-Z search are shown in Figures 2.7 and 2.8. Signals are produced through gg-fusion or via $b\bar{b}$ production.[8] A and a can be produced in association with a Z boson through a top quark loop, or by resonant production of H or A, which can then decay directly to $Z + a$. The sizeable coupling between the Z and the H and A bosons makes the mono-Z signature one of the most sensitive search channels for 2HDM+a models.

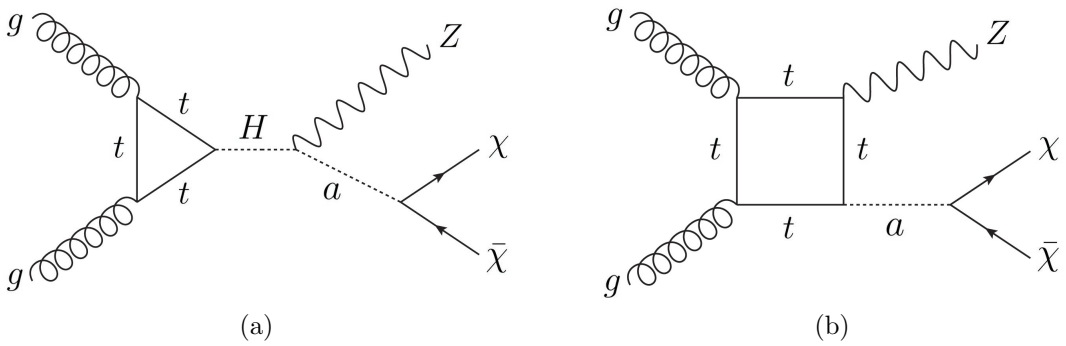

Figure 2.7: 2HDM+a model Feynman diagrams that produce mono-Z signatures via gg-fusion. H can be replaced with A in (a), and a can be replaced with A in (b).

[7] One problem with 2HDMs is that they can introduce tree-level flavour-changing neutral currents (FCNCs), whereby the flavour of a particle changes without a change in electric charge. In the SM, the Yukawa interactions are automatically diagonalized along with the mass matrix; this forbids FCNCs in the Standard Model at tree-level, and they only appear in higher-order corrections where they are suppressed by the GIM mechanism. With two Higgs doublets, the Yukawa interactions are in general not diagonalizable. Therefore, in order to be compatible with this property of the Standard Model and experiment, any viable 2HDM must forbid or suppress tree-level FCNCs. Type-II models naturally exclude tree-level FCNCs by requiring all right-handed quarks of a given charge to couple to a single Higgs doublet [38].

[8] $b\bar{b}$ becomes the dominant production mode at high $\tan\beta$ because the coupling of H, A, and a to bottom quarks is proportional to $\tan\beta$.

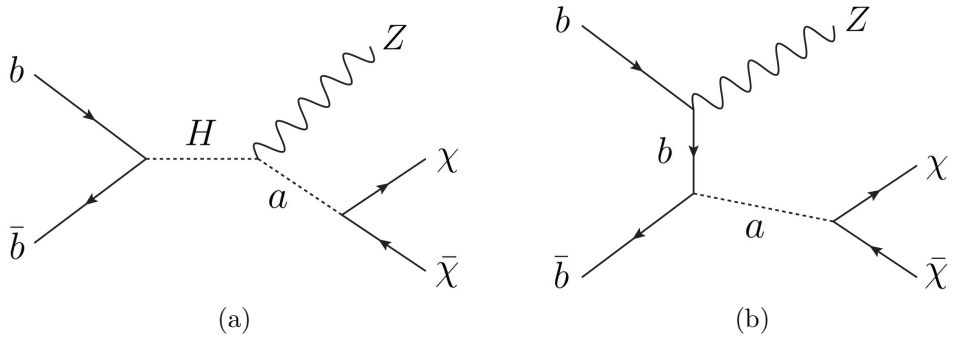

Figure 2.8: 2HDM+a model Feynman diagrams that produce mono-Z signatures via bb-induced production. H can be replaced with A in (a), and a can be replaced with A in (b).

In total there are 14 free parameters in 2HDM+a models [39]:

$$\{m_h, m_H, m_{H^\pm}, m_A, m_a, m_\chi, \lambda_{\mathrm{P1}}, \lambda_{\mathrm{P2}}, \lambda_3, g_\chi, v, \tan\beta, \alpha, \theta\} \tag{2.8}$$

m_h, m_H, $m_{H^\pm}$, m_A, and m_a are the scalar/pseudo-scalar masses, and m_χ is the DM particle mass. The λ parameters are the quartic couplings between the doublets and pseudo-scalar singlet. g_χ is the pseudo-scalar/DM coupling as seen in Equation 2.7, v is the Higgs field VEV (246 GeV), $\tan\beta$ is the ratio of the two VEVs, and α and θ are the mixing angles of the neutral CP-even (scalar) and CP-odd (pseudo-scalar) weak eigenstates respectively. m_h and v are fixed by observation.

Several assumptions are made in order to reduce the number of free parameters in these models. The alignment limit is assumed so that the lighter of the two CP-even mass eigenstates, h, is identified as the SM Higgs boson. Hence $m_h = 125$ GeV and $m_H > m_h$. The mass of the pseudo-scalars is restricted so that $m_A > m_a$. To further simplify the phenomenology and evade constraints from electroweak precision measurements, $m_A = m_H = m_{H^\pm}$ in all models. λ_3 is set to 3 to ensure stability of the Higgs potential, and $\lambda_{\mathrm{P1}} = \lambda_{\mathrm{P2}} = 3$ as well to maximize the trilinear couplings between CP-even and CP-odd neutral eigenstates. For 2HDM+a searches the DM mass is also fixed, putting the focus more on searching for the pseudo-scalar mediators a and A. To ensure a sizeable branching ratio of $a \to \chi\bar{\chi}$ for $m_a > 100$ GeV, the DM coupling and mass are set to $g_\chi = 1$ and $m_\chi = 10$ GeV. These assumptions [35] collectively reduce the total number of free parameters to four: m_a, m_A, $\tan\beta$ and $\sin\theta$.

If no dark matter signal is observed, exclusion limits are set for the four free parameters in a total of eight exclusion scans:

- 1D sinθ scan for sinθ = [0.1-0.9] (m_A = 1000 GeV, m_a = 350 GeV, tanβ = 1.0)
- 1D sinθ scan for sinθ = [0.1-0.9] (m_A = 600 GeV, m_a = 200 GeV, tanβ = 1.0)
- 2D (tanβ, m_A) scan for tanβ = [0.3-20], m_A = [300-2000] GeV (m_a = 250 GeV, sinθ = 0.35 and 0.7)
- 2D (tanβ, m_a) scan for tanβ = [0.3-20], m_a = [100-500] GeV (m_A = 600 GeV, sinθ = 0.35 and 0.7)
- 2D (m_A, m_a) scan for m_a = [100-500] GeV, m_A = [300-2000] GeV (tanβ = 1.0, sinθ = 0.35 and 0.7)

This choice of benchmark scans and parameters is agreed upon by the LHC Dark Matter Working Group. The details of these recommendations are covered in Chapter 4 of [35].

2.2.5 Invisible Higgs decays

The Higgs boson may itself be a portal to dark matter. Of particular interest is the rate at which the Higgs decays to invisible particles. The SM predicts that the Higgs decays invisibly via $h \to ZZ \to 4\nu$ with a branching ratio of 0.1%. If this branching ratio is found to be larger than predicted, then this would indicate BSM physics. The ATLAS experiment has yet to measure $h \to ZZ \to 4\nu$; the current best upper limit on the branching ratio is 26%, obtained using 36.1 fb^{-1} from the combination of Run 1 and partial Run 2 datasets [40].

The focus of this dissertation is the search for dark matter in the mono-Z final state with the full Run 2 dataset, and its interpretation within simplified models and 2HDM+a models. It should be noted, however, that the mono-Z analysis is combined with an invisible Higgs search in which h is produced in association with a Z boson; the Higgs decays to invisible particles and the Z decays leptonically, yielding the same $Z(\ell\ell)$ + invisible final state of interest as in the mono-Z search. While the analysis strategy is influenced by the combination of searches, only mono-Z results will be presented in this dissertation.

Chapter 3

The ATLAS Experiment

3.1 The Large Hadron Collider

The LHC is located at the CERN laboratory near Geneva, Switzerland, and lies along the border with France. The 27 km tunnel that now contains the LHC was first occupied by the Large Electron Positron (LEP) collider from 1989-2000, which carried out e^+e^- collisions at up to 209 GeV. The LEP tunnel was modified in 2001 to make way for the LHC, which has been in operation since 2010. An illustration of the CERN complex as it is today is shown in Figure 3.1. The protons used in the LHC first begin their journey from a canister of hydrogen gas. The gas is ionized to produce free protons (H^-) that are then accelerated to 50 MeV by the linear accelerator LINAC 2. They are then injected into the facility's smallest synchrotron, the Proton Synchrotron Booster (PSB), in which they are accelerated to 1.4 GeV. The next stage is the Proton Synchrotron (PS), which accelerates the protons to 25 GeV, followed by the Super Proton Synchrotron (SPS), which in turn accelerates them to 450 GeV. The protons are then split into two beams and injected into the LHC. The two beams circulate the ring in different pipes and in opposite directions. It takes about 20 minutes to completely fill the LHC, and another 25 minutes to ramp up the energy of each beam to 6.5 TeV. Collisions occur at 13 TeV centre-of-mass energies at designated interaction points (IPs) that are located at the four main detector sites along the LHC ring. Collisions may occur for up to 10 hours before the beams are dumped due to significant intensity degradation.

Proton beams are not continuous streams of particles, but instead are made up of bunches of protons that occupy "buckets" along the beam. This structure is governed

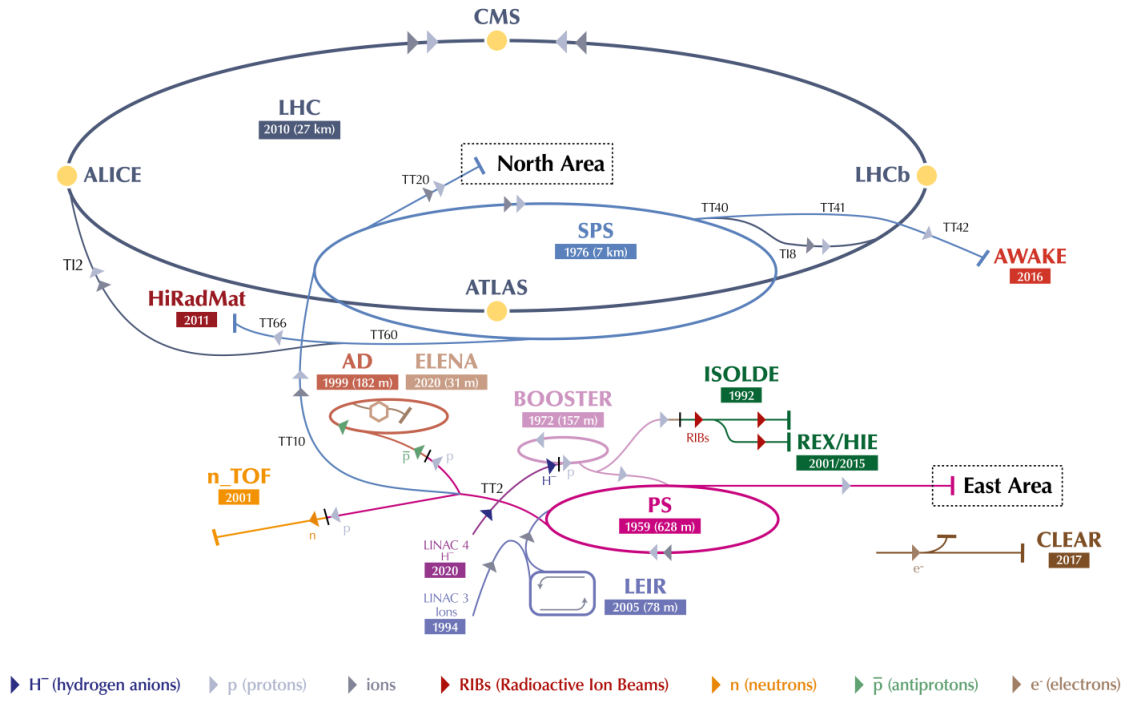

Figure 3.1: The CERN accelerator complex [41].

by the radio-frequency (RF) cavities that are used to accelerate the protons along the LHC ring. An RF cavity consists of an electric field that oscillates between two directions. If a proton enters the cavity with exactly the right timing and energy (known as a synchronous proton), it will experience zero acceleration as it passes through; if a proton enters the cavity and does not have the ideal timing or energy, it will be physically accelerated or decelerated towards that synchronous frequency. This forces the protons into discrete packets known as bunches. If the RF frequency is tuned to be an integer value (i.e. a harmonic) of the accelerator's revolution frequency, then stable regions called buckets can be formed. The LHC RF cavities operate at a frequency of $f_{\mathrm{RF}} = 400$ MHz , and the revolution frequency for a proton is $f_{\mathrm{rev}} = 11.245$ kHz. Setting $f_{\mathrm{RF}} = nf_{\mathrm{rev}}$, this gives $n \approx 35640$ buckets. Any number of buckets can be filled with bunches or be left empty. At the LHC, only every 10th bucket is considered, meaning a maximum of 3564 buckets can be used. This number is further reduced to 2808 buckets to facilitate beam control and to ensure that bunches collide at the four detector IPs.

Once the beams are circulating at maximum energy, they are squeezed into collision at each IP. Given that $f_{\mathrm{RF}} = 400$ MHz, and that at most every 10th bucket

is used, the minimum time between a bunch crossing is $1/f_{\mathrm{RF}} \times 10 = 25$ ns. For a proton revolution frequency of 11.245 kHz, and assuming the nominal number of buckets of 3564, this corresponds to 11.245 kHz $\times$ 3564 = 40 million bunch crossings per second. Each bunch contains 1.2×10^{11} protons, but the probability for two protons to collide is very small; in Run 2 there was an average of 34 proton-proton collisions per bunch crossing. At a crossing rate of 40 MHz, this corresponds to more than 1 billion proton-proton collisions per second.

3.2 The ATLAS Detector

The ATLAS (**A** **T**oroidal **L**HC **A**pparatu**s**) detector [43] is one of the two multipurpose particle detectors at the LHC. A schematic of the detector is shown in Figure 3.2 [42]. Assembly took place from 2003-2008, with the Run 1 data-taking period taking place from 2010-2012 at 7 and 8 TeV centre-of-mass energies, and Run 2 from 2015-2018 at 13 TeV. The ATLAS detector is positioned at one of the four LHC IPs, and protons are brought to collision at its centre. It was designed to measure a variety of particle signatures. Several technologies are used to serve this purpose. The

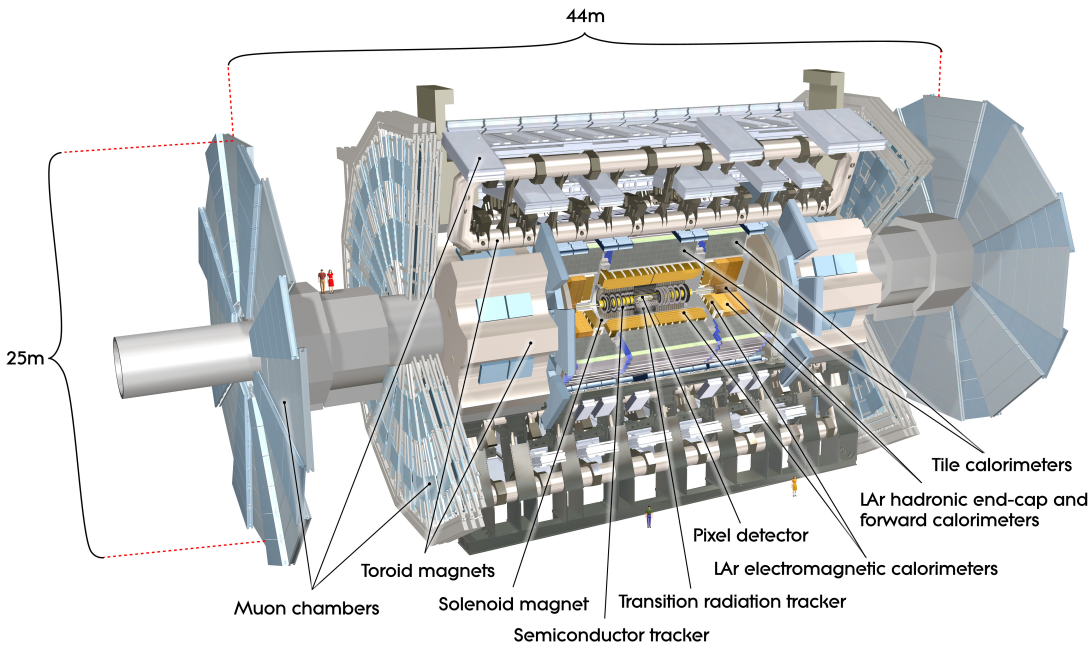

Figure 3.2: Computer generated image of the ATLAS detector [42].

innermost layer of the detector is known as the inner detector, which is designed to measure tracks of charged particles. The middle layers consist of the electromagnetic and hadronic calorimetry systems, in which particles shower and deposit energy. The largest and outermost systems make up the muon spectrometer, designed to measure the tracks of muons which are able to escape the detector. Each subsystem has barrel and end-cap components; the barrel components are cylindrical and lie parallel to the beam pipe, whereas the end-cap components are disk-shaped and intersect the beam axis beyond the barrel.

The large size of the ATLAS detector and its magnet systems is also noteworthy. An important motivation for the design of the ATLAS detector was to search for the Higgs boson. For example, four leptons are produced in the "golden decay" $H \to ZZ \to 4\ell$, so maximizing energy and momentum resolution for the leptons was a priority. The momentum resolution of a charged particle improves when under the influence of a strong magnetic field (bends the path more), or when traversing a long path length (allows more time for the path to bend). The magnet designs of ATLAS and CMS were each chosen to prioritize one of these properties. The CMS approach uses a solenoid magnet that produces a 4 Tesla magnetic field; momentum measurements benefit from a strong field and precise tracking, but suffer from a high probability for multiple scatterings with dense detector material. The ATLAS approach is an air core toroid magnet; the magnetic field is only 2 Tesla, but a longer lever arm allows for precision to be recovered. The main downside to this approach is that the magnetic field is very complicated and must be carefully mapped.

In the ATLAS detector coordinate system, the x-axis points into the centre of the LHC ring, the y-axis points upward, and the z-axis lies parallel to the beam pipe. (θ, ϕ) coordinates are commonly used, where θ is the polar angle measured from the z-axis, and ϕ is the azimuthal angle around the z-axis. Furthermore, the polar angle is frequently replaced by the pseudorapidity:

$$\eta = -\ln\left[\tan\left(\frac{\theta}{2}\right)\right] \tag{3.1}$$

This quantity is preferred to θ because particles are generally produced uniformly as a function of η (less perpendicular to the z-axis, more towards the z-axis), and differences in η values are Lorentz invariant with respect to longitudinal boosts along the z-axis; the latter is particularly useful in hadron collisions where the interacting partons each carry some longitudinal momentum, and hence the rest frame of the

collision has an a priori unknown boost along the z-axis.

3.2.1 Inner detector

The inner detector (ID) is located at the centre of the ATLAS detector, directly outside the beam pipe. Its purpose is to provide highly granular charged particle track measurements. The ID is encased in the ATLAS solenoid magnet, which supplies a 2 Tesla magnetic field and bends charged particle paths in the azimuthal direction.

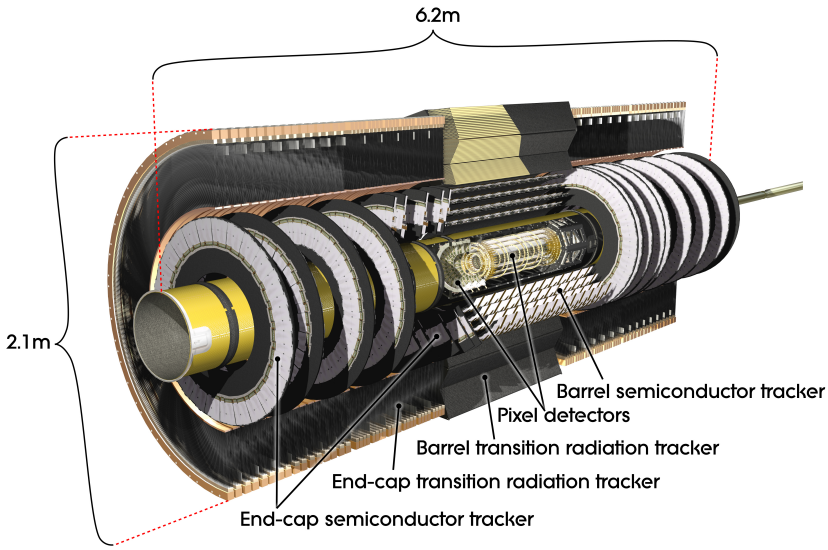

Figure 3.3: Computer generated image of the ATLAS inner detector [44].

A diagram of the ID [43] is shown in Figure 3.3 [44]. The ID is composed of three subsystems: the pixel detector and semiconductor tracker (SCT) cover $|\eta| < 2.5$, and the transition radiation tracker (TRT) which covers $|\eta| < 2.0$. The pixel detector and SCT are composed of silicon pixel modules and silicon microstrips respectively. When a charged particle passes through one of these sensors, electrons are ejected from the silicon atoms and a current is produced. The pixel detector is closest to the IP and provides the highest granularity of spatial measurements, with a minimum pixel size of 50×400 μm^2. Each track is measured across three layers in the pixel detector and eight layers in the SCT. The TRT typically provides 36 track measurements, and is composed of straw tube ionization chambers. The space between the tubes is filled with a matrix of polymer materials that has different dielectric properties than the tubes themselves. Transition radiation is produced when a charged particle passes through two media with different dielectric constants; the profile of the transition

radiation allows the TRT to provide discrimination between electrons and pions, in addition to prioritizing track measurements.

Before Run 2 began, the ID was upgraded to include a fourth layer between the beam pipe and innermost pixel layer, a distance of 3.3 cm from the beam axis. This insertable b-layer (IBL) was designed to improve on the tracking efficiency of the ID, with 50×250 μm^2 pixels and other technological improvements [45]. A new, smaller beam pipe was installed in the ATLAS detector to accommodate this extension.

3.2.2 Calorimeters

The ATLAS calorimeters [43] are designed to induce and measure electromagnetic and hadronic showers. Figure 3.4 [46] illustrates the layout of each main subsystem. The electromagnetic and hadronic calorimeters are sampling calorimeters, consisting of alternating layers of absorber and detector materials. Absorber layers are dense (e.g. lead, copper, steel) and are used to induce showers and absorb their energy; detector layers are used to measure particle energies, and usually consist of scintillators or gas/liquid ionization chambers.

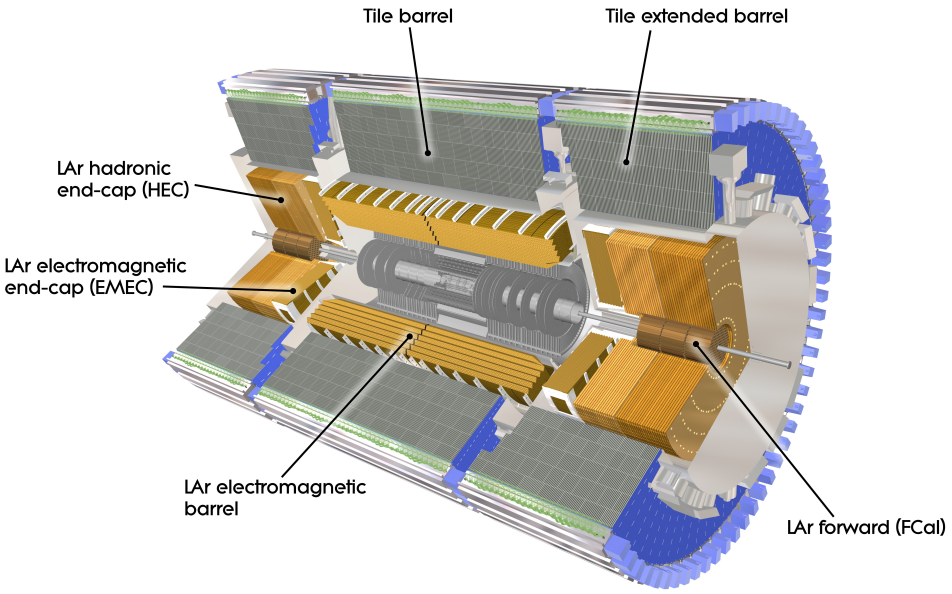

Figure 3.4: Computer generated image of the ATLAS calorimeters [46].

The electromagnetic calorimeter is designed to measure electromagnetic showers produced by photons and electrons. It lies just outside the solenoid magnet, and is di-

vided into barrel (EMB) and end-cap (EMEC) systems. The EMB covers $|\eta| < 1.475$, and the EMEC covers $1.4 < |\eta| < 3.2$. Lead absorbers and liquid argon (LAr) ionization chambers are the primary technologies used throughout the EMB and EMEC. In addition to providing high signal rates in regions of large flux near the beam line, LAr does not denature and is robust to radiation damage. Electromagnetic showers ionize the LAr, and an electric field causes the ions to drift, producing a current proportional to the deposited energy. The electronic readout is done in transverse segments known as cells. In addition, the LAr calorimeter has an accordion-shaped geometry that allows for continuous azimuthal coverage.

Hadrons typically begin showering in the electromagnetic calorimeter but deposit most of their energy in the hadronic calorimeter. The hadronic calorimeter surrounds the electromagnetic calorimeter, and is composed of the tile calorimeter in the barrel/extended barrel regions, and LAr calorimetry in the hadronic end-cap (HEC) and forward (FCal) systems. The tile calorimeter covers $|\eta| < 1.7$. Steel is used as the absorber material, and plastic scintillators are used in the detector layers. Signals obtained from the scintillator tiles are directed to photomultiplier tubes (PMTs) and read out. The design of the tile calorimeter was chosen for its low cost and modular assembly. The barrel region also experiences much lower radiation levels than the end-cap and forward regions, so it does not need to be especially radiation hard. In the end-cap region, the HEC covers the range $1.5 < |\eta| < 3.2$. Copper is used as the absorber material, and LAr is again used in the ionization chambers.

The FCal covers the highest η region from $3.1 < |\eta| < 4.9$. It contains one electromagnetic and two hadronic components. LAr is again used in this high flux region as the detector layer. Copper absorber sheets are placed perpendicular to the beam line with hundreds of holes drilled into them, parallel to the beam. Copper (tungsten) electrodes are inserted into these holes in the EM (hadronic) modules which also act as absorber material. Optical readout fibres are wound around the electrode and lie in the LAr ionization gap inside the tube. This design allows for high signal rates and a very dense calorimeter.

3.2.3 Muon spectrometer

The muon spectrometer (MS) [43] is the outermost and largest subsystem of the ATLAS detector, and is illustrated in Figure 3.5 [47]. Its purpose is to measure the tracks of muons, which are capable of escaping the detector.

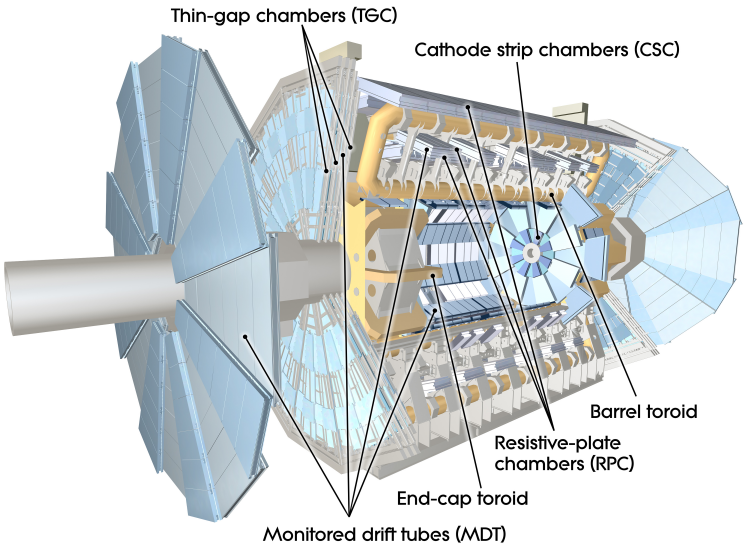

Figure 3.5: Computer generated image of the ATLAS muon spectrometer [47].

The barrel region ($|\eta| < 2.0$) is divided into eight octants to preserve symmetry with the eight coils of the toroid magnet. There are three radial layers of monitored drift tube (MDT) chambers in the barrel. Each tube consists of an anode wire in the centre of a cathode tube. The gas inside of the tube becomes ionized when a muon passes through; the charges collect on the anode wire, and a signal is read out. MDT chambers are stiff and robust, and provide high mechanical precision. The other main technology used in the barrel are resistive plate chambers (RPCs). RPCs are used for triggering on muon events and providing a second position measurement. They are paired with MDTs on the outer two rings of the muon spectrometer. Each RPC unit consists of two gas detector layers spanned by an electric field. Each gap is sandwiched by resistive graphite electrodes and are readout by strip panels. A signal is produced by the drift motion of avalanche electrons that form along the ionizing tracks.

The end-cap ($2.0 < |\eta| < 2.7$) also consists of multiple wheels of MDT chambers. In addition, cathode strip multi-wire proportional chambers (CSCs) are used close to the beam line, where radiation levels exceed the counting rate permissible for MDTs. The end-cap CSCs are arranged in a wheel formation at both ends of the detector. Each wheel is segmented in ϕ into eight small chambers and eight large chambers. Anode wires run radially outwards, and cathode strip layers run perpendicular to the wires, with a ionization chambers between. When a muon passes through and ionizes the gas, charges are collected onto the cathode strips. The position of the muon is

determined by interpolating the amount of charge deposition on each strip. Thin gap chambers (TGCs) are used for triggering in the end-cap. TGCs are ideal in the forward region because they provide finer granularity where there is less curvature in the muon paths due to the positioning of the end-cap toroids. They also provide a secondary ϕ measurement to complement the MDTs.

3.2.4 Trigger, data aquisition, and reconstruction

Collisions occur at a rate of 40 MHz, which is far too high to save every event to disk. The trigger system [43, 48] is responsible for identifying potentially interesting events and reducing the data output rate to about 1 kHz. The trigger is split into two main systems: the Level-1 (L1) hardware trigger, and the High-Level Trigger (HLT). The L1 trigger operates at the hardware level, and has dedicated access to data from the calorimeters and the RPCs and TGCs in the muon spectrometer. An event is likely to pass the L1 trigger if it contains a significant, localized energy deposit in the calorimeter(s), or an energetic muon in the spectrometer. A decision is made to either accept or reject the event within 2.5 μs. If an event is accepted, data from all detector subsystems is read out to buffers in the data acquisition system, where it is held until the HLT makes a decision. The HLT is a software-based trigger that utilizes more sophisticated requirements on the overall event kinematics and/or small regions of interest (RoIs). The average HLT processing time is 235 ms [48]. The maximum rate of 1 kHz is capped by the availability of computing resources at the HLT CPU farm. Once accepted by the HLT, event data are transferred to the ATLAS Tier-0 centre to undergo reconstruction. Particle objects are reconstructed from low-level detector signals. Track measurements in the ID and MS are used to reconstruct muons [49]. Electrons and tau leptons are reconstructed from a combination of energy deposits in the calorimeters and tracks in the ID [50, 51]. Photons and jets are primarily reconstructed from the calorimeter signals [50, 52]. Jets are reconstructed from calorimeter objects known as topological clusters that are formed according to the anti-k_t algorithm [53]. After reconstruction, events are moved to storage for offline analysis.

3.2.5 Proton-proton collisions and the Run 2 dataset

A proton-proton collision can be broken down into two main parts: the *hard scatter* and the *underlying event*. This is illustrated schematically in Figure 3.6. A

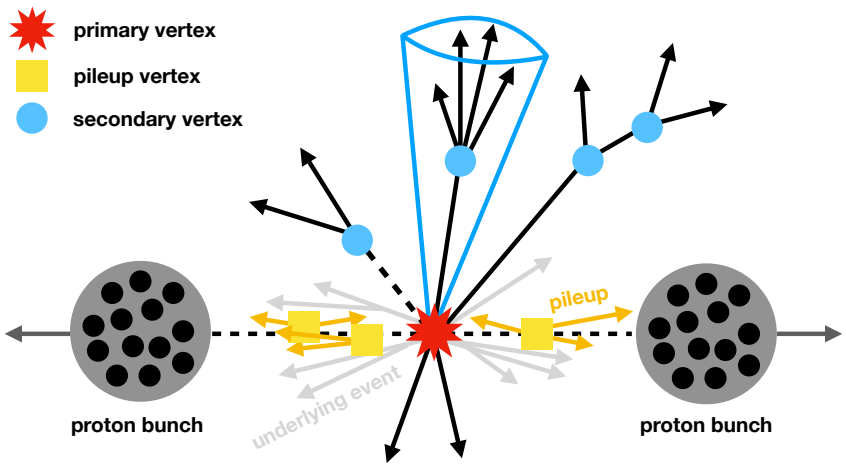

Figure 3.6: Schematic diagram of a bunch crossing that results in one hard scatter.

hard scatter occurs when two protons undergo an inelastic collision, and two of their constituent partons interact to produce new particles. The location at which this occurs is called the *primary vertex*. Physicists are most interested in hard scatter events, but hadron collisions are unfortunately more complicated than this. When two partons from two different protons interact, the leftover partons are no longer in a colour singlet state; these remaining partons will typically produce particles with low transverse momentum. This is the underlying event, and it may overlap with the hard scatter. Furthermore, there is an average of 34 collisions per bunch crossing in Run 2; this is shown in Figure 3.7 for each of the 2015-2018 data-taking periods. The consequence of this is that multiple proton pairs interact during a single bunch crossing; this phenomenon is known as *pileup*. Pileup events produce low transverse momentum particles, and hence also produce particles that may overlap with the hard scatter particles of interest. Mitigating pileup and accounting for its effects are major experimental challenges at the LHC.

The total number of proton-proton collisions that occur during a given period depends on a quantity known as the *luminosity*. The *instantaneous luminosity* L is a measure of the number of collisions produced in a detector, per unit area, per unit time ($[\text{cm}^{-2}\ \text{s}^{-1}]$). It is defined using beam parameters as [54]

$$L = \frac{f_{\text{rev}} N_1 N_2}{4\pi\sigma_x\sigma_y}, \tag{3.2}$$

where N_1 and N_2 are the number of protons per bunch in each beam, and σ_x/σ_y are

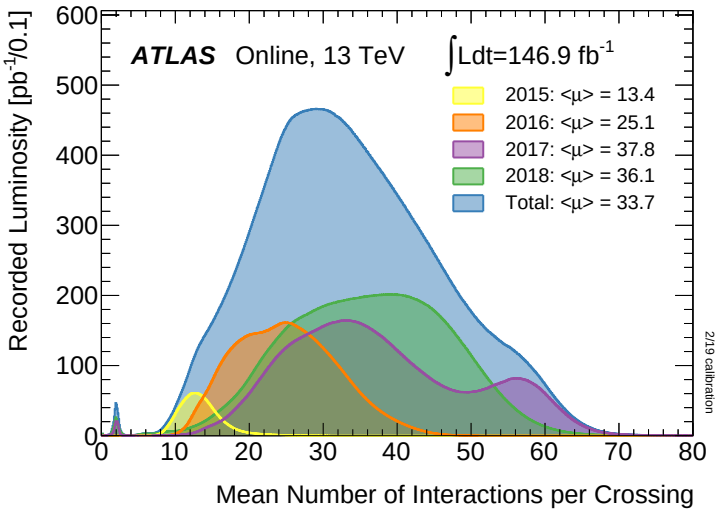

Figure 3.7: The average number of interactions per bunch crossing for Run 2 [55].

the radii of the beam in the x/y-directions at a given IP. N_1 and N_2 are constantly measured during collisions using beam current monitors. σ_x and σ_y are determined routinely using van der Meer scans [54], a method in which the overlap between each beam is varied to determine their effective areas. During Run 2 the peak instantaneous luminosity achieved was 2.1×10^{34} cm^{-2} s^{-1}. The *integrated luminosity* $\mathcal{L}$ is the integral of L over time, and gives a measure of the total number of collisions produced per unit area. The units of $\mathcal{L}$ are typically quoted in inverse femtobarn (fb), where 1 barn $= 10^{-28}$ m^2, and 1 femtobarn $= 10^{-43}$ m^2. The luminosity can be used to determine the number of events produced for a given process with cross section σ. σ has units of area, and quantifies how likely a particular process is to occur – the larger the cross section, the more probable the interaction. For a given process, the total number of events produced, N, is equivalent to

$$N = \sigma \int Ldt = \sigma \mathcal{L}. \tag{3.3}$$

The integrated luminosity does not simply correspond to the amount of data saved to disk. During data-taking various issues with detector components may render some recorded data unusable for physics analysis. These issues are monitored while data is recorded and their impact on the data quality is fully diagnosed later. Data is recorded in runs, which nominally cover the time from when the LHC is filled to when the beam is dumped. Furthermore, runs are split into lumi-blocks (LBs), time

intervals of about one minute in length. After data is recorded, good run lists (GRLs) are assembled based on which LBs are approved to be suitable for analysis; several GRLs are defined based on the type of analyses they can be used for. For the Run 2 13 TeV pp collision data-taking period, the final GRL corresponds to an integrated luminosity of $\mathcal{L} = 139$ fb^{-1}.

Chapter 4

Analysis Selections and Simulation

4.1 Overview of analysis strategy

The goal of this analysis is to search for dark matter in the mono-Z final state with the full Run 2 dataset of 139 fb^{-1}, and to interpret the results in terms of simplified models and 2HDM+a models. The analysis builds upon previous iterations of the search that were carried out with 13.3 fb^{-1} [56] and 36.1 fb^{-1} [57, 39]. Mono-Z dark matter events produce a unique signature in the ATLAS detector: a Z boson decaying into leptons paired with a significant amount of *missing transverse energy*. Missing transverse energy is a standard quantity used in collider DM searches because it is used to infer the presence of non-interacting particles. For example, neutrinos are produced in pp collisions but do not interact with the detector. DM is also invisible to the detector, so the strategy is similar. The *missing transverse momentum*, $\vec{E}_{\mathrm{T}}^{\mathrm{miss}}$, is defined as the negative vector sum of transverse[1] momenta of all "hard" reconstructed objects (electrons, photons, taus, muons, and jets) and the leftover "soft" term obtained from the other reconstructed ID tracks originating from the hard scatter vertex [58]:

$$\vec{E}_{\mathrm{T}}^{\mathrm{miss}} = -\left(\sum_{\text{electrons}} \vec{p}_{\mathrm{T}} + \sum_{\text{photons}} \vec{p}_{\mathrm{T}} + \sum_{\tau\text{-leptons}} \vec{p}_{\mathrm{T}} + \sum_{\text{muons}} \vec{p}_{\mathrm{T}} + \sum_{\text{jets}} \vec{p}_{\mathrm{T}} + \sum_{\text{soft}} \vec{p}_{\mathrm{T}} \right) \quad (4.1)$$

$\vec{p}_{\mathrm{T}}$ indicates the transverse momentum vector for each object. Any non-zero $\vec{E}_{\mathrm{T}}^{\mathrm{miss}}$ vector is produced by a transverse momentum imbalance in the event, and is therefore a measure of the total $\vec{p}_{\mathrm{T}}$ produced by invisible particles. The final state $\chi\bar{\chi}$ DM pair predicted by simplified and 2HDM+a models will hence manifest in the $\vec{E}_{\mathrm{T}}^{\mathrm{miss}}$ vector.

[1] Perpendicular to the beam axis.

The magnitude of the missing transverse momentum is the missing transverse energy, $|\vec{E}_{\mathrm{T}}^{\mathrm{miss}}| \equiv E_{\mathrm{T}}^{\mathrm{miss}}$.

In order to isolate potential DM events that contain the $Z(\ell\ell) + E_{\mathrm{T}}^{\mathrm{miss}}$ signature, specific requirements are applied to the data before analysis. Requirements are specified at the object-level and at the event-level. These requirements collectively define the *signal region* of the analysis. This region is optimized to have high signal efficiency, and contain a maximal amount of DM signal events and a minimal amount of *background* events. Background events are produced by Standard Model processes that produce events with $Z(\ell\ell) + E_{\mathrm{T}}^{\mathrm{miss}}$; for example, $Z(\ell\ell) + Z(\nu\nu)$ events produce similar signatures as $Z(\ell\ell)+\chi\bar{\chi}$ events. Estimating the background sources in the signal region is an essential part of the analysis. The main background processes in the mono-Z analysis are summarized in Table 4.1. When possible it is ideal to estimate background sources from data using control regions that are enriched in background events. However, sometimes it is necessary to use simulation.

Table 4.1: Summary of analysis backgrounds.

Background	Estimaton method	Background fraction
$ZZ \to \ell\ell\nu\nu$	Simulation	43%
$WZ \to \ell\nu\ell\ell$	3ℓ control region	28%
Non-resonant $\ell\ell$	$e\mu$ control region	16%
$Z(\ell\ell)$+jets	γ+jets control region	12%
$ttV(V)$, VVV	Simulation	$< 1\%$

The ZZ background is the dominant background in the analysis, with two leptons originating from a Z and real $E_{\mathrm{T}}^{\mathrm{miss}}$ from neutrinos. This background is estimated from simulation, including electroweak corrections. WZ background events contain two leptons from a Z, real $E_{\mathrm{T}}^{\mathrm{miss}}$ from a neutrino, and an additional lepton that is not reconstructed. Data from a three-lepton control region is used to obtain a scale factor for the WZ simulation in the signal region. The non-resonant $\ell\ell$ backgrounds include WW, Wt, t, $t\bar{t}$, and $Z \to \tau\tau$ sources that produce two leptons that do not come from a Z as well as real $E_{\mathrm{T}}^{\mathrm{miss}}$ from neutrinos. These sources are estimated using data in an $e\mu$ control region where two leptons with opposite flavour are studied. The last major background is the Z+jets background, which contains two leptons from a Z and fake $E_{\mathrm{T}}^{\mathrm{miss}}$, i.e. $E_{\mathrm{T}}^{\mathrm{miss}}$ that is produced from jet mis-measurements, not from neutrinos. This background is estimated entirely from data using a γ+jets control region. The remaining $ttV(V)$ and VVV backgrounds are small and are estimated from simulation.

Simulation samples are used for many aspects of the analysis, including signal region optimization and background estimation. Common Standard Model processes may be used by several ATLAS analyses, while signal simulation samples are generally used by only one or few analyses. Hard scatter events are simulated from Feynman diagrams with advanced Monte Carlo (MC) generators. The events are then propagated through various additional stages, including parton shower simulation and underlying event/pileup simulations. Events are then fed into the ATLAS detector simulator, based on the GEANT4 [59] package, which simulates detector signals from impinging particles. The end results are simulation samples that can be used to compare directly with data.

Simulation is used throughout the analysis to understand the data, but the signal region remains *blinded*, i.e. the data result is not revealed until all signals, backgrounds, and their systematic errors are well understood. This prevents biases that could emerge if the data are seen before the analysis strategy is finalized. If dark matter events exist in the signal region, there would be an excess of events compared to the total Standard Model background prediction. The total number of events can be used to look for an excess, but more sensitivity can be obtained by looking for an excess in a kinematic distribution. This distribution is known as the *discriminating* distribution/variable of the analysis. The $E_{\mathrm{T}}^{\mathrm{miss}}$ is a natural candidate, and was used in past iterations of the analysis; however, a quantity known as the *transverse mass* is shown to give significantly improved discrimination between signal and background. The transverse mass for a two-particle system is defined as

$$m_{\mathrm{T}}^2 \equiv \left(E_{\mathrm{T},1} + E_{\mathrm{T},2}\right)^2 - \left(\vec{p}_{\mathrm{T},1} + \vec{p}_{\mathrm{T},2}\right)^2, \tag{4.2}$$

where $E_{\mathrm{T},1}$ and $E_{\mathrm{T},2}$ are the transverse energies for each particle, and $\vec{p}_{\mathrm{T},1}$ and $\vec{p}_{\mathrm{T},2}$ are their transverse momenta. The transverse mass is now defined for a two-Z system where $ZZ \to \ell\ell\nu\nu$. The transverse energy can be expressed in terms of the Z mass as $E_{\mathrm{T}}^2 = m_Z^2 + |\vec{p}_{\mathrm{T}}|^2$. If one Z decays to a pair of leptons ($\vec{p}_{\mathrm{T},1} \equiv \vec{p}_{\mathrm{T}}^{\,\ell\ell}$) and the other decays to neutrinos ($\vec{p}_{\mathrm{T},2} \equiv \vec{E}_{\mathrm{T}}^{\mathrm{miss}}$), the transverse mass, m_{T}^{ZZ}, can be expressed as

$$(m_{\mathrm{T}}^{ZZ})^2 = \left(\sqrt{m_Z^2 + |\vec{p}_{\mathrm{T}}^{\,\ell\ell}|^2} + \sqrt{m_Z^2 + |\vec{E}_{\mathrm{T}}^{\mathrm{miss}}|^2}\right)^2 - \left(\vec{p}_{\mathrm{T}}^{\,\ell\ell} + \vec{E}_{\mathrm{T}}^{\mathrm{miss}}\right)^2. \tag{4.3}$$

m_{T}^{ZZ} is a powerful variable because it is invariant under a longitudinal boost and

depends only weakly on a transverse boost [60].[2] Note that m_{T}^{ZZ} is expressed for a two-Z system even though simplified and 2HDM+a models do not contain two Z bosons. Ideally the m_{T} would be defined in terms of the Z-mediator system, and hence would include the mass of the mediator in place of the second m_Z term in Equation 4.3. In practice this would mean redefining the m_{T} for each dark matter signal sample; furthermore, the sensitivity is found not to depend on the actual choice of mass in this variable. For these reasons the choice is made to use one definition of m_{T}^{ZZ} that includes m_Z in place of the mediator mass. m_{T}^{ZZ} is observed to be a suitable discriminant variable for both simplified model and 2HDM+a model signals.

After assessing all SM backgrounds, as well as the systematic errors associated to the backgrounds and signal samples, the signal region is unblinded. The agreement between the observed data and prediction as a function of m_{T}^{ZZ} is assessed using a statistical analysis. A discovery may be claimed if a significant excess in data is observed. If no excess is observed, certain combinations of dark matter model parameters may be excluded by the data. *Exclusion limits* are set to quantify this parameter space.

4.2 Object selection

The main physics objects of interest in the analysis are electrons, muons, jets, and $E_{\mathrm{T}}^{\mathrm{miss}}$. When processing collision events in either data or simulation, requirements are placed on the available reconstructed objects in order to select only the objects that are of interest. This is known as *object selection*. These selections are applied to electrons, muons, and jets. The missing transverse momentum is calculated from the objects that pass all requirements.

Electrons

Electrons are reconstructed from energy deposits in the calorimeter that are matched to tracks in the ID. Before they are analyzed, energy and position corrections, determined from data, are applied to all electrons in both data and simulation. These calibrations are obtained from the actual detector performance with respect to its

[2] The usefulness of transverse mass variables has been proven historically. For example, for the W mass measurement m_{T}^{W} is used as it does not strongly depend on p_{T}^{W}. The argument is similar for using m_{T}^{ZZ} as a discriminant instead of $E_{\mathrm{T}}^{\mathrm{miss}}$, as m_{T}^{ZZ} only weakly depends on the $Z\chi\bar{\chi}$ transverse momentum.

expected performance in the reconstruction algorithm.

Table 4.2: Electron object selection criteria.

ID	Selection	Description
LLoose	Baseline likelihood	Loose
PT7	p_{T} cut before overlap removal	$p_{\mathrm{T}} > 7$ GeV
ETA	Detector acceptance	$\lvert\eta_{\mathrm{calo}}\rvert < 2.47$
QUAL	Good object quality	Remove electrons with a bad cluster
Z0	Longitudinal impact parameter	$\lvert\Delta z_0 \sin\theta\rvert < 0.5$ mm
D0	Transverse impact parameter	$\lvert d_0$ significance$\rvert < 5$
ISO	Isolation	Loose
OR	Overlap removal	Remove electrons overlapping with muons and jets
PT20	p_{T} cut after OR	$p_{\mathrm{T}} > 20$ GeV
LMed	Likelihood after OR	Medium

The list of electron object selection requirements are presented in Table 4.2. Electron identification is done using a likelihood discriminator that depends on the track-cluster matching, track quality, and shower shapes [61]. These baseline electrons are required to have *loose* likelihood[3] with $p_{\mathrm{T}} > 7$ GeV and within $|\eta_{\mathrm{calo}}| < 2.47$, where η_{calo} is the η coordinate as measured from the calorimeter cluster centre. Electrons that are reconstructed using a bad cluster[4] are ignored. Requirements on the impact parameters d_0 and z_0 are also applied. The transverse impact parameter d_0 is defined as the shortest distance between a track and the beam line in the transverse direction. The longitudinal impact parameter z_0 is the distance along the z-axis between the primary vertex and the point on the track used to evaluate d_0. Electrons are required to have *loose* isolation[5] as determined from cones of energy deposits and tracks surrounding the electron. Electrons then undergo overlap removal (OR) with muons and jets. Overlap removal is critical to avoid double counting reconstructed objects. Overlap occurs when one real object is reconstructed as two or more objects, or if

[3]Electrons with *loose* likelihood identification require at least two hits in the pixel detector, and seven total hits in the pixel and SCT detectors [61].

[4]An electron cluster is identified as bad if any one of these criteria are met: (1) a dead front end board is present in the first or second sampling; (2) a dead HV region affects the three samplings; (3) there is a masked cell in the core.

[5]For electrons with *loose* isolation, the surrounding transverse energy within $\Delta R = 0.2$ must be less than 20% of the electron transverse momentum, and surrounding tracks within $\Delta R = 0.2$ must have less than 15% of the electron transverse momentum [62].

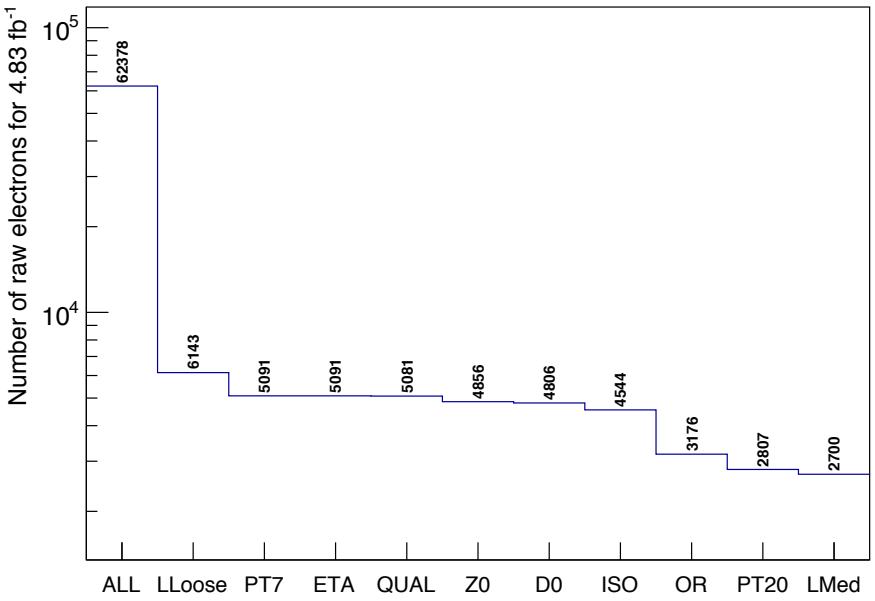

Figure 4.1: Electron object selection cutflow for simulated $pp \to ZZ \to \ell\ell\nu\nu$ events. The content of each bin corresponds to the raw electron count for 4.83 fb^{-1} of effective integrated luminosity (corresponding to 10k simulated events).

two real objects are reconstructed as one object. The strategy for overlap removal is presented in [63]. Electrons are uniquely defined after overlaps are removed. One additional $p_{\mathrm{T}} > 20$ GeV cut is required in addition to requiring *medium* likelihood.[6] The electrons that pass all object selections are known as *selected* electrons. Figure 4.1 illustrates the electron object selection cutflow for a $pp \to ZZ \to \ell\ell\nu\nu$ simulation sample.

Each selected electron has associated scale factors for reconstruction, identification, isolation, and trigger efficiencies. These scale factors are calculated by dedicated working groups, and are made to account for the efficiency differences in simulation with respect to data. In general these scale factors are close to but less than 1, as simulation tends to be more efficient than data. Each scale factor is multiplied onto the event weight in simulation so that the number of reconstructed electrons agree with data.

[6]Electrons with *medium* likelihood identification must satisfy the *loose* requirements and have one of the pixel hits occur in the innermost pixel layer. This requirement helps to suppress converted photon backgrounds [61].

Muons

Momentum corrections are applied to reconstructed muons in both data and simulation before beginning the object selection. The muon selection requirements are summarized in Table 4.3, and their impact on the cutflow is shown in Figure 4.2. Muons are first required to have *loose* quality identification[7] with $|\eta| < 2.5$. Muons are then required to be of *combined* type, meaning that the muon has a full track in both the ID and muon spectrometer, with $p_{\mathrm{T}} > 7$ GeV before overlap removal. Additional track requirements in the pixel detector, SCT, and TRT are also applied.[8] Requirements on the impact parameters z_0 and d_0 are also applied, and muons must have *loose* isolation.[9] Overlap removal is then performed, where muons that overlap with jets are discarded. Finally, the remaining muons are required to have $p_{\mathrm{T}} > 20$ GeV and have *medium* quality.[10] The remaining muons are *selected* muons.

Table 4.3: Muon object selection criteria.

ID	Selection	Description
`Loose`	Baseline quality	Loose, $\|\eta\| < 2.5$
`COMB`	Muon type	Combined
`PT7`	p_{T} cut before overlap removal	$p_{\mathrm{T}} > 7$ GeV
`TRK`	ID track requirements	Hits in pixel detector, SCT, TRT
`Z0`	Longitudinal impact parameter	$\|\Delta z_0 \sin\theta\| < 0.5$ mm
`D0`	Transverse impact parameter	$\|d_0$ significance$\| < 3$
`ISO`	Isolation	Loose
`OR`	Overlap removal	Remove muons overlapping with jets
`PT20`	p_{T} cut after OR	$p_{\mathrm{T}} > 20$ GeV
`Med`	Quality after OR	Medium

As for electrons, muons in simulation have associated scale factors for reconstruc-

[7] *Loose* quality muons include all four reconstructed muon types: *stand-alone*, *combined*, *segment-tagged*, or *calorimeter-tagged* [49].

[8] These track requirements are a subset of the *combined* requirement and so do not reduce the number of muons.

[9] Muons with *loose* isolation are required to have the maximum between the following two quantities be less than 16% of the muon transverse momentum: (1) the sum of track transverse momenta within $\Delta R = 0.2$, and (2) the sum of track transverse momenta within $\Delta R = 0.3$ plus 0.4 times the sum of transverse energies of neutral objects within $\Delta R = 0.2$.

[10] *Medium* quality muons are the ATLAS default selection. Only *stand-alone* and *combined* muons are used in order to reduce reconstruction and calibration systematic uncertainties [49].

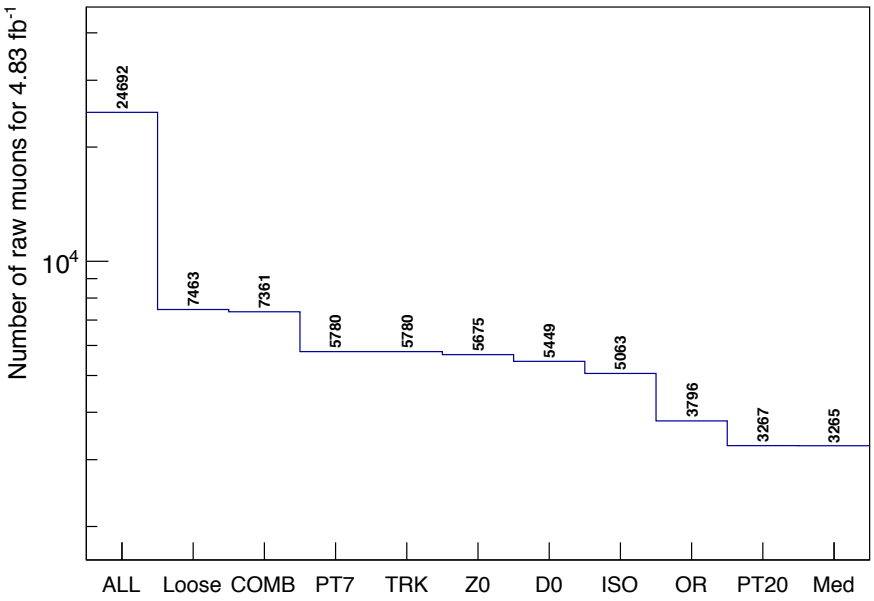

Figure 4.2: Muon object selection cutflow for simulated $pp \to ZZ \to \ell\ell\nu\nu$ events. The content of each bin corresponds to the raw muon count for 4.83 fb^{-1} of effective integrated luminosity (corresponding to 10k simulated events).

tion, isolation, and track-to-vertex-association (TTVA) efficiency differences. These factors are multiplied into the event weight so that the number of muons in simulation matches what is expected in data.

Jets

The jets used in the analysis are reconstructed using the anti-k_t algorithm with radius $R = 0.4$. *Particle flow* (PFlow) jets are used, which are reconstructed using both energy deposits in the calorimeter and tracks in the ID; the tracks are used to determine the contribution of charged particle momenta in a jet, and their corresponding calorimeter energy deposits are ignored to avoid double counting [52]. Using the ID in this way provides a more accurate jet reconstruction compared to using the calorimeter alone. Before analysis, jets are modified according to a dedicated calibration sequence, including energy corrections and the mitigation of pileup contributions [64].

Table 4.4 summarizes jet object selection requirements. All jets in the analysis are required to have $p_{\mathrm{T}} > 30$ GeV, and jets with $|\eta| < 4.5$ are used for overlap removal

Table 4.4: Jet object selection criteria.

ID	Selection	Description
JPT	p_{T} cut before overlap removal	$p_{\mathrm{T}} > 30$ GeV
ETA45	η cut before overlap removal	$\lvert\eta\rvert < 4.5$
OR	Overlap removal	Remove jets overlapping with electrons
JVT	Jet vertex tagger requirement	JVT > 0.5 for jets with $20 < p_{\mathrm{T}} < 60$ GeV, $\lvert\eta\rvert < 2.4$
ETA25	η cut after overlap removal	$\lvert\eta\rvert < 2.5$

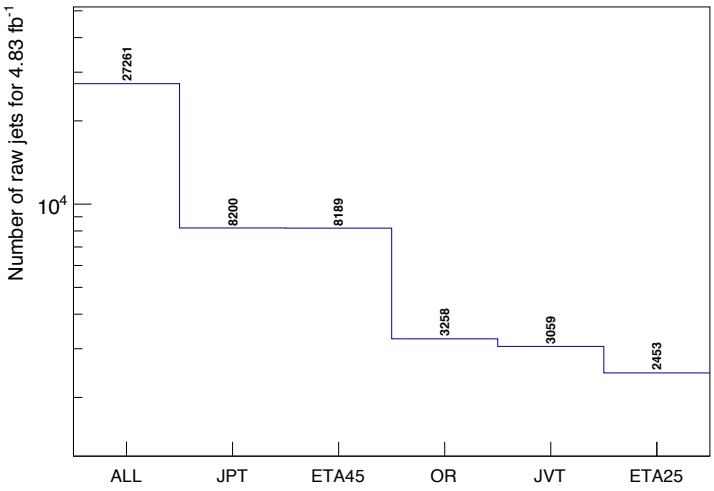

Figure 4.3: Jet object selection cutflow for simulated $pp \to ZZ \to \ell\ell\nu\nu$ events. The content of each bin corresponds to the raw jet count for 4.83 fb^{-1} of effective integrated luminosity (corresponding to 10k simulated events).

with electrons. Pileup is further suppressed by requiring a minimum threshold on the jet vertex tagger (JVT) variable [65].[11] Finally, the jets used in the analysis are required to have $|\eta| < 2.5$. Figure 4.3 illustrates the jet object selection cutflow for ZZ simulation events. *Selected* jets pass all object selections.

b-jets are composed of the decay products of b-hadrons, are used in the analysis to suppress top quark backgrounds. b-hadrons have a sufficiently long lifetime and can travel a few millimetres from the primary vertex before decaying. b-jets are identified

[11] The JVT is a multivariate combination of N_{Vtx}, the number of reconstructed primary vertices, and the jet-vertex-fraction, the fraction of the total momentum of tracks in a jet that is associated to the primary vertex. Requiring a minimum on the JVT variable helps to suppress pileup jets.

(or *tagged*) by this secondary, displaced vertex using the MV2c10 algorithm [66]. A working point of 85% is used, corresponding to the efficiency for the tagger to identify b-jets in simulated $t\bar{t}$ events.

The JVT and b-tagging algorithms have corresponding efficiency scale factors for simulation. These factors are multiplied onto the event weight for each selected b-jet.

4.3 Event preselection

After object selection, further requirements are made at the event level using the selected objects. The purpose of *event preselection* is to remove events that should not be considered at all in the analysis. The preselection requirements are as follows:

- Vertex requirement: The presence of at least one primary vertex is required.
- Event cleaning: Events with fake jets are removed. These jets are identified as coming from non-collision backgrounds, such as cosmic ray showers or noise bursts in the calorimeter.
- Single lepton triggers: Events are required to have fired at least one single electron or muon trigger. The list of triggers considered is given in Table 4.5. All triggers are unprescaled.[12] Trigger efficiency scale factors for each lepton are multiplied onto the event weight in simulation to match the efficiencies observed in data.
- Lepton trigger matching: One of the selected electrons or muons must have fired a single lepton trigger.
- Electron crack region veto: In 2015-2016 data and simulation, an ATLAS software known issue causes a mismatch between tracks and clusters for some electrons in the calorimeter crack region ($1.37 < |\eta_{\text{calo}}| < 1.52$). Events containing these types of electrons are ignored.

In addition to the list above, further preselection requirements are applied to data:

[12] Unprescaled triggers allow all passing events to be recorded, whereas prescaled triggers only allow a fraction of passing events to be recorded. Prescaled triggers are usually used to record events with very high rates. These prescale factors must be taken into account in order to compare data with simulation when prescaled triggers are used (one can either prescale the simulation or unprescale the data using a weighting procedure).

- The GRL requirement is applied so that only data from useful lumiblocks are considered.
- Ignore data events from high pileup runs in 2015 and 2016 with poor quality high p_{T} clusters due to saturated EMEC-IW cells.
- Reject data events containing various detector and readout errors from the SCT and LAr/Tile calorimeters.

Table 4.5: List of unprescaled single lepton triggers. 2016 is split into periods before and after the instantaneous luminosity reached above 10^{34} cm^{-2} s^{-1}. †: For run 298687, `HLT_e24_lhmedium_nod0_L1EM20VH` is used instead of `HLT_e26_lhtight_nod0_ivarloose`. ††: `HLT_e26_lhtight_nod0` is used only in 2018 for run numbers $\geq$ 349169.

Period	Single electron triggers	Single muon triggers
2015	`HLT_e24_lhmedium_L1EM20VH` or `HLT_e60_lhmedium` or `HLT_e120_lhloose`	`HLT_mu20_iloose_L1MU15` or `HLT_mu50`
Early 2016	`HLT_e26_lhtight_nod0_ivarloose`† or `HLT_e60_lhmedium_nod0` or `HLT_e140_lhloose_nod0`	`HLT_mu24_ivarmedium` or `HLT_mu50`
Late 2016, 2017, 2018	`HLT_e26_lhtight_nod0_ivarloose` or `HLT_e60_lhmedium_nod0` or `HLT_e140_lhloose_nod0` or `HLT_e26_lhtight_nod0`††	`HLT_mu26_ivarmedium` or `HLT_mu50`

4.4 Event selection

After event preselection, the selected objects are used collectively to apply *event selections*. Various kinematic requirements are applied in order to isolate potential dark matter events with a mono-Z signature while simultaneously suppressing Standard Model background processes. These requirements define the analysis signal region, and are categorized into requirements on either leptons, $E_{\mathrm{T}}^{\mathrm{miss}}$, or jets. Table 4.6 summarizes the event selections.

The lepton requirements are as follows. In order to identify events with a Z boson decaying into leptons, two electrons or muons with opposite sign are required ($\ell^+\ell^-$ = e^+e^- or $\mu^+\mu^-$), where the leading lepton, ℓ_1, must have $p_{\mathrm{T}}^{\ell_1} > 30$ GeV, and the

Table 4.6: Signal region event selection criteria ($\ell = e, \mu$).

Category	Event selection	Background suppressed
Leptons	$p_{\mathrm{T}}^{\ell_1}$ ($p_{\mathrm{T}}^{\ell_2}$) > 30 (20) GeV	—
	Veto events with $p_{\mathrm{T}}^{\ell_3} > 7$ GeV	WZ
	76 GeV $< m_{\ell\ell} <$ 106 GeV	Non-resonant $\ell^+\ell^-$
	$\Delta R_{\ell\ell} < 1.8$	Non-resonant $\ell^+\ell^-$, Z+jets
$E_{\mathrm{T}}^{\mathrm{miss}}$	$E_{\mathrm{T}}^{\mathrm{miss}} > 90$ GeV	Z+jets
	$\mathcal{S} > 9$	Z+jets
Jets	Veto events containing a b-jet	t, $t\bar{t}$

sub-leading lepton, ℓ_2, must have $p_{\mathrm{T}}^{\ell_2} > 20$ GeV. In addition, the invariant mass of the lepton pair $m_{\ell\ell}$ must be within 15 GeV of $m_Z = 91$ GeV: $76 < m_{\ell\ell} < 106$ GeV. This requirement suppresses events that contain two leptons that do not come from a Z, such as WW and other non-resonant $\ell^+\ell^-$ processes. Events containing a third lepton ℓ_3 with $p_{\mathrm{T}}^{\ell_3} > 7$ GeV (and fulfilling a looser selection) are vetoed in order to suppress WZ processes. Finally, to ensure that the Z has a sizeable boost, the two leptons are required to have a small angular distance between them: $\Delta R_{\ell\ell} < 1.8$ (where $\Delta R = \sqrt{\Delta\phi^2 + \Delta\eta^2}$). This cut also helps to reduce non-resonant $\ell^+\ell^-$ backgrounds, which are more likely to have large $\Delta R_{\ell\ell}$ if the two leptons come from two separate W bosons.

Requirements on the $E_{\mathrm{T}}^{\mathrm{miss}}$ are also applied in order to enhance potential dark matter signals and reduce the Z+jets background. Z+jets events do not contain real $E_{\mathrm{T}}^{\mathrm{miss}}$, but jet mis-measurements cause Z+jets events to contain significant amounts of fake $E_{\mathrm{T}}^{\mathrm{miss}}$. This introduces large amounts of background events, mostly at low $E_{\mathrm{T}}^{\mathrm{miss}}$. To reduce this, events are required to have $E_{\mathrm{T}}^{\mathrm{miss}} > 90$ GeV. In addition, the quality of the $E_{\mathrm{T}}^{\mathrm{miss}}$ is assessed using a quantity called the $E_{\mathrm{T}}^{\mathrm{miss}}$ *significance*, $\mathcal{S}$. This variable is designed to provide discrimination power against events with $E_{\mathrm{T}}^{\mathrm{miss}}$ produced by object mis-measurements. The $E_{\mathrm{T}}^{\mathrm{miss}}$ significance is defined to be [67]

$$\mathcal{S}^2 = \frac{|\vec{E}_{\mathrm{T}}^{\mathrm{miss}}|^2}{\sigma_{\mathrm{L}}^2(1-\rho_{\mathrm{LT}}^2)}, \tag{4.4}$$

where σ_{L}^2 is the total variance of all objects longitudinal to the $E_{\mathrm{T}}^{\mathrm{miss}}$, and ρ_{LT} is the correlation factor of the longitudinal and transverse variances. Events are more likely

to have high significance when $E_{\mathrm{T}}^{\mathrm{miss}}$ is large, and/or the objects in the event have small total variance. Hence events with large $\mathcal{S}$ are more likely to have real $E_{\mathrm{T}}^{\mathrm{miss}}$; events are required to have $\mathcal{S} > 9$ in order to isolate DM signal events.

Finally, events that contain jets identified to originate from bottom quarks (b-jets) are vetoed to reduce top quark backgrounds, as $t \to Wb$ is the dominant decay of the top quark.

4.4.1 Signal region optimization

The requirements on $\Delta R_{\ell\ell}$, $E_{\mathrm{T}}^{\mathrm{miss}}$, and $\mathcal{S}$ are obtained by an *optimization* procedure using simulation. When signal and background have similar behaviour, it may be difficult to determine which threshold value is optimal to enhance a potential signal while also suppressing backgrounds. The optimal requirement on each of these variables is obtained by optimizing the *signal significance*, defined as [68]

$$Z = \sqrt{2\left((s+b)\ln\left[\frac{(s+b)(b+\sigma^2)}{b^2+(s+b)\sigma^2}\right] - \frac{b^2}{\sigma^2}\ln\left[1+\frac{s\sigma^2}{b(b+\sigma^2)}\right]\right)} \tag{4.5}$$

where s is the number of expected signal events, and $b \pm \sigma$ is the predicted number of background events. Larger Z corresponds to more separation between signal and background. With this metric, each variable is optimized by incrementing the cut value for the variable of interest while holding all other variables fixed. Then the significance is calculated at each step, and the maximum significance is obtained for the optimal cut value. This is done for the cut values of $\Delta R_{\ell\ell}$, $E_{\mathrm{T}}^{\mathrm{miss}}$, and $\mathcal{S}$.[13] Two other variables are also studied: the azimuthal angle between the $E_{\mathrm{T}}^{\mathrm{miss}}$ and Z boson, $\Delta\phi(\vec{E}_{\mathrm{T}}^{\mathrm{miss}}, \vec{p}_{\mathrm{T}}^{Z})$, and the fractional p_{T}, $||\vec{E}_{\mathrm{T}}^{\mathrm{miss}} + \sum \vec{p}_{\mathrm{T}}^{\mathrm{jets}}| - p_{\mathrm{T}}^{Z}|/p_{\mathrm{T}}^{Z}$. However, these two variables are found to have very little discriminating power and are removed from the analysis. The optimization is done for a select number of benchmark mono-Z signal points using simulation samples. The background errors are approximated using what was observed for the 36.1 fb^{-1} result.

An important goal during the optimization process is, if feasible, to maintain one signal region for simplified models, 2HDM+a models, and the $ZH(inv)$ signal. As long as significant sensitivity is not sacrificed for a given model, having one signal region is preferred because it leads to a simpler analysis and background estimates. Some differences are seen in the optimal cut values between the models; for example,

[13] The distributions of significance as a function of cut value are checked to avoid local minima.

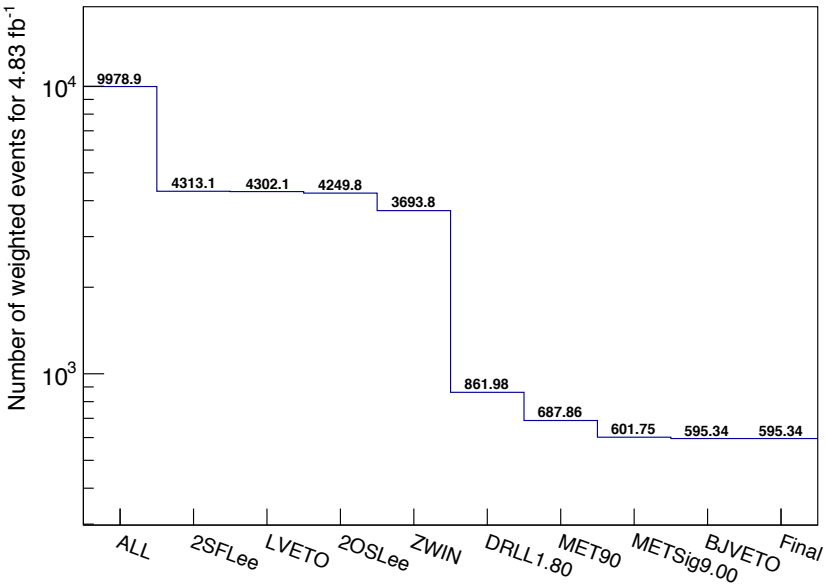

(a) ee channel.

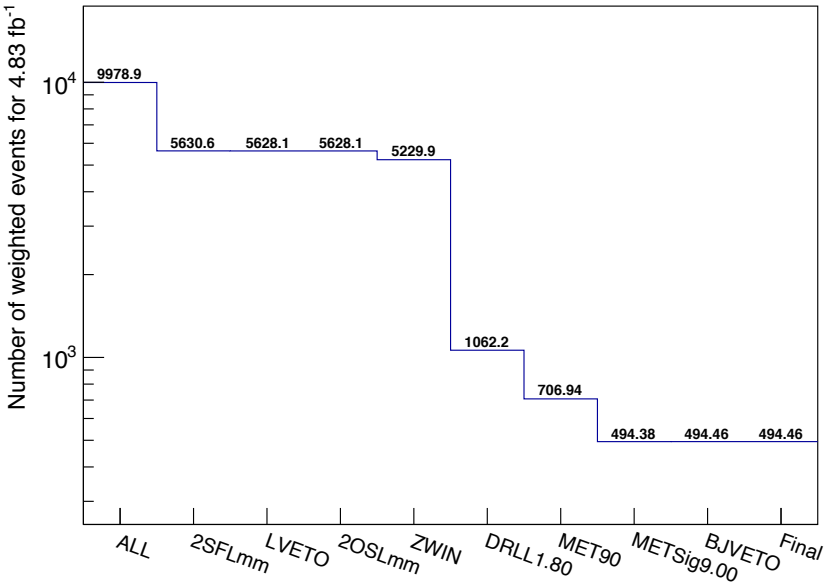

(b) $\mu\mu$ channel.

Figure 4.4: Event selection cutflow for simulated $pp \to ZZ \to \ell\ell\nu\nu$ events corresponding to 4.83 fb^{-1} of effective integrated luminosity (corresponding to 10k simulated events). The labels in the plots are as follows: `ALL`: all events that pass preselection; `2SFL`: two same flavour leptons; `LVETO`: third lepton veto; `2OSL`: two opposite sign leptons; `ZWIN`: m_Z window requirement; `DRLL`: $\Delta R_{\ell\ell}$ requirement; `MET`: $E_{\mathrm{T}}^{\mathrm{miss}}$ requirement; `METSig`: $\mathcal{S}$ requirement; `BJVETO`: b-jet veto. Note that the $\mu\mu$ yield increases after the `BJVETO` requiement because of the application of b-tagging efficiency scale factors at this step.

most signals have an optimal $\mathcal{S}$ cut near 9, but some heavier 2HDM+a signals benefit from a higher threshold closer to 12, leading to an increase in sensitivity by up to 10% for some signals. This analysis prioritizes having a common signal region for all DM and $ZH(inv)$ signal types, but future analyses may have slightly increased sensitivity if separate high and low mass signal regions are implemented. Figure 4.4 illustrates the optimized signal region event selections on $pp \to ZZ \to \ell\ell\nu\nu$ simulation for both ee and $\mu\mu$ channels.

Once the signal region is optimized, a related optimization study is performed to determine the best discriminating variable for the analysis. This test identifies if a variable has increased sensitivity due to the shape of its distribution between signal and background. The three variables studied are $E_{\mathrm{T}}^{\mathrm{miss}}$ (a benchmark discriminant in collider DM searches), $\mathcal{S}$, and m_{T}^{ZZ}. The significance Z is calculated per bin as a function of each variable. For both simplified model and 2HDM+a signals, marginal differences are seen when using $E_{\mathrm{T}}^{\mathrm{miss}}$ and $\mathcal{S}$ as discriminants, but a significant gain in sensitivity is observed when using m_{T}^{ZZ} (about 10% for simplified model signals and 20% for 2HDM+a signals). From this improvement, it is decided to use m_{T}^{ZZ} as the discriminant variable for both simplified model and 2HDM+a signals.

4.5 Simulation samples

Simulation samples are produced using advanced Monte Carlo generators. Three commonly used generators are MadGraph [69], Powheg [70], and Sherpa [71]. These generators are capable of simulating hard scatter events for renormalizable and effective field theories. From the Lagrangian, generators produce all possible Feynman diagrams needed to calculate the matrix elements for a given phase space point up to a given order in perturbation. MC methods are then used to produce events in a statistical manner such that the probability densities for each process to occur in reality are accounted for. MC events are generally produced with an associated weight different from 1. After the hard scatter is simulated, events are modified to include showering and hadronization effects such as the underlying event, initial and final state radiation of extra jets, and multiple parton interactions. Pythia [72] is one of the most commonly used MC generators for simulating parton showering. Finally, simulated samples are processed by the ATLAS detector simulator, Geant4, in order to emulate detector-specific effects, such as particle interactions with the detector material.

In an effort to reduce the size of samples used in analyses, both the data and simulation samples are reduced to files called derivations. Derivations are trimmed sets of data that contain additional requirements on the objects and/or events. The mono-Z analysis uses HIGG2D1 derivations because they only include events with two or more leptons. Details of these requirements are summarized in Table 4.7. Two leptons are required with very loose identification requirements, and any single lepton, dilepton, or trilepton trigger must be passed.

Table 4.7: HIGG2D1 derivation requirements.

Requirement	Description
Object requirement	$N(e) + N(\mu) \geq 2$
E_{T} cut for electrons	> 15 GeV for leading, > 5 GeV for sub-leading
p_{T} cut for muons	> 15 GeV for leading, > 5 GeV for sub-leading
Mass cut	$M(2\ell) > 5$ GeV
Quality cut for electrons	`DFCommonElectronsLHVeryLoose` for leading
Quality cut for muons	`DFCommonMuonsPreselection` for leading, `DFCommonGoodMuon` for sub-leading
Trigger requirement	`HLT_e.*` or `HLT_mu.*` or `HLT_2e.*` or `HLT_2mu.*` or `HLT_3e.*` or `HLT_3mu.*`

Before simulation samples can be compared directly to data, they must be modified in two major ways. The first is that the samples need to be properly normalized in order to reflect the total integrated luminosity of the data. Each simulation sample has an associated cross section σ corresponding to a certain number of simulated events, N_{sim}, where N_{sim} corresponds to the sum of event weights. However, N_{sim} is actually a subset of the real number of generated events; this is because filters are applied during event generation that discard events that are known not to be of interest. For example, events in the final signal samples are required to have $E_{\mathrm{T}}^{\mathrm{miss}} > 40$ GeV, because anything lower than this is not studied in the analysis. Hence N_{sim} does not correspond to the true cross section of the sample. To account for this, the cross section for all samples must be scaled by a generator filter efficiency, ϵ_{gen}, which is 1 if no filters are applied. From Equation 3.3, the integrated luminosity corresponding to a simulated sample is therefore

$$\mathcal{L}_{\mathrm{sim}} = \frac{N_{\mathrm{sim}}}{\sigma \epsilon_{\mathrm{gen}}}. \tag{4.6}$$

Simulated samples must be scaled by $\mathcal{L}_{\text{data}}/\mathcal{L}_{\text{sim}}$, where $\mathcal{L}_{\text{data}} = 139$ fb^{-1}, so that the normalization matches the data.

The second major correction is due to pileup. Simulated samples are generated according to the distribution of the average number of pileup events per bunch crossing; this distribution is an approximation for what corresponds to the actual dataset. The simulated distribution will differ compared to the real one, so run-dependent reweighting must be applied to each event to recover the actual μ distribution (as shown in Figure 3.7). This is called *pileup reweighting*.

4.5.1 Signal samples

$pp \to Z(\ell^+\ell^-) + \chi\bar{\chi}$ events are simulated using MadGraph5 according to the simplified model and 2HDM+a model frameworks. Events are calculated to NLO in QCD and LO in QED. The parton distribution function used in the simulation is calculated using the NNPDF2.3 parameterization [73]. Events are then passed to Pythia8 for simulation of hadronization, parton showering, and the underlying event, before detector simulation with Geant4. Simplified model signals are produced for several values of m_χ and m_{med}, with $g_\chi = 1.0$, $g_q = 0.25$, and assuming the minimal width approximation for the mediator. These samples are listed in Tables 4.8 and 4.9 for axial-vector and vector mediator models respectively. The cross section, generator filter efficiency, and dataset ID (DSID) are given for each sample. In total, 43 samples are simulated with axial-vector mediators and 17 are simulated with vector mediators. The reconstructed samples are chosen based on the expected sensitivity of the analysis. For 2HDM+a signals, simulation is done with parameters fixed as described in Section 2.2.4, with $m_H = m_A = m_{H^\pm}$ and $m_\chi = 10$ GeV. Signals are produced for various values of $\tan\beta$, $\sin\theta$, m_H, and m_a, and are summarized in Table 4.10 Production via bb and gg fusion are simulated separately for each process. 78 2HDM+a samples are simulated in total.

Table 4.8: List of axial-vector simplified model signal samples. The fixed parameters are $g_\chi = 1.0$ and $g_q = 0.25$. Cross sections are calculated to precision on the order of 0.1%.

m_χ (GeV)	m_{med} (GeV)	σ (fb)	ϵ_{gen}	DSID
1	10	1.59×10^4	0.119	310577
1	50	1990	0.456	310578
1	100	660	0.654	310579
1	150	3.27	0.739	310580
1	200	193	0.785	310581
1	300	85.3	0.833	310582
1	400	44.5	0.858	310583
1	500	25.3	0.875	310584
1	600	15.5	0.887	310585
1	650	12.4	0.892	310617
1	750	8.20	0.899	310586
1	900	4.66	0.907	310587
1	1050	2.81	0.914	310588
1	1200	1.75	0.919	310589
5	1	208	0.313	310599
5	30	3810	0.309	310590
10	10	88.7	0.448	310600
25	80	624	0.601	310591
30	50	21.8	0.672	310601
50	130	181	0.718	310592
55	100	8.84	0.766	310602
75	180	72.3	0.775	310593
75	400	39.3	0.860	310612
75	750	7.90	0.899	310614
80	150	4.73	0.810	310603
100	100	1.29	0.852	310610
105	200	2.88	0.835	310604
125	280	18.4	0.831	310594
150	400	20.2	0.861	310613
155	300	1.30	0.865	310605
175	380	6.56	0.860	310595
225	480	2.74	0.879	310596
250	400	0.176	0.895	310611
250	750	4.62	0.901	310615
275	580	1.33	0.891	310597
350	730	0.534	0.903	310598
205	400	0.684	0.882	310606
255	500	0.394	0.893	310607
300	630	0.959	0.894	310618
305	600	0.242	0.901	310608
325	750	1.79	0.902	310616
330	650	0.192	0.904	310619
380	750	0.125	0.912	310609

Table 4.9: List of vector simplified model signal samples. The fixed parameters are $g_\chi = 1.0$ and $g_q = 0.25$. Cross sections are calculated to precision on the order of 0.1%.

m_χ (GeV)	m_{med} (GeV)	σ (fb)	ϵ_{gen}	DSID
1	400	42.2	0.858	310634
1	750	7.98	0.897	310635
10	10	168	0.375	310620
30	50	59.5	0.610	310621
55	100	31.5	0.729	310622
80	150	20.3	0.780	310623
100	100	3.04	0.834	310632
105	200	14.2	0.813	310624
155	300	7.94	0.848	310625
205	400	4.84	0.871	310626
250	400	0.621	0.894	310633
255	500	3.13	0.883	310627
305	600	2.10	0.893	310628
325	750	5.98	0.900	310636
380	750	1.22	0.905	310629
455	900	0.738	0.912	310630
425	880	2.34	0.909	310631

Table 4.10: List of 2HDM+a model signal samples. The fixed parameters are m_χ = 10 GeV and $m_H = m_A = m_{H^\pm}$. Cross sections are calculated to precision on the order of 0.1%.

$\tan\beta$	$\sin\theta$	m_H (GeV)	m_a (GeV)	Process	σ (fb)	ϵ_{gen}	DSID
0.3	0.35	400	250	gg	16.0	0.928	313204
0.3	0.35	600	100	gg	15.7	0.989	313196
0.3	0.35	600	400	gg	0.907	0.974	313200
0.3	0.35	1750	250	gg	1.91	0.987	313208
1.0	0.35	225	100	gg	235	0.750	313182
1.0	0.35	225	100	bb	13.4	0.724	313183
1.0	0.35	600	200	gg	9.73	0.990	313184
1.0	0.35	600	200	bb	0.0666	0.988	313185
1.0	0.35	700	400	gg	2.05	0.985	346236
1.0	0.35	700	400	bb	0.0136	0.984	313186
1.0	0.35	800	450	gg	1.23	0.990	346237
1.0	0.35	800	450	bb	0.00848	0.989	313187
1.0	0.35	1000	350	gg	1.07	0.995	313188
1.0	0.35	1000	350	bb	0.00842	0.992	313189
1.0	0.35	1000	600	gg	0.377	0.992	313190
1.0	0.35	1000	600	bb	0.00284	0.992	313191
1.0	0.35	1600	100	gg	0.410	0.992	313192
1.0	0.35	1600	100	bb	0.0109	0.894	313193
1.0	0.35	1600	250	gg	0.286	0.991	313194
1.0	0.35	1600	250	bb	0.00355	0.966	313195
1.0	0.7	300	250	gg	7.70	0.808	313234
1.0	0.7	300	250	bb	0.205	0.744	313235
1.0	0.7	350	200	gg	173	0.905	313212
1.0	0.7	350	200	bb	2.51	0.897	313213
1.0	0.7	400	250	gg	49.5	0.914	313236
1.0	0.7	400	250	bb	0.433	0.903	313237
1.0	0.7	500	250	gg	34.4	0.974	313238
1.0	0.7	500	250	bb	0.237	0.973	313239
1.0	0.7	600	100	gg	27.2	0.992	313220
1.0	0.7	600	100	bb	0.220	0.973	313221
1.0	0.7	600	200	gg	23.2	0.990	313256
1.0	0.7	600	200	bb	0.162	0.984	313257
1.0	0.7	600	250	gg	20.2	0.988	313222
1.0	0.7	600	250	bb	0.137	0.985	313223
1.0	0.7	600	300	gg	16.4	0.984	313224
1.0	0.7	600	300	bb	0.109	0.982	313225
1.0	0.7	600	350	gg	9.52	0.977	313226
1.0	0.7	600	350	bb	0.0614	0.975	313227
1.0	0.7	600	400	gg	4.14	0.965	313228

1.0	0.7	600	400	bb	0.0261	0.961	313229
1.0	0.7	600	450	gg	1.52	0.941	313230
1.0	0.7	600	450	bb	0.00917	0.922	313231
1.0	0.7	600	500	gg	0.274	0.920	313232
1.0	0.7	600	500	bb	0.00145	0.870	313233
1.0	0.7	700	250	gg	11.7	0.992	313240
1.0	0.7	700	250	bb	0.0829	0.988	313241
1.0	0.7	800	250	gg	6.97	0.993	313242
1.0	0.7	800	250	bb	0.0501	0.986	313243
1.0	0.7	900	250	gg	4.41	0.994	313244
1.0	0.7	900	250	bb	0.0348	0.983	313245
1.0	0.7	1000	250	gg	2.95	0.993	313246
1.0	0.7	1000	250	bb	0.0258	0.979	313247
1.0	0.7	1000	350	gg	1.89	0.994	313218
1.0	0.7	1000	350	bb	0.0146	0.988	313219
1.0	0.7	1200	100	gg	2.19	0.992	313214
1.0	0.7	1200	100	bb	0.0476	0.902	313215
1.0	0.7	1250	250	gg	1.43	0.991	313248
1.0	0.7	1250	250	bb	0.0156	0.968	313249
1.0	0.7	1500	500	gg	0.177	0.994	313216
1.0	0.7	1500	500	bb	0.00172	0.986	313217
1.0	0.7	1500	250	gg	0.939	0.990	313250
1.0	0.7	1500	250	bb	0.01206	0.960	313251
1.0	0.7	1750	250	gg	0.746	0.988	313252
1.0	0.7	1750	250	bb	0.0106	0.953	313253
1.0	0.7	2000	250	gg	0.651	0.987	313254
1.0	0.7	2000	250	bb	0.00978	0.951	313255
5.0	0.35	400	250	gg	3.11	0.915	313205
5.0	0.35	400	250	bb	13.2	0.906	313206
5.0	0.35	600	100	gg	1.21	0.992	313197
5.0	0.35	600	100	bb	5.09	0.988	313198
5.0	0.35	600	400	gg	0.692	0.966	313201
5.0	0.35	600	400	bb	2.80	0.963	313202
5.0	0.35	1750	250	gg	0.00972	0.985	313209
5.0	0.35	1750	250	bb	0.0838	0.963	313210
30.0	0.35	400	250	bb	19.6	0.903	313207
30.0	0.35	600	100	bb	18.1	0.943	313199
30.0	0.35	600	400	bb	7.89	0.961	313203
30.0	0.35	1750	250	bb	2.45	0.962	313211

4.5.2 Background samples

Simulation samples are also needed to study the SM backgrounds relevant to the analysis. Background samples are used for signal region optimization as well as for validation of in-situ background estimation techniques. They may also be used when it is not feasible to use data-driven background estimates.

Diboson samples

There are three sources of diboson backgrounds in the analysis: ZZ, WZ, and WW. The ZZ and WZ backgrounds are the largest backgrounds in the analysis; these processes contain two leptons produced from a Z decay. The WW process is a source of non-resonant $\ell\ell$ events, where two leptons come from two different W bosons. Table 4.11 summarizes the diboson samples used for background estimation and/or validation in the analysis. Samples generated with Sherpa are the default, with one Powheg WW sample used as a cross check.

Table 4.11: List of diboson simulation samples.

Background	Process	$\sigma \times \epsilon_{\text{gen}}$ (fb)	Generator	DSID
ZZ	$pp \to ZZ \to \ell\ell\nu\nu$	749	Sherpa	345666
	$gg \to ZZ \to \ell\ell\nu\nu$	18.1	Sherpa	345723
WZ	$pp \to WZ \to \ell\ell\ell\nu$	4570	Sherpa	364253
	$gg \to WZ \to qq\ell\ell$	47.4	Sherpa	364284
	$pp \to WZ \to \ell\ell\ell\nu jj$	3430	Sherpa	363358
WW	$pp \to WW \to \ell\nu\ell\nu$	1.06×10^4	Powheg+Pythia	361600
	$gg \to WW \to \ell\nu\ell\nu$	482	Sherpa	345718
ZZ/WW	$pp \to \ell\nu\ell\nu$	1.25×10^4	Sherpa	364254
	$pp \to \ell\ell\nu\nu jj$	116	Sherpa	364285

Z+jets samples

Z+jets processes contain multiple jets and are one of the most challenging backgrounds to estimate in the analysis. What is referred to as the Z+jets background is composed of $Z(ee)$+jets and $Z(\mu\mu)$+jets processes. These events are identified by two leptons and with an invariant mass close to m_Z. For $Z(\tau\tau)$+jets processes, the τ-lepton mostly decays hadronically, but it also decays leptonically via $\tau \to W(\ell\bar{\nu}_\ell)+\nu_\tau$, where $\ell = e, \mu$. If two τ leptons decay leptonically, these events will contain two

leptons that do not come from a Z; therefore $Z(\tau\tau)$ events are contained in the non-resonant $\ell\ell$ background estimate.

Table 4.12: List of $Z(ee)$+jets and $Z(\mu\mu)$+jets simulation samples. All samples are generated with SHERPA.

Background	$\max(H_{\mathrm{T}}, p_{\mathrm{T}}^{Z})$ (GeV)	HF	$\sigma \times \epsilon_{\mathrm{gen}}$ (fb)	DSID
$Z(\mu\mu)$+jets	$\{0, 70\}$	$\not{C}\not{B}'$	1.59×10^6	364100
		$C\not{B}'$	2.18×10^5	364101
		B'	1.24×10^5	364102
	$\{70, 140\}$	$\not{C}\not{B}'$	7.31×10^4	364103
		$C\not{B}'$	1.98×10^4	364104
		B'	1.20×10^4	364105
	$\{140, 280\}$	$\not{C}\not{B}'$	2.37×10^4	364106
		$C\not{B}'$	9040	364107
		B'	5690	364108
	$\{280, 500\}$	$\not{C}\not{B}'$	4650	364109
		$C\not{B}'$	2210	364110
		B'	1450	364111
	$\{500, 1000\}$	—	1740	364112
	$\{1000, E_{\mathrm{CM}}\}$	—	144	364113
	—	—	634	308093
$Z(ee)$+jets	$\{0, 70\}$	$\not{C}\not{B}'$	1.59×10^6	364114
		$C\not{B}'$	2.18×10^5	364115
		B'	1.23×10^5	364116
	$\{70, 140\}$	$\not{C}\not{B}'$	7.44×10^4	364117
		$C\not{B}'$	1.98×10^4	364118
		B'	1.23×10^4	364119
	$\{140, 280\}$	$\not{C}\not{B}'$	2.44×10^4	364120
		$C\not{B}'$	9140	364121
		B'	5930	364122
	$\{280, 500\}$	$\not{C}\not{B}'$	4750	364123
		$C\not{B}'$	2220	364124
		B'	1460	364125
	$\{500, 1000\}$	—	1760	364126
	$\{1000, E_{\mathrm{CM}}\}$	—	145	364127
	—	—	632	308092

Tables 4.12 and 4.13 summarize all Z+jets samples used in the analysis. Samples are produced from SHERPA with 0, 1, and 2 jets at NLO, and 3 and 4 jets at LO

Table 4.13: List of $Z(\tau\tau)$+jets simulation samples. All samples are generated with SHERPA.

Background	$\max(H_{\mathrm{T}}, p_{\mathrm{T}}^{Z})$ (GeV)	HF	$\sigma \times \epsilon_{\mathrm{gen}}$ (fb)	DSID
$Z(\tau\tau)$+jets	$\{0, 70\}$	$\not{C}\not{B}'$	1.59×10^{6}	364100
		$C\not{B}'$	2.18×10^{5}	364101
		B'	1.25×10^{5}	364102
	$\{70, 140\}$	$\not{C}\not{B}'$	7.41×10^{4}	364103
		$C\not{B}'$	1.97×10^{4}	364104
		B'	1.20×10^{4}	364105
	$\{140, 280\}$	$\not{C}\not{B}'$	2.42×10^{4}	364106
		$C\not{B}'$	9100	364107
		B'	5340	364108
	$\{280, 500\}$	$\not{C}\not{B}'$	4670	364109
		$C\not{B}'$	2220	364110
		B'	1470	364111
	$\{500, 1000\}$	—	1760	364112
	$\{1000, E_{\mathrm{CM}}\}$	—	145	364113
	—	—	633	308094

in QCD. The samples are produced in "slices." Each slice has a specific transverse momentum requirement that is determined using the maximum value of p_{T}^{Z} and H_{T}, where H_{T} is defined to be the scalar sum of all jet p_{T}. Each slice has a defined range for which $\max(H_{\mathrm{T}}, p_{\mathrm{T}}^{Z})$ falls into, from 0 up to the centre-of-mass energy, E_{CM} = 13 TeV. Slices are also categorized according to which heavy flavour (HF) quark scheme is used for jets initiated by b- and c-quarks. Samples either (1) exclude b- and c-jets (marked as $\not{C}\not{B}'$ in Tables 4.12 and 4.13), (2) include c-jets and exclude b-jets (marked as $C\not{B}'$), or (3) include b-jets (marked as B'). Each process also includes one electroweak sample in which the Z is produced by a t-channel process with 2, 3, and 4 jets at LO EW.

Top quark samples

Top quarks are a background source of leptons and $E_{\mathrm{T}}^{\mathrm{miss}}$ through the decay $t \to W(\ell\nu) + b$. Hence top quark processes mainly contribute to non-resonant $\ell\ell$ backgrounds with two leptons coming from W's. They also contribute to very small backgrounds involving vector bosons, $t\bar{t}V$ and $t\bar{t}VV$. Table 4.14 summarizes the top quark samples used in the analysis. POWHEG or MADGRAPH generators are used in

combination with Pythia for all samples.

Table 4.14: List of top quark simulation samples.

Background	Process	$\sigma \times \epsilon_{\text{gen}}$ (fb)	Generator	DSID
Wt	Wt	3.79×10^4	Powheg+Pythia	410646
	$W\bar{t}$	3.79×10^4	Powheg+Pythia	410647
t	t-channel t	3.70×10^4	Powheg+Pythia	410658
	t-channel $\bar{t}$	2.22×10^4	Powheg+Pythia	410659
	s-channel t	2030	Powheg+Pythia	410644
	s-channel $\bar{t}$	1230	Powheg+Pythia	410645
$t\bar{t}$	—	8.77×10^4	Powheg+Pythia	410472
$t\bar{t}V(V)$	$t\bar{t}W$	603	MadGraph+Pythia	410155
	$t\bar{t}Z(\nu\nu)$	155	MadGraph+Pythia	410156
	$t\bar{t}Z(qq)$	528	MadGraph+Pythia	410157
	$t\bar{t}WW$	9.90	MadGraph+Pythia	410081
	$t\bar{t}Z(ee)$	44.3	MadGraph+Pythia	410218
	$t\bar{t}Z(\mu\mu)$	44.3	MadGraph+Pythia	410219

Triboson samples

Triboson (VVV) processes account for less than 1% of the total background. Table 4.15 lists the Sherpa samples used in the analysis.

Table 4.15: List of triboson simulation samples. All samples are generated with Sherpa.

Background	Process	$\sigma \times \epsilon_{\text{gen}}$ (fb)	DSID
VVV	$WWW \to 3\ell 3\nu$	7.20	364242
	$WWZ \to 4\ell 2\nu$	1.80	364243
	$WWZ \to 2\ell 4\nu$	3.55	364244
	$WZZ \to 5\ell\nu$	0.188	364245
	$WZZ \to 3\ell 3\nu$	0.743	364246
	$ZZZ \to 6\ell$	0.0145	364247
	$ZZZ \to 4\ell 2\nu$	0.0866	364248
	$ZZZ \to 2\ell 4\nu$	0.171	364249

4.6 Kinematic distributions

Figures 4.5 and 4.6 show the m_{T}^{ZZ}, $E_{\mathrm{T}}^{\mathrm{miss}}$, $\mathcal{S}$, and $\Delta R_{\ell\ell}$ distributions in the signal region as obtained from simulation. The plotted simplified model signal has $m_{\chi} = 1$ GeV, $m_{\mathrm{med}} = 900$ GeV, and the 2HDM+a signal has $\tan\beta = 1.0$, $\sin\theta = 0.7$, $m_H = 600$ GeV, $m_a = 400$ GeV, and $m_{\chi} = 10$ GeV. More distributions are shown in Appendix B.

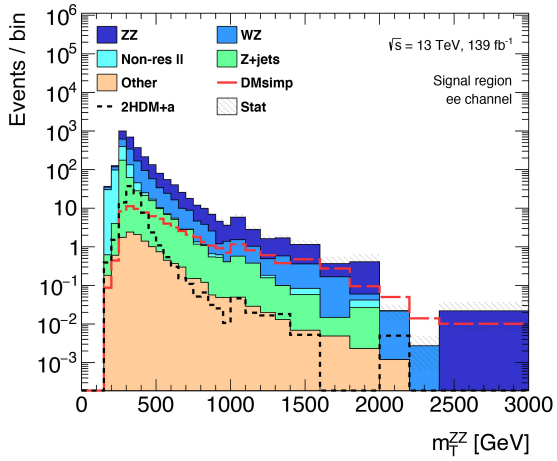

(a) m_{T}^{ZZ}, ee channel.

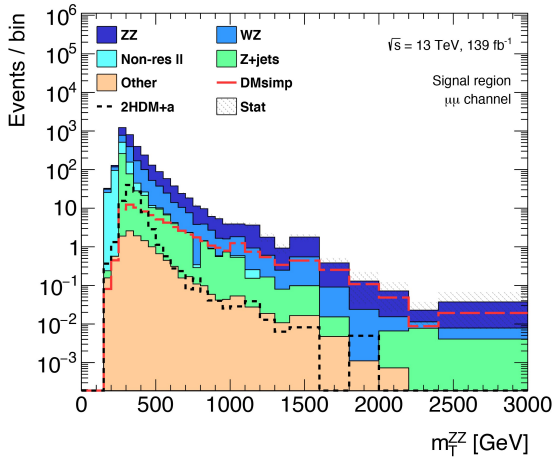

(b) m_{T}^{ZZ}, $\mu\mu$ channel.

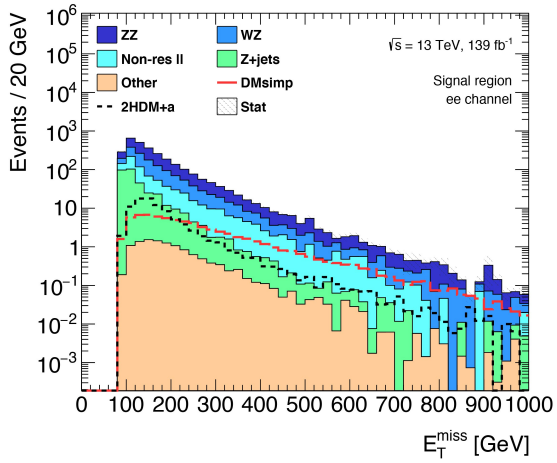

(c) $E_{\mathrm{T}}^{\mathrm{miss}}$, ee channel.

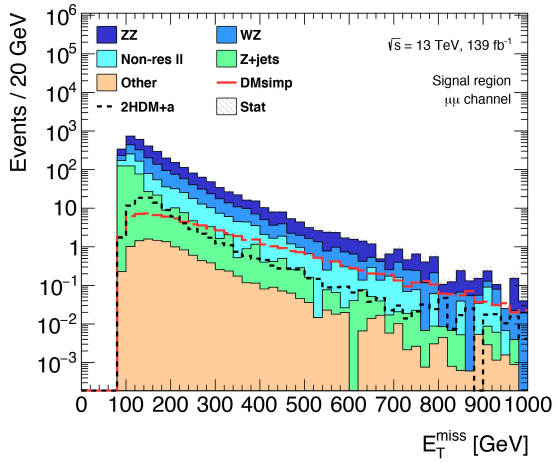

(d) $E_{\mathrm{T}}^{\mathrm{miss}}$, $\mu\mu$ channel.

Figure 4.5: Simulated m_{T}^{ZZ} and $E_{\mathrm{T}}^{\mathrm{miss}}$ distributions in the signal region. The plotted simplified model signal has $m_{\chi} = 1$ GeV, $m_{\mathrm{med}} = 900$ GeV, and the 2HDM+a signal has $\tan\beta = 1.0$, $\sin\theta = 0.7$, $m_H = 600$ GeV, $m_a = 400$ GeV, $m_{\chi} = 10$ GeV. Statistical errors are included.

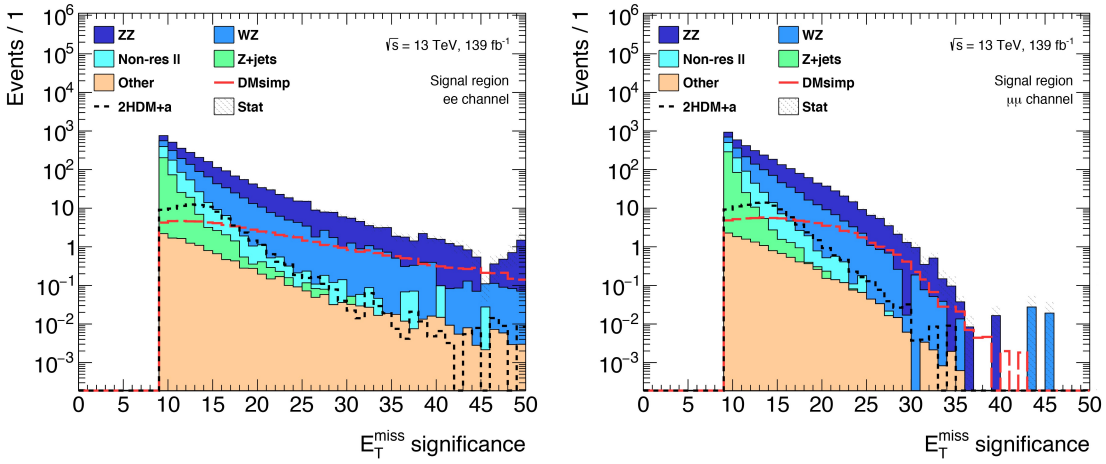

(a) $\mathcal{S}$, ee channel.

(b) $\mathcal{S}$, $\mu\mu$ channel.

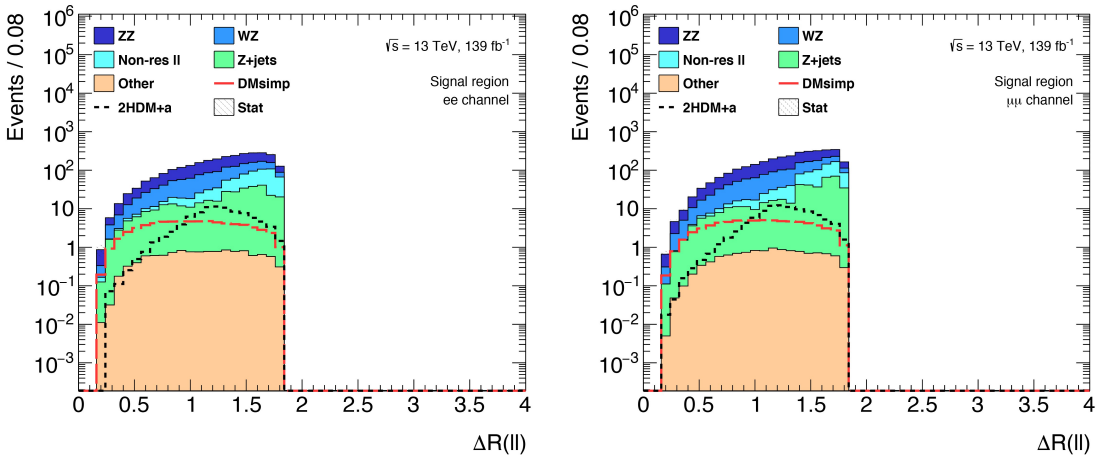

(c) $\Delta R_{\ell\ell}$, ee channel.

(d) $\Delta R_{\ell\ell}$, $\mu\mu$ channel.

Figure 4.6: Simulated $\mathcal{S}$ and $\Delta R_{\ell\ell}$ distributions in the signal region. The plotted simplified model signal has $m_\chi = 1$ GeV, $m_{\text{med}} = 900$ GeV, and the 2HDM+a signal has $\tan\beta = 1.0$, $\sin\theta = 0.7$, $m_H = 600$ GeV, $m_a = 400$ GeV, $m_\chi = 10$ GeV. Statistical errors are included.

Chapter 5

Signal and Background Estimates

5.1 Systematic uncertainties

The analysis is affected by several sources of systematic uncertainty. Systematic errors are categorized as either experimental or theoretical. Experimental errors arise from detector effects while theoretical errors come from uncertainties in the cross section calculation. These uncertainties affect all simulated samples in the analysis, as well as data-driven estimates that use simulation in the estimation procedure. These errors are entered into the final statistical fit as nuisance parameters.

5.1.1 Experimental uncertainties

There are several sources of experimental systematic uncertainties in the analysis that must be accounted for. Systematic errors are provided by combined performance working groups. Variations of $+1\sigma$ and -1σ are provided for each systematic source; these variations may affect either event weights (e.g. efficiency scale factor uncertainties) or event kinematics (e.g. electron energy resolution uncertainty). These systematic variations are each applied one by one, object and event selections are repeated, and their effect on the total event yield in the signal region is assessed. Tables 5.1 and 5.2 summarize all sources of experimental systematic uncertainties considered. Descriptions of these systematics are also given below.

Electron uncertainties

All electrons in simulation are calibrated and have their energy smeared to match what is observed in data; these corrections impose systematic uncertainties on the electron energy scale and resolution. Efficiency scale factors are also applied to simulation per electron to account for differences between data and simulation in reconstruction, isolation, identification, and trigger efficiencies. Nuisance parameters are assigned for each of these. For electron identification, an expanded list is used in order to allow for future combinations with other analyses.

Muon uncertainties

Simulated muons have their momenta calibrated and smeared to match data, and corresponding systematic uncertainties on the muon momentum scale and resolution are assigned. Momentum scale systematics are split into charge-dependent (sagitta[1] uncertainties) and charge-independent variations, and momentum resolution systematics are assigned separately for the inner detector and muon spectrometer. Uncertainties in the efficiency scale factors for muon reconstruction, isolation, track-to-vertex association, and trigger efficiencies are also considered.

Jet uncertainties

Jet systematic uncertainties are in general the largest experimental systematics in the analysis. Uncertainties in the jet energy scale are studied using approximately 20 parameters that account for η-intercalibration uncertainties, flavour-specific uncertainties, high p_{T} jet uncertainties, and several sources of pileup uncertainties. The jet energy resolution is parameterized using seven parameters and an additional nuisance parameter to account for resolution differences compared to data. Efficiency uncertainties are considered for the jet vertex tagger efficiency scale factor and various flavour tagging efficiencies.

[1]The sagitta is used to determine the momentum of muons. A muon track will typically leave three hits in the MS. If a line is draw between the first and last hits, the distance between the line and the second hit is the muon sagitta. This distance can be used to infer the muon momentum. A muon with $p_{\mathrm{T}} = 1$ TeV typically corresponds to a sagitta of about 1 mm.

Missing transverse momentum uncertainties

$E_{\mathrm{T}}^{\mathrm{miss}}$ uncertainties are estimated from track-based soft term parameters, since uncertainties on the electrons, muons, and jets in the $E_{\mathrm{T}}^{\mathrm{miss}}$ calculation are accounted for using the above systematics. Momentum scale uncertainties in the soft term are calculated according to the direction of the $\vec{p}_{\mathrm{T}}$ sum of all hard objects in the $E_{\mathrm{T}}^{\mathrm{miss}}$, defined as $\vec{p}_{\mathrm{T}}^{\,\mathrm{hard}}$. Nuisance parameters are assigned for uncertainties in the soft term momentum scale parallel to $\vec{p}_{\mathrm{T}}^{\,\mathrm{hard}}$ and momentum resolution uncertainties parallel and perpendicular to $\vec{p}_{\mathrm{T}}^{\,\mathrm{hard}}$.

Other uncertainties

Simulated samples have pileup reweighting applied so that the simulated μ distribution matches what is observed in data. The associated uncertainty from this procedure is estimated using a dedicated nuisance parameter. In addition, the uncertainty in the combined 2015-2018 integrated luminosity is 1.7% (2.4 fb^{-1}) [54], obtained using the LUCID-2 detector [74] for the primary luminosity measurements. This uncertainty affects all simulated samples and in-situ estimates.

Table 5.1: List of electron and muon experimental systematic uncertainties. Each nuisance parameter corresponds to $\pm 1\sigma$ variations.

Source of uncertainty	**Nuisance parameter**
Electrons	
Energy scale	`EG_SCALE_ALL` (full sim), `EG_SCALE_AF2` (fast sim)
Energy resolution	`EG_RESOLUTION_ALL`
Reconstruction efficiency scale factor	`EL_EFF_Reco_TOTAL_1NPCOR_PLUS_UNCOR`
Isolation efficiency scale factor	`EL_EFF_Iso_TOTAL_1NPCOR_PLUS_UNCOR`
Identification efficiency scale factor	`EL_EFF_ID_CorrUncertaintyNP{0-15}`, `EL_EFF_ID_SIMPLIFIED_UncorrUncertaintyNP{0-17}`
Trigger efficiency scale factor	`EL_EFF_Trigger_TOTAL_1NPCOR_PLUS_UNCOR`
Trigger efficiency	`EL_EFF_TriggerEff_TOTAL_1NPCOR_PLUS_UNCOR`
Muons	
Inner detector track	`MUON_ID`
Muon spectrometer track	`MUON_MS`
Momentum scale	`MUON_SCALE`
Momentum scale (charge dependent)	`MUON_SAGITTA_RESBIAS`, `MUON_SAGITTA_RHO`
Reconstruction efficiency scale factor	`MUON_EFF_RECO_STAT`, `MUON_EFF_RECO_SYS`
Isolation efficiency scale factor	`MUON_EFF_ISO_STAT`, `MUON_EFF_ISO_SYS`
TTVA efficiency scale factor	`MUON_EFF_TTVA_STAT`, `MUON_EFF_TTVA_SYS`
Trigger efficiency scale factor	`MUON_EFF_TrigStatUncertainty`, `MUON_EFF_TrigSystUncertainty`

Table 5.2: List of jet, $E_{\mathrm{T}}^{\mathrm{miss}}$, and other experimental systematic uncertainties. Each nuisance parameter corresponds to $\pm 1\sigma$ variations.

Source of uncertainty	**Nuisance parameter**
Jets	
Energy scale	JET_EffectiveNP_{1-8}
Energy scale, η inter-calibration	JET_EtaIntercalibration_Modelling, JET_EtaIntercalibration_TotalStat, JET_EtaIntercalibration_NonClosure_highE, JET_EtaIntercalibration_NonClosure_negEta, JET_EtaIntercalibration_NonClosure_posEta
Energy scale, flavour	JET_Flavor_Response, JET_Flavor_Composition
Energy scale, b-jets	JET_BJES_Response
Energy scale, corrections for high p_{T} jets	JET_PunchThrough_MC16, JET_SingleParticle_HighPt
Energy scale, pileup correction	JET_Pileup_OffsetMu, JET_Pileup_OffsetNPV, JET_Pileup_PtTerm, JET_Pileup_RhoTopology
Energy resolution	JET_JER_EffectiveNP_{1,2,3,4,5,6,7restTerm}
Energy resolution, data/MC differences	JET_JER_DataVsMC16
Jet vertex tagger efficiency scale factor	JET_JvtEfficiency
Flavour tagging efficiency scale factor	FT_EFF_B_systematics, FT_EFF_C_systematics, FT_EFF_Light_systematics, FT_EFF_extrapolation, FT_EFF_extrapolation_from_charm
Missing transverse momentum	
Momentum scale	MET_SoftTrk_Scale
Momentum resolution	MET_SoftTrk_ResoPara, MET_SoftTrk_ResoPerp
Other	
Pileup reweighting	PRW_DATASF
Total integrated luminosity	Luminosity

5.1.2 Theoretical uncertainties

In addition to experimental systematics, simulated samples also have systematic uncertainties from various theoretical sources. These include QCD scale, parton distribution function, and parton shower uncertainties. These sources produce uncertainty on the number of events in the signal region.

QCD scale uncertainties

From the QCD factorization ansatz [75], the cross section for a hard process resulting from the collision of two protons with momenta p_1 and p_2 can be written as

$$\sigma = \int \mathrm{d}x_1 f_1(x_1, \mu_F^2) \int \mathrm{d}x_2 f_2(x_2, \mu_F^2)\, \hat{\sigma}(x_1 p_1, x_2 p_2, \mu_R^2), \tag{5.1}$$

where partons 1 and 2 have PDFs f_1 and f_2 and proton momentum fractions x_1 and x_2 respectively. $\hat{\sigma}$ is the cross section for the hard scatter process between the two partons. μ_R and μ_F are the QCD renormalization and factorization scales. Both scales are arbitrary and arise from finite order perturbation theory; μ_R is related to the renormalization of ultraviolet divergences, and μ_F qualitatively corresponds to the resolution at which the proton is being probed. The main assumption of this formula is that at high energies the timescale of the parton-parton collision is much shorter than the parton-parton interactions within a single proton. Hence, the two interacting partons can be treated as free with definite momentum. The total cross section is then calculated from the probability (modelled by the PDFs) for two partons with given momentum fractions to interact. $\hat{\sigma}$ is calculated to some finite order n in α_s according to $\hat{\sigma} = \alpha_s\hat{\sigma}^{(0)} + \alpha_s^2\hat{\sigma}^{(1)} + ... + \alpha_s^n\hat{\sigma}^{(n-1)} + \mathcal{O}(\alpha_s^{n+1})$. The uncertainties on μ_F and μ_R provide an estimate of $\mathcal{O}(\alpha_s^{n+1})$, i.e. missing higher order terms in the perturbative expansion of the partonic cross section.

PDF uncertainties

The determination of the parton distribution functions f_1 and f_2 in Equation 5.1 are subject to several sources of error. Intra-PDF systematic uncertainties describe errors within a given PDF set. Such systematics arise from experimental uncertainties in the datasets used in the PDF fits, and uncertainties in the functional forms used in the fits. Inter-PDF systematics arise from differences between various PDF sets. These uncertainties can be related to, for example, the flavour scheme used in the calculation of a PDF, or nuclear effects. Missing higher order corrections in the DGLAP evolution are estimated from the QCD scale uncertainties.

Parton showering uncertainties

Parton showering uncertainties arise from the parameterization used for the modelling of parton showering and hadronization in simulation. For example, the Pythia MC generator uses the A14 tune, a standardized parameterization specific to ATLAS and constructed from comparisons to Run 1 data. This parameterization has an associated set of 10 "eigenvariations" that are used to quantify the error in the A14 tune. These uncertainties account for variations of the parameters controlling initial/final state radiation, multi-parton interactions, and colour reconnection.

5.2 Signal estimation

Simulated samples are used to estimate dark matter m_{T}^{ZZ} distributions in the signal region; the signal samples are subject to experimental and theoretical sources of error. In addition, techniques are used to create synthetic signal samples in order to cover more parameter space without the need for additional reconstructed samples. This section describes the signal m_{T}^{ZZ} distributions, the evaluation of their systematic uncertainties, and how synthetic signal samples are produced/validated.

5.2.1 Signal m_{T}^{ZZ} distributions

The signal m_{T}^{ZZ} distributions are estimated from simulation. The dependence of these distributions on the model parameters is described in this section. Figure 5.1 illustrates the signal region m_{T}^{ZZ} distributions for simplified model samples with varying m_{χ} and fixed m_{med}. As m_{χ} becomes larger the cross section decreases, leading to smaller yields for signals with heavier masses. For s-channel simplified models, the cross section strongly depends on whether or not $m_{\mathrm{med}} > 2m_{\chi}$ (recall Figure 2.6); if m_{χ} becomes larger than this, the mediator cannot produce the dark matter particles on-shell, and the cross section sharply decreases. For signals with $m_{\mathrm{med}} > 2m_{\chi}$, the m_{T}^{ZZ} shape does not depend on m_{χ} for a fixed m_{med}, only the cross section changes. Similarly, Figure 5.2 shows the m_{T}^{ZZ} dependence on m_{med} for fixed m_{χ}. The cross

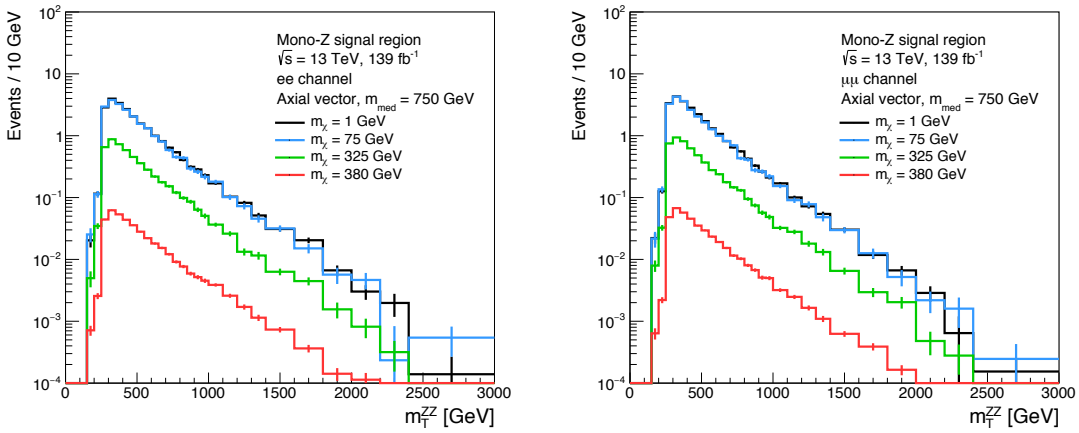

(a) ee channel.

(b) $\mu\mu$ channel.

Figure 5.1: m_{T}^{ZZ} distributions for simplified model signals with varying m_{χ} and $m_{\mathrm{med}} = 750$ GeV. Statistical errors are included.

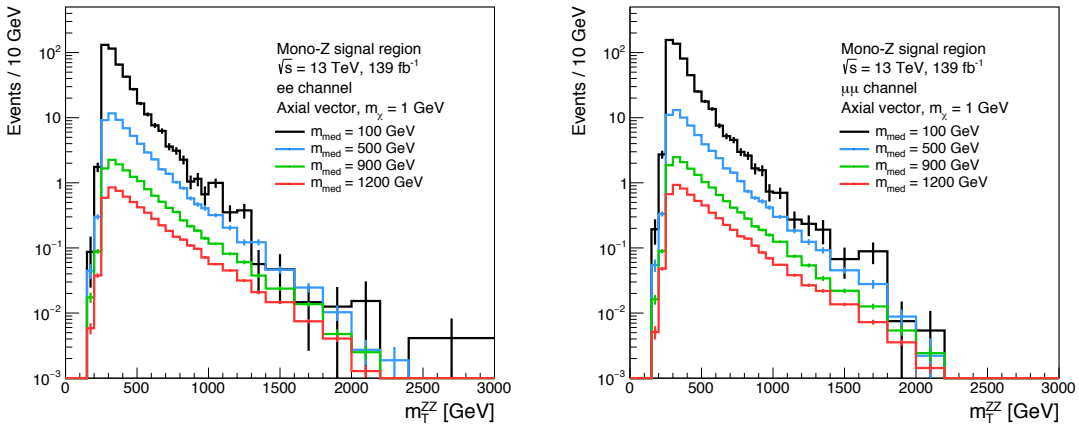

(a) ee channel. (b) $\mu\mu$ channel.

Figure 5.2: m_{T}^{ZZ} distributions for simplified model signals with varying m_{med} and $m_{\chi} = 1$ GeV. Statistical errors are included.

section also decreases with increasing m_{med}, and the m_{T}^{ZZ} distribution becomes more spread towards higher values for larger m_{med}.

For 2HDM+a models, the behaviour of the m_{T}^{ZZ} distribution on the model parameters is more complicated, as there are many parameters and different production modes. Figure 5.3 shows signal region m_{T}^{ZZ} distributions for signals with varying m_A

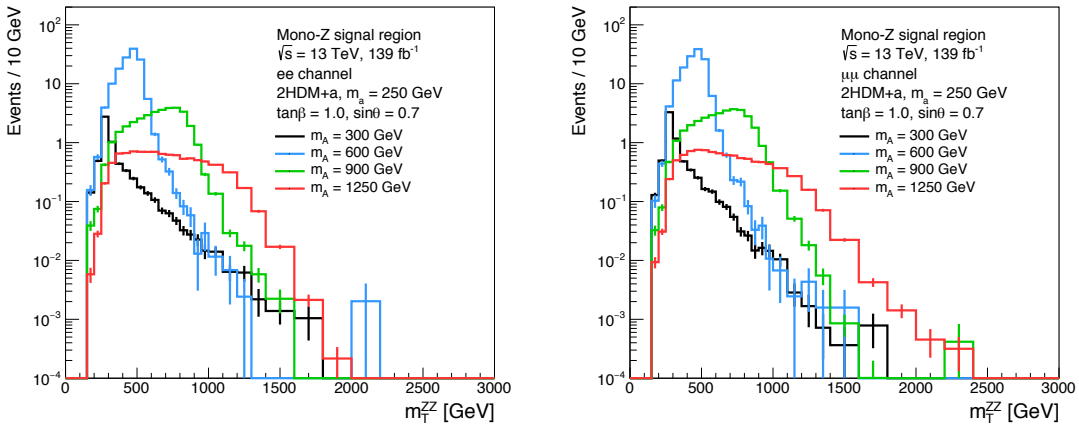

(a) ee channel. (b) $\mu\mu$ channel.

Figure 5.3: m_{T}^{ZZ} distributions for 2HDM+a model signals with varying m_A. Other parameters are fixed to $m_a = 250$ GeV, $\tan\beta = 1.0$, and $\sin\theta = 0.7$. Statistical errors are included.

and all other parameters fixed. The resonant enhancement for when $m_A > m_a + m_Z$ is clearly seen here (see Figures 2.7a and 2.8a). For $m_a = 250$ GeV, $m_A = 300$ GeV is not heavy enough to produce the a and Z bosons on-shell, and the cross section is suppressed; when $m_A = 600$ GeV, there is enough mass energy to produce them on-shell, and the cross section is enhanced. As m_A increases beyond this threshold, the m_{T}^{ZZ} is pushed upwards and the cross section decreases. A similar effect is seen in Figure 5.4 for signals with varying m_a. With m_A fixed to 600 GeV, the cross section decreases rapidly for $m_a = 500$ GeV compared to the other signals, as this point is right on the on-shell threshold. The kinematics do not strongly depend on m_a as long as $m_A > m_a + m_Z$.

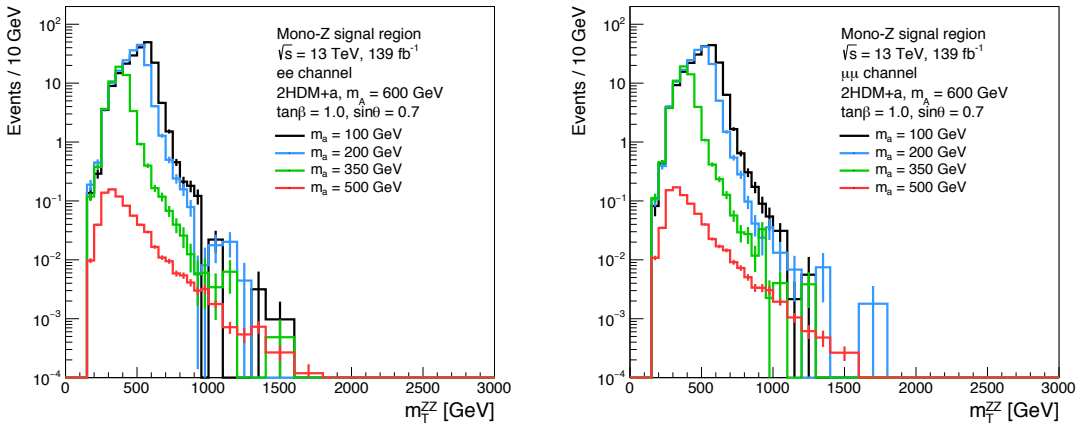

(a) ee channel.

(b) $\mu\mu$ channel.

Figure 5.4: m_{T}^{ZZ} distributions for 2HDM+a model signals with varying m_a. Other parameters are fixed to $m_A = 600$ GeV, $\tan\beta = 1.0$, and $\sin\theta = 0.7$. Statistical errors are included.

The m_{T}^{ZZ} dependence on $\tan\beta$ is illustrated in Figure 5.5. In this case the dependence is governed by the interplay of gg and bb production for type-II 2HDM+a models, for which the coupling of H, A, and a to top quarks is proportional to $\cot\beta$, while the coupling to bottom quarks is proportional to $\tan\beta$. Therefore gg production modes dominate for $\tan\beta \lesssim 1$, and bb production dominates for $\tan\beta \gtrsim 5$, with a transition region between where both modes contribute equally. This property leads to a non-trivial dependence of m_{T}^{ZZ} on $\tan\beta$. Figure 5.6 demonstrates the m_{T}^{ZZ} dependence on $\sin\theta$. In 2HDM+a models the HZa coupling is proportional to $\sin\theta$, so the cross section increases with increasing $\sin\theta$, and to first approximation there is no shape dependence.

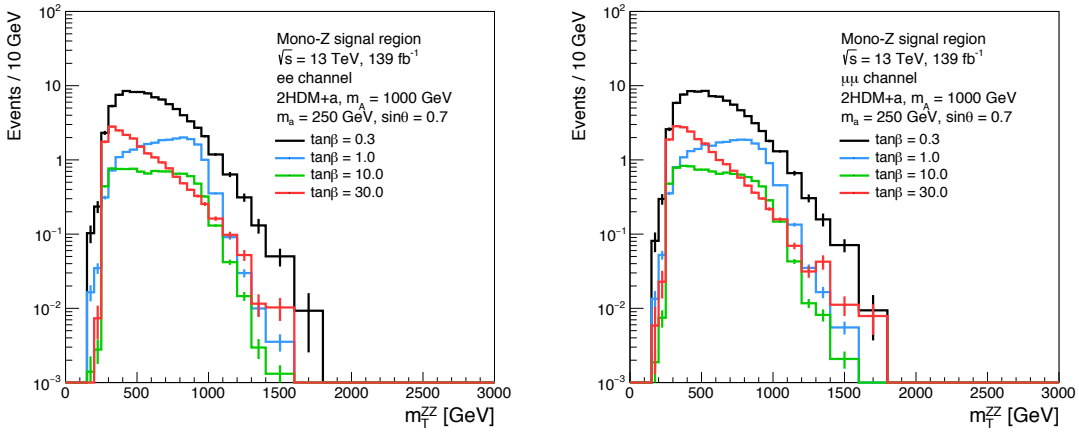

(a) ee channel. (b) $\mu\mu$ channel.

Figure 5.5: m_{T}^{ZZ} distributions for 2HDM+a model signals with varying $\tan\beta$. Other parameters are fixed to $m_A = 1000$ GeV, $m_a = 250$ GeV, and $\sin\theta = 0.7$. Statistical errors are included.

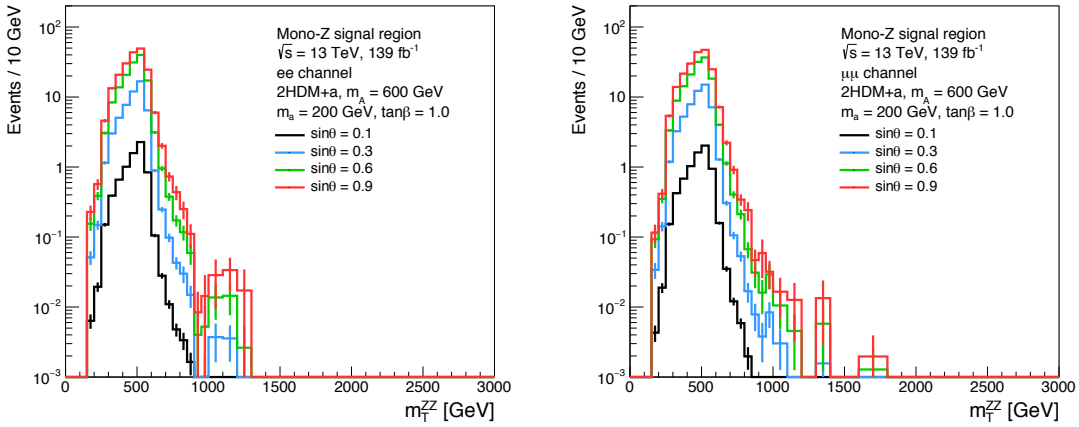

(a) ee channel. (b) $\mu\mu$ channel.

Figure 5.6: m_{T}^{ZZ} distributions for 2HDM+a model signals with varying $\sin\theta$. Other parameters are fixed to $m_A = 600$ GeV, $m_a = 200$ GeV, and $\tan\beta = 1.0$. Statistical errors are included.

5.2.2 Signal uncertainties

Experimental and theoretical systematic uncertainties are estimated on the signal m_{T}^{ZZ} distributions. The impact of experimental systematic errors on mono-Z simplified model signals is shown in Figure 5.7; the results for 2HDM+a signals are very similar and can be found in Appendix C. The plots show the total systematic error from all experimental sources on the total event yield in the signal region, as a function of different model parameters. Each experimental source of systematic error has $+1\sigma$ and -1σ variations. By design, each systematic source is uncorrelated with the other sources, so the total error is the sum of all individual errors in quadrature.[2] The experimental systematic error on the total signal region yield is 2-4% for all signal samples. The error can be calculated symmetrically from the maximum of the $\pm 1\sigma$ variations, or left as asymmetric. For the final statistical analysis, errors are calculated asymmetrically as a function of m_{T}^{ZZ} bin, and each experimental systematic is

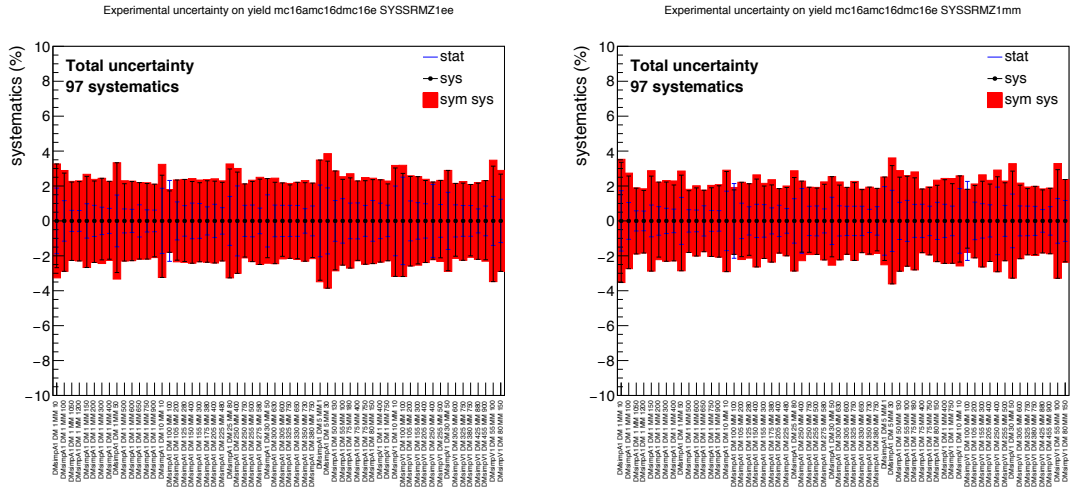

(a) ee channel.

(b) $\mu\mu$ channel.

Figure 5.7: Experimental systematic uncertainties on the total signal region event yield for simplified model signal samples. The blue error bar represents the statistical error. The black error bar represents the asymmetric systematic error, and the red band indicates the symmetrized systematic error.

[2] $+1\sigma$ and -1σ variations for a given systematic can produce positive or negative changes in the signal region yield. All positive errors are added in quadrature to give the total upwards variation on the yield, and all negative errors are added in quadrature to give the downwards variation. If both variations for a given systematic produce positive (negative) changes in the yield, then only the largest is included in the positive (negative) sum, and the other is ignored.

modelled using a binned nuisance parameter.

For PDF and QCD scale uncertainties, alternate event weights are included during event generation. For PDF systematics, sources of inter- and intra-PDF uncertainties are assessed; 100 error sets of the default PDF set `NNPDF30_nlo_as_0118` are provided, as well as weights for the two alternative sets `CT14nlo` and `MMHT2014nlo68cl`. For the QCD scale uncertainties, variations are applied to the renormalization and factorization scales μ_R and μ_F (both set to 1.0 by default); the six variations used in ATLAS analyses have (μ_R, μ_F) = (0.5, 0.5), (0.5, 1.0), (1.0, 0.5), (1.0, 2.0), (2.0, 1.0), and (2.0, 2.0).

By convention, theoretical uncertainties are calculated on the signal *acceptance* instead of on the yield.[3] The acceptance is the fraction of events remaining in the signal region compared to the number of events before any cuts are made. It is defined as

$$a = \frac{n}{N_{\text{sim}}} = \epsilon_{\text{gen}} \frac{n}{N}, \tag{5.2}$$

where n is the number of events after all selections, and N_{sim} is the number of events generated that corresponds to the cross section. It can also be written in terms of the generator filter efficiency, $\epsilon_{\text{gen}} = N/N_{\text{sim}}$, where N is the number of events in the sample derivation file.

The error on the acceptance is calculated according to recommendations as follows. Let s be the sum of event weights before any cuts (s_0 = nominal, s_j = varied due to PDF or QCD scale variation), and let y be the sum of event weights in the signal region (y_0 = nominal, y_j = varied due to PDF or QCD scale variation), where $j = 1, ...100$ for intra-PDF variations, $j = 1, 2$ for inter-PDF variations, and $j = 1, ...6$ for QCD scale variations. Let y_j^N be the normalized yield in the signal region: $y_j^N = (s_0/s_j)y_j$. For the intra-PDF uncertainty, the $\pm 1\sigma$ variations in y_j^N are calculated using the 15.87% and 84.14% quantiles. For the inter-PDF and QCD scale uncertainties, the recommendation is to take the envelope of y_j^N with respect to the nominal to get the $\pm 1\sigma$ variations:

$$+1\sigma = \max(\max(y_j^N - y_0), 0) \tag{5.3a}$$

$$-1\sigma = \min(\min(y_j^N - y_0), 0) \tag{5.3b}$$

[3]Differences in the acceptance due to theoretical systematics are treated as experimental and are therefore evaluated within ATLAS. Theoretical uncertainties on the signal yield (cross section) are treated as purely theoretical and are left to theorists to calculate.

Then the signal acceptance is calculated as $a = y/s$.

The impact of theoretical uncertainties on the acceptance is very small. Intra- and inter-PDF errors are in general less than 1% for both simplified and 2HDM+a model signal samples. QCD scale systematics are slightly larger, reaching about 1% for most signals and about 2-3% for a few 2HDM+a samples. Figures illustrating these systematics are shown in Appendix C for all reconstructed signal samples.

For the parton showering uncertainties on the signal acceptance, samples are manually generated for each of the 10 eigen-variations of the Pythia A14 tune. These uncertainties account for variations in the ISR/FSR, multiparton interaction, and colour reconnection parameter of the tune. Once the samples are generated, events are run through a set of selection requirements that mimic the set performed on reconstructed samples. Then, for each variation, the difference in the signal acceptance with respect to the nominal acceptance is calculated. As per ATLAS recommendations, the differences are summed in quadrature (separately for positive and negative variations) to obtain the asymmetric up and down variations.

Tables summarizing the total parton shower error on the acceptance for a selection of signals are given in Appendix C. In general the errors are on the order of 1-4%. For simplified model signals with very light masses ($m_{\text{med}} \sim 10$ GeV) the errors can be larger, closer to 10%. 2HDM+a parton shower errors are similar in general, about 1-4%. However, for larger $\tan\beta$ values the error can be larger, near 10-15%. It is also seen that lighter masses have slightly larger errors. There is no clear dependence on $\sin\theta$. Based on the validation results, a systematic error of 10% is applied to all 2HDM+a samples with $\tan\beta \leq 10$, and 15% is applied to samples with $\tan\beta > 10$.

5.2.3 Emulation techniques

The goal of emulation is to use the available reconstructed signal samples to produce m_{T}^{ZZ} histograms representing signals with different parameter values. These methods are necessary due to restrictions on the number of samples/events that can be generated and reconstructed for one analysis. The ATLAS reconstruction procedure is computationally intensive; with dozens of groups requesting millions of events to be generated and reconstructed, the amount of computing resources dedicated to this task is limited. Therefore emulation techniques are implemented in order to span the parameter space without the need for additional reconstructed samples.

Simplified model emulation

For simplified model signal samples, the main result facilitated by the LHC Dark Matter Working Group is the 2D (m_{med}, m_χ) mass plane for $g_\chi = 1.0$ and $g_q = 0.25$. In the on-shell region where $m_{\text{med}} > 2m_\chi$, the kinematics for signals with fixed m_{med} do not depend on m_χ. As demonstrated in Section 5.2.1, the kinematic distributions and signal region acceptance are constant for signals with the same m_{med}, and only the cross section changes.[4] Therefore the m_{T}^{ZZ} distribution of a reconstructed sample at (m_{med}, m_χ) can be used to emulate a new signal at (m_{med}, m'_χ) using a simple cross section scaling. Equation 5.4 shows the axial-vector (AV) scale factor obtained from the cross section ratio:

$$k^{AV}_{\text{emulate}} = \frac{\sigma^{AV}(m_{\text{med}}, m'_\chi)}{\sigma^{AV}(m_{\text{med}}, m_\chi)} \tag{5.4}$$

Hence only the cross section for the signal with (m_{med}, m'_χ) needs to be computed, rather than an entirely new reconstructed sample.

For vector signal sample emulation the technique is similar. As for the axial-vector case, the m_{T}^{ZZ} histograms from reconstructed vector samples at (m_{med}, m_χ) are scaled to obtain a new histograms with (m_{med}, m'_χ). However, the method is further extended so that emulation is also performed from axial-vector to vector signals. This extension exploits the fact that the kinematics in the on-shell region are nearly identical between axial-vector and vector signals. Therefore an axial-vector signal at (m_{med}, m_χ) can be used to emulate a vector signal at (m_{med}, m'_χ); therefore the vector (V) emulation scale factor can be calculated using two vector signal cross sections, or using one from each model[5]:

$$k^{V}_{\text{emulate}} = \frac{\sigma^{V}(m_{\text{med}}, m'_\chi)}{\sigma^{V}(m_{\text{med}}, m_\chi)} = \frac{\sigma^{V}(m_{\text{med}}, m'_\chi)}{\sigma^{AV}(m_{\text{med}}, m_\chi)} \tag{5.5}$$

Figure 5.8 illustrates the samples used for the 2D mass grid for axial-vector and vector models. Reconstructed samples are represented by black points, and emulated samples by blue points. For the axial-vector model there are 43 reconstructed samples and 39 emulated samples. For the vector model there are 17 reconstructed samples and 55 emulated samples. The ability to emulate from axial-vector to vector signals

[4] Additional validation plots illustrating this can be found in Appendix D.1.

[5] Equation 5.5 suggests that $\sigma^{AV}(m_{\text{med}}, m_\chi) = \sigma^{V}(m_{\text{med}}, m_\chi)$. This is true in the on-shell region where the cross sections typically agree within 5%.

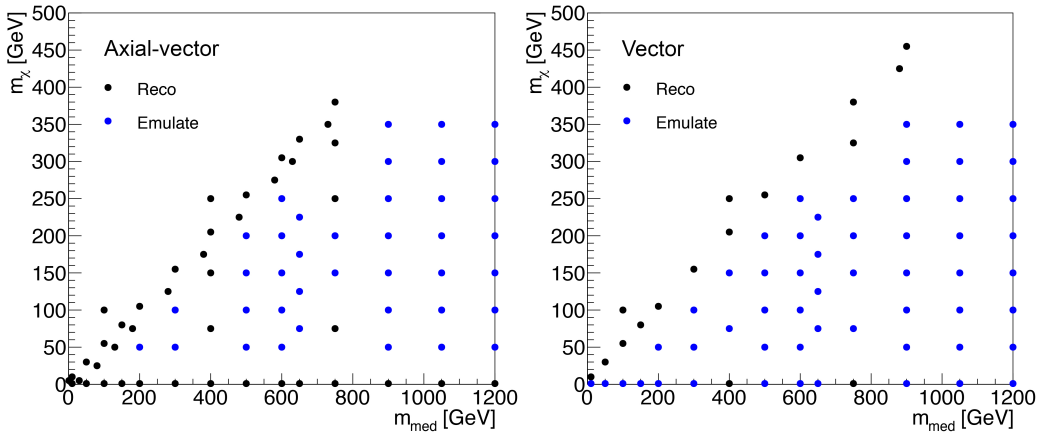

(a) Axial-vector grid.

(b) Vector grid.

Figure 5.8: Grid of (m_χ, m_{med}) values for reconstructed and emulated (a) axial-vector and (b) vector simplified model signal samples.

means that fewer reconstructed vector signals are required.

2HDM+a matrix element reweighting

2HDM+a model signals require more complicated reweighting methods due to the complexity of the model. MadGraph *matrix element reweighting* is the method used for the 2D $\tan\beta$ vs m_a/m_A scans (total of 4) and 1D $\sin\theta$ scans (total of 2). This method uses ratios of matrix elements to obtain modified MC weights:

$$w_{\text{new}}^{\text{MC}} = \frac{|M_{\text{new}}|^2}{|M_{\text{orig}}|^2} \times w_{\text{orig}}^{\text{MC}} \tag{5.6}$$

These weights are calculated by MadGraph during event generation for different values of $\tan\beta$ and/or $\sin\theta$, and are stored in the sample file. During the analysis of reconstructed samples, the weights can be accessed and applied to events to produce m_{T}^{ZZ} distributions as if they were produced from samples with modified $\tan\beta$ and/or $\sin\theta$ parameters. A modified weight exists for each event, so matrix element reweighting is performed event-by-event.

Figure 5.9 shows example parameter grids for ($\tan\beta$, m_A) scans with $\sin\theta = 0.7$ and 0.35. The 12 black points at $\sin\theta = 0.7$ and $\tan\beta = 1$ represent reconstructed samples. For these particular scans, each reconstructed sample contains modified weights to reweight vertically between different $\tan\beta$ values, as well as to reweight between grids from $\sin\theta = 0.7$ to $\sin\theta = 0.35$. gg production dominates at low

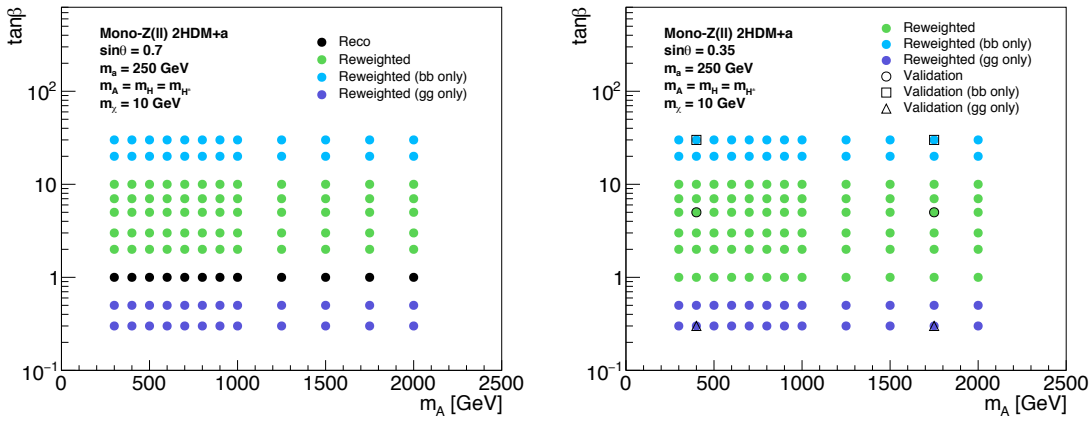

(a) $\sin\theta = 0.7$. (b) $\sin\theta = 0.35$.

Figure 5.9: Grid of $(\tan\beta,\ m_A)$ values for reconstructed and matrix element reweighted 2HDM+a signal samples. Sample points have $m_a = 250$ GeV.

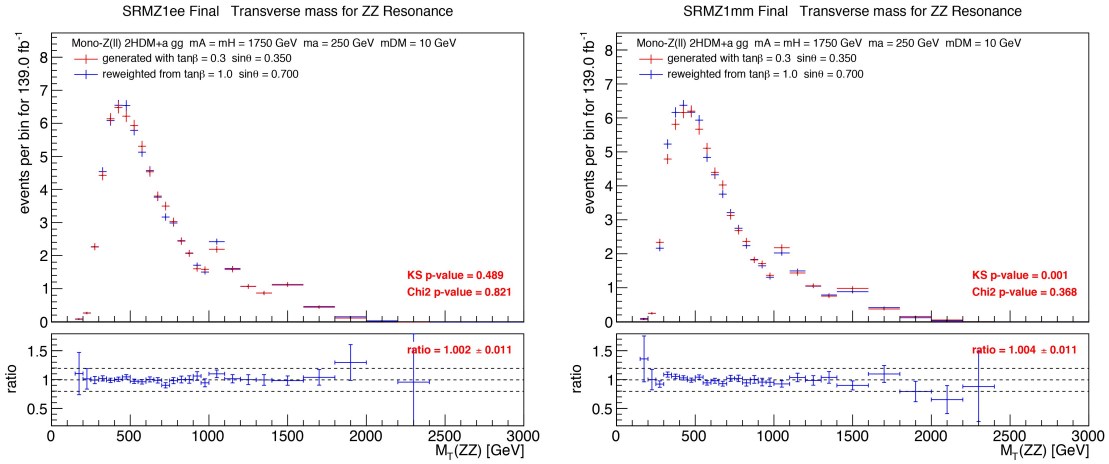

(a) ee channel. (b) $\mu\mu$ channel.

Figure 5.10: Matrix element reweighting validation in the m_{T}^{ZZ} distribution. Results are shown for the 2HDM+a signal sample with $m_A = 1750$ GeV and $m_a = 250$ GeV. The red histogram is the m_{T}^{ZZ} from a reconstructed sample generated with $\sin\theta = 0.35$ and $\tan\beta = 0.3$. The blue histogram is the m_{T}^{ZZ} produced using matrix element reweighting from a reconstructed sample with $\sin\theta = 0.7$ and $\tan\beta = 1.0$. p-values are shown for the Kolmogorov-Smirnov and χ^2 tests.

$\tan\beta$, so only the gg component of the reconstructed samples are reweighted down to $\tan\beta < 1$. Likewise, bb production dominates at high $\tan\beta$, so only the bb component is reweighted to $\tan\beta > 10$. Reconstructed validation samples are produced with $\sin\theta = 0.35$ in order to validate the reweighting technique. Additional grids for the $\tan\beta$

vs m_a scans and $\sin\theta$ scans are outlined in Appendix D.2. There are 20 validation samples across all scans.

Figure 5.10 shows validation examples for the sample with ($\tan\beta$, $\sin\theta$) = (0.3, 0.35), m_A = 1750 GeV, and m_a = 250 GeV. The m_{T}^{ZZ} distributions from the reconstructed sample agree well with the reweighted distribution from a sample produced with ($\tan\beta$, $\sin\theta$) = (1.0, 0.7). The ratio of the distributions across the entire m_{T}^{ZZ} range is very close to 1, meaning that both the shape and normalization of the distribution are well reproduced. In general the normalization for all reweighted samples is within 4% of the expected validation sample normalization. One outlier is the case for reweighting from ($\tan\beta$, $\sin\theta$) = (1.0, 0.7) to (30, 0.35) for the sample with m_A = 600 GeV, m_a = 100 GeV. In this case the reweighted normalization differs by 15% compared to the validation sample. A conservative *non-closure* systematic uncertainty of 15% is applied to reweighted signal samples with $\tan\beta \geq 20$ and $\sin\theta$ = 0.35. Additional validation results can be found in Appendix D.2.

2HDM+a histogram reweighting

Matrix element reweighting cannot be used to emulate signal samples with different masses. There is not enough overlap in momentum space between two parameter points with different masses to produce statistically reliable matrix element weights. *Histogram reweighting* is used instead to emulate signal samples with different values of m_A and/or m_a. Histogram reweighting is performed on reconstructed samples using truth-level information. Truth particles are the particles that are produced by the MC generator, before they are modified by the reconstruction algorithm. Truth-level information is stored in the reconstructed samples for the purpose of histogram reweighting. For the samples to be emulated, only truth-level information is needed instead of full reconstruction. The reweighting is done in 3D using the following kinematic quantities:

- $p_{\mathrm{T}}^{Z,\mathrm{truth}}$ – transverse momentum of the Z boson, obtained from the lepton pair
- $p_{\mathrm{T}}^{\chi\chi,\mathrm{truth}}$ – transverse momentum of dark matter pair
- $\Delta\phi(Z,\chi\chi)^{\mathrm{truth}}$ – azimuthal angle between the Z and dark matter pair

3D histograms of these truth-level quantities are obtained for the reconstructed base samples, and for the target samples that are to be emulated from the base samples.

Then, for a given target sample, weights are calculated from the ratio of the target histogram divided by the base:

$$w_{\mathrm{HR}} = \frac{h_{\mathrm{target}}(p_{\mathrm{T}}^{Z,\mathrm{truth}}, p_{\mathrm{T}}^{\chi\chi,\mathrm{truth}}, \Delta\phi^{\mathrm{truth}})}{h_{\mathrm{base}}(p_{\mathrm{T}}^{Z,\mathrm{truth}}, p_{\mathrm{T}}^{\chi\chi,\mathrm{truth}}, \Delta\phi^{\mathrm{truth}})} \tag{5.7}$$

These weights are then applied event-by-event when processing the reconstructed sample in order to produce a new m_{T}^{ZZ} distribution for the target (m_a, m_A) point.

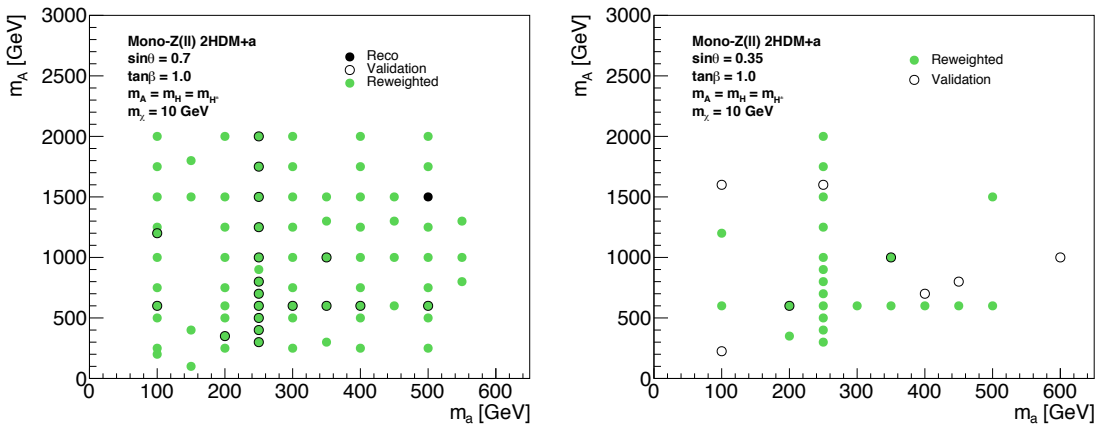

(a) $\sin\theta = 0.7$.

(b) $\sin\theta = 0.35$.

Figure 5.11: Grid of (m_A, m_a) values for reconstructed and histogram reweighted 2HDM+a signal samples. Sample points have $\tan\beta = 1.0$.

Figure D.5 shows the (m_A, m_a) sample grids. For the $\sin\theta = 0.7$ scan, four different base reconstructed samples were initially tested for the reweighting procedure; however, the sample at (m_a, m_A) = (500, 1500) GeV was shown to produce the best results for reweighting across the entire plane. Histogram reweighting was initially planned for the $\sin\theta = 0.35$ plane, but complications arose. In this plane histogram reweighting and matrix element reweighting are used simultaneously – matrix element reweighting is used to reweight reconstructed samples from $\sin\theta = 0.7$ to 0.35, and histogram reweighting is used to reweight between masses. However, the application of matrix element and histogram reweighting in the $\sin\theta = 0.35$ plane has been unsuccessful; reweighted samples show large shape and normalization differences compared to validation samples. Therefore the $\sin\theta = 0.35$ plane is obtained using samples produced from matrix element reweighting that are in this plane by coincidence.

3D histogram reweighting is shown to work well for the $\sin\theta = 0.7$ plane. While the shapes are well reproduced compared to validation samples, small normalization

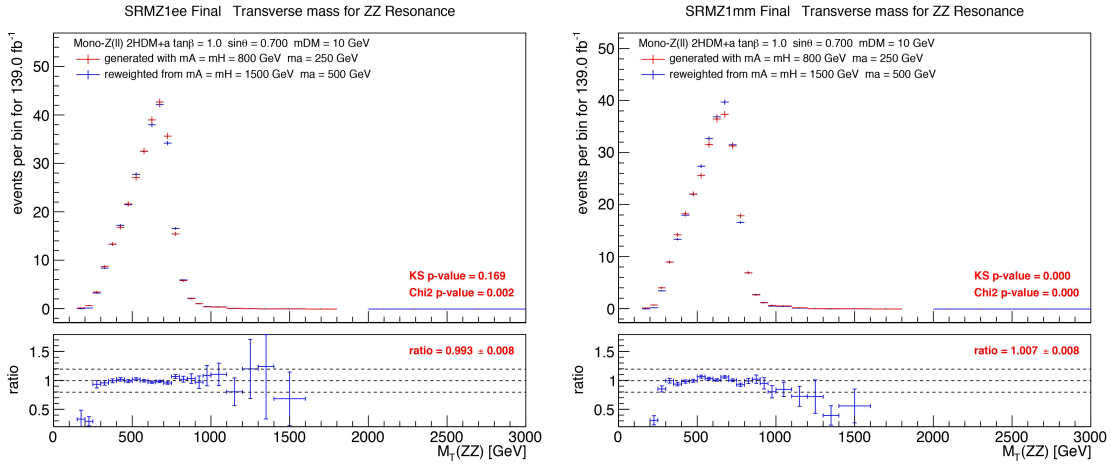

(a) ee channel. (b) $\mu\mu$ channel.

Figure 5.12: Histogram reweighting validation in the m_{T}^{ZZ} distribution. Results are shown for a 2HDM+a signal sample with $\tan\beta = 1.0$ and $\sin\theta = 0.7$. The red histogram is the m_{T}^{ZZ} from a reconstructed sample generated with $m_A = 800$ GeV and $m_a = 250$ GeV. The blue histogram is the m_{T}^{ZZ} produced using matrix element reweighting from a reconstructed sample with $m_A = 1500$ GeV and $m_a = 500$ GeV. p-values are shown for the Kolmogorov-Smirnov and χ^2 tests.

differences are observed; this is corrected with a global scale correction for all samples of 1.099 for the ee channel and 1.053 for the $\mu\mu$ channel. A validation example is shown in Figure 5.12 for samples with $\tan\beta = 1.0$ and $\sin\theta = 0.7$, reweighting from $(m_a,\ m_A) = (1500,\ 500)$ GeV to $(800,\ 250)$ GeV. In this figure the normalization correction has been applied, and the m_{T}^{ZZ} distributions agree. Overall the normalizations for reweighted samples agree with the validation samples within 4% after the correction. A few outlier targets with $m_a \leq 400$ GeV are observed with normalization differences between 7-12%; a conservative non-closure systematic error of 15% is assigned to target samples with $m_a \leq 400$ GeV. Additional validation results, including normalization comparisons for all validation samples, can be found in Appendix D.3.

5.3 Background estimation

Various methods are used to estimate the main analysis backgrounds: ZZ, WZ, non-resonant $\ell\ell$, Z+jets, and $ttV(V)/VVV$ processes. The m_{T}^{ZZ} distribution, including for any associated systematic errors, is required for each background. Unlike signal, which can only be estimated from simulation, SM backgrounds may be estimated

in-situ using data. When feasible, it is always preferable to use data in place of simulation for background estimation. If it is not possible to use data entirely, a partial in-situ method may be used, where the m_{T}^{ZZ} normalization/yield is obtained from data and the shape is taken from simulation. Otherwise, simulation is used for both the m_{T}^{ZZ} normalization and shape.

5.3.1 ZZ

$ZZ \to \ell^+\ell^-\nu\bar{\nu}$ events are the largest source of background in the analysis. They contain two leptons from a Z boson and real $E_{\mathrm{T}}^{\mathrm{miss}}$ from another Z decaying into neutrinos, as for $Z(\ell\ell) + E_{\mathrm{T}}^{\mathrm{miss}}$ dark matter signals, making it an irreducible background in the mono-Z search. The three underlying processes that make up this background are $qq \to ZZ \to \ell^+\ell^-\nu\bar{\nu}$, $gg \to ZZ \to \ell^+\ell^-\nu\bar{\nu}$, and $qq \to \ell^+\ell^-\nu\bar{\nu}jj$ with two Z's produced electroweakly via two W/Z bosons radiated from the interacting quarks.

Data-driven methods are investigated for the ZZ background estimate, but they are determined to be less reliable than an estimate from simulation alone; the attempted methods include a 4ℓ control region that suffers from low statistics, and $Z\gamma$ reweighting method that produces large systematic uncertainties. Therefore the ZZ background is estimated entirely using simulation from Sherpa, and the 4ℓ and $Z\gamma$ estimates are used to validate the agreement between ZZ events in data and simulation. These samples are produced at NLO in QCD. The $qq \to ZZ \to \ell^+\ell^-\nu\bar{\nu}$ sample is simulated at LO in EW and has additional NLO EW corrections [76] applied. The corrections are applied at truth-level as a function of $p_{\mathrm{T}}^{\nu\nu,\mathrm{truth}}$ (equivalent to truth $E_{\mathrm{T}}^{\mathrm{miss}}$). Two correction schemes are provided, which differ depending on how the EW corrections are factorized with respect to QCD corrections (either additive or multiplicative). The average of the two corrections is used as the EW correction for the Sherpa $qq \to \ell^+\ell^-\nu\bar{\nu}$ sample. Figure 5.13 shows the corrected $p_{\mathrm{T}}^{\nu\nu,\mathrm{truth}}$ distributions compared to the nominal one. The corrections are significant, and overall they reduce the nominal $qq \to \ell^+\ell^-\nu\bar{\nu}$ signal region yield by 10%.

Systematic errors on the simulated m_{T}^{ZZ} distribution are obtained from both experimental and theoretical sources. Experimental systematic errors on the total signal region yield range from 3-5% depending on the subprocess. Theoretical uncertainties on both shape and normalization are considered. PDF and parton shower uncertainties on the yield are about 2-3% for all subprocesses. QCD scale uncertainties are larger, about 5% for qq yields and 25-40% for the gg yield. The electroweak uncer-

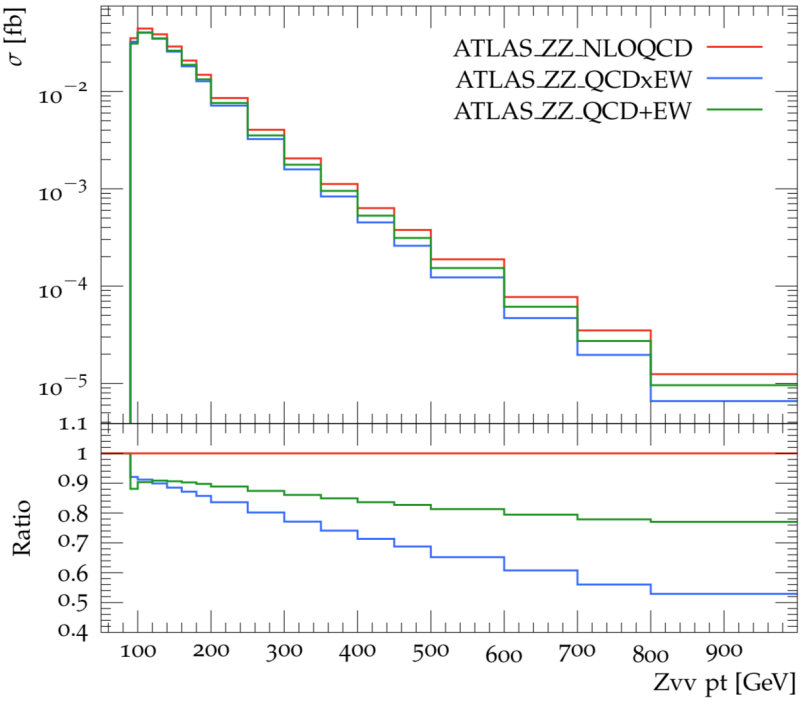

Figure 5.13: $p_{\mathrm{T}}^{\nu\nu,\mathrm{truth}}$ distributions for SHERPA $qq \to ZZ \to \ell^+\ell^-\nu\bar{\nu}$ samples with no correction (red), with multiplicative EW corrections (blue), and with additive EW corrections (green) [77]. The ratio indicates the difference with respect to the nominal distribution.

tainty is taken to be the difference between the average and the additive/multiplicative correction schemes, yielding an uncertainty of a few percent at low m_{T}^{ZZ} up to 10-15% in the upper m_{T}^{ZZ} tail. Studies confirm that the uncertainties in the m_{T}^{ZZ} shape due to QCD, parton shower, and EW sources have a significant impact on the dark matter limits.

5.3.2 WZ

$WZ \to \ell\nu\ell^+\ell^-$ events are the second largest background source in the analysis where the lepton from the W is not reconstructed. This may happen if the lepton is contained within a jet, fails object identification, or is outside the ATLAS detector acceptance. The WZ background is estimated from a combination of simulation and data, as was done for the 36.1 fb^{-1} result [57]; the shape of the m_{T}^{ZZ} distribution is obtained from simulation, and the normalization is corrected using data in a 3-lepton control region. This control region is similar to the signal region except that events are required to contain a third lepton. This requirement defines four orthogonal cate-

gories that contain either $ee+e$, $ee+\mu$, $\mu\mu+e$, or $\mu\mu+\mu$. The scale factor to correct the WZ simulation in the signal region is the ratio of the number of WZ events in the 3ℓ control region observed in data divided by the number of events in the 3ℓ control region predicted by simulation. The number of WZ data events in the signal region is then estimated using Equation 5.8:

$$\begin{aligned} N^{2\ell\mathrm{SR}}_{WZ,\mathrm{data}} &= N^{2\ell\mathrm{SR}}_{WZ,\mathrm{MC}} \times \frac{N^{3\ell\mathrm{CR}}_{WZ,\mathrm{data}}}{N^{3\ell\mathrm{CR}}_{WZ,\mathrm{MC}}} = N^{2\ell\mathrm{SR}}_{WZ,\mathrm{MC}} \times \mathrm{SF}_{WZ} \\ &= N^{3\ell\mathrm{CR}}_{WZ,\mathrm{data}} \times \frac{N^{2\ell\mathrm{SR}}_{WZ,\mathrm{MC}}}{N^{3\ell\mathrm{CR}}_{WZ,\mathrm{MC}}} = N^{3\ell\mathrm{CR}}_{WZ,\mathrm{data}} \times \mathrm{TF}_{WZ} \end{aligned} \tag{5.8}$$

$N^{2\ell\mathrm{SR}}_{WZ,\mathrm{MC}}$ is the number of WZ simulation events in the signal region, $N^{3\ell\mathrm{CR}}_{WZ,\mathrm{MC}}$ is the number of WZ simulation events in the control region, and $N^{3\ell\mathrm{CR}}_{WZ,\mathrm{data}}$ is the number of WZ data events in the control region.[6] The normalization scale factor, SF_{WZ}, is computed for each of the four 3ℓ categories, and the average is used as the final scale factor. The transfer factor TF_{WZ} is the ratio of the number of simulated events in the signal region divided by the number of simulated events in the control region. The systematic uncertainties on the WZ estimate are assessed using this simulation-dependent transfer factor.

Table 5.3: 3ℓ control region event selection criteria.

3ℓ control region
Two SFOS leptons with $p_{\mathrm{T}}^{\ell_1}$ ($p_{\mathrm{T}}^{\ell_2}$) > 30 (20) GeV
Third lepton with $p_{\mathrm{T}}^{\ell_3} > 20$ GeV
Veto events with additional loose leptons with $p_{\mathrm{T}} > 7$ GeV
76 GeV $< m_{\ell\ell,\mathrm{SFOS}} <$ 106 GeV
$m_{\mathrm{T}}^{W} > 60$ GeV
$\mathcal{S} > 3$
Veto events containing a b-jet

The 3ℓ control region event selections are summarized in Table 5.3. In general

[6] Simulation is used to estimate the non-WZ contributions in the 3ℓ control region. These contributions are subtracted from the total data in the control region to obtain the WZ component in data, $N^{3\ell\mathrm{CR}}_{WZ,\mathrm{data}}$.

they are similar to the signal region definition, except that an additional third lepton with $p_{\mathrm{T}} > 20$ GeV is required, and events containing a fourth lepton are ignored. The requirement on $m_{\ell\ell}$ is taken from the two same-flavour opposite-sign (SFOS) leptons. If all three leptons in the event have the same flavour, then the two leptons with opposite sign that produce $m_{\ell\ell}$ closest to m_Z mass are assumed to be the pair coming from the Z. In order to help select events with a W, a new requirement on the transverse mass of the W, m_{T}^W, is also applied. This quantity is calculated assuming that the third lepton comes from the W, and that the $E_{\mathrm{T}}^{\mathrm{miss}}$ is produced only from the neutrino of the W:

$$m_{\mathrm{T}}^W = \sqrt{2p_{\mathrm{T}}^{\ell} E_{\mathrm{T}}^{\mathrm{miss}} \left(1 - \cos(\Delta\phi)\right)} \tag{5.9}$$

In this case $\Delta\phi$ is the angle between the $\vec{p}_{\mathrm{T}}^{\,\ell}$ and $\vec{E}_{\mathrm{T}}^{\mathrm{miss}}$. The $E_{\mathrm{T}}^{\mathrm{miss}}$ significance requirement is loosened to $\mathcal{S} > 3$ and no $E_{\mathrm{T}}^{\mathrm{miss}}$ cut is applied in order to increase the statistics in the control region.

Across all control regions, the total scale factor is calculated to be 1.031 ± 0.011 (stat), increasing the signal region WZ prediction from simulation by about 3%. As mentioned, the systematic uncertainties on the WZ background are estimated on the transfer factor. Experimental systematics have an impact of 3-6% on the simulated signal region yield. For the theoretical sources, QCD scale uncertainties have the largest impact at about 8%, and PDF uncertainties are 3%.

5.3.3 Non-resonant $\ell\ell$

There are several sources of non-resonant $\ell\ell$ backgrounds: WW, Wt, single t, $t\bar{t}$, and $Z \to \tau\tau$. These processes can produce two same flavour, opposite sign leptons that do not come from a Z (although their $m_{\ell\ell}$ happens to be within $m_Z \pm 15$ GeV), as well as $E_{\mathrm{T}}^{\mathrm{miss}}$ from neutrinos. This occurs when multiple W bosons are produced and decay leptonically to the same flavour. For example, two W's can be directly produced and both decay via $W \to \ell\nu$, or they can be produced in the decays of top quarks or τ leptons via $t \to W(\ell\nu)b$ and $\tau \to \ell\nu\nu_\tau$.

Non-resonant $\ell\ell$ background sources are estimated using an $e\mu$ (different flavour lepton) control region, following the same method as in [57]. The method is similar to the WZ estimate in that the m_{T}^{ZZ} distribution is taken from simulation, with a normalization correction obtained from data in the control region. The $e\mu$ control region selections are identical to the signal region definition in Table 4.6, except that

two opposite flavour leptons are required (one electron and one muon). The method then exploits the fact that the probability for non-resonant processes to produce two same flavour leptons is half of the probability for them to produce opposite flavour leptons. In other words, the ratio for the processes to produce ee:$\mu\mu$:$e\mu/\mu e$ is 1:1:2. Because the $e\mu$ control region is identical to the signal region except for the requirement of opposite sign leptons, once the number of $e\mu$ events is known, then the number of ee and $\mu\mu$ events can be inferred to be half that number, modulo an efficiency factor. The number of non-resonant ee and $\mu\mu$ events in data in the signal region are given by

$$N^{\mathrm{SR}}_{ee,\mathrm{data}} = \frac{1}{2} \times \epsilon_{\ell\ell} \times N^{\mathrm{CR}}_{e\mu,\mathrm{data}} \tag{5.10}$$

and

$$N^{\mathrm{SR}}_{\mu\mu,\mathrm{data}} = \frac{1}{2} \times \frac{1}{\epsilon_{\ell\ell}} \times N^{\mathrm{CR}}_{e\mu,\mathrm{data}}, \tag{5.11}$$

where $N^{\mathrm{CR}}_{e\mu,\mathrm{data}}$ is the number of opposite flavour non-resonant events in the $e\mu$ control region in data,[7] and $\epsilon^2_{\ell\ell} = N_{ee}/N_{\mu\mu}$ is to account for the reconstruction efficiency differences between an electron pair and a muon pair. N_{ee} and $N_{\mu\mu}$ are the number of events from non-resonant sources that contain ee and $\mu\mu$ with invariant mass within $m_Z \pm 15$ GeV. $\epsilon_{\ell\ell}$ is estimated from data, with an estimate from simulation performed as a cross check. Furthermore, $\epsilon_{\ell\ell}$ is calculated in bins of p_{T} and η, as the reconstruction efficiency depends on the lepton p_{T} and the location in the detector.

Systematic uncertainties are estimated on $\epsilon_{\ell\ell}$ and from experimental and theoretical systematics on the simulation. The statistical error on the data in the control region is assigned as a systematic error. Additional systematics on $\epsilon_{\ell\ell}$ are assigned due the choice of (p_{T},η) bins and from the statistical errors on N_{ee} and $N_{\mu\mu}$. Experimental sources produce approximately 7% uncertainty on the normalization. PDF and QCD scale systematics are estimated on the $t\bar{t}$, WW, and Wt processes; in general these each yield less than 2% uncertainty on the normalization, except for the QCD scale uncertainty on $t\bar{t}$, which is closer to 10%.

5.3.4 Z+jets

The Z+jets background is the fourth largest background in the analysis. These events contain two leptons that are produced from a Z and jets that are mis-measured as fake

[7] In the $e\mu$ control region, simulation is used to estimate the number of data events that do not come from non-resonant sources; these events are then subtracted from the total data to obtain the number of non-resonant $e\mu$ events in data, $N^{\mathrm{CR}}_{e\mu,\mathrm{data}}$.

$E_{\mathrm{T}}^{\mathrm{miss}}$. The Z+jets background is difficult to estimate while maintaining control of the systematic errors; previous estimates in this search saw systematic uncertainties as large as 100% [57]. To improve on this, a new, fully data-driven method is developed to estimate the Z+jets background using reweighted γ+jets events. A complete description of this technique is presented in Chapter 6.

5.3.5 Other backgrounds

$t\bar{t}V$, $t\bar{t}VV$, and VVV processes produce multiple leptons and neutrinos. These backgrounds are suppressed due to the rejection of events with b-jets and third leptons, and make up less than 1% of the total background. They are estimated entirely using simulation. Experimental, PDF, and QCD scale systematics are assessed. In total the normalization error is 12-13% for all processes.

5.3.6 Summary

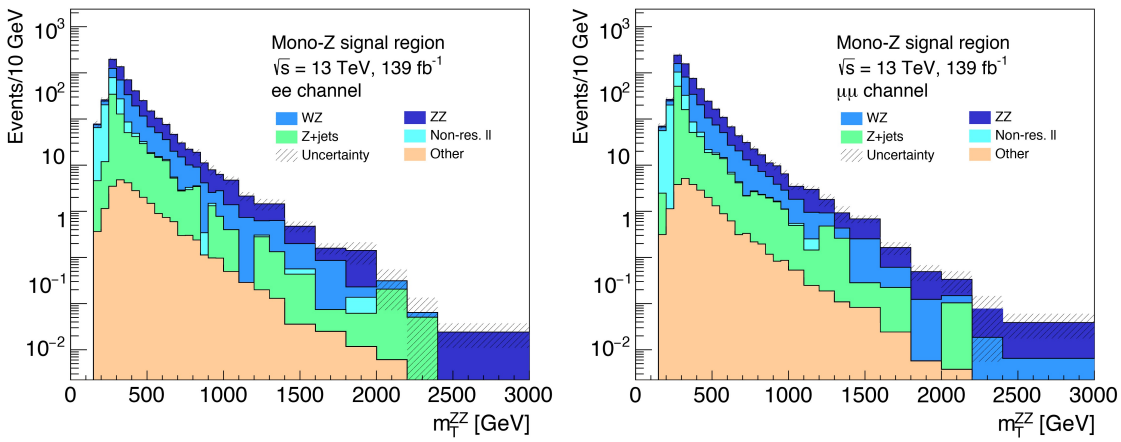

(a) ee channel. (b) $\mu\mu$ channel.

Figure 5.14: Predicted background m_{T}^{ZZ} distributions in the signal region. The uncertainty includes statistical and systematic sources of error for all processes. The last bin includes overflow content.

Figure 5.14 shows the m_{T}^{ZZ} distributions in the ee and $\mu\mu$ channels for all background estimates, and Table 5.4 summarizes the corresponding yields and uncertainties for each process. The background m_{T}^{ZZ} distributions are used in the statistical analysis with the predicted signal distributions in order to test for evidence of dark matter in the signal region.

Table 5.4: Predicted background yields in the signal region for 139 fb^{-1}. The first error quoted per process is the statistical uncertainty, and the second error is the systematic uncertainty (symmetrized using the average of the high and low variations).

Process	Subprocess	ee channel	$\mu\mu$ channel
ZZ	$qqZZ$	$1056.1 \pm 10.9 \pm 74.9$	$1199.7 \pm 11.7 \pm 71.7$
	$ggZZ$	$125.0 \pm 0.9 \pm 41.2$	$138.6 \pm 1.0 \pm 45.5$
	EW $qqZZ$	$18.4 \pm 0.5 \pm 1.2$	$18.9 \pm 0.5 \pm 1.3$
WZ	—	$785.2 \pm 6.0 \pm 32.5$	$868.9 \pm 6.6 \pm 37.4$
Non-resonant $\ell\ell$	—	$444.5 \pm 5.9 \pm 45.6$	$499.6 \pm 6.4 \pm 46.7$
Z+jets	—	$324.7 \pm 2.9 \pm 132.1$	$409.3 \pm 3.2 \pm 161.7$
Other	$ttV(V)$	$6.1 \pm 0.2 \pm 0.8$	$5.6 \pm 0.2 \pm 0.7$
	VVV	$5.9 \pm 0.1 \pm 0.7$	$6.2 \pm 0.1 \pm 0.7$
Total		$2765.9 \pm 14.1 \pm 177.8$	$3146.7 \pm 15.2 \pm 203.9$

Chapter 6

Z+jets Background Estimate Using γ+jets Reweighting

6.1 Overview

The Z+jets background is a source of fake $E_{\mathrm{T}}^{\mathrm{miss}}$ produced from mis-measured jets, usually yielding events with low $E_{\mathrm{T}}^{\mathrm{miss}}$; it is difficult to model, so in-situ estimates are preferred to simulation. The γ+jets reweighting method is a technique developed to improve on the ABCD method that was used in the previous iteration of the analysis (described in Section 5 of [57]). The γ+jets method improves on the statistical uncertainty of the Z+jets background estimate by utilizing a data sample enriched in γ+jets events, which have a much higher cross section than Z+jets. It also provides better control of the systematic uncertainties on the estimate by minimizing the use of simulation.

The goal of the γ+jets technique is to use reweighted γ+jets events in data to estimate the Z+jets background. In practice this means taking the ratio of simulated Z+jets and γ+jets distributions to obtain a weight $w(x)$ that depends on the observable x,

$$w(x) = \frac{Z\text{+jets}_{\mathrm{MC}}(x)}{\gamma\text{+jets}_{\mathrm{MC}}(x)}, \tag{6.1}$$

and applying this weight event-by-event to γ+jets events in data to obtain an estimate of the Z+jets background. γ+jets events are obtained from a control region that is identical to the signal region except that the Z boson is replaced with a photon. One of the major advantages of the reweighting method is that systematic errors in the

Z+jets and γ+jets simulation are expected to partially cancel in the ratio $w(x)$.

The viability of a 1D p_{T} reweighting method is shown theoretically in [78] in the regime where $p_{\mathrm{T}} \gg m_Z$ and the Z/γ kinematics are similar. However, there is no explicit Z p_{T} cut in the analysis, and so modifications to the reweighting scheme are necessary in order to achieve acceptable agreement between Z+jets and reweighted γ+jets events that include the entire p_{T} spectrum. The scheme that produced the best agreement between reweighted γ+jets simulation and Z+jets simulation uses a 2×2D reweighting method; two independent 2D weights are used, and the weight in Equation 6.1 is a product of two 2D weights: $w = w_1 \times w_2$.

This chapter is organized as follows. Section 6.2 defines the object and event selections used for the γ+jets control region, and the simulated samples used are presented in Section 6.3. The details of the reweighting scheme are discussed in Section 6.4. The validation of the method using simulation is described in Section 6.5, followed by the results obtained with data in Section 6.6. Finally, systematic uncertainties assigned to the estimate are discussed in Section 6.7, with a detailed comparison to the Z+jets prediction from simulation in Section 6.8. In this chapter, the "reweighting method/scheme" and "the reweighting" are in reference to the γ+jets reweighting technique. This chapter describes the method as performed for the m_{T}^{ZZ} distribution. The entire method was also performed for the $E_{\mathrm{T}}^{\mathrm{miss}}$ distribution; the results are summarized in Appendix E.1.

6.2 Object and control region selections

Table 6.1 summarizes the object-level requirements for photons considered in the γ+jets control region. The final selected photons have *loose* isolation,[1] *tight* identification,[2] and $p_{\mathrm{T}}^{\gamma} > 60$ GeV; these selections are chosen to roughly mimic those performed on electrons and muons. The author requirement means that objects reconstructed as photons or both electrons and photons are considered. Prescaled single photon triggers are needed in order to obtain the p_{T} spectrum below 120/140 GeV (thresholds for the lowest unprescaled single photon triggers); the list of prescaled

[1]For photons with *loose* isolation, the surrounding transverse energy within $\Delta R = 0.2$ must be less than 20% of the photon transverse momentum, and surrounding tracks within $\Delta R = 0.2$ must have less than 15% of the photon transverse momentum.

[2]The *loose* identification for photons is based on several discriminating variables in the HCAL and the middle layer of the ECAL. *Tight* photons use tighter requirements on the discriminant variables in addition to information from the ECAL strip layer.

Table 6.1: Photon object selections. Photons that pass all requirements are used for the event selection in the γ+jets control region.

Requirement	Details
Good object quality	Remove photons with bad clusters
Author	Require photon or ambiguous author
Cleaning	Remove photons with a large fraction of energy from bad cells
Calorimeter acceptance	Require $\lvert\eta_{\text{calo}}\rvert < 1.37$ or $1.52 < \lvert\eta_{\text{calo}}\rvert < 2.37$
Photon p_{T}	Require photon $p_{\text{T}} > 10$ GeV
Identification	Require *loose* ID
High voltage removal	Remove photons with bad HV EMEC clusters
Isolation	Require *fixed cut loose* isolation
Overlap removal	Remove overlap with electrons, muons, and jets
Photon p_{T}	Require $p_{\text{T}}^{\gamma} > 60$ GeV
Identification	Require *tight* ID
Trigger	Require that the event fired a single photon trigger
Trigger matching	Require that a selected photon fired a single photon trigger

and unprescaled triggers used are provided in Table 6.2. Prescaled triggers down to 60 GeV are required because, although no explicit Z p_{T} cut is made in the analysis, the $\Delta R_{\ell\ell}$ requirement renders an implicit cut near $p_{\text{T}}^{Z} > 60$ GeV.[3] A photon must pass any one of these triggers.

Table 6.2: List of single photon triggers.

Single photon trigger	Prescaled	Year
`HLT_g50_loose_L1EM15`	Y	all
`HLT_g60_loose`	Y	all
`HLT_g70_loose`	Y	all
`HLT_g80_loose`	Y	all
`HLT_g100_loose`	Y	all
`HLT_g120_loose`	N	2015
`HLT_g140_loose`	N	2016-18

Table 6.3 lists the event-level selections used to define the γ+jets control region. For convenience the cuts are listed alongside the nominal signal region selections that are applied to Z+jets events. The γ+jets control region requirements are chosen to mimic the signal region, but a photon is used in place of the $Z \to \ell\ell$ where possible. Instead of forming a Z from e^+e^- or $\mu^+\mu^-$ and vetoing events with extra leptons, the γ+jets region requires one photon (passing all requirements in Table 6.1) and vetos events with a lepton above $p_{\text{T}} > 7$ GeV. The steps at which w_1 and w_2 are applied are

[3]The effect of the $\Delta R_{\ell\ell}$ cut can be seen in the signal region p_{T}^{Z} distribution in Figure B.4. Since $p_{\text{T}}^{Z} > 60$ GeV for Z+jets, the photon in γ+jets events is also required to have $p_{\text{T}}^{\gamma} > 60$ GeV.

also labelled in Table 6.3; these steps are primarily chosen to minimize the statistical error of the weights. w_1 is applied after the b-jet veto, and w_2 is applied after the $E_{\mathrm{T}}^{\mathrm{miss}}$ cut. For the Z+jets simulation, all of the Z-specific cuts must be applied before the weights are calculated/applied as there is no equivalent cut for γ+jets events. Therefore all of the dilepton requirements are applied before reweighting.

Table 6.3: List of signal region and γ+jets control region selections.

Signal region	γ+jets control region
2 same flavour leptons	Lepton veto
Third lepton veto	
2 opposite sign leptons	
$76 < m_{\ell\ell} < 106$ GeV	1 photon
$\Delta R_{\ell\ell} < 1.8$	
b-jet veto	
—	$\times w_1$
$E_{\mathrm{T}}^{\mathrm{miss}} > 90$ GeV	
—	$\times w_2$
$\mathcal{S} > 9$	

6.3 Simulation samples

The γ+jets control region contains γ+jets and $\gamma+V$ events ($V = W/Z$), so simulation of these processes are needed to study this control region. The full list of samples used are given in Table 6.4. SHERPA 2.2 samples are used when available to match the analysis Z+jets samples, and `JETM4` derivations are used in place of HIGG2D1 because they store the necessary single photon trigger information. In order to ensure that the proper cancellations occur in the reweighting method, it is critical that the same generator and QCD/EW order is used for the γ+jets and Z+jets simulation.

Table 6.4: List of γ+jets and γ+V simulation samples.

Process	Subprocess	p_{T}^{γ} (GeV)	σ (fb)	DSID
γ+jets	—	{35, 70}	4.40×10^7	364542
		{70, 140}	4.53×10^6	364543
		{140, 280}	3.76×10^5	364544
		{280, 500}	2.19×10^4	364545
		{500, 1000}	1470	364546
		{1000, E_{CM}}	29.8	364547
γ+$Z(\nu\nu)$	—	{35, 70}	5260	364517
		{70, 140}	1340	364518
		{140, E_{CM}}	245	364519
γ+$Z(\ell\ell)$	ee	{35, 70}	6290	364502
		{70, 140}	491	364503
		{140, E_{CM}}	63.5	364504
	$\mu\mu$	{35, 70}	6290	364507
		{70, 140}	494	364508
		{140, E_{CM}}	63.3	364509
	$\tau\tau$	{35, 70}	6290	364512
		{70, 140}	494	364513
		{140, E_{CM}}	63.4	364514
γ+$Z(qq)$	—	{140, 280}	656	305440
		{280, 500}	77.0	305441
		{500, 1000}	10.4	305442
		{1000, 2000}	0.461	305443
		{2000, ∞}	0.00430	305444
γ+$W(\ell\nu)$	$e\nu$	{35, 70}	1.91×10^4	364523
		{70, 140}	1920	364524
		{140, E_{CM}}	297	364525
	$\mu\nu$	{35, 70}	1.91×10^4	364528
		{70, 140}	1920	364529
		{140, E_{CM}}	297	364530
	$\tau\nu$	{35, 70}	1.91×10^4	364533
		{70, 140}	1930	364534
		{140, E_{CM}}	300	364535
γ+$W(qq)$	—	{140, 280}	1660	305435
		{280, 500}	242	305436
		{500, 1000}	37.0	305437
		{1000, 2000}	1.82	305438
		{2000, ∞}	0.0169	305439

6.4 Reweighting scheme

The ultimate goal of the reweighting method is to obtain agreement in the m_{T}^{ZZ} distribution between Z+jets events in the signal region and reweighted γ+jets events in the control region. To achieve this, weights are used to reweight γ+jets events in the control region so that their kinematic distributions emulate the Z+jets distributions. The weights are calculated and applied as early as possible in the cutflow to minimize the statistical error of the weights; this is especially important when using 2D weights. However, applying the weights early means that subsequent cuts still need to be applied; after reweighting, if a variable is used in the event selection but not in the reweighting itself, the Z+jets and γ+jets distributions may no longer agree. Ideally, a unique weight would be used early in the cutflow and perfect agreement would be obtained in all kinematic variables. This proved not to be feasible for this analysis.

The Z resonant production causes significant differences in the kinematics between Z+jets and γ+jets events in a $p_{\mathrm{T}}^{Z/\gamma}$ range near m_Z. Because of this, obtaining acceptable agreement for events for all p_{T} proved to be a difficult endeavour. One method adopted in [79] uses 1D p_{T} reweighting in addition to smearing of the $E_{\mathrm{T}}^{\mathrm{miss}}$ component parallel to the photon. This method was attempted but did not produce acceptable Z/γ agreement in the object-based $E_{\mathrm{T}}^{\mathrm{miss}}$ significance, $\mathcal{S}$. Smearing was eventually abandoned and several more complicated reweighting schemes were tested instead. The following 1D and 2D schemes were attempted:

- 1D: p_{T}; $E_{\mathrm{T}}^{\mathrm{miss}}$; $\mathcal{S}$
- 2×1D: $p_{\mathrm{T}} \times E_{\mathrm{T}}^{\mathrm{miss}}$; $p_{\mathrm{T}} \times \mathcal{S}$; $p_{\mathrm{T}} \times E_{\mathrm{T}}^{\mathrm{miss}}$ parallel to Z/γ; $E_{\mathrm{T}}^{\mathrm{miss}} \times \mathcal{S}$
- 2D: $p_{\mathrm{T}} \times E_{\mathrm{T}}^{\mathrm{miss}}$; $p_{\mathrm{T}} \times E_{\mathrm{T}}^{\mathrm{miss}}$ parallel to Z/γ; $p_{\mathrm{T}} \times \Sigma E_{\mathrm{T}}$; $E_{\mathrm{T}}^{\mathrm{miss}} \times \mathcal{S}$

Here 2×1D means two independent 1-dimensional reweightings, whereas 2D is a true 2-dimensional reweighting. In general it was found that a reweighting that explicitly included $\mathcal{S}$ was necessary in order to obtain Z/γ agreement in that variable. Furthermore, the $E_{\mathrm{T}}^{\mathrm{miss}}$ and $\mathcal{S}$ are strongly correlated, and reweighting one without the other generally leads to poor results. The theory paper referenced above describes how a 1D p_{T} reweighting can be used in the regime where $p_{\mathrm{T}} \gg m_Z$. Since the analysis considers low p_{T} as well, there needs to be a correction to account for the difference between Z+jets and γ+jets due to the Z mass. This can be achieved through a reweighting that includes the ΣE_{T} of the event. This is theoretically motivated as follows: in a

p_{T} regime near m_Z, the momentum transfer Q^2 for Z+jets and γ+jets processes will differ; $Q^2 \sim (p_{\mathrm{T}}^{\gamma})^2$ for γ+jets, whereas $Q^2 \sim (p_{\mathrm{T}}^{Z})^2 + m_Z^2$ for Z+jets events. Therefore Q^2 encapsulates kinematic differences due to m_Z; the Q^2 of the event can be estimated with the ΣE_{T}, since the momentum transfer increases with the total sum of transverse energy in the event. Hence a 2D reweighting with $p_{\mathrm{T}} \times \Sigma E_{\mathrm{T}}$ accounts for significant differences between Z+jets and γ+jets due to m_Z. Therefore, the first 2D reweighting is done using $w_1 = w_1(p_{\mathrm{T}}, \Sigma E_{\mathrm{T}})$, which can be written more explicitly in terms of the Z+jets and γ+jets yields as

$$w_1(p_{\mathrm{T}}, \Sigma E_{\mathrm{T}}) = \frac{Z\text{+jets}_{\mathrm{MC}}(p_{\mathrm{T}}, \Sigma E_{\mathrm{T}})}{\gamma\text{+jets}_{\mathrm{MC}}(p_{\mathrm{T}}, \Sigma E_{\mathrm{T}})}. \tag{6.2}$$

Furthermore the first weight takes into account the large p_{T} differences that are caused by the prescaled trigger scale factors that are applied for photons for $p_{\mathrm{T}}^{\gamma} < 120/140$ GeV.

$w_1(p_{\mathrm{T}}, \Sigma E_{\mathrm{T}})$ does the majority of the work to bring the reweighted γ+jets events into agreement with Z+jets. However, as mentioned earlier, the $E_{\mathrm{T}}^{\mathrm{miss}}$ significance still shows small differences that are not corrected through reweighting with p_{T} and/or ΣE_{T}; this is suspected to be due to differences in the photon and electron/muon resolutions that are used in the calculation of $\mathcal{S}$, which are not accounted for in $w_1(p_{\mathrm{T}}, \Sigma E_{\mathrm{T}})$. Therefore it is necessary to include a second weight that uses $\mathcal{S}$, and because it is highly correlated with $E_{\mathrm{T}}^{\mathrm{miss}}$, this suggests reweighting both together. However, the ultimate goal is to obtain agreement in the m_{T}^{ZZ} distribution, and this is not achieved by reweighting $E_{\mathrm{T}}^{\mathrm{miss}}$ and $\mathcal{S}$ in 2D. Instead, m_{T}^{ZZ} is reweighted with $\mathcal{S}$, and $w_2 = w_2(m_{\mathrm{T}}^{ZZ}, \mathcal{S})$ is applied after the $E_{\mathrm{T}}^{\mathrm{miss}}$ requirement to avoid requiring it in the weight. w_2 is therefore, in terms of Z+jets and γ+jets yields,

$$w_2(m_{\mathrm{T}}^{ZZ}, \mathcal{S}) = \frac{Z\text{+jets}_{\mathrm{MC}}(m_{\mathrm{T}}^{ZZ}, \mathcal{S})}{\gamma\text{+jets}_{\mathrm{MC}}(m_{\mathrm{T}}^{ZZ}, \mathcal{S})}. \tag{6.3}$$

It is also important to note that w_1 is largely independent from w_2; this is seen when applying the second weight and observing that the p_{T} and ΣE_{T} distributions are little modified.

In addition to the variables used in the reweighting procedure, the steps in the cutflow at which the weights are applied are also thoroughly investigated. The Z-specific cuts, such as $\Delta R_{\ell\ell}$ and $m_{\ell\ell}$, are necessarily applied before the weights are obtained, as there is no equivalent cut for γ+jets events. The b-jet veto can be applied before the weights are calculated as it mainly targets top backgrounds and

does not cause a large drop in Z/γ+jets statistics. w_1 is applied at this stage. w_2 would ideally be applied here as well, but acceptable $E_{\mathrm{T}}^{\mathrm{miss}}$ agreement is not obtained after applying $w_2(m_{\mathrm{T}}^{ZZ}, \mathcal{S})$, leading to poor Z/γ agreement in the m_{T}^{ZZ} distribution after the $E_{\mathrm{T}}^{\mathrm{miss}}$ requirement. Therefore $w_2(m_{\mathrm{T}}^{ZZ}, \mathcal{S})$ is applied after the $E_{\mathrm{T}}^{\mathrm{miss}}$ selection. The statistics used for w_2 are reduced but the systematic error introduced is small. Another solution would be to include $E_{\mathrm{T}}^{\mathrm{miss}}$ in a 3D weight, but sparsely populated 3D bins would produce unreliable weights.

In summary, a 2×2D reweighting scheme has been developed to estimate the m_{T}^{ZZ} distribution for the Z+jets background. Equation 6.1 can be rewritten to describe the total event weight in terms of all four reweighting variables as

$$w(p_{\mathrm{T}}, \Sigma E_{\mathrm{T}}, m_{\mathrm{T}}^{ZZ}, \mathcal{S}) = w_1(p_{\mathrm{T}}, \Sigma E_{\mathrm{T}}) \times w_2(m_{\mathrm{T}}^{ZZ}, \mathcal{S}). \tag{6.4}$$

w_2 is calculated with w_1 applied, w_1 is calculated and applied after the b-jet veto, and w_2 is calculated and applied after the $E_{\mathrm{T}}^{\mathrm{miss}}$ requirement, as outlined in Table 6.3.

6.5 Validation of reweighting scheme

Before applying the weights to data, the method is first validated using simulation. Figure 6.1 shows the first 2D weight $w_1(p_{\mathrm{T}}, \Sigma E_{\mathrm{T}})$, calculated using the ratio of γ+jets to either $Z(ee)$+jets or $Z(\mu\mu)$+jets, depending on the channel; the same γ+jets events

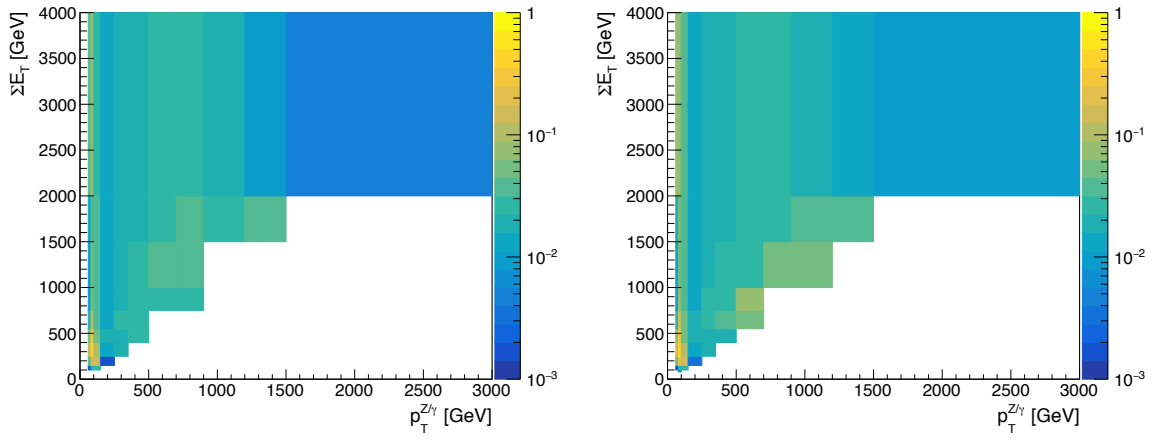

(a) ee channel.

(b) $\mu\mu$ channel.

Figure 6.1: Distribution of $w_1(p_{\mathrm{T}}, \Sigma E_{\mathrm{T}})$. The colour scheme indicates the weight value in each bin.

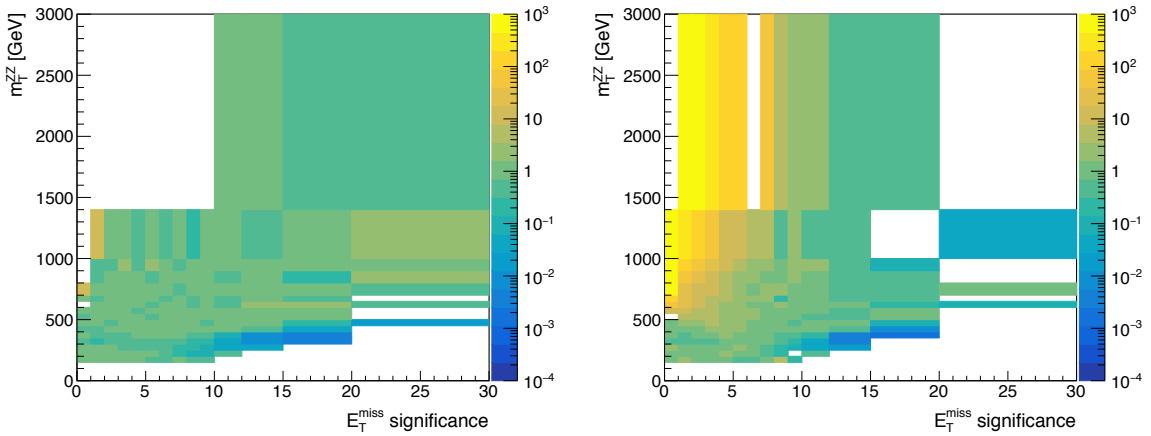

(a) ee channel. (b) $\mu\mu$ channel.

Figure 6.2: Distribution of $w_2(m_{\mathrm{T}}^{ZZ}, \mathcal{S})$. The colour scheme indicates the weight value in each bin.

are used for both ee and $\mu\mu$ channels, but are reweighted differently. In general $w_1 \ll 1$ due to the much larger cross section of γ+jets production compared to Z+jets; note that $w_1 \sim 1$ at low p_{T} where the prescale weights make the distributions between the two processes comparable. As discussed, some differences remain in the upper tails of the m_{T}^{ZZ}, $\mathcal{S}$, and $E_{\mathrm{T}}^{\mathrm{miss}}$ distributions after applying w_1, hence the necessity of a second weight. The 2D distribution of w_2 is shown in Figure 6.2. These weights are calculated with w_1 applied, so in general they are close to 1. Bins with low statistics may occasionally have negative weights; if this happens the weight is set to 0. The statistical error on the weights is treated as a systematic error in the reweighting method.

The validity of the method is tested by assessing the m_{T}^{ZZ} agreement between Z+jets simulation in the signal region and reweighted γ+jets simulation in the control region after all event selections. This is shown in Figure 6.3. The γ+jets distributions agree well with the Z+jets distributions. The agreement in the MC ratio gives a measure of the *closure* of the method. Bins where the ratio is different from 1 indicates where coarser bins are used compared to the ones used for the final discriminant; this is done to obtain more events in the upper tails of $\mathcal{S}$ and m_{T}^{ZZ} so that w_2 is more reliable. The related systematic error on the final estimate is discussed in the next section. The signal region predictions for Z+jets and reweighted γ+jets are given in Table 6.5. The reweighted γ+jets events agree within statistical errors with the Z+jets prediction, indicating that the method is reliable and that the weights may

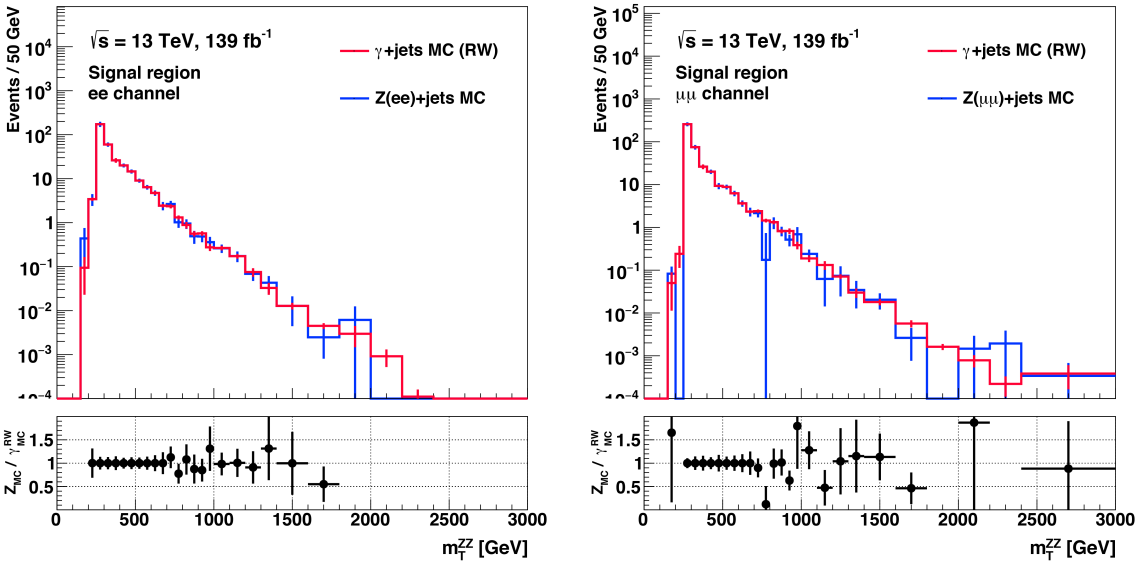

(a) ee channel.

(b) $\mu\mu$ channel.

Figure 6.3: m_{T}^{ZZ} from simulation after applying w_1 and w_2, with all cuts applied. Error bars shown are statistical.

Table 6.5: Signal region predictions from Z+jets and reweighted γ+jets simulation for 139 fb^{-1}. The errors quoted are statistical.

Channel	Z+jets MC	γ+jets MC
ee	328 ± 25	327 ± 6
$\mu\mu$	410 ± 30	417 ± 8

be applied to γ+jets data.

6.6 Results from data

The first step in looking at γ+jets in data is to study the data/MC agreement in the γ+jets control region without any reweighting applied. The photon p_{T}, ΣE_{T}, $E_{\mathrm{T}}^{\mathrm{miss}}$, and $\mathcal{S}$ are shown in Figure 6.4. The variables are shown after the b-jet veto. The photon p_{T} is in general well-modelled with a slight uniform data/MC deficit. The effect of the prescaled single photon triggers can be seen below 120/140 GeV. A data/MC deficit of ∼20% is seen in $E_{\mathrm{T}}^{\mathrm{miss}}$ near 100 GeV and in m_{T}^{ZZ} across most of the distribution. This deficit is due to mis-modelling in the γ+jets jet multiplicity, for which a deficit is also seen for $N_{\mathrm{jets}} > 2$. The $E_{\mathrm{T}}^{\mathrm{miss}}$ and m_{T}^{ZZ} data/MC deficits

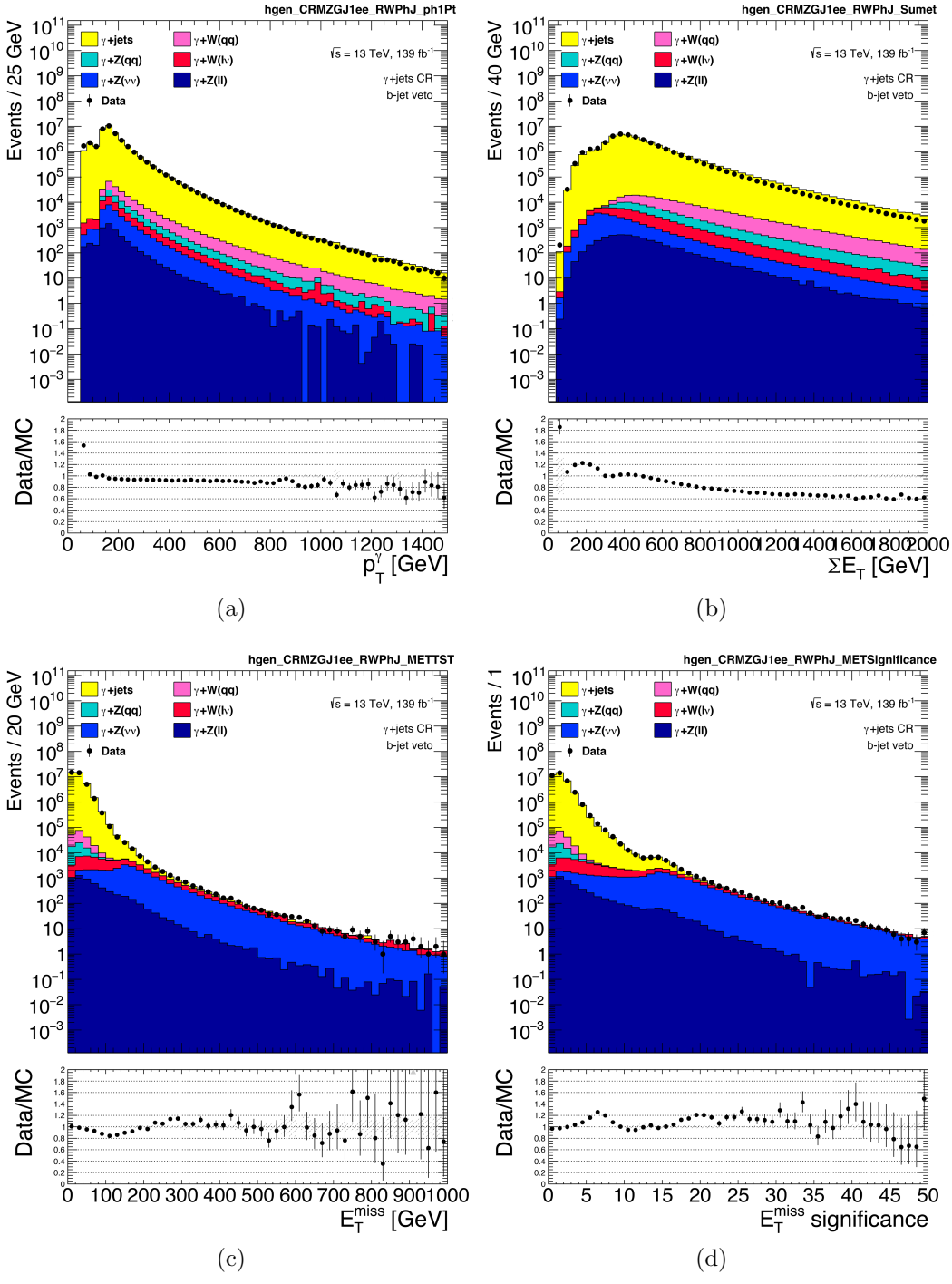

Figure 6.4: (a) p_{T}^{γ}, (b) ΣE_{T}, (c) $E_{\mathrm{T}}^{\mathrm{miss}}$, and (d) $\mathcal{S}$ in the γ+jets control region after the b-jet veto.

disappear when $N_{\text{jets}} \leq 1$ is required. This is indicative of jet/fake $E_{\text{T}}^{\text{miss}}$ mis-modelling at high jet multiplicities. Other distributions, including photon and jet kinematics, are observed to be well-modelled by the simulation.

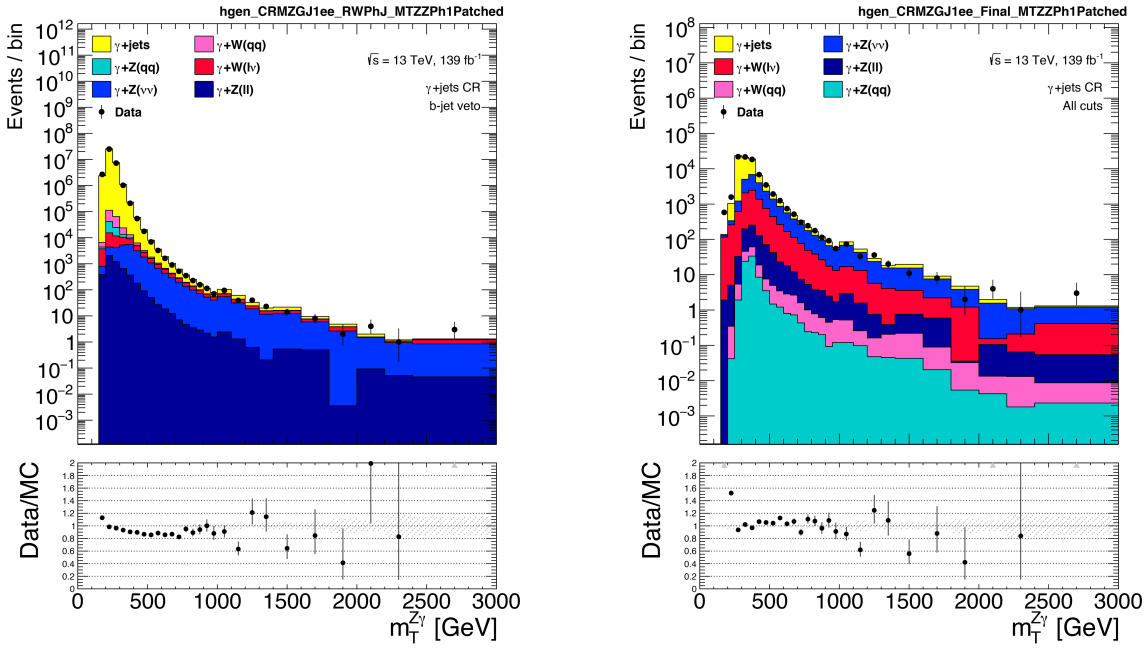

(a) (b)

Figure 6.5: m_{T}^{ZZ} in the γ+jets control region (a) after the b-jet veto and (b) after all selection requirements.

Figure 6.5 shows the m_{T}^{ZZ} distribution after the b-jet veto and after all selections. The data sample obtained from the γ+jets control region is enriched in γ+jets events, but also contains contributions from γ+V processes. γ+jets events dominate at low m_{T}^{ZZ}, with contributions from γ+Z and γ+W processes becoming dominant in the intermediate and upper tails. Processes such as γ+$Z(\nu\nu)$ and γ+$W(\ell\nu)$ produce real $E_{\text{T}}^{\text{miss}}$, and hence they contribute most at higher $E_{\text{T}}^{\text{miss}}$ and m_{T}^{ZZ}. These non-γ+jets processes are included in the reweighted data that is obtained from the control region. In order to isolate events that come from γ+jets, these γ+V processes need to be removed from the data. The amount of reweighted γ+V events in the data is estimated using simulation. The 2×2D weights are applied to γ+V simulation, which is then subtracted from the reweighted data in order to obtain the final in-situ γ+jets estimate. The subtraction is done after all selections.

The final m_{T}^{ZZ} estimate from γ+jets data in the signal region is shown in Figure 6.6. The corresponding numerical estimates are summarized in Table 6.6 with sta-

tistical errors only. Excellent agreement is observed between data and simulation. Systematic errors on the final estimates are discussed in the next section.

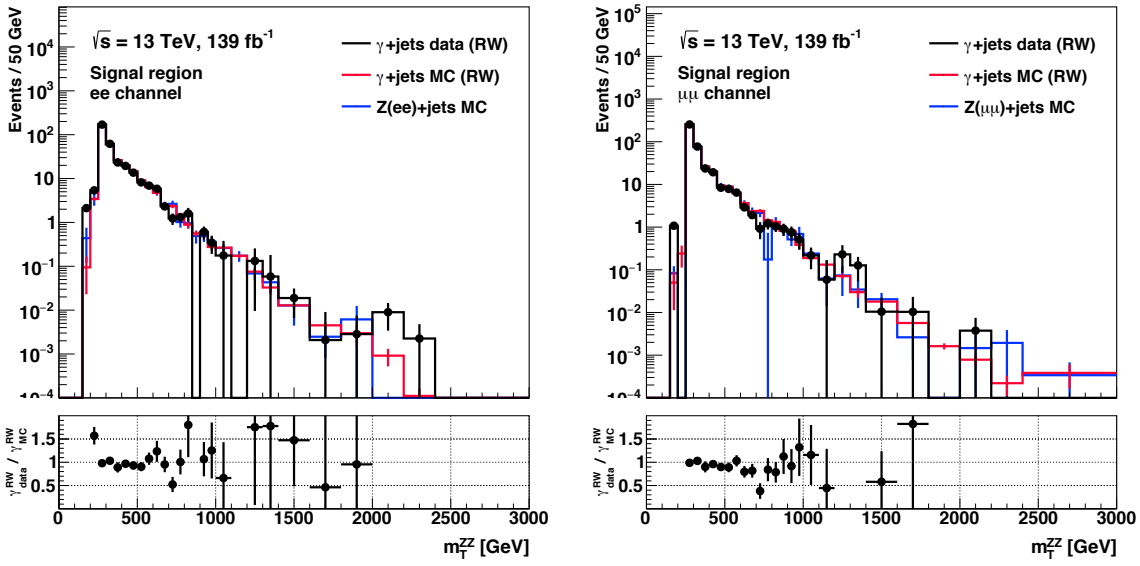

(a) ee channel.

(b) $\mu\mu$ channel.

Figure 6.6: m_{T}^{ZZ} estimate from γ+jets data compared to simulation in the signal region. Error bars shown are statistical.

Table 6.6: Signal region estimates from reweighted γ+jets data compared to Z+jets and reweighted γ+jets simulation for 139 fb^{-1}. The errors quoted are statistical.

Channel	Z+jets MC	γ+jets MC	γ+jets data
ee	328 ± 25	327 ± 6	325 ± 3
$\mu\mu$	410 ± 30	417 ± 8	409 ± 3

6.7 Systematic uncertainties

Non-closure

Small differences are seen between Z+jets and reweighted γ+jets simulation in the validation of the method. This is treated as a source of systematic error on the estimate. Non-closure can be introduced to the reweighting method (1) if the $E_{\mathrm{T}}^{\mathrm{miss}}$ or m_{T}^{ZZ} binning used in the reweighting is different than the final discriminant binning, and/or (2) if variables used in the selection variables are not used in the reweighting

itself. The method is designed to avoid (2), but the issue of (1) is not avoided because coarser m_{T}^{ZZ} bins are used in w_2 to reduce the statistical error in the upper tails. This leads to some non-closure in the method as is shown in the ratio in Figure 6.3. The systematic error due to non-closure is calculated for each bin b by taking the absolute difference between Z+jets and reweighted γ+jets yields and then dividing by the Z+jets prediction ($= |N_b^{\gamma} - N_b^{Z}|/N_b^{Z}$). Non-closure is only introduced for $m_{\mathrm{T}}^{ZZ} > 700$ GeV where coarse bins are used in the reweighting. The effect on the total yield is only 1-3% and is summarized in Appendix E.2.

γ+V subtraction

The γ+jets-enriched dataset obtained from the γ+jets control region is contaminated by γ+V processes. γ+V simulation is used to estimate the contribution and is then subtracted from the data. A systematic error is associated with this procedure because the real γ+V contribution in the data sample is not known. Instead the γ+V processes are validated in a γ+V control region. Specifically, a γ+$W(\ell\nu)$ control region is used that is identical to the γ+jets control region except that events are required to have one lepton with $p_{\mathrm{T}} > 20$ GeV.

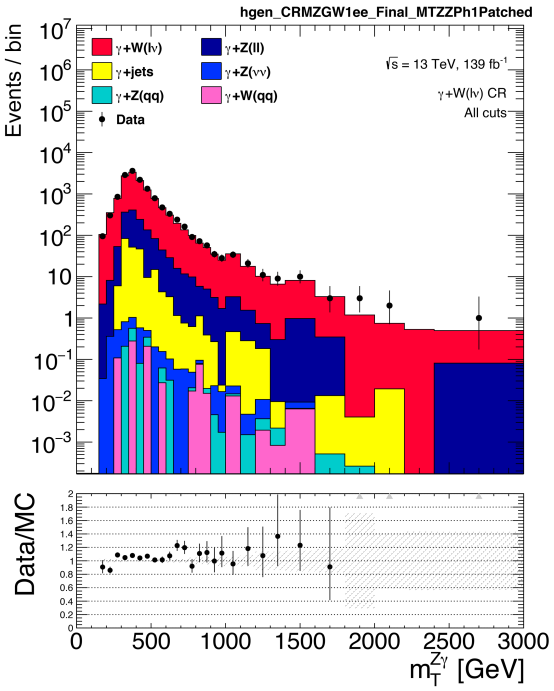

Figure 6.7: m_{T}^{ZZ} in the γ+$W(\ell\nu)$ control region.

The m_{T}^{ZZ} in the γ+$W(\ell\nu)$ control region is shown in Figure 6.7. The systematic

error due to the subtraction is assigned using the ratio of data to simulation. The systematic is taken to be the larger data/MC difference in the m_{T}^{ZZ} in either the γ+jets or the $\gamma+V$ control region (comparing Figure 6.5b to Figure 6.7), whichever is more conservative for a given bin. The largest data/MC ratio per bin is taken as the relative error on the $\gamma+V$ contribution in the data in the γ+jets control region. This error is then propagated to the γ+jets estimate in data during the subtraction.

Table 6.7: $\gamma+V$ subtraction systematic on the Z+jets m_{T}^{ZZ} estimate for 139 fb^{-1}. The total unbinned error is calculated assuming uncorrelated bins.

Channel	m_{T}^{ZZ} (GeV)						Total
	[250,300]	[300,350]	[350,400]	[400,450]	[450,500]	[500,550]	
ee	0.3%	1.0%	2.9%	6.2%	8.1%	7.4%	1.2%
$\mu\mu$	0.2%	1.0%	2.9%	5.7%	8.3%	7.8%	0.6%

The subtraction systematic error for the first six m_{T}^{ZZ} bins is given in Table 6.7. Normally the total unbinned systematic error would be calculated using the change in the data/MC ratio of the total data yield, but this is not possible because a combination of two separate regions is used to assign the $\gamma+V$ MC error. The total error is therefore calculated by assuming that bins are uncorrelated; the relative error on the total is calculated to be

$$r_{\mathrm{total}} = \frac{\sigma_{\mathrm{total}}}{y_{\mathrm{total}}} = \frac{\sqrt{\sum_i (y_i r_i)^2}}{\sum_i y_i} \tag{6.5}$$

where y_i is the subtracted data yield in bin i, and r_i is its relative error.

Statistical errors in 2×2D weights

The 2×2D weights used in the reweighting method have statistical errors. Fluctuating the weights according to these errors will modify the reweighting and hence the estimate in data. This systematic error is estimated by varying the 2D histograms used to calculate the weights and assessing the change in the final discriminant variable.

The 2D histograms h_1 and h_2 from Z+jets and γ+jets simulation are used to create the 2D weights w_1 and w_2. h_1 and h_2 are varied for a given pseudo-experiment. For each 2D bin in h_1 and h_2, the new content is drawn from a Gaussian distribution, where the mean of the Gaussian is the sum of weights content from the nominal histogram, and the 1σ error is set equal to the statistical error on the nominal sum of

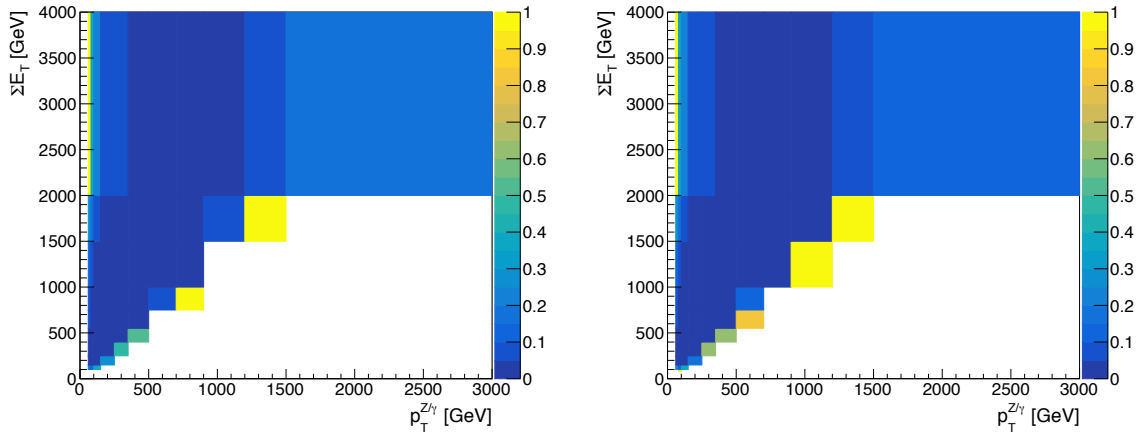

(a) ee channel. (b) $\mu\mu$ channel.

Figure 6.8: $w_1(p_{\mathrm{T}}, \Sigma E_{\mathrm{T}})$ statistical errors. The colour scheme is the error on each bin between 0-100%.

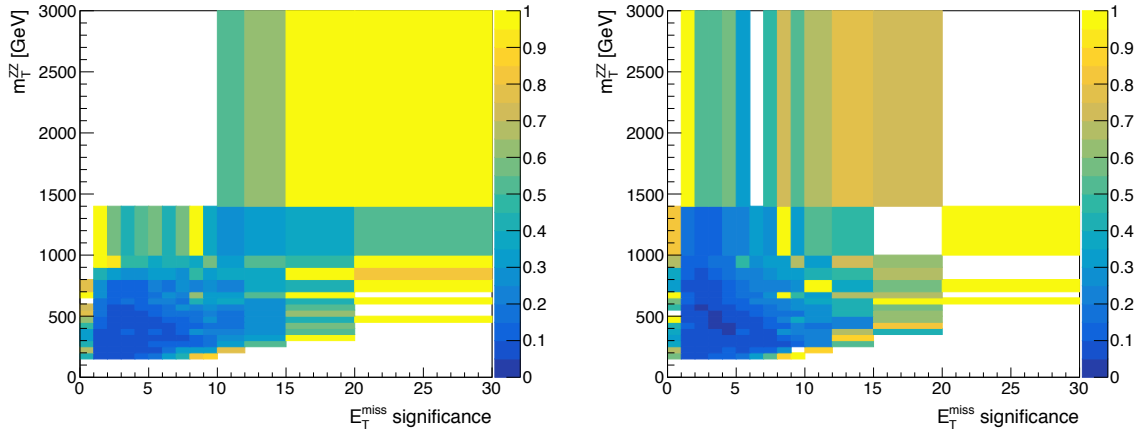

(a) ee channel. (b) $\mu\mu$ channel.

Figure 6.9: $w_2(E_{\mathrm{T}}^{\mathrm{miss}}, m_{\mathrm{T}}^{ZZ})$ statistical errors. The colour scheme is the error on each bin between 0-100%.

weights content. To understand the impact of each weight, one can vary h_1 (leaving h_2 nominal), vary h_2 (leaving h_1 nominal), or vary both h_1 and h_2. The 2D histograms are varied for several pseudo-experiments and a modified m_{T}^{ZZ} distribution is obtained for each experiment. Then the RMS for each bin is calculated and assigned as the systematic due to statistical fluctuations in the weights.

Figures 6.8 and 6.9 show the statistical errors on the nominal weights w_1 and w_2. The statistical errors on w_1 are less than 5-10% across most bins. The statistical errors

on w_2 are considerably larger in some bins, especially at higher values of $\mathcal{S}$ and m_{T}^{ZZ} where the Z+jets MC statistics are most lacking. The fluctuations in h_2 and hence w_2 dominate the statistical variation in the final m_{T}^{ZZ} distributions. Varying only h_1 produces negligible variation (less than 1%) in the final discriminants: varying h_1 and h_2 compared to varying only h_2 produces the same RMS on the discriminants after all selections. Table 6.8 summarizes the systematic errors due to statistical fluctuations in the 2×2D weights, obtained with 50 pseudo-experiments.

Table 6.8: Systematic error on the Z+jets m_{T}^{ZZ} estimate due to statistical fluctuations in the weights for 139 fb^{-1}. The total unbinned error is calculated using all m_{T}^{ZZ} bins.

Channel	m_{T}^{ZZ} (GeV)						Total
	[250,300]	[300,350]	[350,400]	[400,450]	[450,500]	[500,550]	
ee	14.5%	10.3%	17.4%	8.9%	11.8%	10.6%	8.7%
$\mu\mu$	6.9%	13.6%	13.8%	12.0%	19.0%	18.5%	5.9%

Mis-modelling in 2×2D weights

As discussed previously, distributions from data and simulation differ in the γ+jets control region. These small differences are likely due to jet and fake $E_{\mathrm{T}}^{\mathrm{miss}}$ mis-modelling in the γ+jets simulation. This introduces a systematic error to the method because mis-modelling is included in the calculation of the weights which is not present in the data. Hence the data kinematics are not reweighted perfectly as they would be if the weights were calculated from data. This mis-modelling systematic is quantified by looking at how the application of the weights changes the m_{T}^{ZZ} data/MC ratio.

The ratios R_1 and R_2 are defined as

$$R_1 = \frac{\gamma\text{+jets}_{\mathrm{data}}^{\mathrm{sub}}}{\gamma\text{+jets}_{\mathrm{MC}}}, \quad R_2 = \frac{\gamma\text{+jets}_{\mathrm{data}}^{\mathrm{sub,RW}}}{\gamma\text{+jets}_{\mathrm{MC}}^{\mathrm{RW}}}. \tag{6.6}$$

Here R_1 is the ratio of γ+jets data/MC before reweighting, and R_2 is the ratio after reweighting. In both R_1 and R_2 the $\gamma+V$ subtraction has been applied to the data. If the data and MC agreed perfectly then R_1 and R_2 would be equal. Therefore studying how R_2 changes with respect to R_1 gives a means to quantify how the application of the weights produces differences between data and simulation. The systematic error is calculated per bin by taking the difference between R_2 and R_1 and dividing by R_1 ($= |R_2 - R_1|/R_1$). Because w_1 and w_2 are applied at two different steps in the event

selection, the data/MC ratio change is assessed after each individual weighting.[4] The results are summarized per m_{T}^{ZZ} bin in Table 6.9.

Table 6.9: Systematic error on the Z+jets m_{T}^{ZZ} estimate due to mis-modelling in the weights for 139 fb^{-1}. The total unbinned error is calculated using all m_{T}^{ZZ} bins.

Channel	m_{T}^{ZZ} (GeV)						Total
	[250,300]	[300,350]	[350,400]	[400,450]	[450,500]	[500,550]	
ee	5.7%	3.3%	0.8%	1.3%	1.5%	3.1%	5.4%
$\mu\mu$	3.3%	3.5%	1.4%	3.6%	4.9%	6.8%	5.3%

Experimental errors in 2×2D weights

The Z+jets and γ+jets simulation samples are subject to experimental systematic uncertainties; these errors must also be propagated to the weights and the final m_{T}^{ZZ} distribution. Table 6.10 summarizes the top experimental systematic uncertainties on the Z+jets and γ+jets samples without reweighting applied. The primary systematic sources are jet and $E_{\mathrm{T}}^{\mathrm{miss}}$ soft term uncertainties.[5] For most of these large systematics, Z+jets processes are affected to a greater extent than γ+jets.[6] A more complete version of Table 6.10 containing all systematics larger than 3% can be found in Appendix E.3.

The most important experimental systematics on the simulation are identified. The impact of the experimental systematics on the weights is then evaluated in the following way. First, the nominal reweighting is done once. This produces the nominal weights w_1^{nom} and w_2^{nom}, as well as the nominal m_{T}^{ZZ} distribution. Then, for each systematic, the reweighting procedure is repeated in the following way:

[4] R_1 and R_2 are calculated before/after applying w_1 (after the b-jet veto). R_1' and R_2' are calculated before/after applying w_2 (after the $E_{\mathrm{T}}^{\mathrm{miss}}$ requirement). The systematic error is calculated for both unprimed and primed ratios and compared. The largest change in the ratio occurs after applying w_2.

[5] The fluctuations observed in the experimental systematics are not caused by statistics, as the statistical error on the total Z+jets yield is only about 7-8% for each variation. $Z(ee)$+jets is more affected by jet systematics than $Z(\mu\mu)$+jets because jet fluctuations in the calorimeter are more likely to affect electrons than muons.

[6] The primary reason for this is because the kinematics between Z+jets and γ+jets are not identical. In Section 6.4, it is argued that the Q^2 between Z+jets and γ+jets differ at low p_{T} due to m_Z. For a fixed Q^2, p_{T}^Z is lower than p_{T}^γ because of m_Z; this creates a lower p_{T} spectrum for the Z+jets process, which in turns leads to lower $E_{\mathrm{T}}^{\mathrm{miss}}$ and jet p_{T} distributions. Therefore the experimental jet and $E_{\mathrm{T}}^{\mathrm{miss}}$ systematics have more impact on Z+jets compared to γ+jets. If a high p_{T} cut ($\gg m_Z$) was made in the analysis, then these systematics would likely decrease considerably in size, as the kinematics would be more similar between the Z+jets and γ+jets processes.

Systematic	γ+jets MC	$Z(ee)$+jets	$Z(\mu\mu)$+jets
JET_Flavor_Composition__1down	+7.9%	+25.0%	+16.2%
MET_SoftTrk_ScaleDown	+7.6%	+13.9%	+19.4%
JET_Pileup_RhoTopology__1down	+4.3%	+18.5%	+7.9%
JET_Flavor_Composition__1up	-8.0%	-13.4%	-17.2%
MET_SoftTrk_ScaleUp	-7.0%	-12.6%	-17.2%
MET_SoftTrk_ResoPerp	+7.0%	+11.9%	+16.4%
JET_Flavor_Response__1up	+4.3%	+13.2%	+6.7%
JET_EtaIntercalibration_Modelling__1down	+3.6%	+11.7%	+7.3%
JET_Pileup_RhoTopology__1up	-4.8%	-7.7%	-9.7%
JET_JvtEfficiency__1up	-9.5%	-3.6%	-4.6%
Total	$^{+17.8}_{-18.9}$%	$^{+43.1}_{-26.3}$%	$^{+37.0}_{-36.5}$%

Table 6.10: Top 10 experimental systematics on Z+jets and γ+jets samples (no reweighting) in the signal region and γ+jets control region. The systematics are ranked by their impact on the γ+jets MC. The total asymmetric error is calculated by adding all of the largest positive and negative variations in quadrature, including experimental systematics not shown in the table.

Systematic	ee		$\mu\mu$	
	Up	Down	Up	Down
JET_Flavor_Composition	-8.8%	+19.5%	-14.8%	+12.3%
JET_Pileup_RhoTopology	-4.6%	+15.1%	-8.8%	+6.4%
MET_SoftTrk_Scale	-5.7%	+5.7%	-9.1%	+10.7%
MET_SoftTrk_ResoPerp	+4.9%	-4.9%	+9.7%	-9.7%
JET_Flavor_Response	+9.4%	-3.5%	+4.4%	-7.3%
JET_EtaIntercalibration_Modelling	-1.5%	+8.8%	-5.7%	+4.9%
JET_Pileup_OffsetMu	+0.7%	+7.5%	-5.7%	+8.5%
JET_EffectiveNP_1	+0.4%	+6.7%	-5.4%	+3.8%
JET_Pileup_OffsetNPV	-1.5%	+6.5%	-5.8%	+6.3%
JET_JvtEfficiency	+6.2%	-4.1%	+4.5%	-3.0%
Total	Positive	Negative	Positive	Negative
	+33.1%	-16.2%	+25.2%	-27.1%

Table 6.11: Impact of top 10 experimental systematics on the reweighted γ+jets prediction. The total asymmetric error is calculated by adding all of the largest positive and negative variations in quadrature, including experimental systematics not shown in the table.

- Process systematic Z+jets and γ+jets samples $\rightarrow$ calculate w_1^{sys}
- Process systematic γ+jets samples with w_1^{nom} applied $\rightarrow$ calculate w_2^{sys}
- Process nominal γ+jets samples with w_1^{sys} and w_2^{sys} applied $\rightarrow$ obtain the varied m_{T}^{ZZ} distribution

Then the change in the discriminant due to variations in the weights is assessed by comparing the varied distributions to the nominal one. Systematics with an impact of more than 1% are included in the calculation. Table 6.11 shows the impact on the total yield for the top 10 systematics; the corresponding table containing all systematics larger than 3% is given in Appendix E.3. By comparing Table 6.11 to Table 6.10, one can assess by how much the experimental systematic impact is reduced by using the reweighting method. The level of cancellation is about 20-40%. The total impact across all experimental systematics per m_{T}^{ZZ} bin on the final estimate is summarized in Table 6.12. Experimental systematic sources produce the dominant systematic errors of the γ+jets reweighting method.

Table 6.12: Systematic error on the Z+jets m_{T}^{ZZ} estimate due to experimental variations in the weights for 139 fb^{-1}. The total unbinned error is calculated using all m_{T}^{ZZ} bins.

Channel	m_{T}^{ZZ} (GeV)						Total
	[250,300]	[300,350]	[350,400]	[400,450]	[450,500]	[500,550]	
ee	$^{+51.3}_{-21.5}$%	$^{+31.0}_{-30.2}$%	$^{+61.2}_{-47.6}$%	$^{+29.0}_{-32.4}$%	$^{+15.0}_{-19.3}$%	$^{+40.6}_{-35.9}$%	$^{+33.1}_{-16.2}$%
$\mu\mu$	$^{+36.0}_{-34.2}$%	$^{+46.1}_{-42.7}$%	$^{+40.3}_{-43.7}$%	$^{+28.6}_{-29.3}$%	$^{+33.5}_{-20.4}$%	$^{+27.8}_{-29.2}$%	$^{+25.2}_{-27.1}$%

QCD and PDF errors in 2×2D weights

The 2×2D weights are also subject to theoretical errors due to PDF and QCD scale uncertainties in the Z+jets and γ+jets MC. These are evaluated using the same method as for the experimental uncertainties in the weights, and by using the inter-PDF, intra-PDF, and QCD scale variational weights that are included in the Sherpa Z+jets MC samples. Results are presented in Table 6.13. The total QCD scale impact is 2-4%. The total inter-PDF impact is 2-3%, and the total intra-PDF impact is 3-5%.

Table 6.13: Systematic error on the Z+jets m_{T}^{ZZ} estimate due to PDF and QCD scale variations in the weights for 139 fb^{-1}. The total unbinned error is calculated using all m_{T}^{ZZ} bins.

Channel	m_{T}^{ZZ} (GeV)						Total
	[250,300]	[300,350]	[350,400]	[400,450]	[450,500]	[500,550]	
ee	$^{+10.5}_{-9.9}$%	$^{+3.3}_{-4.0}$%	$^{+10.3}_{-6.1}$%	$^{+7.5}_{-5.0}$%	$^{+4.1}_{-7.7}$%	$^{+1.7}_{-5.1}$%	$^{+5.6}_{-6.3}$%
$\mu\mu$	$^{+9.2}_{-10.8}$%	$^{+1.3}_{-3.5}$%	$^{+8.3}_{-6.1}$%	$^{+4.1}_{-5.3}$%	$^{+4.9}_{-9.0}$%	$^{+1.4}_{-4.5}$%	$^{+3.7}_{-6.9}$%

6.8 Comparison to Z+jets simulation

The final Z+jets estimates are 325 ± 3 (stat) $^{+118}_{-68}$ (sys) in the ee channel and 409 ± 3 (stat) $^{+117}_{-113}$ (sys) in the $\mu\mu$ channel. Table 6.14 summarizes the reweighted estimate compared to the prediction from Z+jets simulation with theoretical and experimental systematics.

Table 6.14: Comparison of γ+jets m_{T}^{ZZ} estimate to Z+jets simulation for 139 fb^{-1}.

Channel	Source	Estimate	Stat. error	Sys. error, unbinned treatment	Sys. error, binned treatment
ee	γ+jets data	325	±0.9%	$^{+36.4}_{-20.9}$%	$^{+48.2}_{-33.4}$%
	Z+jets sim.	328	±7.6%	$^{+42.9}_{-28.4}$%	$^{+50.0}_{-36.1}$%
$\mu\mu$	γ+jets data	409	±0.7%	$^{+28.6}_{-27.6}$%	$^{+40.0}_{-38.9}$%
	Z+jets sim.	410	±7.3%	$^{+37.5}_{-39.9}$%	$^{+56.1}_{-51.0}$%

The systematic error is calculated using two different methods. The unbinned treatment is obtained by assessing the change in the total Z+jets signal region yield, calculated from the quadratic sum of all the total errors per source (the last columns in Tables 6.7, 6.8, 6.9, 6.12, 6.14, and E.10). The binned treatment is done by quadratically summing the errors per bin (partially given in the same tables). The binned treatment produces errors that are about 10% larger compared to the unbinned treatment. The reason for the difference is because, for a given systematic variation, the bin-by-bin fluctuations can be larger than the fluctuation induced on the total yield. The binned treatment is done bin-by-bin and does not consider correlations between

bins, whereas correlations are automatically accounted for when only considering the yield. This effect is exacerbated for the experimental systematic uncertainty, as many individual experimental sources are added together bin-by-bin to calculate the total. The total error on the estimate could be more accurately calculated if, for example, all experimental sources were used individually in the fit; this was deemed unnecessary for Z+jets, a relatively small background. Furthermore, limits were run considering all experimental sources individually in the fits, and no significant change was observed. The analysis uses the m_{T}^{ZZ} distribution for the statistical analysis, so a binned treatment is required to calculate the systematic histograms that are used in the fit. The unbinned treatment gives a more accurate prediction of the total error, while the binned treatment more accurately represents the errors used by the fitting package.

Overall Table 6.14 shows that the Z+jets estimate from the γ+jets reweighting method produces a result with smaller statistical and systematic errors than simulation, and has the advantage of being largely obtained from data.

Chapter 7

Results and Interpretations

7.1 Unblinded signal region

An excess in data is first assessed by unblinding the signal region and observing the m_{T}^{ZZ} agreement between the data and predicted background. Figure 7.1 illustrates the unblinded mono-Z signal regions with data and background overlaid. In general the data agrees within ∼10-15% of the background prediction in the most populated

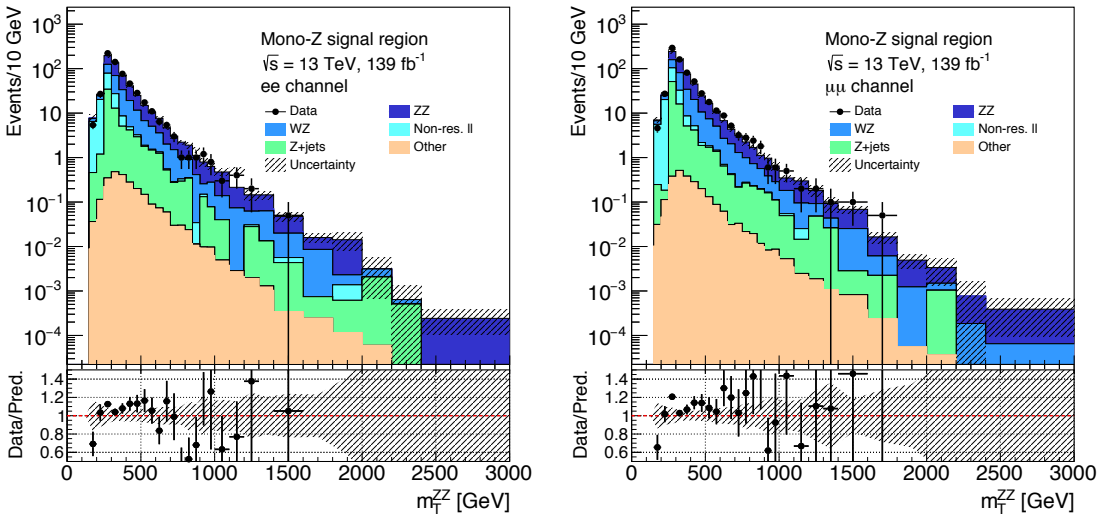

(a) ee channel.

(b) $\mu\mu$ channel.

Figure 7.1: Signal region data and background m_{T}^{ZZ} distributions. The ratio illustrates the agreement between the data and background prediction. The last bin includes overflow content.

Table 7.1: Number of observed data events in the signal region compared to the total background prediction for 139 fb^{-1}. The first error quoted per process is the statistical uncertainty, and the second error is the systematic uncertainty (symmetrized using the average of the high and low variations).

	ee channel	$\mu\mu$ channel
Total background	$2766 \pm 14 \pm 178$	$3147 \pm 15 \pm 204$
Data	2984	3519

bins, with a small overall excess in data. Table 7.1 summarizes the number of observed data events compared to the total background prediction in each channel. In the ee channel there are 2984 events observed in data, compared to a background prediction of 2766 ± 14 (stat) ± 178 (sys) events. Likewise, there are 3519 events observed in the $\mu\mu$ channel, compared to a background prediction of 3147 ± 15 (stat) ± 204 (sys) events. After the signal region has been unblinded, the next step is to perform a statistical analysis to test for a potential dark matter signal.

7.2 Statistical treatment

Once all signal and background processes are estimated, the signal region is unblinded and the data is compared to what is predicted. The m_{T}^{ZZ} histograms for signal, background, and data are used to construct a binned *likelihood function* that is used for hypothesis testing. For m_{T}^{ZZ} histograms with N bins, the likelihood function is constructed as [80]:

$$L(\mu, \boldsymbol{\theta}) = \prod_{i}^{N} \frac{(\mu s_i + b_i)^{n_i}}{n_i!} e^{-(\mu s_i + b_i)} \times \prod_{j}^{M} G(\theta_{i,j}) \tag{7.1}$$

The first factor in Equation 7.1 is the product of Poisson probabilities to observe n_i events for each signal region bin i that has $\mu s_i + b_i$ expected events. s_i and b_i are the predicted signal and background yields in each bin, and μ is the signal strength parameter (also called the *parameter of interest*). $\mu = 0$ corresponds to the background-only hypothesis, and $\mu = 1$ is the signal+background hypothesis. The dependence of the signal and background predictions on the systematic uncertainties is described by a set of nuisance parameters $\vec{\theta}$ ($\equiv \boldsymbol{\theta} = (\theta_1, \theta_2, ...)$), which are each parameterized by a Gaussian distribution. The second factor in Equation 7.1 is

a product of these Gaussian terms over all N bins and M systematics. The M systematics are assumed to be uncorrelated between each other, and systematics are treated as correlated across all N bins.

The nominal fit result is obtained by maximizing the likelihood function with respect to all parameters for a given signal sample. This function is referred to as the *maximum likelihood*, $L(\hat{\mu}, \hat{\boldsymbol{\theta}})$, where $\hat{\mu}$ and $\hat{\boldsymbol{\theta}}$ are the *unconditional maximum likelihood estimators*; these parameter values maximize the likelihood, and are the most probable estimates for the parameters given the data and signal+background prediction. For the purpose of hypothesis testing, the maximum likelihood is used to compare the $\hat{\mu}$ hypothesis against other potential μ hypotheses. This is done using the *profile likelihood ratio* [81]

$$\lambda(\mu) = \frac{L(\mu, \hat{\hat{\boldsymbol{\theta}}}(\mu))}{L(\hat{\mu}, \hat{\boldsymbol{\theta}})}, \tag{7.2}$$

where the numerator is the *profiled likelihood* for μ, and $\hat{\hat{\boldsymbol{\theta}}}$ are the *conditional maximum likelihood estimators* for $\boldsymbol{\theta}$ evaluated at fixed μ. The maximum likelihood is in the denominator, meaning $0 \leq \lambda(\mu) \leq 1$. The profile likelihood ratio gives a measure of the compatibility between a hypothesized μ and the $\hat{\mu}$ that is observed in data. If μ is close to $\hat{\mu}$, then the two hypotheses are compatible and $\lambda(\mu)$ will be close to 1. Conversely, if μ is very different than $\hat{\mu}$, the two hypotheses are incompatible and $\lambda(\mu)$ will be much less than 1. Hence smaller values of $\lambda(\mu)$ indicate greater incompatibility between μ and $\hat{\mu}$.

Hypothesis tests are performed using the profile likelihood ratio. The first important test is to check for evidence of a positive DM signal; this is known as a discovery hypothesis test. The discovery *test statistic*, q_0, is constructed using $\lambda(0)$ [81],

$$q_0 = \begin{cases} -2 \ln \frac{L(0, \hat{\hat{\boldsymbol{\theta}}}(0)))}{L(\hat{\mu}, \hat{\boldsymbol{\theta}})} & \hat{\mu} \geq 0 \\ 0 & \hat{\mu} < 0 \end{cases}, \tag{7.3}$$

where $\mu \geq 0$ and $q_0 \geq 0$. q_0 is used to test if the observed $\hat{\mu}$ is compatible with the background-only hypothesis; larger values of q_0 correspond to increasing incompatibility between $\hat{\mu}$ and $\mu = 0$. The discovery p-value, p_0, is defined as [81]

$$p_0 = \int_{q_{0,\text{obs}}}^{\infty} f(q_0|0) \mathrm{d}q_0 = P(q_0 \geq q_{0,\text{obs}}|0), \tag{7.4}$$

where $q_{0,\text{obs}}$ is the observed q_0 value as obtained from data, and $f(q_0|0)$ is the probability distribution of q_0 under the $\mu = 0$ hypothesis. p_0 is the probability of a q_0 value to be as or more discrepant with respect to the null hypothesis than the observed q_0. $f(q_0|0)$ can be obtained by generating MC toys or by using asymptotic formulae, which predict $f(q_0|0)$ in the limit of large number of events. According to the work of Wilks [82] and Wald [83], the profile likelihood ratio is $-2\ln\lambda(\mu) = \frac{(\mu-\hat{\mu})^2}{\sigma^2} + \mathcal{O}\left(1/\sqrt{n}\right)$ for a dataset of n events, and $\hat{\mu}$ has a Gaussian distribution with variance σ^2. Asymptotics are used for hypothesis testing in this search. A small p-value indicates tension with the $\mu = 0$ hypothesis. p_0 is typically expressed in terms of the quantile of a standard Gaussian.[1] A p-value of 1.3×10^{-3} indicates a 3σ probability (0.13% chance) to observe a more discrepant test statistic, given that the $\mu = 0$ hypothesis is true; a p-value of 2.9×10^{-7} represents a 5σ probability (0.00003% chance) to observe a more discrepant test statistic under the $\mu = 0$ hypothesis. 3σ corresponds to *evidence* for a signal, and 5σ is the threshold to claim a *discovery*.

In the case that no excess is observed in data, exclusion limits are set on the signal strength for each of the DM model points; these are then translated into limits on the parameters of the models. Upper limits on the signal strength are calculated using the CL_s method [84]. The strategy is similar for a discovery, but now the goal is to test different μ hypotheses against $\hat{\mu}$ and find the maximum signal strength that can be excluded, given that no excess is observed in data. The appropriate test statistic is $\tilde{q}_\mu$, defined to be [81]

$$\tilde{q}_\mu = \begin{cases} -2\ln\frac{L(\mu,\hat{\hat{\boldsymbol{\theta}}}(\mu))}{L(0,\hat{\hat{\boldsymbol{\theta}}}(0))} & \hat{\mu} < 0 \\ -2\ln\frac{L(\mu,\hat{\hat{\boldsymbol{\theta}}}(\mu))}{L(\hat{\mu},\hat{\boldsymbol{\theta}})} & 0 \leq \hat{\mu} \leq \mu \\ 0 & \hat{\mu} > \mu \end{cases}, \tag{7.5}$$

and it is assumed that $\mu \geq 0$. Larger values of $\tilde{q}_\mu$ are interpreted as greater incompatibility between measurement and the μ hypothesis. The corresponding p-value, p_μ, is then defined as [81]

$$p_\mu = \int_{\tilde{q}_{\mu,\text{obs}}}^{\infty} f(\tilde{q}_\mu|\mu)\mathrm{d}\tilde{q}_\mu = P(\tilde{q}_\mu \geq \tilde{q}_{\mu,\text{obs}}|\mu), \tag{7.6}$$

which is the probability to observe a $\tilde{q}_\mu$ greater than or equal to the observed $\tilde{q}_{\mu,\text{obs}}$,

[1] The significance is equal to $Z = \Phi^{-1}(1 - p_0)$, where Φ^{-1} is the inverse cumulative distribution function of a standard Gaussian.

given that the μ hypothesis is true. $f(\tilde{q}_\mu|\mu)$ is the probability density function of $\tilde{q}_\mu$ under the μ hypothesis, and $\tilde{q}_{\mu,\text{obs}}$ is the value of $\tilde{q}_\mu$ computed from the data.

To test against the $\mu = 1$ (signal + background) hypothesis, the p-value p_{s+b} is defined from p_μ [81]:

$$p_{s+b} = \int_{\tilde{q}_{\mu,\text{obs}}}^{\infty} f(\tilde{q}_\mu|s+b)\mathrm{d}\tilde{q}_\mu = P(\tilde{q}_\mu \geq \tilde{q}_{\mu,\text{obs}}|s+b), \tag{7.7}$$

p_{s+b} is the probability to observe a $\tilde{q}_\mu$ greater than or equal to the observed $\tilde{q}_{\mu,\text{obs}}$, given that the $\mu = 1$ hypothesis is true. Performing exclusion tests with p_{s+b} is known as the CL_{s+b} method. This analysis uses the CL_s method, where the p-value, or the CL_s value, is defined to be [81]

$$\text{CL}_s \equiv \frac{p_{s+b}}{1-p_b}, \tag{7.8}$$

with

$$p_b = \int_{-\infty}^{\tilde{q}_{\mu,\text{obs}}} f(\tilde{q}_\mu|b)\mathrm{d}\tilde{q}_\mu = P(\tilde{q}_\mu \leq \tilde{q}_{\mu,\text{obs}}|b). \tag{7.9}$$

The smaller the CL_s value for a given signal, the more incompatibility there is between data and the $\mu = 1$ hypothesis, and hence the easier it is to exclude. μ values that give $\text{CL}_s < 0.05$ are excluded at the 95% confidence level (CL), and the value of μ for which $\text{CL}_s = 0.05$ is the upper limit on the signal strength, $\mu^{95\%}_{\text{upper}}$. An upper limit is calculated for each signal sample; all limits are then collectively used to produce exclusion regions for the dark matter models that are considered. The statistical analysis is carried out using HistFitter [80], a software framework used for statistical data analysis and hypothesis testing. The fit results are extracted from HistFitter to produce exclusion contours.

7.3 Simplified model interpretation

7.3.1 Fit results

This section presents example fit results for the benchmark axial-vector signal sample with (m_χ, m_{med}) = (1, 500) GeV, a sample that is expected to be excluded. These results are obtained from a fit of the signal+background model to the data. The ee and $\mu\mu$ channel histograms are estimated separately and are combined in the fit,

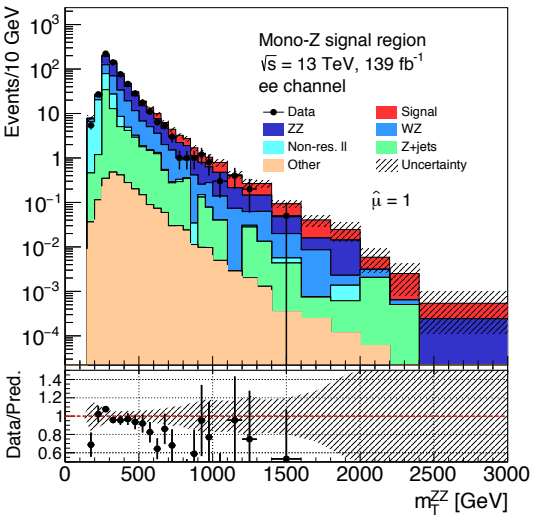

(a) Pre-fit, ee channel.

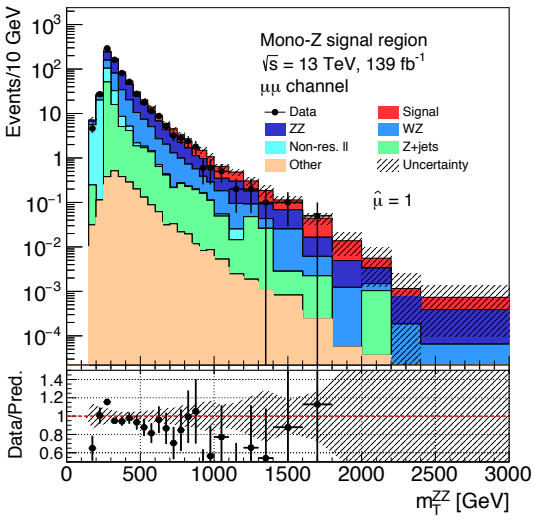

(b) Pre-fit, $\mu\mu$ channel.

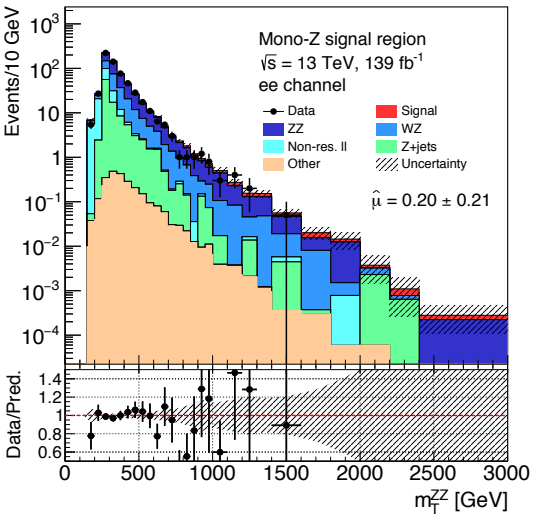

(c) Post-fit, ee channel.

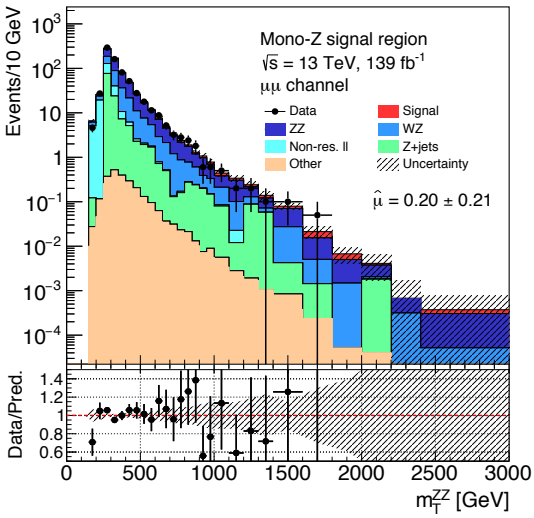

(d) Post-fit, $\mu\mu$ channel.

Figure 7.2: Pre- and post-fit m_{T}^{ZZ} distributions for the benchmark axial-vector signal with $(m_\chi, m_{\mathrm{med}}) = (1, 500)$ GeV. The ratio illustrates the agreement between the data and signal+background prediction. The best-fit signal strength is $\hat{\mu} = 0.20 \pm 0.21$. The last bin includes overflow content.

producing one value of $\hat{\mu}$. Pre- and post-fit m_{T}^{ZZ} distributions for the benchmark signal are shown in Figure 7.2. Table 7.2 summarizes the corresponding pre- and post-fit yields for each signal and background process. Before the fit $\hat{\mu} = 1$, and the best-fit value is $\hat{\mu} = 0.20 \pm 0.21$, consistent with 0. The discovery p-value is $p_0 = 0.31$,

corresponding to a significance of 0.51σ. Although there is a small excess in the data before the fit, the signal is found to be negligible after the likelihood is maximized.

Table 7.2: Summary of pre- and post-fit yields for the signal+background model compared to data for 139 fb^{-1}. The signal process is the benchmark axial-vector signal with (m_χ, m_{med}) = (1, 500) GeV. The pre-fit background-only prediction is also repeated for comparison. The errors quoted are calculated from the quadratic sum of statistical and systematic uncertainties.

	ee channel	$\mu\mu$ channel
Observed events	2984	3519
Yields after fit		
$qqZZ$	1078.4 ± 83.7	1226.3 ± 77.2
$ggZZ$	144.3 ± 43.0	160.1 ± 47.6
EW $qqZZ$	18.7 ± 1.3	19.5 ± 1.3
WZ	798.1 ± 23.3	888.7 ± 26.1
Non-resonant $\ell\ell$	428.5 ± 25.6	484.9 ± 26.5
Z+jets	485.5 ± 64.2	598.7 ± 66.6
$ttV(V)$	6.3 ± 0.8	5.7 ± 0.7
VVV	5.9 ± 0.7	6.3 ± 0.7
AV signal, (m_χ, m_{med}) = (1, 500) GeV	59.7 ± 62.2	65.0 ± 67.7
Total	3025.5 ± 43.3	3455.1 ± 46.0
Yields before fit		
$qqZZ$	1056.1 ± 75.7	1199.7 ± 72.6
$ggZZ$	125.0 ± 41.2	138.6 ± 45.5
EW $qqZZ$	18.4 ± 1.3	18.9 ± 1.4
WZ	785.2 ± 33.0	868.9 ± 38.0
Non-resonant $\ell\ell$	444.5 ± 45.9	499.6 ± 47.1
Z+jets	324.74 ± 132.1	409.3 ± 161.7
$ttV(V)$	6.1 ± 0.8	5.6 ± 0.7
VVV	5.9 ± 0.7	6.2 ± 0.7
AV signal, (m_χ, m_{med}) = (1, 500) GeV	299.9 ± 23.3	325.8 ± 23.9
Total	3065.8 ± 181.4	3472.5 ± 207.4
Total (background only)	2765.9 ± 178.3	3146.7 ± 204.4

The quality of the fit is diagnosed by calculating *pulls* and *rankings* for each nuisance parameter. Figure 7.3 shows the pulls for all nuisance parameters in the

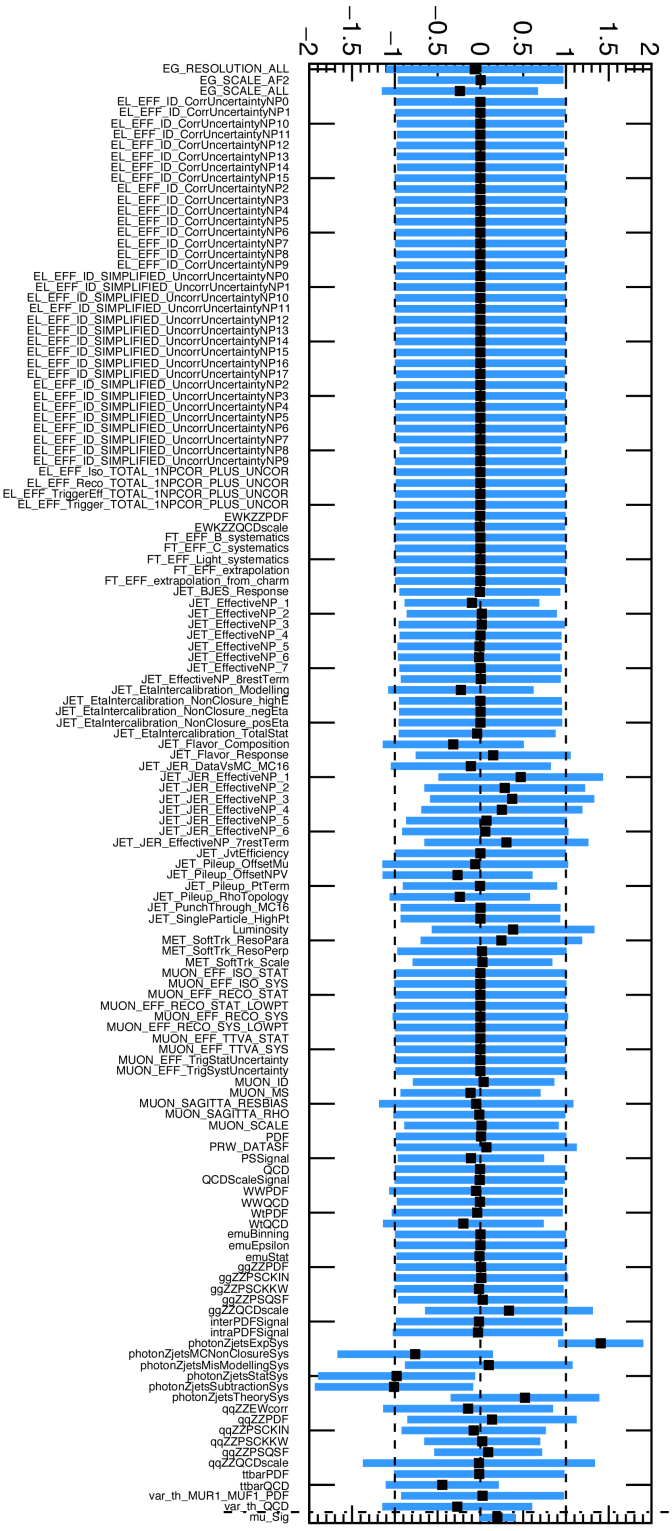

Figure 7.3: Nuisance parameter pulls for the benchmark axial-vector signal with (m_χ, m_{med}) = (1, 500) GeV. The black square indicates the post-fit value for each nuisance parameter, and the blue bar represents its post-fit error. The post-fit $\hat{\mu}$ value is also included at the bottom of the figure.

fit to the benchmark axial-vector signal. The pulls illustrate how far each nuisance parameter was "pulled" from its initial value of 0 ± 1. In general most nuisance parameters remain consistent with 1. Some of the larger experimental systematics, such as those affecting jets, are pulled more than others. Most notably, the Z+jets background has some of the strongest pulls, with the experimental systematic nuisance parameter ending up outside the initial 1σ error. The Z+jets background has the largest systematic errors in the analysis, so its nuisance parameters provide the most freedom in the fit.

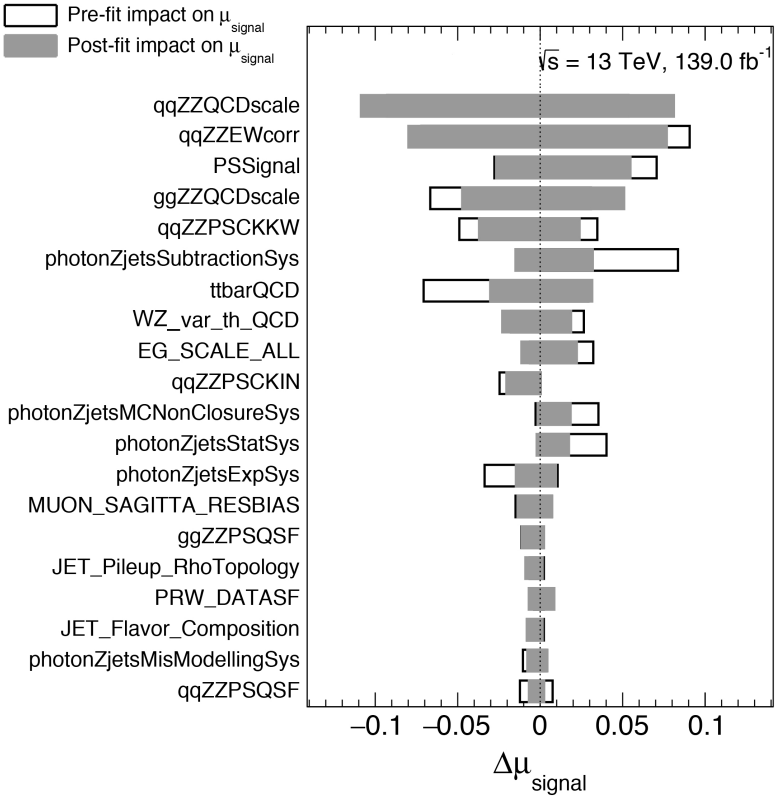

Figure 7.4: Nuisance parameter rankings for the benchmark axial-vector signal with $(m_\chi,\ m_{\mathrm{med}}) = (1,\ 500)$ GeV. The top 20 nuisance parameters are ordered by their post-fit impact on the signal strength.

The rankings for the top 20 nuisance parameters are shown in Figure 7.4. Rankings show the impact that each systematic has on the signal strength parameter. For a given nuisance parameter, its ranking is calculated by redoing the fit four times, with the parameter fixed to (1) its pre-fit value $+1\sigma$, (2) its pre-fit value -1σ, (3) its post-fit value $+1\sigma$, and (4) its post-fit value -1σ. All other parameters are initially

set to their best-fit values and are allowed to float during the fit. After the fit, the change in the signal strength, $\Delta\mu$, is obtained. The ranking is a measure of how the variations of a given nuisance parameter affect the signal strength. This procedure is repeated for every nuisance parameter, and they are ranked by the size of $\Delta\mu$. The ZZ EW, QCD, and parton shower systematics have the largest rankings, in addition to the Z+jets systematics, WZ and $t\bar{t}$ QCD scale systematics, and some experimental systematics.

Discovery hypothesis tests are performed for all simplified model signal samples. Of all 154 signals, none are found to have $p_0 < 0.05$, meaning all signal models are consistent with the background-only hypothesis. The smallest p-value observed is $p_0 = 0.084$, corresponding to a significance of only 1.4σ. Since no significant models are found, exclusion regions are computed for all simplified model signals.

7.3.2 Exclusion limits

The main simplified model results are two exclusion limits on the (m_{med}, m_χ) mass plane for axial-vector and vector mediators. This set of limits is coordinated by the LHC Dark Matter Working Group in order to allow comparison between ATLAS, CMS, and other experiments. Expected and observed CL_s values are calculated for each signal sample in these planes. The expected values are calculated independently of the data, assumed to be equal to the total background prediction. The observed values are calculated using the actual observed data. The CL_s values are then obtained for each signal in the (m_{med}, m_χ) plane. The region contained by the contour with $\text{CL}_s < 0.05$ is excluded at the 95% CL.

The exclusion limit results are shown in Figure 7.5 for axial-vector and vector models. In both plots the lower left region contains the excluded signal samples. There is a slight post-fit excess in data which leads to weaker observed limits compared to expected; overall the observed limits are about 1σ worse than the expected limits. The relic density line [85] indicates the (m_{med}, m_χ) pair that would produce the correct dark matter relic density that is observed in the universe; the calculation of this line assumes that the simplified models of interest are the only sources of dark matter in the universe. The purple dashed line indicates the previous 36.1 fb^{-1} observed limit [57]. The on-shell line is indicated by $m_{\text{med}} = 2m_\chi$. The dark matter pair is produced by a resonance of the mediator particle. Below the line where $m_{\text{med}} > 2m_\chi$ there is enough mass energy to produce the dark matter particles on-

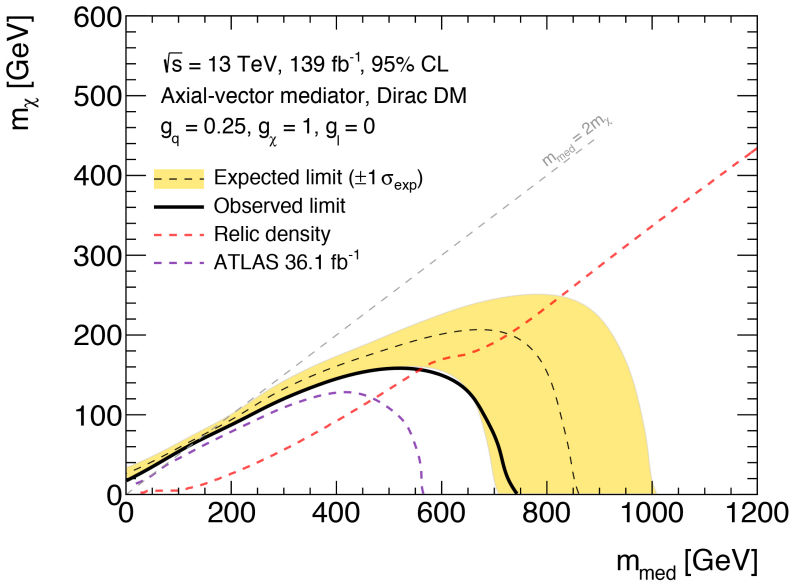

(a) Axial-vector exclusion limit.

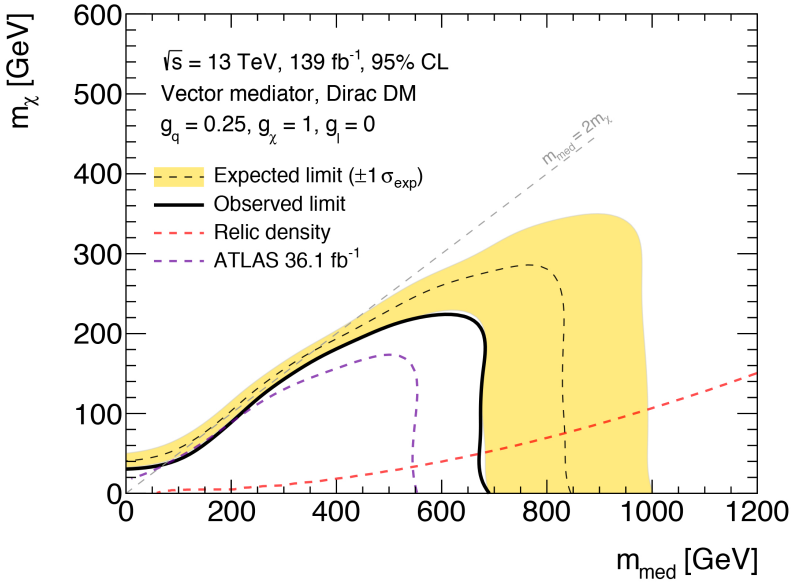

(b) Vector exclusion limit.

Figure 7.5: (m_{med}, m_χ) exclusion limits for axial-vector and vector simplified models with $g_q = 0.25$, $g_\chi = 1$, and $g_\ell = 0$. The black dashed line indicates the expected limit, and the yellow band shows the expected $\pm 1\sigma$ error band. The solid black line indicates the observed limit. The relic density prediction [85] is shown by the dashed red line, and the previous observed limit with 36.1 fb^{-1} [57] is shown by the dashed purple line. The 2D mass region contained by the observed contour in the lower left is excluded at the 95% CL.

shell. The signal production cross section is heavily suppressed in the off-shell region where $m_{\text{med}} < 2m_{\chi}$, but a small area is excluded at low mass. For the axial-vector limit, the reach in m_{med} extends to almost 750 GeV, and the maximum reach in m_{χ} is 160 GeV for $m_{\text{med}} = 520$ GeV. Similarly, the vector limit reaches m_{med} slightly below 700 GeV, with a maximum reach in m_{χ} of 220 GeV for $m_{\text{med}} = 600$ GeV. Compared to the 36.1 fb^{-1} result with a maximum reach in m_{med} of ∼550 GeV, the new axial-vector (vector) results are improved by ∼36% (27%).

7.4 2HDM+a model interpretation

7.4.1 Fit results

Fits are tested for 2HDM+a signal samples. In general the diagnostics are similar as for the benchmark simplified model results presented in Section 7.3.1. Discovery hypothesis tests are performed for all 2HDM+a signals. Of the 480 signal models tested, about 10 signals have a p_0 ∼0.01-0.02, suggesting some tension with the background-only hypothesis. However the maximum significance observed for any signal is only 2.3σ, which is not statistically unexpected out of many hundreds of signal models. No significant excess is observed for any 2HDM+a model, so exclusion limits are set using all signals.

7.4.2 Exclusion limits

Eight parameter scans are produced for the 2HDM+a model. Once again this set of limits is agreed upon by the LHC Dark Matter Working Group. The first scans discussed are the $\tan\beta$-mass scans. Figure 7.6 shows the ($\tan\beta$, m_A) limits for $\sin\theta$ = 0.35 and 0.7 with $m_a = 250$ GeV. The excluded regions are in the centre of the plots. The contour is affected by the interplay between gg-fusion and bb-induced signal processes. gg processes dominate for $\tan\beta < 1$, and signals with large cross sections are easier to exclude, so the contour is wide in this region. As $\tan\beta$ increases, the gg cross section decreases and the contour narrows; eventually the bb contribution becomes significant and the cross section grows, causing the contour to widen again at high $\tan\beta$. Samples with $\sin\theta = 0.35$ have higher cross sections at high $\tan\beta$ than samples with $\sin\theta = 0.7$; likewise, samples with $\sin\theta = 0.7$ have higher cross sections at low $\tan\beta$ than samples with $\sin\theta = 0.35$. This leads to a better exclusion in the

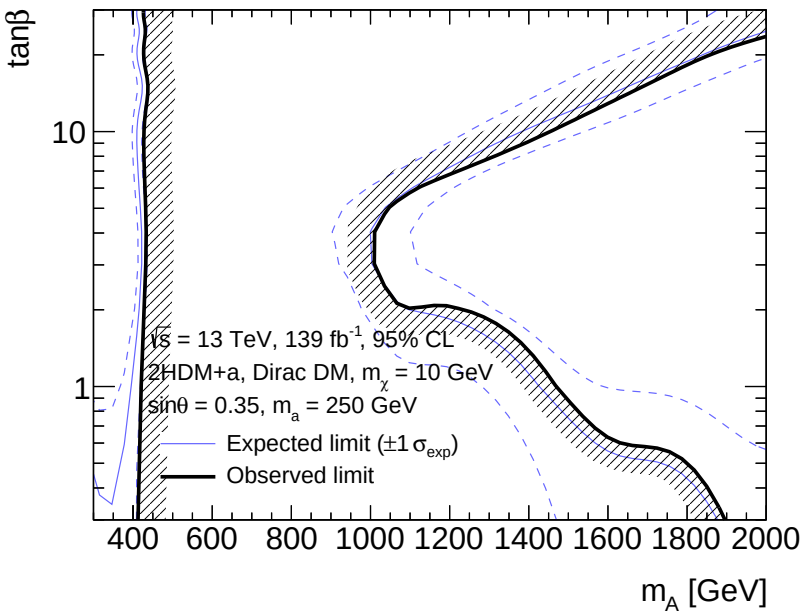

(a) Exclusion limit for $\sin\theta = 0.35$.

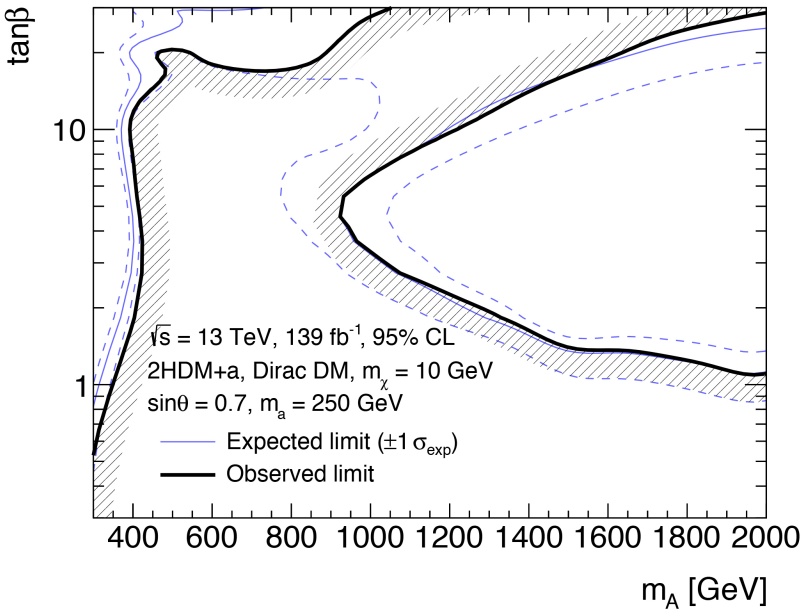

(b) Exclusion limit for $\sin\theta = 0.7$.

Figure 7.6: $(\tan\beta,\ m_A)$ exclusion limits for 2HDM+a models with $m_a = 250$ GeV and $m_\chi = 10$ GeV. The purple solid line indicates the expected limit, and the purple dashed line indicates the $\pm 1\sigma$ error on the expected limit. The black solid line indicates the observed limit, and the hash shows the excluded region. The central region contained by the observed contour is excluded at the 95% CL.

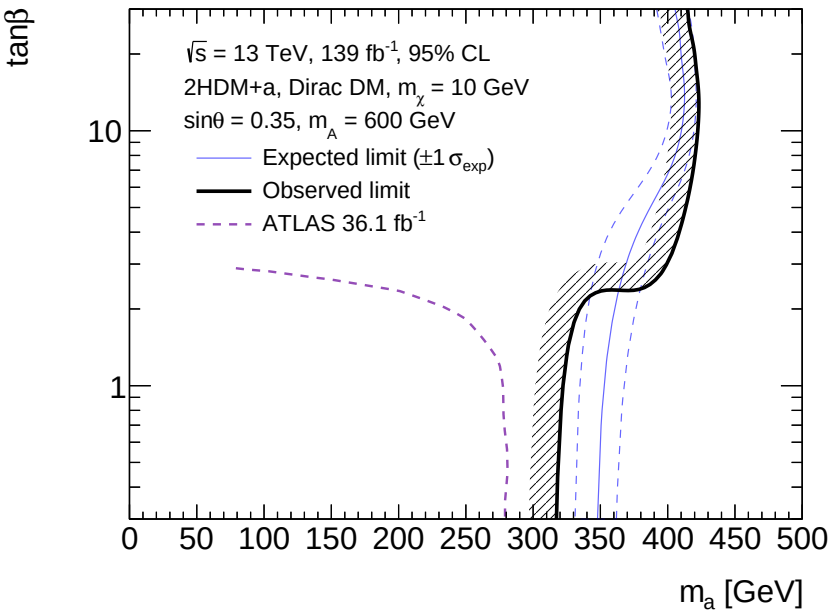

(a) Exclusion limit for $\sin\theta = 0.35$. Includes the 36.1 fb^{-1} observed limit [39].

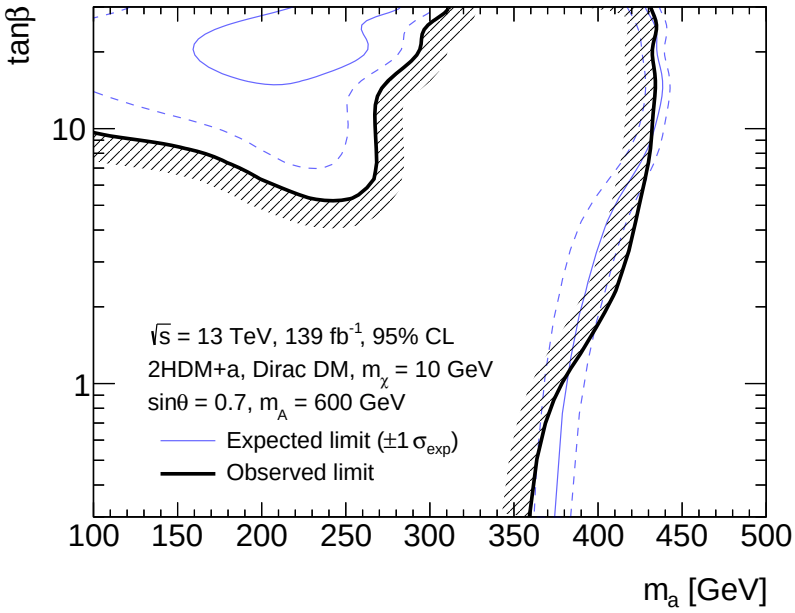

(b) Exclusion limit for $\sin\theta = 0.7$.

Figure 7.7: $(\tan\beta,\ m_a)$ exclusion limits for 2HDM+a models with $m_A = 600$ GeV and $m_\chi = 10$ GeV. The purple solid line indicates the expected limit, and the purple dashed line indicates the $\pm 1\sigma$ error on the expected limit. The black solid line indicates the observed limit, and the hash shows the excluded region. The left-hand region contained by the observed contour is excluded at the 95% CL.

$\sin\theta = 0.35$ plane at high $\tan\beta$, and better exclusion for $\sin\theta = 0.7$ at low $\tan\beta$. The loss in sensitivity at low m_A is because A becomes too light to produce $Z + a$ on-shell, leading to a reduced cross section. The cross section also decreases as m_A becomes very heavy. Figure 7.7 illustrates the ($\tan\beta$, m_a) exclusion limits for $\sin\theta =$ 0.35 and 0.7 with $m_A = 600$ GeV. The excluded regions are the left-hand areas of the plots. The shapes of these limits are not as dependent on gg and bb contributions, but in general the excluded area does grow by extending further to the right as $\tan\beta$ increases. Again the exclusion region in the $\sin\theta = 0.35$ plane is larger than the $\sin\theta = 0.7$ plane. The sensitivity worsens for large m_a because the cross section for $A \to Z + a$ decreases. Figure 7.7a includes the previous exclusion limit with 36.1 fb^{-1} [39]. The new contour now extends upwards beyond $\tan\beta = 3$ due to the inclusion of bb-induced signal contributions that were not included for the previous result. For $\tan\beta = 1.0$, the observed reach in m_a has improved from 280 GeV to 320 GeV (14% improvement).

The (m_A, m_a) exclusion limits are shown in Figure 7.8. The regions contained by the observed contours are excluded. For the $\sin\theta = 0.35$ plane, the observed 36.1 fb^{-1} exclusion limit [39] is included for comparison; the highest m_A excluded has improved from 1 TeV to ∼1.5 TeV for $m_a = 100$ GeV, and the highest m_a excluded has increased from 340 GeV to ∼405 GeV for $m_A = 1.2$ TeV. The lower half of the contour is cut off for $m_a < 250$ GeV as there are not enough signal points to interpolate reliably in this region. For the $\sin\theta = 0.7$ plane, the highest m_A excluded is ∼1.6 TeV for m_a = 100 GeV, and the maximum reach in m_a obtained is ∼460 GeV for $m_A = 1$ TeV. For both limits, the line at $m_A = m_a + m_Z$ corresponds to the on-shell line for the A and H bosons. As demonstrated in Figures 2.7a and 2.8a, sensitivity is lost when $m_a + m_Z > m_A$ or m_H. Similarly, sensitivity decreases for m_A values near 1.5-1.6 TeV due to the cross section becoming too small to be observable with 139 fb^{-1}.

Finally, Figure 7.9 shows the 1D $\sin\theta$ upper limit scans for (m_A, m_a) = (600, 200) GeV and (1000, 350) GeV. In these plots the upper limit on the signal strength, $\mu^{95\%}_{\text{upper}}$, is plotted as a function of $\sin\theta$. Any $\sin\theta$ value for which $\mu^{95\%}_{\text{upper}} < 1$ is excluded.[2] The previous observed limits with 36.1 fb^{-1} are included. For the lighter mass scan with (m_A, m_a) = (600, 200) GeV, the excluded range has improved from $0.24 < \sin\theta < 0.90$ to $0.15 < \sin\theta < 0.90$; similarly, for the scan with (m_A, m_a) = (1000, 350) GeV, the excluded range improves from $0.43 < \sin\theta < 0.90$ to $0.20 < \sin\theta < 0.90$.

[2] $\mu^{95\%}_{\text{upper}}$ is equivalent to $\sigma^{95\%}_{\text{upper}}/\sigma_{\text{theory}}$, where $\sigma^{95\%}_{\text{upper}}$ is the upper limit on the cross section of the signal model, and σ_{theory} is the nominal cross section of the signal model.

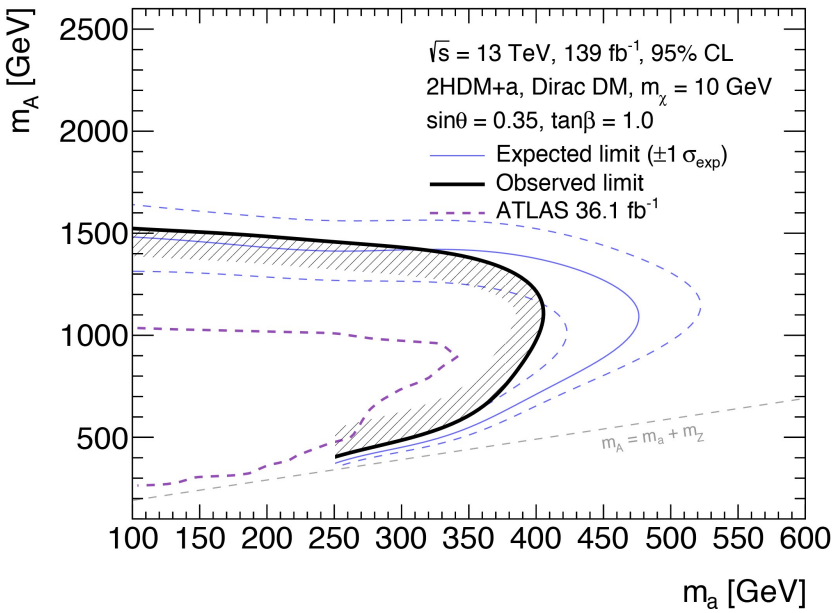

(a) Exclusion limit for $\sin\theta = 0.35$. Includes the 36.1 fb^{-1} observed limit [39].

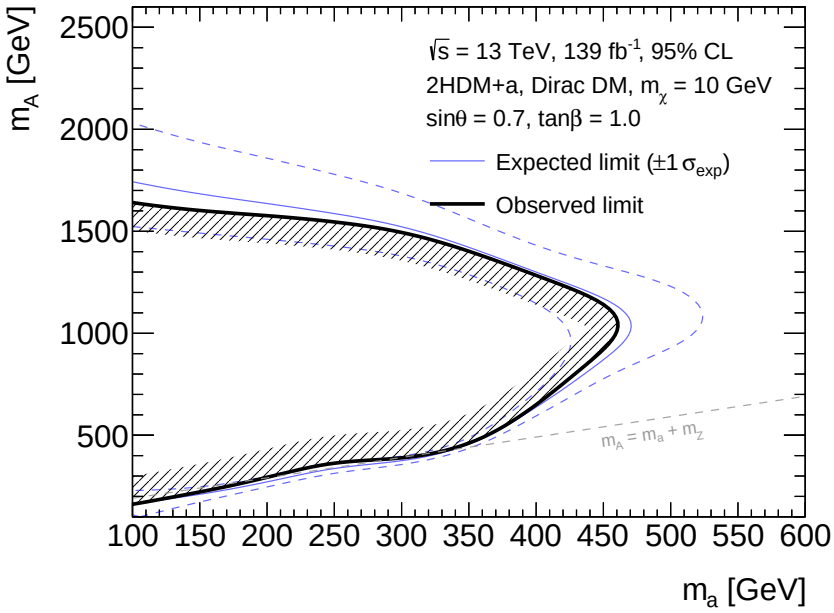

(b) Exclusion limit for $\sin\theta = 0.7$.

Figure 7.8: (m_A, m_a) exclusion limit for 2HDM+a models with $\tan\beta = 1.0$ and m_χ = 10 GeV. The purple solid line indicates the expected limit, and the purple dashed line indicates the $\pm 1\sigma$ error on the expected limit. The black solid line indicates the observed limit, and the hash shows the excluded region. The region contained in the contour is excluded at the 95% CL.

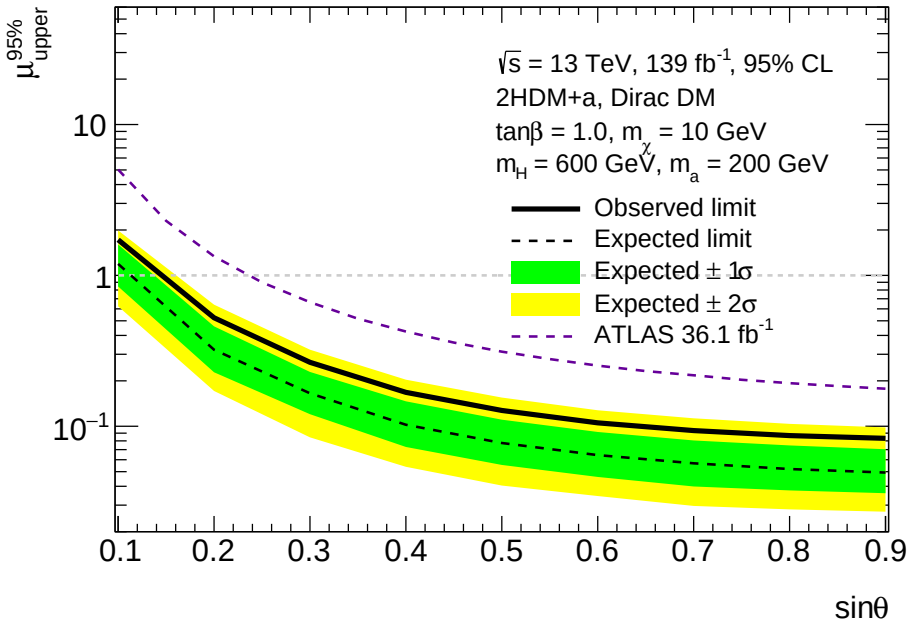

(a) Exclusion limit for $m_A = 600$ GeV, $m_a = 200$ GeV.

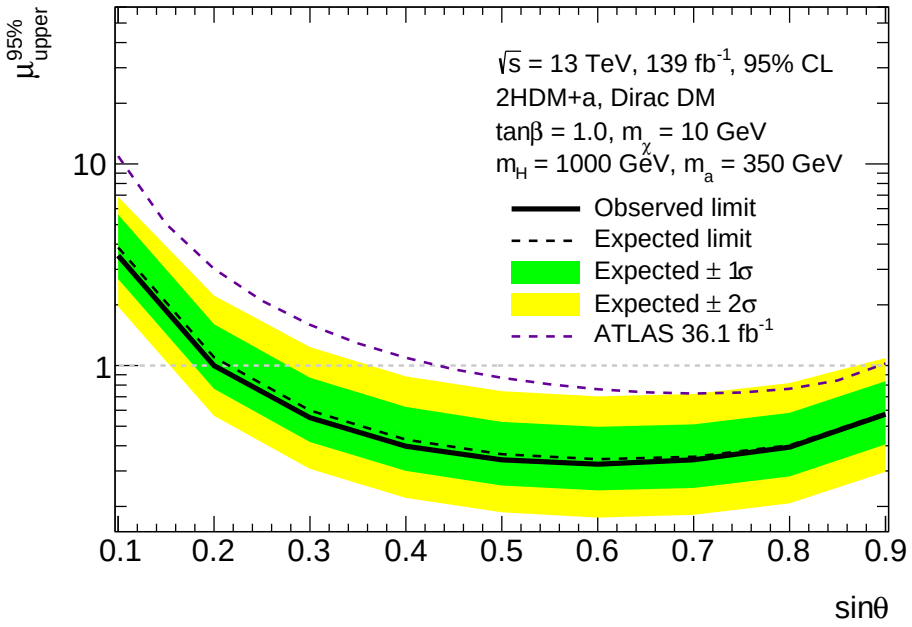

(b) Exclusion limit for $m_A = 1000$ GeV, $m_a = 350$ GeV.

Figure 7.9: $\sin\theta$ exclusion limits for 2HDM+a models with $\tan\beta$ =1.0 and $m_\chi = 10$ GeV. The dashed line indicates the expected limit. The green (yellow) bands indicate the $\pm 1\sigma$ ($\pm 2\sigma$) error on the expected limit. The solid black line is the observed limit. The region where the observed limit extends below $\mu^{95\%}_{\text{upper}} = 1$ is excluded at the 95% CL. Both plots include the 36.1 fb^{-1} observed limits [39].

7.5 Comparisons to other searches

7.5.1 Direct detection

The 2D mass exclusion limits for simplified models can be compared with direct detection limits. Direct detection experiments set limits on the DM-nucleon scattering cross section as a function of m_χ by searching for dark matter particles interacting with the detector. There are spin-dependent (SD) and spin-independent (SI) limits depending on the detector material. The dark matter particle scatters with the spin of the isotope, which is approximately due to an unpaired proton (p) or neutron (n). If the medium does not have an unpaired nucleon, then limits are set on the SI case, and it is assumed that $\sigma^p_{\mathrm{SI}} = \sigma^n_{\mathrm{SI}}$. Otherwise the unpaired proton or neutron will affect the scattering cross section, and limits are set separately on either σ^p_{SD} or σ^n_{SD}. For the results shown here, the axial-vector limit is translated into a SD limit on the DM-proton scattering cross section, while the vector limit is translated into a SI limit on the DM-nucleon scattering cross section. The recommended formulae for this procedure are [85]

$$\sigma_{\mathrm{SD}} \simeq 2.4 \times 10^{-42}\ \mathrm{cm}^2 \times \left(\frac{g_q g_\chi}{0.25}\right)^2 \left(\frac{1\ \mathrm{TeV}}{m_{\mathrm{med}}}\right)^4 \left(\frac{\mu_{N\chi}}{1\ \mathrm{GeV}}\right)^2 \tag{7.10}$$

and

$$\sigma_{\mathrm{SI}} \simeq 6.9 \times 10^{-41}\ \mathrm{cm}^2 \times \left(\frac{g_q g_\chi}{0.25}\right)^2 \left(\frac{1\ \mathrm{TeV}}{m_{\mathrm{med}}}\right)^4 \left(\frac{\mu_{N\chi}}{1\ \mathrm{GeV}}\right)^2 \tag{7.11}$$

for axial-vector and vector models respectively. $\mu_{N\chi} = m_N m_\chi/(m_N + m_\chi)$ is the reduced mass of the nucleon and dark matter particle, with $m_N \simeq 0.939$ GeV.

Figure 7.10 shows the translated limit results for SD and SI cases. The region contained by the observed contour in the upper left is excluded by this search. The 90% CL is used to match the convention of the direct detection experiments, for which some of the latest results are shown. The mono-Z limits are most competitive at low m_χ.[3] Most direct detection experiments that involve nuclear recoils have maximum sensitivity when m_χ is near the atomic mass of the medium, and most experiments

[3]It is worth noting that, unlike the direct detection results, the collider limit "turns over" and passes through multiple cross section values for a single value of m_χ; this is because the 2D mass limits in Figure 7.5 have two m_{med} values for m_χ above ∼20 GeV, and so two values of $\sigma_{\mathrm{SI/SD}}$ are calculated from Equations 7.11 and 7.10 for a fixed m_χ.

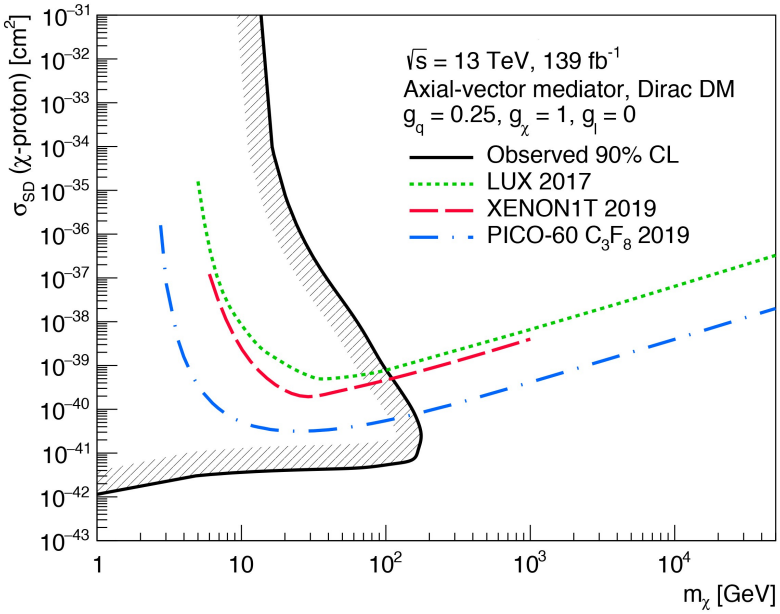

(a) Axial-vector (spin-dependent) exclusion limit on the proton scattering cross section. Direct detection results are shown for the LUX [86], XENON1T [87], and PICO-60 [4] collaborations.

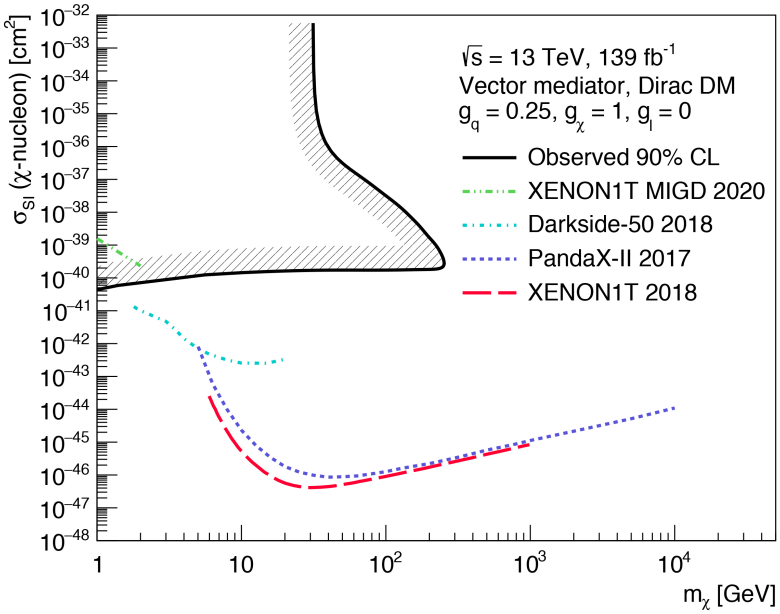

(b) Vector (spin-independent) exclusion limit on the nucleon scattering cross section. Direct detection results are shown for the XENON1T [3, 88], DarkSide-50 [6], and PandaX-II [5] collaborations.

Figure 7.10: Direct detection exclusion limits for axial-vector and vector simplified models with $g_q = 0.25$, $g_\chi = 1$, and $g_\ell = 0$. Limits are set on the DM-nucleon scattering cross section as a function of m_χ. The upper left region contained by the observed limit is excluded at the 90% CL.

lose sensitivity for $m_\chi < \sim$3-5 GeV.[4] For the SD limit, the observed limit reaches $\sim 10^{-41}$-10^{-42} for 1 GeV $< m_\chi <$ 100 GeV. For the SI case, the limit is closer to $\sim 10^{-40}$ for 1 GeV $< m_\chi <$ 100 GeV.

7.5.2 Other ATLAS results

The results of this dissertation are compared to the results of other ATLAS dark matter searches. There are two general categories of simplified model DM searches at colliders. The mono-Z search falls into the broader category of mono-X searches, where events containing $E_{\mathrm{T}}^{\mathrm{miss}}$ and $X = Z$, W, γ, h, or a jet, are studied. The second category is resonance searches, usually performed with two jets (a dijet system), where the s-channel mediator decays back into $q\bar{q}$ instead of $\chi\bar{\chi}$. The results of mono-X and resonance searches are combined into summary figures which contain the overlaid results of several searches. Figure 7.11 shows a summary of (m_χ, m_{med}) limits

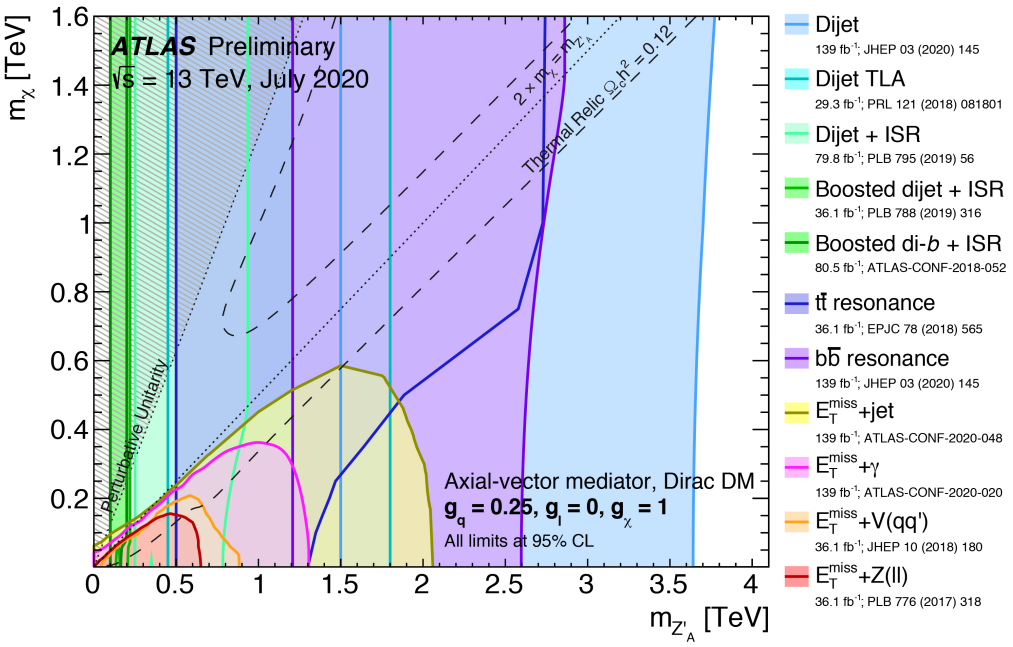

Figure 7.11: Summary figure of limits on (m_χ, m_{med}) from ATLAS axial-vector simplified model searches [89]. Includes the mono-Z result with 36.1 fb^{-1} (red curve), which can be directly compared to the 139 fb^{-1} result in Figure 7.5a. Note that $m_{Z'_A}$ is equivalent to m_{med}.

[4]Some detectors, e.g. XENON1T [88], can achieve limits at lower mass by searching for the ejection of an atomic electron (the Migdal effect) or a photon (Bremsstrahlung radiation) from DM-nucleon scattering.

for the latest public ATLAS axial-vector simplified model searches with $g_q = 0.25$, $g_\chi = 1$, and $g_\ell = 0$ [89]. The results in the summary figure use various amounts of Run 2 data, and the mono-Z limit shown is the 36.1 fb^{-1} result; this limit can be compared with the result from this dissertation in Figure 7.5a. The summary illustrates the complementarity between mono-Z, mono-$V(q\bar{q})$, mono-γ, and mono-jet searches. Mono-jet results typically dominate the mono-X category due to the high probability for a quark to radiate a gluon compared to a Z or γ. Compared to mono-X searches, resonance searches exclude larger mass ranges and are mostly independent of m_χ; nearly the entire phase space with $m_{\text{med}} < 3.6$ TeV and $m_\chi < 1.6$ TeV is excluded by at least one search.

The translation to limits on direct detection experiments is also done here; the corresponding ATLAS summary figure of (m_χ, $\sigma_{\text{SD}}^{\chi\text{-proton}}$) limits is shown in Figure 7.12, which can be compared to the result from this dissertation in Figure 7.10a. In

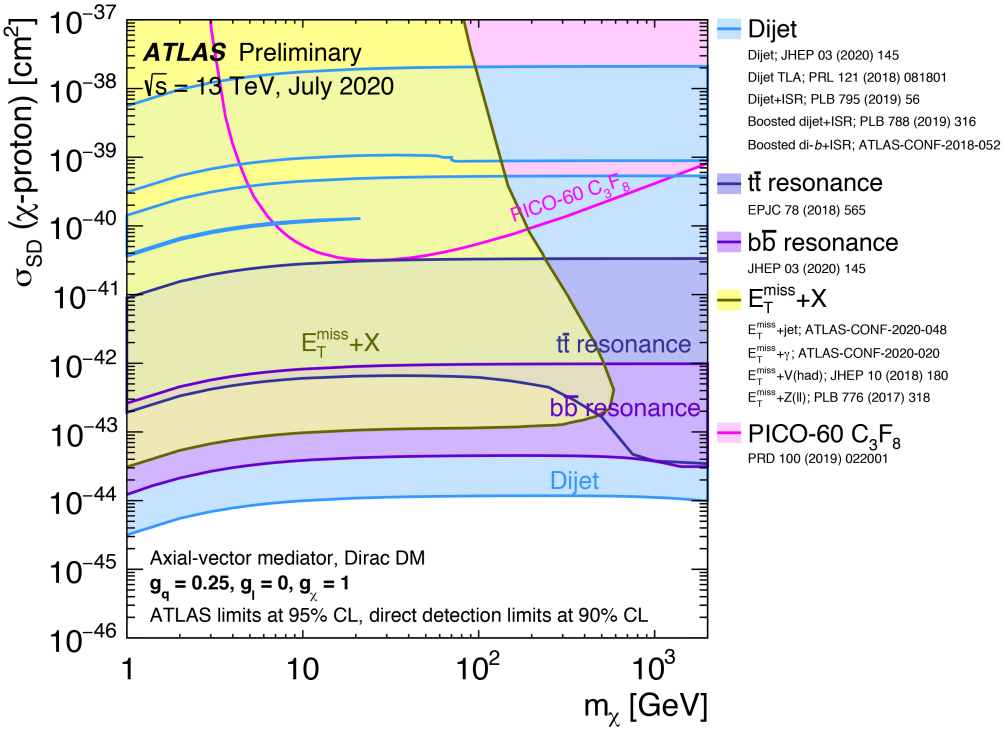

Figure 7.12: Summary figure of limits on (m_χ, $\sigma_{\text{SD}}^{\chi\text{-proton}}$) from ATLAS axial-vector simplified model searches [89]. Although the reference to the mono-Z result with 36.1 fb^{-1} is included, only a generic mono-X limit is shown, which is dominated by the mono-jet result. This figure can be compared to the 139 fb^{-1} mono-Z result in Figure 7.10a.

the summary figure the mono-X results have been combined into one exclusion limit, which is dominated by the 139 fb^{-1} mono-jet result. The PICO-60 C_3F_8 result [4] is overlaid for comparison. For the given model and coupling assumptions, the ATLAS searches are sensitive to regions not yet achievable by direct detection experiments.

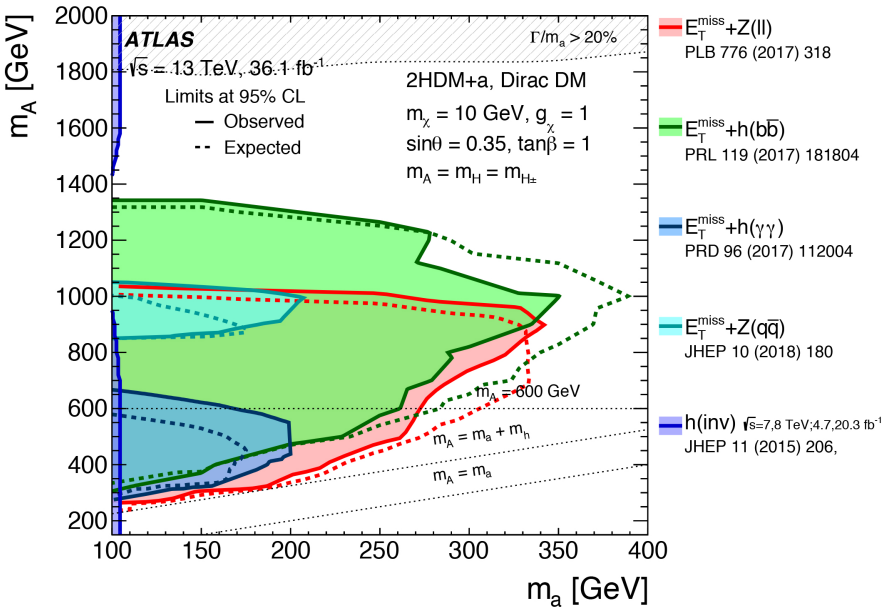

Figure 7.13: Summary figure of limits on (m_a, m_A) from ATLAS 2HDM+a model searches [39]. Includes the mono-Z result with 36.1 fb^{-1} (red curve), which can be directly compared to the 139 fb^{-1} result in Figure 7.8a.

For 2HDM+a models, several ATLAS searches with 139 fb^{-1} are currently in progress. Public limits on (m_a, m_A) with 36.1 fb^{-1} are shown in Figure 7.13 for several searches [39]. These results use $\sin\theta = 0.35$, $\tan\beta = 1.0$, and $m_\chi = 10$ GeV. The mono-Z result with 139 fb^{-1} to be compared with is in Figure 7.8a. Although the summary figure has yet to be updated beyond 36.1 fb^{-1}, it nonetheless illustrates the different sensitivities of the various searches. In contrast to simplified models, the mono-Z signature is one of the most sensitive search channels for 2HDM+a models due to the large coupling between the Z and the H/A bosons. Furthermore, the mono-$Z(\ell\ell)$ search has significantly higher sensitivity than the mono-$Z(qq)$ search, which suffers from large QCD backgrounds, even though the branching ratio of $Z \to qq$ is larger than for $Z \to ee/\mu\mu$ (69.9% and 6.7% and respectively). The mono-Z limit with 139 fb^{-1} is a great improvement and eclipses both the mono-Z and mono-$h(b\bar{b})$ results with 36.1 fb^{-1}. It will be interesting to see how the other results evolve with

the full Run 2 dataset.

7.5.3 CMS mono-Z result

The mono-Z search has been performed by the CMS collaboration with 137 fb^{-1} [90]. A comparison of results between ATLAS and CMS is always ideal when possible. In the case of a discovery, each collaboration must corroborate the results of the other. For a dark matter search with no observed signal it is useful nonetheless; in this case, the two results are obtained completely independently using different strategies, and yet the results obtained are comparable.

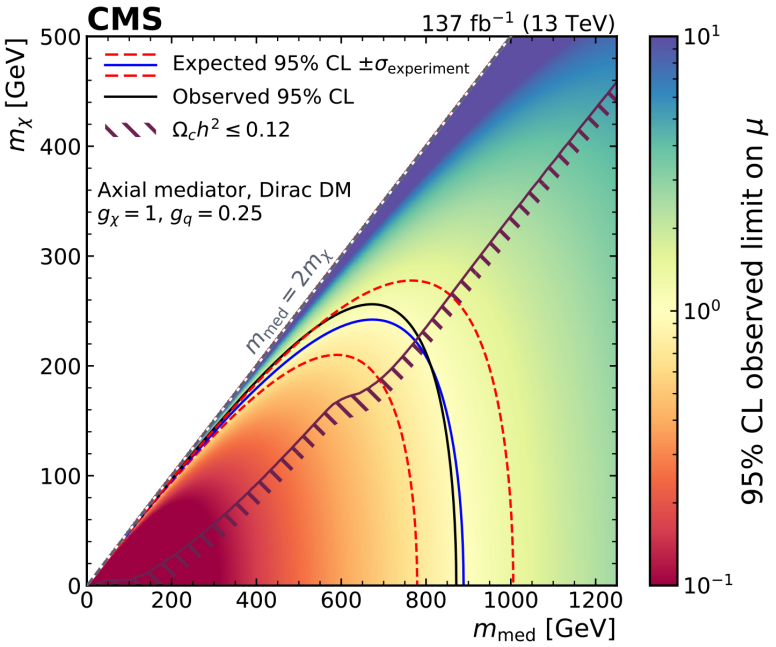

Figure 7.14: CMS mono-Z simplified model limits on (m_χ, m_{med}) with 137 fb^{-1} [90].

Figure 7.14 shows CMS mono-Z axial-vector simplified model (m_{med}, m_χ) limit, which can be compared to the results from this dissertation in Figure 7.5a. Overall the expected limits between the two experiments are extremely similar, with a maximum reach in m_{med} between 850-900 GeV from both experiments. While the ATLAS expected limit reaches $m_\chi \simeq 200$ GeV, the CMS expected limit extends higher to about $m_\chi \simeq 240$ GeV. CMS observes a tiny excess in data compared to background, leading to very good agreement between observed and expected limits. In the ATLAS result a larger (albeit still insignificant) excess is seen, leading to worse observed limits compared to expected.

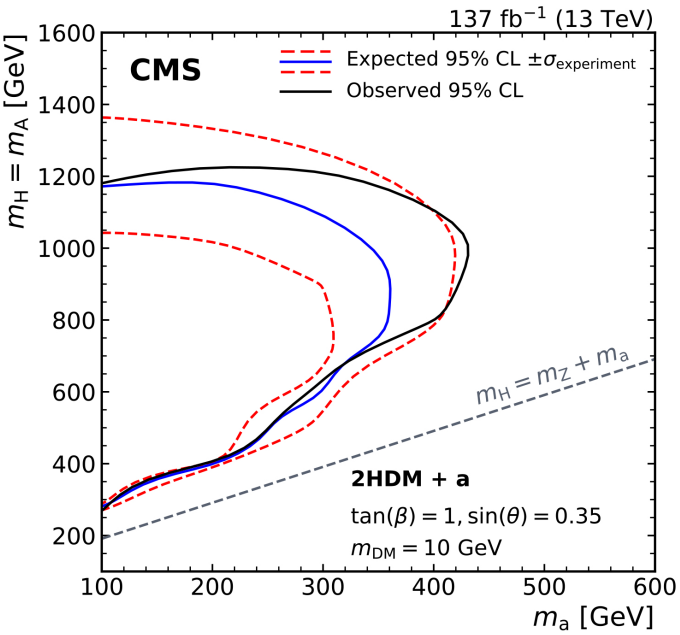

Figure 7.15: CMS mono-Z 2HDM+a limits on (m_a, m_A) with 137 fb^{-1} [90].

For 2HDM+a model results, the CMS (m_a, m_A) limit for $\sin\theta = 0.35$ and $\tan\beta = 1.0$ is shown in Figure 7.15, to be compared with the result from this analysis in Figure 7.8a. In this case the ATLAS expected limit is better than the CMS expected limit, reaching about $m_a = 470$ GeV compared to ∼350 GeV, and $m_A = 1.5$ TeV compared to ∼1.2 TeV. The CMS observed limit is better than expected, reaching out to $m_a = 430$ GeV. The ATLAS observed limit is worse than expected, but it is comparable to CMS observed limit in terms of reach in m_a, and is better in terms of reach in m_A.

Chapter 8

Conclusions and Future Prospects

A search for dark matter in the mono-Z final state has been performed with the ATLAS Run 2 dataset of 139 fb^{-1}. Simplified models and 2HDM+a models are studied as per recommendation from the LHC Dark Matter Working Group. The signal region selections are optimized to isolate $Z(\ell\ell) + E_{\mathrm{T}}^{\mathrm{miss}}$ events, and m_{T}^{ZZ} is used as the discriminating variable. The ZZ background is estimated from simulation with NLO EW corrections applied. WZ and non-resonant $\ell\ell$ backgrounds are estimated using simulation and scale factors obtained from data in the 3ℓ and $e\mu$ control regions. The Z+jets background is estimated using a fully data-driven γ+jets reweighting technique, significantly reducing the systematic uncertainty compared to the estimate from simulation. No significant excess in data is observed in the signal region, and exclusion limits are set on the dark matter models considered. The results complement direct detection limits, other ATLAS dark matter searches, and are in agreement with the CMS mono-Z result.

Future prospects

So far there has been no evidence for the existence of dark matter produced at the LHC, but the search for dark matter is far from over. If dark matter is indeed rarely produced in pp collisions then more data will be critical to its discovery. Run 3 at the LHC is currently scheduled to start in early 2022 with data taking until the end of 2024. During this time the LHC will be producing pp collisions at twice the instantaneous luminosity compared to Run 2, and the total dataset since Run 1 is projected to reach about 350 fb^{-1}. Run 3 collisions are also expected to take place

at 14 TeV centre-of-mass energies, providing more discovery potential for heavy BSM particles. Beyond this, the LHC will be upgraded for the High Luminosity LHC (HL-LHC), which is scheduled to begin collisions in 2027 and run for more than 10 years; it is expected to produce collisions at 5-7.5 times the Run 2 luminosity and yield a dataset on the order of 3000 fb^{-1}, over 20 times more data than the dataset used in this dissertation; this will vastly increase the discovery potential for dark matter in the ATLAS mono-Z search and all other LHC searches.

In addition to a larger dataset, all searches will benefit from the Run 3 and HL-LHC upgrades to the ATLAS detector. These upgrades are to allow for similar detector performance while operating in a high luminosity environment. The most significant upgrades are to the inner detector, including the new inner tracking detector (ITK) [91]. The ITK will provide precision charged particle trajectories and vertex reconstruction at high luminosities. In the forward region, the muon new small wheels (NSWs) [92] will improve low p_{T} muon reconstruction, and the high-granularity timing detector (HGTD) [93] will aid in track-to-vertex association, improving the reconstruction performance for both forward leptons and jets. Upgrades to the trigger and data acquisition (TDAQ) systems [94] will include, for example, new feature extraction processors in the L1 calorimeter trigger, allowing for higher granularity data from the LAr calorimeter and providing improved electron reconstruction and $E_{\text{T}}^{\text{miss}}$ pileup corrections.

Independent of the dataset and detector upgrades, there are ways to extend and improve the mono-Z analysis itself. In terms of the analysis methodology, some avenues for improvement have been identified. The Run 2 result is obtained using a fit to signal and background m_{T}^{ZZ} distributions in the signal region. It is often beneficial to extend the fit to include data and prediction in control regions as well. This may reduce correlated systematic uncertainties in the signal region, and the normalization for a given background in the signal region may be constrained by the data/background agreement in a related control region; for example, a $ZZ \to 4\ell$ control region may have useable statistics with the HL-LHC dataset to effectively constrain the ZZ background systematic uncertainties. It is also observed in the Run 2 analysis that there are differences in the optimal selections between simplified and 2HDM+a models; the same is true for samples with high mass compared to low mass. Therefore a future analysis may benefit from having multiple signal regions for different signal models and/or for high and low mass signals. Furthermore, as the mono-Z analysis becomes more sensitive to very high mass signals, it will be essential

to revisit the lepton isolation requirement; high mass signal events can be expected to have a highly boosted pair of leptons very close together in ΔR, and they will fail the standard lepton isolation requirement. Hence a dilepton-based isolation should be used for these types of heavy signals. With regards to 2HDM+a models, some weaknesses are seen in the signal reweighting methods; matrix element reweighting begins to break down at high $\tan\beta$, and histogram reweighting in the $\sin\theta = 0.35$ plane was unsuccessful when used simultaneously with matrix element reweighting. Further studies will be needed to address these issues and avoid the need for additional reconstructed samples. It may also be interesting to revisit the discriminating variable used for mono-Z signals. m_{T}^{ZZ} was found to be an effective variable in the Run 2 analysis, but there may be significant gain if a machine learning technique is used instead. For example, the invisible Higgs search uses a boosted decision tree (BDT) discriminant. Compared to $E_{\mathrm{T}}^{\mathrm{miss}}$, the BDT discriminant provided a 20% improvement in the expected upper limit on the $H \rightarrow$ invisible branching ratio. This method was deemed to be ill-suited for the dark matter signals due to the large number of signal samples that would need to be used to train the BDT. Other machine learning methods, such as parameterized neural networks [95], are capable of interpolating between parameters and may be promising for the mono-Z DM search.

The number of interpretations performed in the mono-Z search may also be extended. The LHC Dark Matter Working Group has recently been focusing on t-channel simplified models, and is working to provide detailed recommendations as was done for s-channel simplified models [85]. As discussed in Appendix A, the Run 2 mono-Z analysis with 139 fb^{-1} is sensitive to a limited mass range, but this could be revisited for Run 3 and/or beyond. The number of interpretations within simplified model and 2HDM+a interpretations can also be extended, for example to include scalar and pseudo-scalar s-channel simplified models. In general the cross sections for these models are many orders of magnitude smaller than for vector and axial-vector models; with a larger dataset these models could be studied in a mono-Z context. For 2HDM+a models, exploring sensitivity at high $\tan\beta$ should be prioritized and signals with varying m_χ should be investigated.

As the LHC continues to be upgraded and take data, direct and indirect detection collaborations will advance their own frontiers as well. For example, the upcoming PICO-500 [96, 97] and LUX-ZEPLIN (LZ) [98] experiments are projected to achieve some of the best upper limits yet on $\sigma_{\mathrm{SD}}(\chi\text{-nucleon})$. Furthermore, at the time of this dissertation, a few anomalous direct and indirect detection results have been observed.

The XENON1T experiment has observed an excess of electron recoil events, providing evidence for solar axion and bosonic dark matter models at around the 3σ level [99], and the Fermi-LAT experiment has observed an excess of γ-rays emitted from the galactic centre [100], which may be explained by dark matter annihilation [101]. In the coming years it will be exciting to see if these signals can be confirmed, while awaiting new results from future collider, direct, and indirect detection searches. The true nature of dark matter has yet to be revealed.

Appendix A

t-channel Simplified Model Signal Studies

t-channel simplified models [32] were initially considered in the mono-Z search. In these models the mediator is a coloured scalar particle and is capable of coupling directly to the Z boson. This is illustrated in Figure A.1.

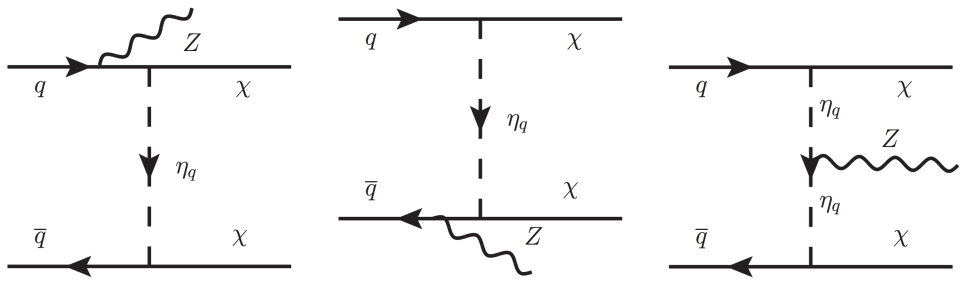

Figure A.1: t-channel Feynman diagrams with the mono-Z signature [32].

Early in the analysis, a study was done to see what kind of exclusion power would be obtainable for mono-Z t-channel signals with the full Run 2 dataset. A small handful of t-channel samples with the mc16a campaign were requested for this purpose. In addition, background estimates in the $E_{\mathrm{T}}^{\mathrm{miss}}$ distribution were available from the 36.1 fb^{-1} analysis [57]. A flat systematic error of 10% was assigned to the new signal $E_{\mathrm{T}}^{\mathrm{miss}}$ distributions, and they were used with the background distributions to run hypothesis tests. Exclusion limits were run to produce CL$_s$ values for 36.1 fb^{-1}. Furthermore, the signal and background $E_{\mathrm{T}}^{\mathrm{miss}}$ histograms were scaled to 140 fb^{-1} (an approximation of the expected Run 2 dataset at the time), and the CL$_s$

Table A.1: Table of CL_s values for t-channel signal samples. The CL_s values for 140 fb^{-1} are obtained using scaled 36 fb^{-1} histograms.

m_{med}	m_χ	CL_s (36 fb^{-1})	CL_s (140 fb^{-1})
50	1	0.094	0.028
55	50	0.144	0.044
300	1	0.812	0.710
300	50	0.809	0.708
500	1	0.908	0.847
550	500	0.982	0.967

values were calculated again. The results are summarized in Table A.1. No samples are excluded with 36 fb^{-1}. With 140 fb^{-1}, the two samples with $m_{med} < 55$ GeV have $CL_s < 0.05$ and so are excluded at the 95% CL. This means that t-channel signals with $m_{med} < \sim$50-100 GeV may be excluded with the full Run 2 dataset. This is a small mass range, and it is dwarfed even by 36.1 fb^{-1} mono-jet limits which extend to mediator masses of over 1.5 TeV [102]. Because of such a small exclusion range, t-channel signals were not studied in the full Run 2 analysis. However, the mediator-Z couplings are unique to the mono-Z signature, and exploring these models in Run 3 should be prioritized.

Appendix B

Simulation Signal Region Distributions

This appendix provides additional simulated signal region distributions to supplement the plots shown in Section 4.4. Figures B.1, B.2, and B.3 illustrate the leading lepton p_{T}, η, and ϕ distributions. p_{T}^{Z} is shown in Figure B.4. The leading jet p_{T} and η distributions are shown in Figures B.5 and B.6, along with the number of jets and b-jets in Figures B.7 and B.8. The distribution of $\Delta\phi(Z, E_{\mathrm{T}}^{\mathrm{miss}})$ is given in Figure B.9.

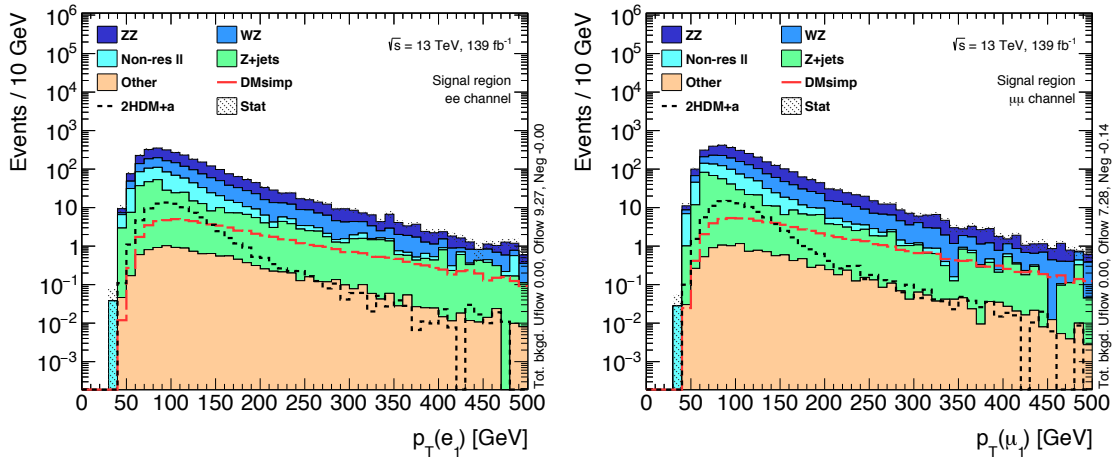

(a) (b)

Figure B.1: Simulated leading lepton p_{T} distributions in the (a) ee and (b) $\mu\mu$ signal regions. The plotted simplified model signal has $m_{\chi} = 1$ GeV, $m_{\mathrm{med}} = 900$ GeV, and the 2HDM+a signal has $\tan\beta = 1.0$, $\sin\theta = 0.7$, $m_{H} = 600$ GeV, $m_{a} = 400$ GeV, $m_{\chi} = 10$ GeV.

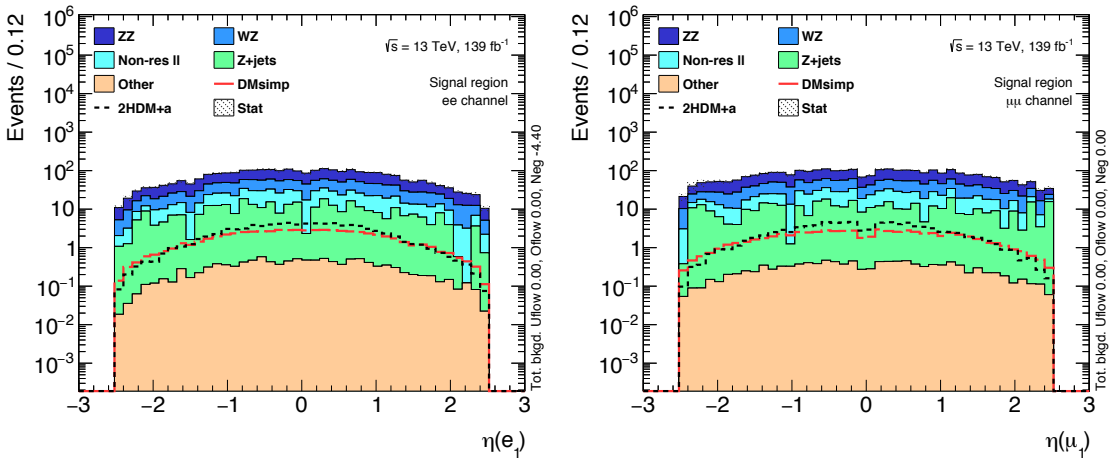

(a) (b)

Figure B.2: Simulated leading lepton η distributions in the (a) ee and (b) $\mu\mu$ signal regions. The plotted simplified model signal has $m_\chi = 1$ GeV, $m_{\text{med}} = 900$ GeV, and the 2HDM+a signal has $\tan\beta = 1.0$, $\sin\theta = 0.7$, $m_H = 600$ GeV, $m_a = 400$ GeV, $m_\chi = 10$ GeV.

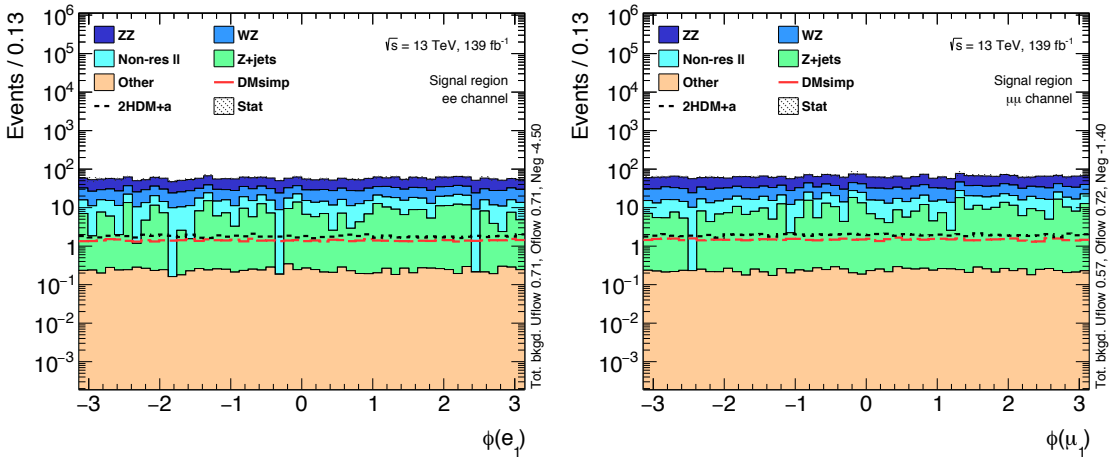

(a) (b)

Figure B.3: Simulated leading lepton ϕ distributions in the (a) ee and (b) $\mu\mu$ signal regions. The plotted simplified model signal has $m_\chi = 1$ GeV, $m_{\text{med}} = 900$ GeV, and the 2HDM+a signal has $\tan\beta = 1.0$, $\sin\theta = 0.7$, $m_H = 600$ GeV, $m_a = 400$ GeV, $m_\chi = 10$ GeV.

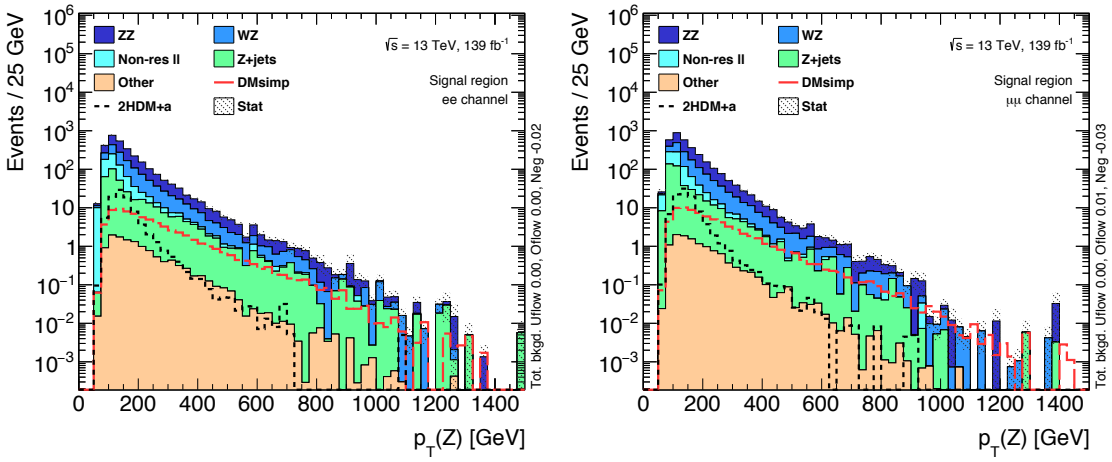

(a) (b)

Figure B.4: Simulated p_{T}^{Z} distributions in the (a) ee and (b) $\mu\mu$ signal regions. The plotted simplified model signal has $m_{\chi} = 1$ GeV, $m_{\mathrm{med}} = 900$ GeV, and the 2HDM+a signal has $\tan\beta = 1.0$, $\sin\theta = 0.7$, $m_{H} = 600$ GeV, $m_{a} = 400$ GeV, $m_{\chi} = 10$ GeV.

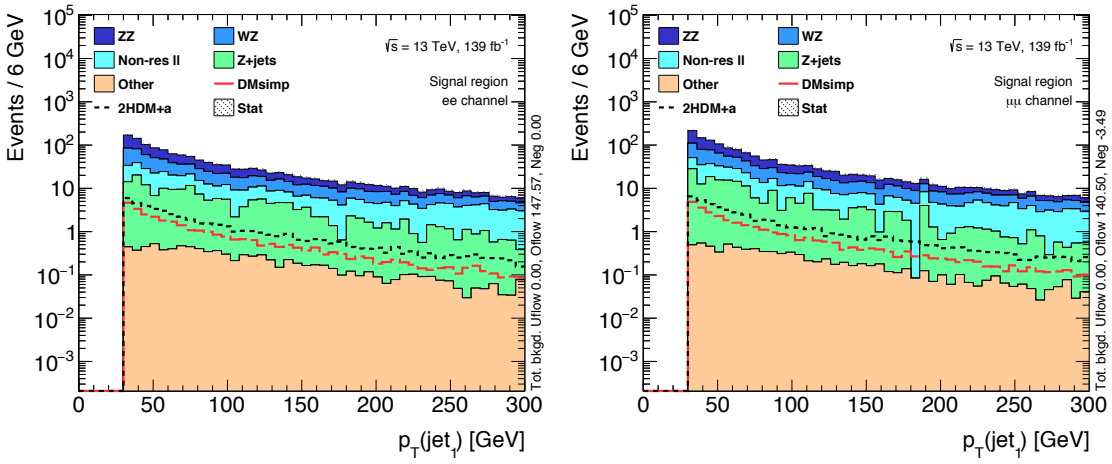

(a) (b)

Figure B.5: Simulated leading jet p_{T} distributions in the (a) ee and (b) $\mu\mu$ signal regions. The plotted simplified model signal has $m_{\chi} = 1$ GeV, $m_{\mathrm{med}} = 900$ GeV, and the 2HDM+a signal has $\tan\beta = 1.0$, $\sin\theta = 0.7$, $m_{H} = 600$ GeV, $m_{a} = 400$ GeV, $m_{\chi} = 10$ GeV.

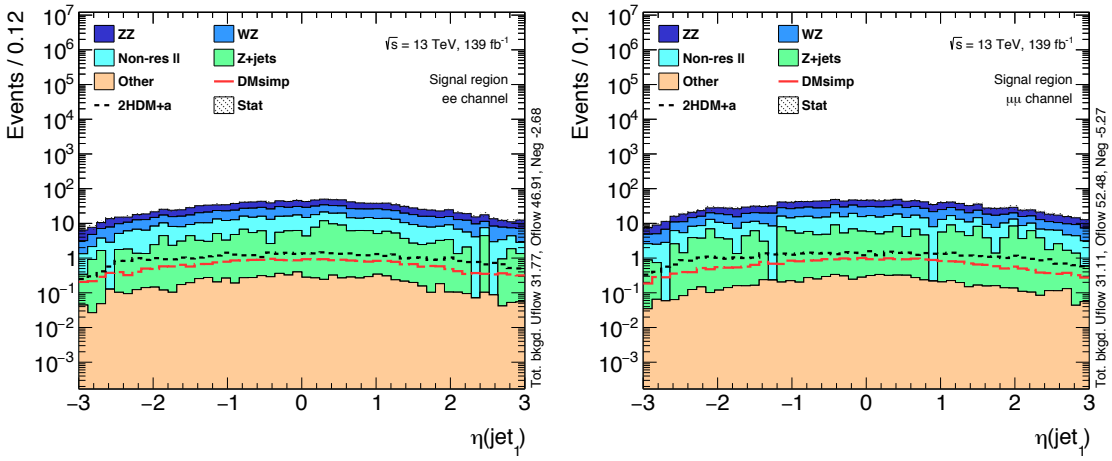

(a) (b)

Figure B.6: Simulated leading jet η distributions in the (a) ee and (b) $\mu\mu$ signal regions. The plotted simplified model signal has $m_\chi = 1$ GeV, $m_{\text{med}} = 900$ GeV, and the 2HDM+a signal has $\tan\beta = 1.0$, $\sin\theta = 0.7$, $m_H = 600$ GeV, $m_a = 400$ GeV, $m_\chi = 10$ GeV.

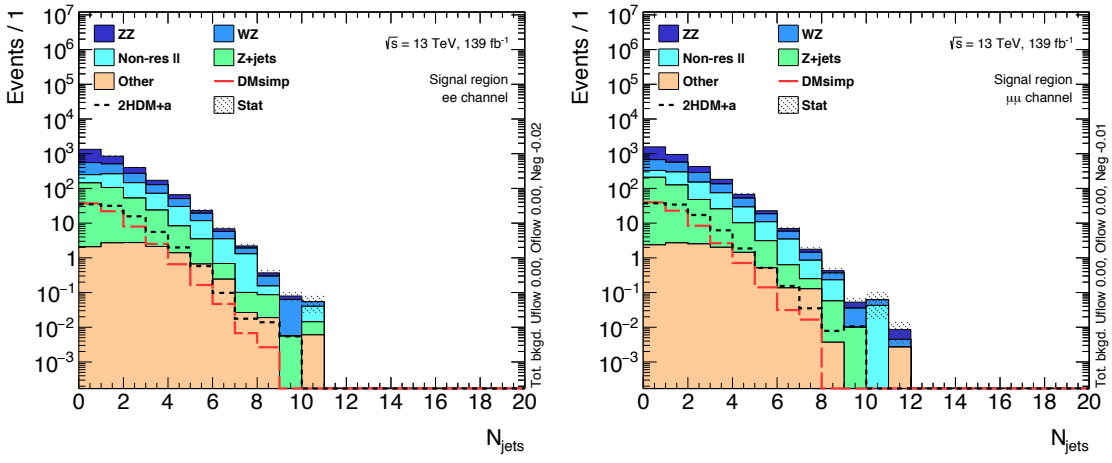

(a) (b)

Figure B.7: Simulated N_{jets} distributions in the (a) ee and (b) $\mu\mu$ signal regions. The plotted simplified model signal has $m_\chi = 1$ GeV, $m_{\text{med}} = 900$ GeV, and the 2HDM+a signal has $\tan\beta = 1.0$, $\sin\theta = 0.7$, $m_H = 600$ GeV, $m_a = 400$ GeV, $m_\chi = 10$ GeV.

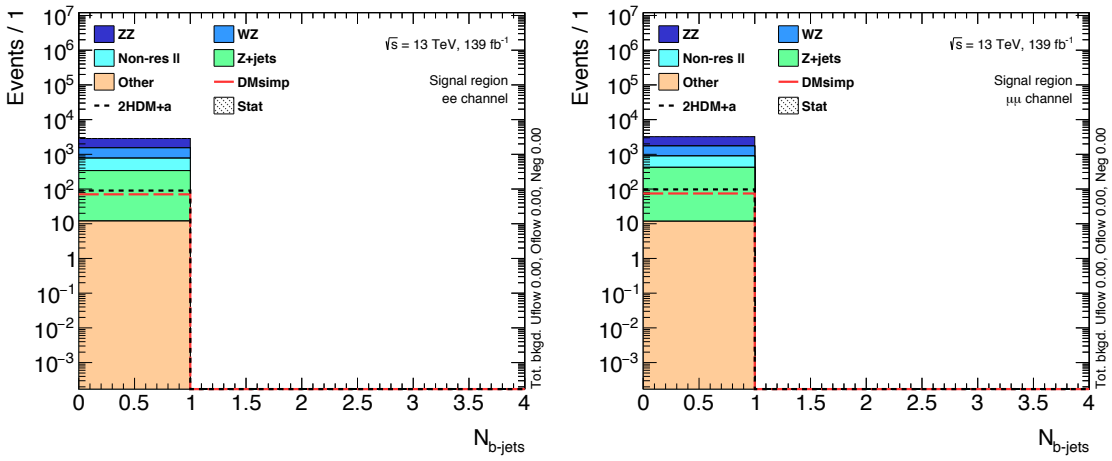

(a) (b)

Figure B.8: Simulated $N_{b\text{-jets}}$ distributions in the (a) ee and (b) $\mu\mu$ signal regions. The plotted simplified model signal has $m_\chi = 1$ GeV, $m_{\text{med}} = 900$ GeV, and the 2HDM+a signal has $\tan\beta = 1.0$, $\sin\theta = 0.7$, $m_H = 600$ GeV, $m_a = 400$ GeV, $m_\chi = 10$ GeV.

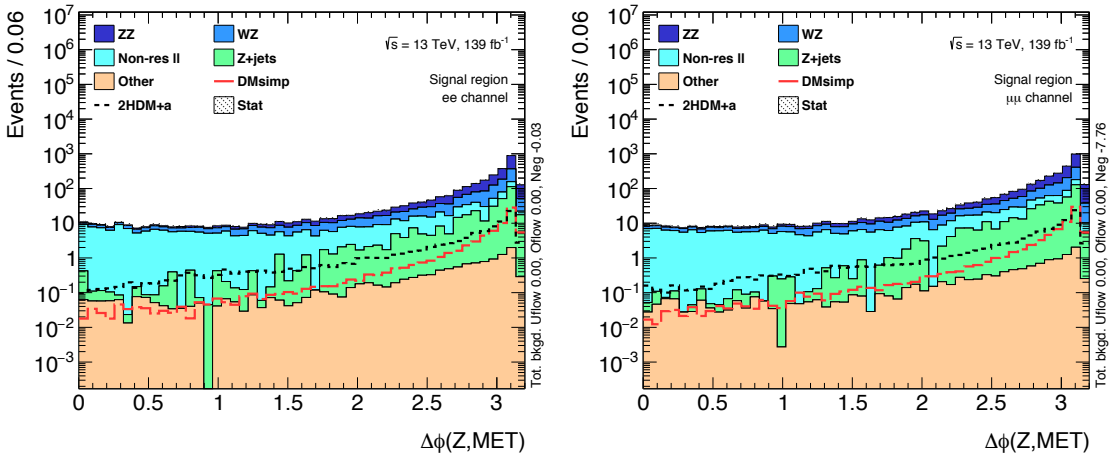

(a) (b)

Figure B.9: Simulated $\Delta\phi(Z, E_{\text{T}}^{\text{miss}})$ distributions in the (a) ee and (b) $\mu\mu$ signal regions. The plotted simplified model signal has $m_\chi = 1$ GeV, $m_{\text{med}} = 900$ GeV, and the 2HDM+a signal has $\tan\beta = 1.0$, $\sin\theta = 0.7$, $m_H = 600$ GeV, $m_a = 400$ GeV, $m_\chi = 10$ GeV.

Appendix C

Signal Systematic Uncertainties

Signal systematics are discussed in Section 5.2.2. This appendix contains figures illustrating the experimental and theoretical uncertainties on the signal. Figure C.1 shows the experimental systematic error for 2HDM+a samples. Figures C.2 and C.3 summarize the intra-PDF theory uncertainties for all reconstructed signals. Figures C.4 and C.5 summarize the inter-PDF theory uncertainties. Figures C.6 and C.7 summarize the QCD scale theory uncertainties. Parton shower systematics for a selection of signal samples are given in Tables C.1 and C.2.[1]

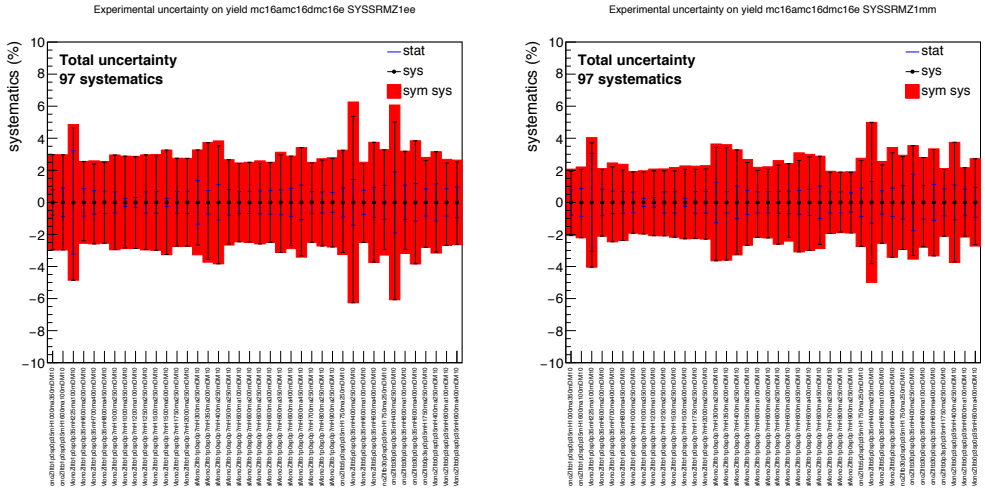

(a) ee channel. (b) $\mu\mu$ channel.

Figure C.1: Experimental systematic uncertainties on the total signal region event yield for 2HDM+a signal samples.

[1]Note that the parton shower fluctuations observed are significant, as the statistical uncertainties on the signal acceptance are only about 3% per variation.

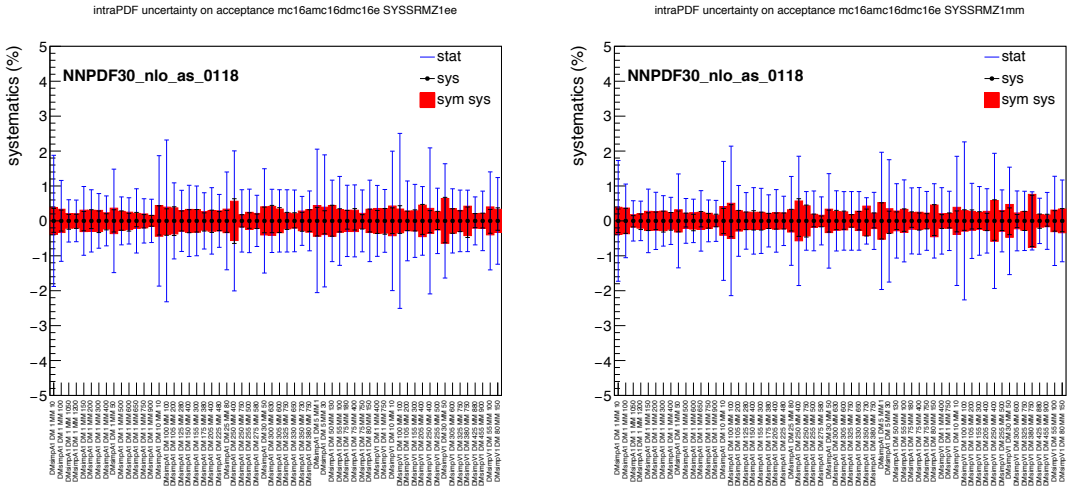

(a) ee channel. (b) $\mu\mu$ channel.

Figure C.2: Intra-PDF systematic uncertainties on the total signal acceptance for simplified model signal samples.

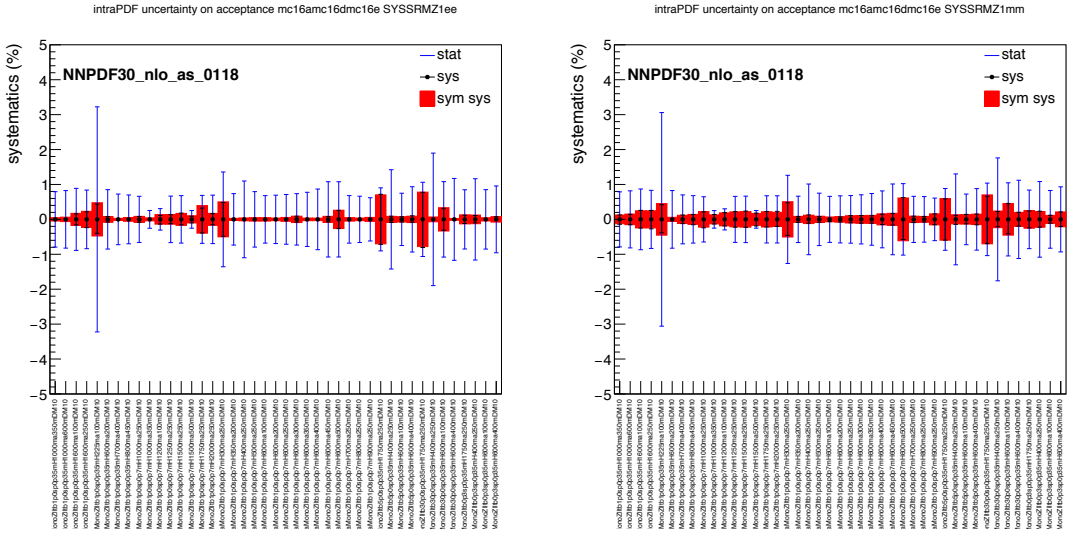

(a) ee channel. (b) $\mu\mu$ channel.

Figure C.3: Intra-PDF systematic uncertainties on the total signal acceptance for 2HDM+a model signal samples.

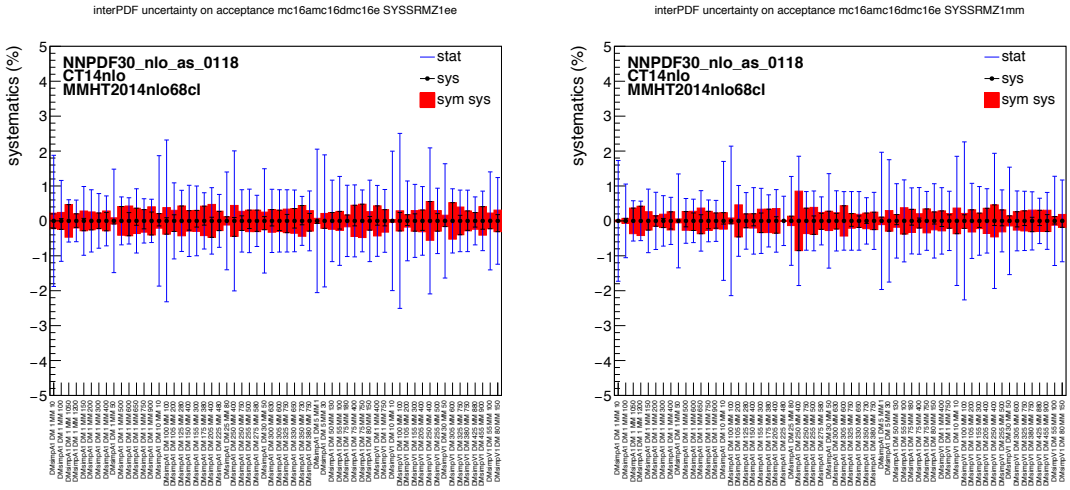

(a) ee channel. (b) $\mu\mu$ channel.

Figure C.4: Inter-PDF systematic uncertainties on the total signal acceptance for simplified model signal samples.

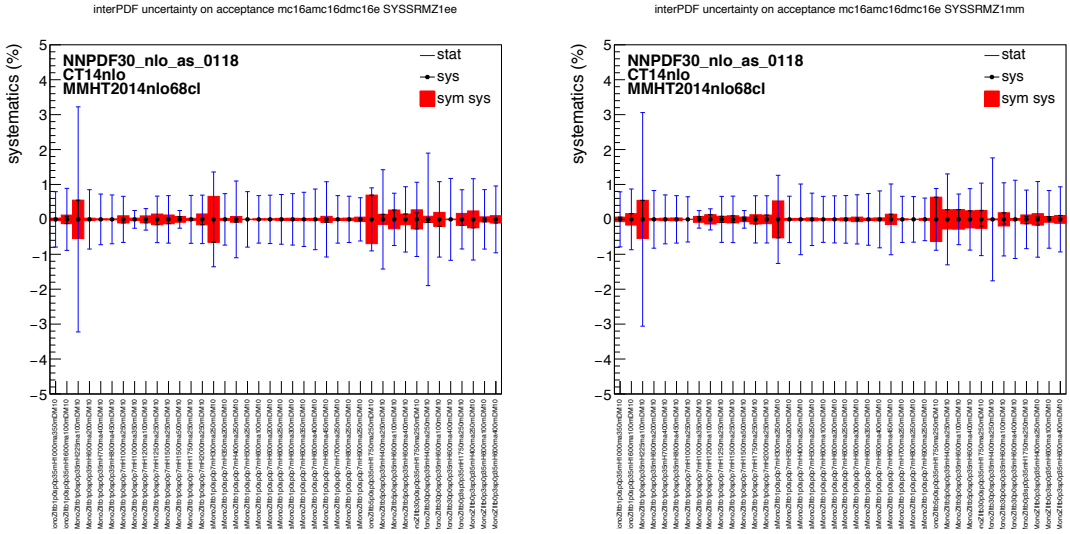

(a) ee channel. (b) $\mu\mu$ channel.

Figure C.5: Inter-PDF systematic uncertainties on the total signal acceptance for 2HDM+a model signal samples.

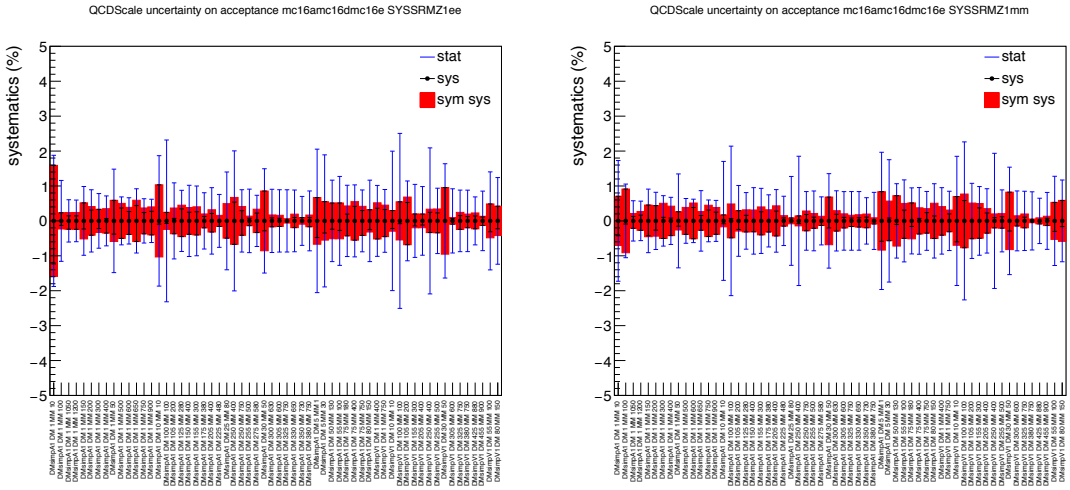

(a) ee channel. (b) $\mu\mu$ channel.

Figure C.6: QCD scale systematic uncertainties on the total signal acceptance for simplified model signal samples.

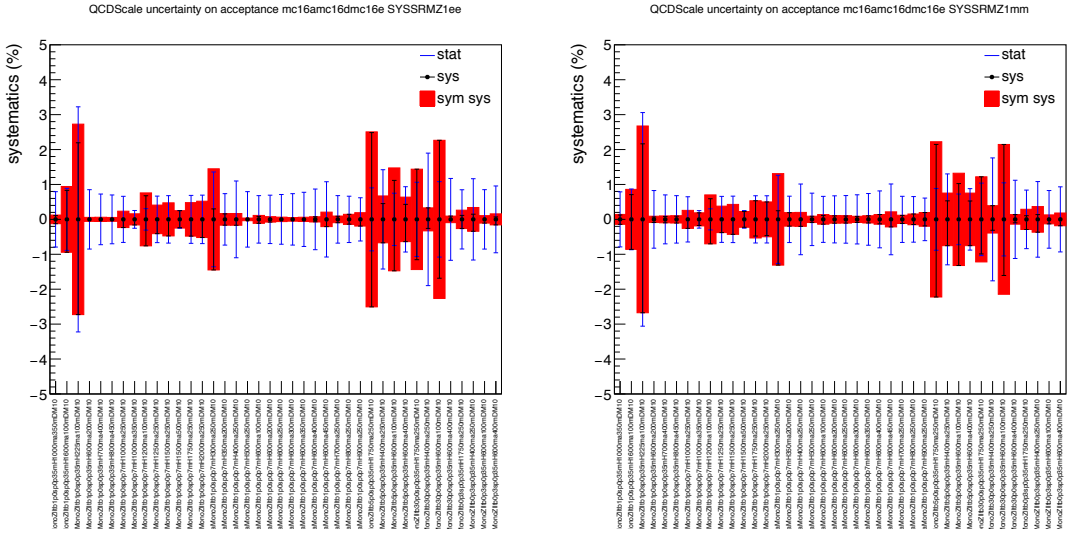

(a) ee channel. (b) $\mu\mu$ channel.

Figure C.7: QCD scale systematic uncertainties on the total signal acceptance for 2HDM+a model signal samples.

Table C.1: Parton shower systematic uncertainties on the total signal acceptance for simplified model signal samples.

m_{med} (GeV)	m_χ (GeV)	Total error (%)	
		ee	$\mu\mu$
10	1	(−0.4,+8.9)	(−10.2,+1.8)
50	1	(−3.0,+3.9)	(−4.2,+1.9)
150	1	(−2.7,+3.7)	(−3.5,+4.2)
	80	(−1.2,+1.6)	(−1.7,+2.5)
200	105	(−2.9,+1.7)	(−0.6,+3.0)
400	1	(−1.8,+1.1)	(−1.2,+1.9)
	75	(−0.6,+2.0)	(−0.1,+3.2)
	150	(−1.9,+2.2)	(−2.3,+1.5)
600	1	(−1.6,+1.6)	(−2.8,+1.9)
750	75	(−1.5,+1.3)	(−1.8,+0.5)
	250	(−1.5,+1.0)	(−0.7,+3.3)
	380	(−1.7,+2.2)	(−2.4,+1.5)
900	1	(−3.4,+1.1)	(−1.9,+2.2)
1200	1	(−1.4,+3.9)	(−2.9,+3.3)

Table C.2: Parton shower systematic uncertainties on the total signal acceptance for 2HDM+a signal samples.

m_H (GeV)	m_a (GeV)	$\tan\beta$	$\sin\theta$	Total error (%)	
				ee	$\mu\mu$
600	200	1.0	0.7	(−0.3, +6.9)	(−5.2, +0.4)
	300	1.0	0.35	(−6.3, +2.2)	(−5.9, +2.6)
		1.0	0.7	(−3.8, +1.0)	(−2.4, +1.0)
1000	250	1.0	0.35	(−3.8, +1.2)	(−1.4, +2.0)
		1.0	0.7	(−3.3, +0.6)	(−4.8, +2.9)
		20.0	0.7	(−10.6, +7.7)	(−15.8, +0.9)
	350	1.0	0.35	(−4.2, +0.8)	(−2.5, +2.8)
		1.0	0.7	(−4.4, +1.1)	(−1.6, +4.1)

Appendix D

Emulation Validation Results

D.1 Simplified model emulation

Simplified model emulation is discussed in Seciton 5.2.3. For this model, the emulation relies on the signal acceptance and kinematics being constant as a function of m_χ for fixed m_{med} in the on-shell region. In Figure D.1, the acceptance is shown for samples with $m_{\text{med}} = 400$ GeV (red) and $m_{\text{med}} = 750$ GeV (blue). For various m_χ the acceptance is constant.

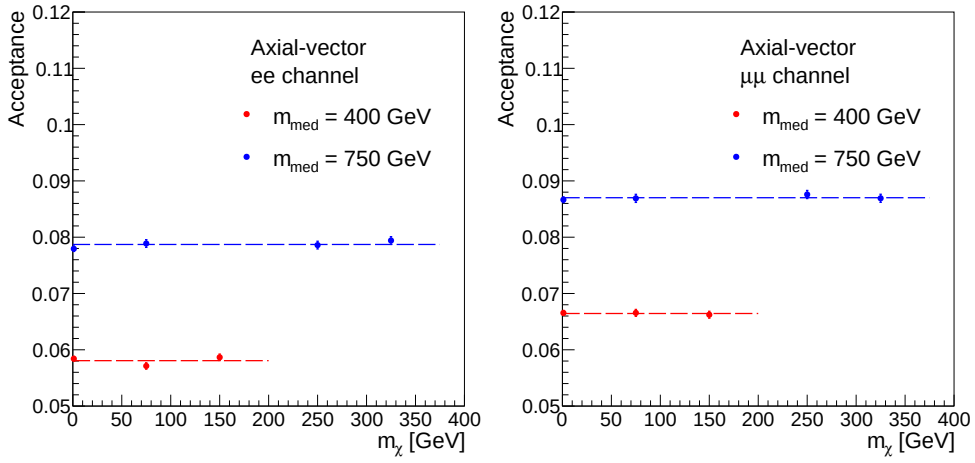

(a) ee channel. (b) $\mu\mu$ channel.

Figure D.1: Signal acceptance for axial-vector samples with $m_{\text{med}} = 400$ GeV (red) and $m_{\text{med}} = 750$ GeV (blue).

Figures D.2 and D.3 show the $E_{\text{T}}^{\text{miss}}$ shape (normalized to unit area) for samples with $m_{\text{med}} = 400$ GeV and $m_{\text{med}} = 750$ GeV respectively. This illustrates that the

kinematics do not change for fixed m_{med} in the on-shell region. The same is true for vector samples as shown in Figure D.4 for $m_{\text{med}} = 750$ GeV. In addition, the comparison of Figure D.4 to Figure D.3 illustrates that the kinematics are similar between axial-vector and vector samples with the same m_{med}.

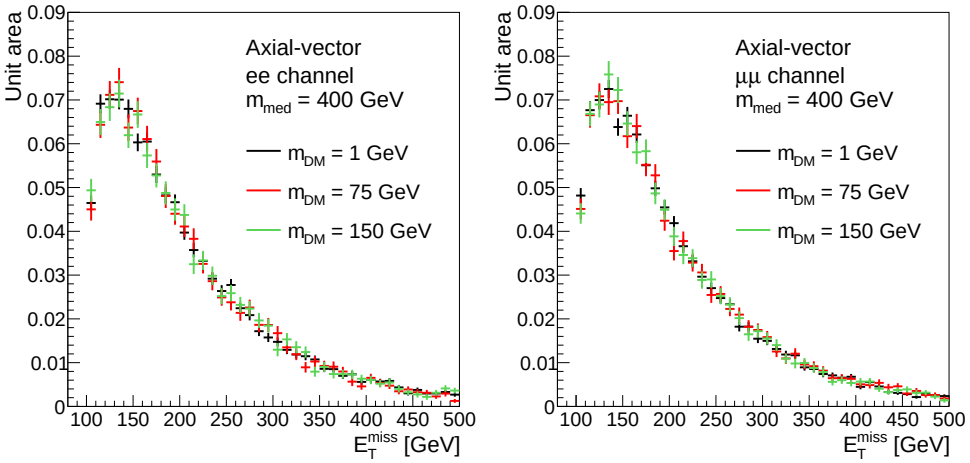

(a) ee channel. (b) $\mu\mu$ channel.

Figure D.2: $E_{\text{T}}^{\text{miss}}$ shape for axial-vector samples with $m_{\text{med}} = 400$ GeV.

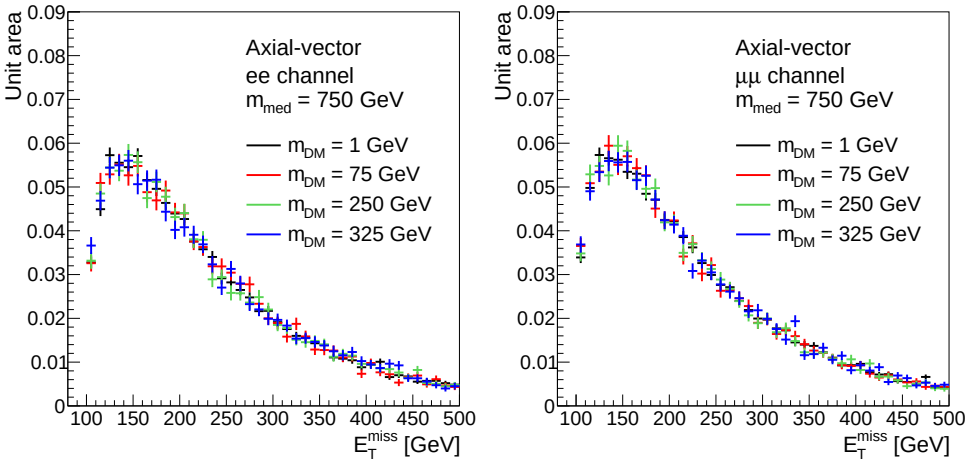

(a) ee channel. (b) $\mu\mu$ channel.

Figure D.3: $E_{\text{T}}^{\text{miss}}$ shape for axial-vector samples with $m_{\text{med}} = 750$ GeV.

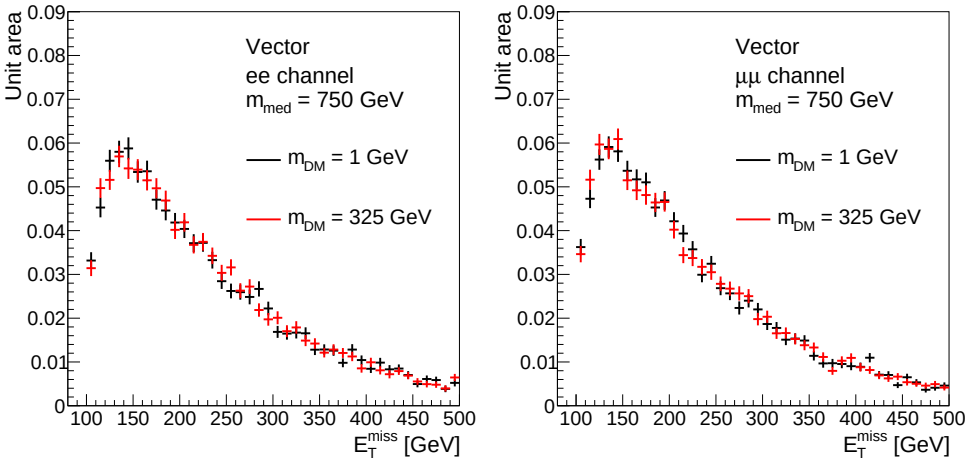

(a) ee channel. (b) $\mu\mu$ channel.

Figure D.4: $E_{\mathrm{T}}^{\mathrm{miss}}$ shape for vector samples with $m_{\mathrm{med}} = 750$ GeV.

D.2 2HDM+a matrix element reweighting

2HDM+a matrix element reweighting is discussed in Section 5.2.3. Additional parameter grids are shown here. Figure D.5 shows the grid of reconstructed and reweighted samples used for the $\tan\beta$ vs m_a scans with $\sin\theta = 0.7$ and 0.35. Similarly Figure D.6 illustrates the 1D $\sin\theta$ scans for samples with $(m_a,\, m_A) = (200,\, 600)$ GeV and $(350,\, 1000)$ GeV.

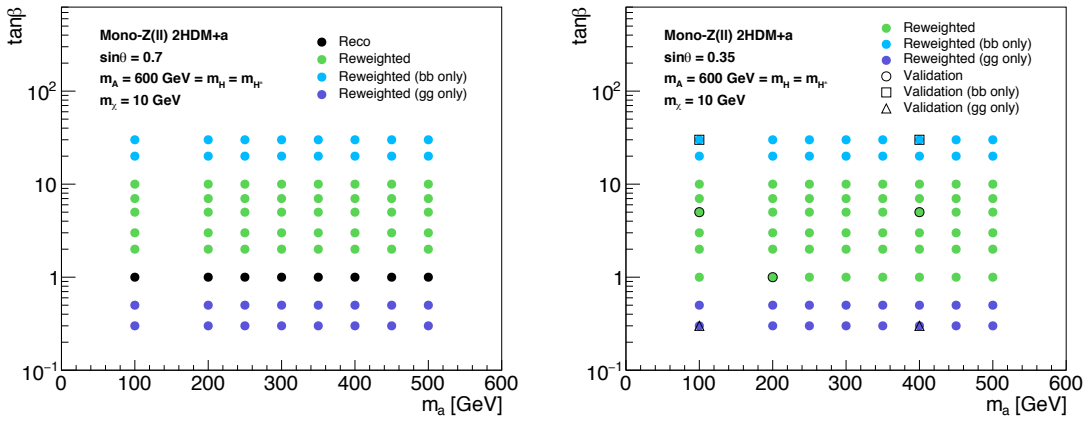

(a) $\sin\theta = 0.7$. (b) $\sin\theta = 0.35$

Figure D.5: Grid of $\tan\beta$ vs m_a values for reconstructed and reweighted 2HDM+a signal samples. Sample points are shown for $m_A = 600$ GeV.

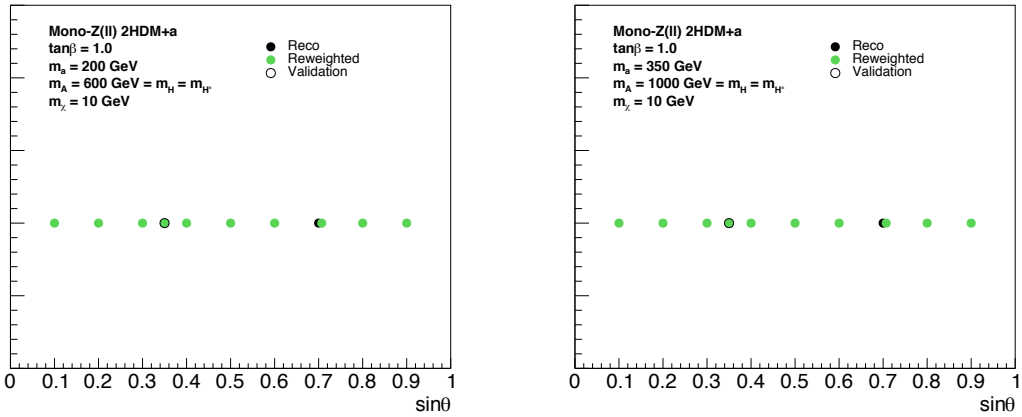

(a) $m_a = 200$ GeV, $m_A = 600$ GeV. (b) $m_a = 350$ GeV, $m_A = 1000$ GeV.

Figure D.6: Grid of $\sin\theta$ values for reconstructed and reweighted 2HDM+a signal samples.

The validation of the method is observed to work well for most validation samples. This is illustrated in Figure D.7, which shows the ratio of the normalizations between reweighted and validation distributions. Most samples show a ratio close to 1, with a standard deviation of about 4%. There are a few outliers that do not perform as well. For example, the most significant issue is seen when reweighting from ($\tan\beta$, $\sin\theta$) = (1.0, 0.7) to (30, 0.35) for the sample with $m_A = 600$ GeV, $m_a = 100$ GeV. The validation plots are shown in Figure D.8. The normalization for the reweighted sample is 12-15% too large. This outlier motivates the 15% non-closure systematic for reweighted samples with $\tan\beta \geq 20$ and $\sin\theta = 0.35$.

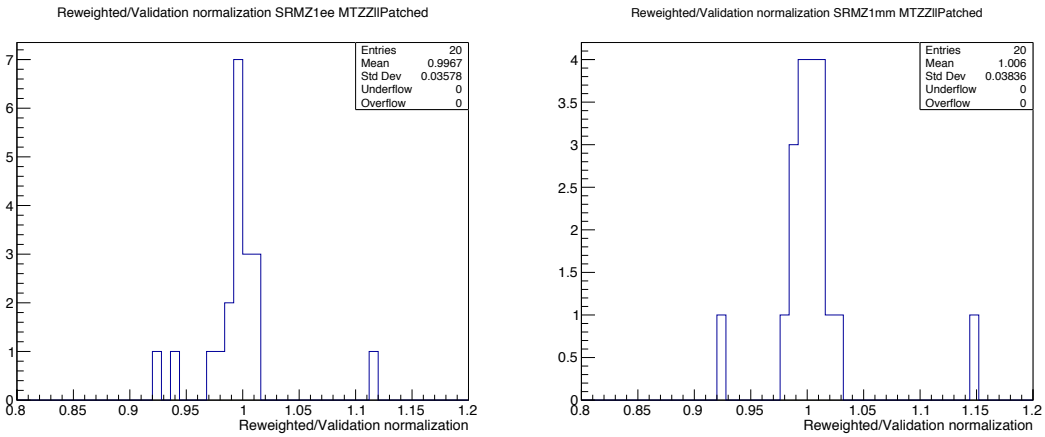

(a) ee channel. (b) $\mu\mu$ channel.

Figure D.7: Ratio of normalizations between 2HDM+a matrix element reweighted samples and validation samples.

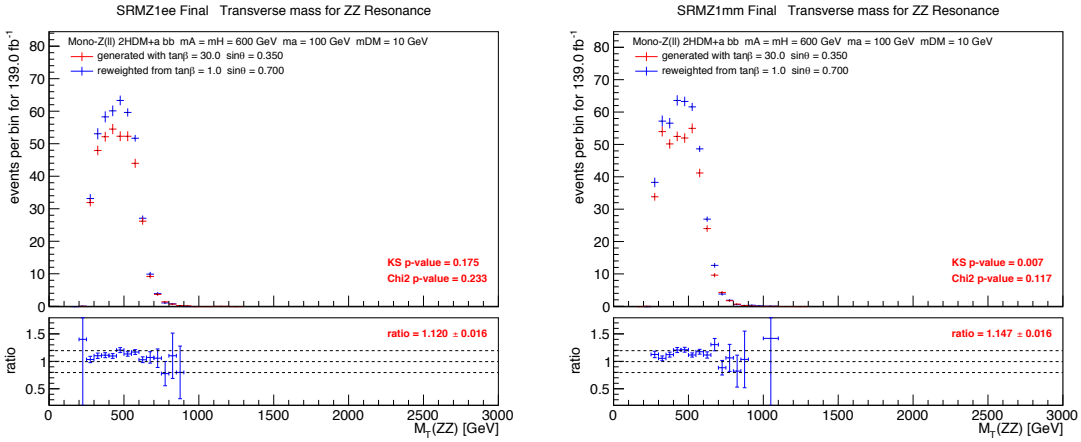

(a) ee channel. (b) $\mu\mu$ channel.

Figure D.8: Matrix element reweighting non-closure in the m_{T}^{ZZ} distribution. Results are shown for a 2HDM+a signal sample with $m_A = 600$ GeV and $m_a = 100$ GeV. The red histogram is the m_{T}^{ZZ} from a reconstructed sample generated with $\sin\theta = 0.35$ and $\tan\beta = 30$. The blue histogram is the m_{T}^{ZZ} produced using matrix element reweighting from a reconstructed sample with $\sin\theta = 0.7$ and $\tan\beta = 1.0$.

D.3 2HDM+a histogram reweighting

2HDM+a histogram reweighting is discussed in Section 5.2.3. The method works well in the $\sin\theta = 0.7$ plane after a global correction to the normalization is applied. Figure D.9 shows the ratio of normalizations for reweighted and validation samples after the

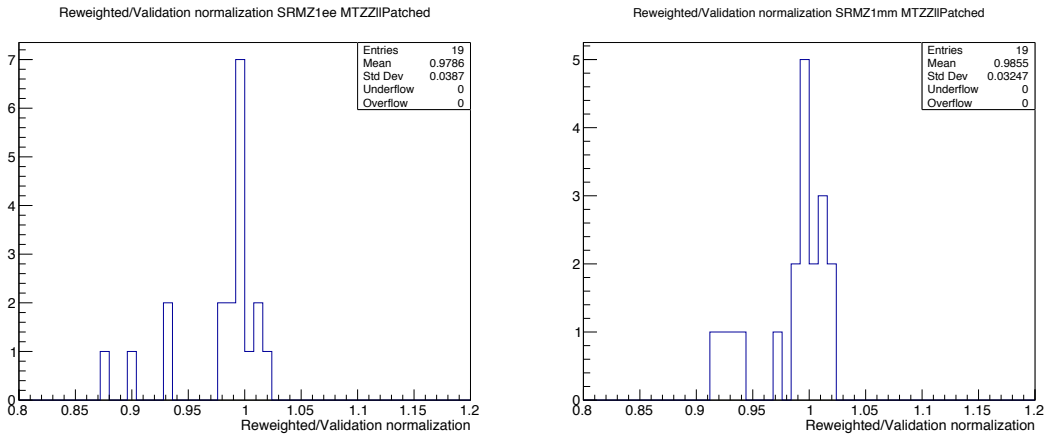

(a) ee channel. (b) $\mu\mu$ channel.

Figure D.9: Ratio of normalizations between 2HDM+a histogram reweighted samples and validation samples.

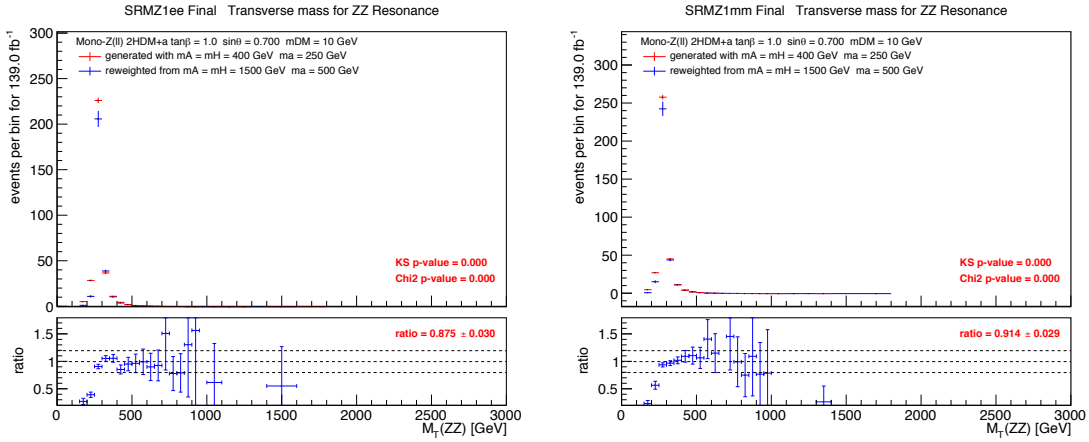

(a) ee channel. (b) $\mu\mu$ channel.

Figure D.10: Histogram reweighting non-closure in the m_{T}^{ZZ} distribution. Results are shown for a 2HDM+a signal sample with $\tan\beta = 1.0$ and $\sin\theta = 0.7$. The red histogram is the m_{T}^{ZZ} from a reconstructed sample generated with $m_A = 400$ GeV and $m_a = 250$ GeV. The blue histogram is the m_{T}^{ZZ} produced using histogram reweighting from a reconstructed sample with $m_A = 1500$ GeV and $m_a = 500$ GeV.

correction. Most reweighted samples are within 4% of the predicted normalization. A few outliers are seen, however. Figure D.10 illustrates the worst case observed, where the overall normalization in the ee channel is off by about 12%. The largest outliers all have $m_a \leq 400$ GeV, so a non-closure systematic of 15% is assigned for any histogram reweighted sample with $\sin\theta = 0.7$, $\tan\beta = 1.0$, and $m_a \leq 400$ GeV.

Appendix E

Supplementary Information for Z+jets Background Estimate Using γ+jets Reweighting

E.1 Estimate using $E_{\mathrm{T}}^{\mathrm{miss}}$

The γ+jets reweighting method used to estimate the Z+jets m_{T}^{ZZ} distribution is described in Chapter 6. This appendix summarizes the method used to estimate the $E_{\mathrm{T}}^{\mathrm{miss}}$ distribution. This is useful if $E_{\mathrm{T}}^{\mathrm{miss}}$ is to be used as the discriminant variable.

Table E.1: List of signal region and γ+jets control region selections for $E_{\mathrm{T}}^{\mathrm{miss}}$ estimate.

Signal region	γ+jets control region
2 same flavour leptons	Lepton veto
Third lepton veto	
2 opposite sign leptons	
$76 < m_{\ell\ell} < 106$ GeV	1 photon
$\Delta R_{\ell\ell} < 1.8$	
b-jet veto	
—	$\times w_1$ $\times w_2$
$E_{\mathrm{T}}^{\mathrm{miss}} > 90$ GeV	
$\mathcal{S} > 9$	

Table E.1 lists the signal region and γ+jets control region definitions. For the $E_{\mathrm{T}}^{\mathrm{miss}}$ discriminant, w_1 and w_2 are both applied after the b-jet veto. As for the m_{T}^{ZZ} estimate, $w_1 = w_1(p_{\mathrm{T}}, \Sigma E_{\mathrm{T}})$. $E_{\mathrm{T}}^{\mathrm{miss}}$ and $\mathcal{S}$ are used in w_2, as the m_{T}^{ZZ} distribution

is not of interest for the $E_{\mathrm{T}}^{\mathrm{miss}}$ estimate. Therefore $w_2 = w_2(E_{\mathrm{T}}^{\mathrm{miss}}, \mathcal{S})$, or defined explicitly:

$$w_2(E_{\mathrm{T}}^{\mathrm{miss}}, \mathcal{S}) = \frac{Z\text{+jets}_{\mathrm{MC}}(E_{\mathrm{T}}^{\mathrm{miss}}, \mathcal{S})}{\gamma\text{+jets}_{\mathrm{MC}}(E_{\mathrm{T}}^{\mathrm{miss}}, \mathcal{S})} \tag{E.1}$$

Therefore the total event weight is

$$w(p_{\mathrm{T}}, \Sigma E_{\mathrm{T}}, E_{\mathrm{T}}^{\mathrm{miss}}, \mathcal{S}) = w_1(p_{\mathrm{T}}, \Sigma E_{\mathrm{T}}) \times w_2(E_{\mathrm{T}}^{\mathrm{miss}}, \mathcal{S}). \tag{E.2}$$

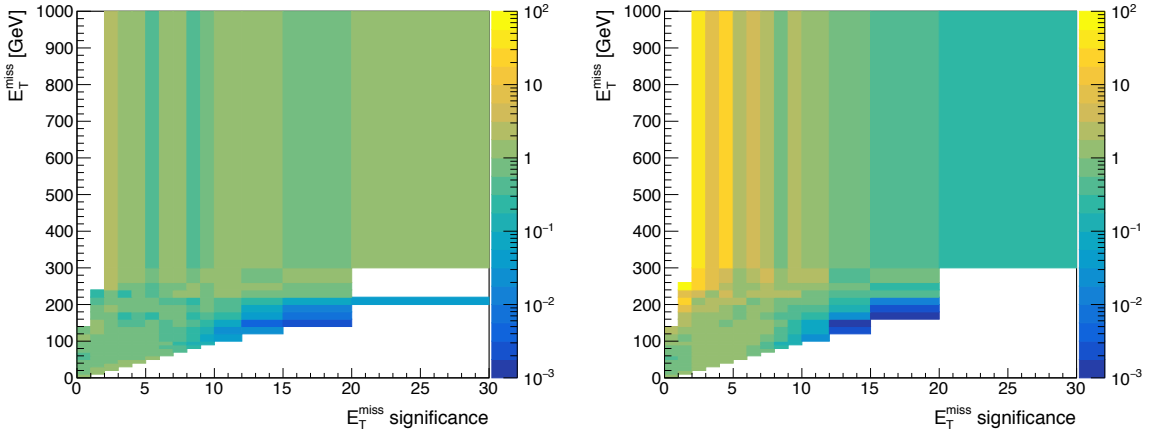

(a) (b)

Figure E.1: Distribution of $w_2(E_{\mathrm{T}}^{\mathrm{miss}}, \mathcal{S})$ for the (a) ee and (b) $\mu\mu$ channel. The z-axis illustrates the weight value in each bin.

w_1 is identical as for the m_{T}^{ZZ} estimate, and is shown in Figure 6.1. w_2 is shown here in Figure E.1. As for the m_{T}^{ZZ} estimate, the method is validated using simulated samples. Figure E.2 illustrates the agreement between reweighted γ+jets events and Z+jets events in the $E_{\mathrm{T}}^{\mathrm{miss}}$ distribution after all selections. The Z+jets and γ+jets yields agree within statistical errors. Now the weights may be applied to data.

Figure E.3 shows the $E_{\mathrm{T}}^{\mathrm{miss}}$ data/MC agreement in the γ+jets control region without reweighting. As for m_{T}^{ZZ}, $\gamma+V$ processes become dominant at intermediate and high $E_{\mathrm{T}}^{\mathrm{miss}}$.

The $E_{\mathrm{T}}^{\mathrm{miss}}$ distribution in data after reweighting is shown in Figure E.4, and the corresponding yields for data and simulation are presented in Table E.2. The total yield in data is in agreement with Z+jets and γ+jets simulation.

The systematic errors on the $E_{\mathrm{T}}^{\mathrm{miss}}$ estimate are calculated in the same way as for m_{T}^{ZZ}. Tables E.3, E.4, E.5, E.6, E.7, and E.8 summarize the binned systematic

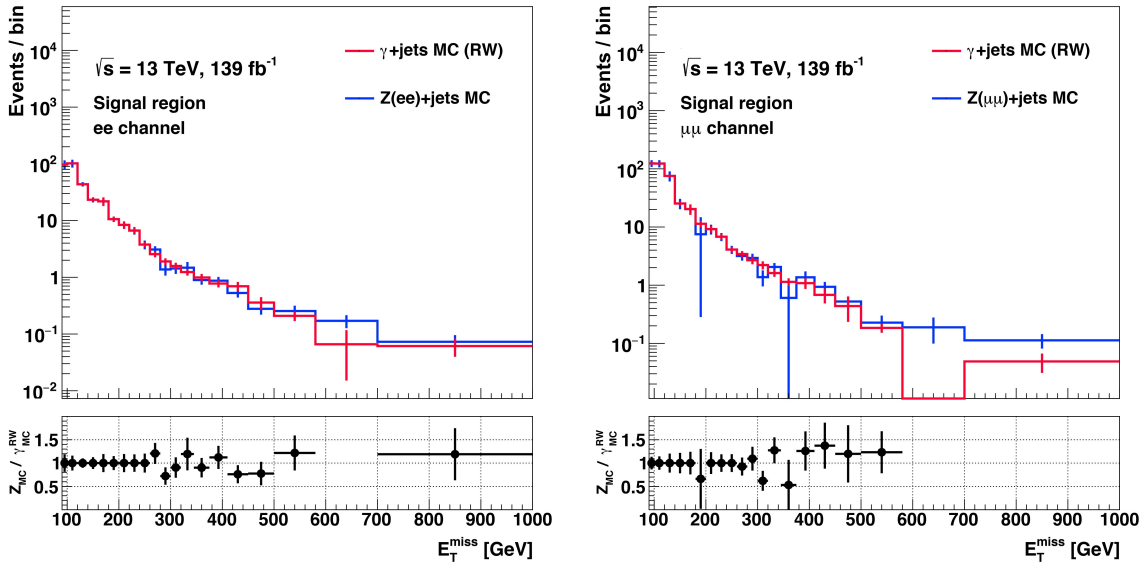

(a) (b)

Figure E.2: $E_{\mathrm{T}}^{\mathrm{miss}}$ from simulation after applying w_1 and w_2, with all cuts applied, in the (a) ee and (b) $\mu\mu$ channel. Error bars shown are statistical.

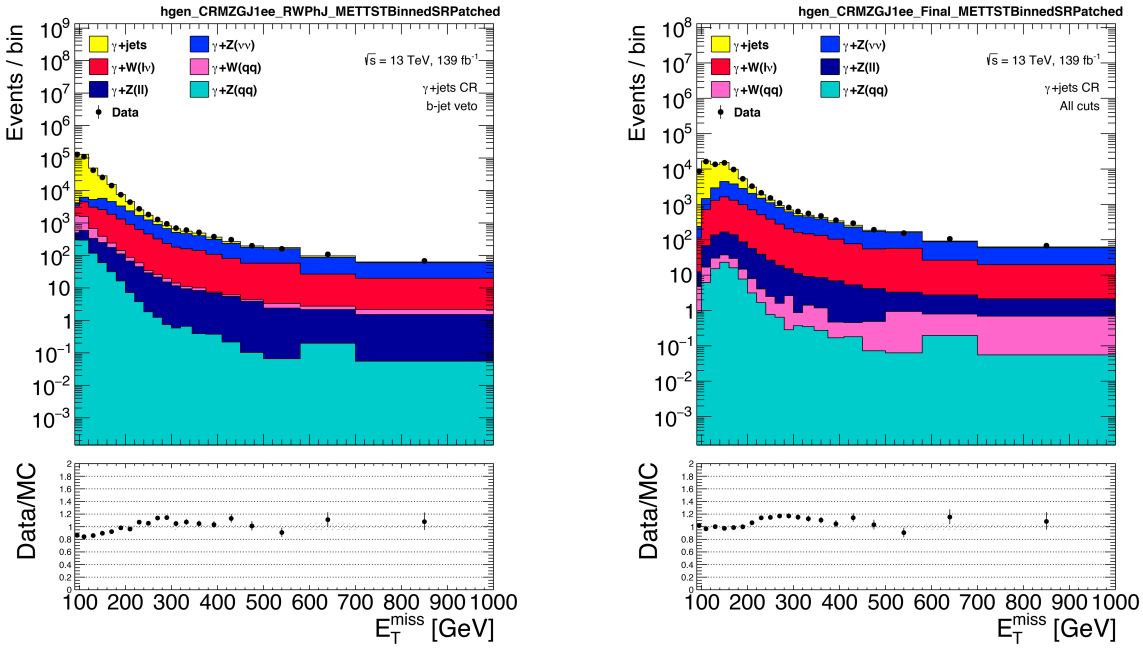

(a) (b)

Figure E.3: $E_{\mathrm{T}}^{\mathrm{miss}}$ above 90 GeV in the γ+jets control region (a) after the b-jet veto and (b) after all selection requirements.

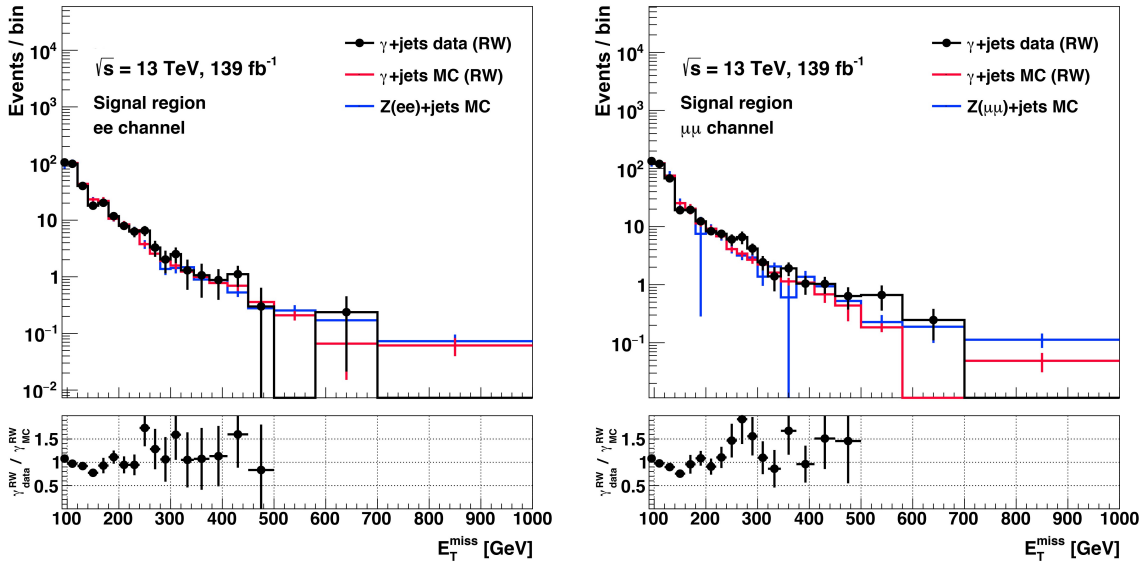

(a) (b)

Figure E.4: $E_{\mathrm{T}}^{\mathrm{miss}}$ estimate from γ+jets data compared to simulation in the (a) ee and (b) $\mu\mu$ signal regions. Error bars shown are statistical.

Table E.2: Signal region estimates from reweighted γ+jets data compared to Z+jets and reweighted γ+jets simulation for 139 fb^{-1}. The errors quoted are statistical.

Channel	Z+jets MC	γ+jets MC	γ+jets data
ee	328 ± 25	328 ± 6	327 ± 4
$\mu\mu$	410 ± 30	414 ± 8	415 ± 4

errors for each source of uncertainty in the method. Figure E.5 shows the $E_{\mathrm{T}}^{\mathrm{miss}}$ distribution in the γ+$W(\ell\nu)$ control region used to estimate the γ+V subtraction systematic. Figure E.6 shows the statistical error on $w_2(E_{\mathrm{T}}^{\mathrm{miss}}, \mathcal{S})$ which are relevant for the systematic error due to statistical fluctuations in the weights. Overall the systematic errors are similar to the errors on the m_{T}^{ZZ} estimate.

Table E.3: Non-closure systematic on the $E_{\mathrm{T}}^{\mathrm{miss}}$ estimate for the first six bins above 260 GeV. The total unbinned error is calculated using all $E_{\mathrm{T}}^{\mathrm{miss}}$ bins.

Channel	$E_{\mathrm{T}}^{\mathrm{miss}}$ (GeV)						Total
	[260,280]	[280,300]	[300,320]	[320,345]	[345,375]	[375,410]	
ee	17.1%	32.2%	10.1%	17.7%	10.3%	11.5%	2.1%
$\mu\mu$	8.0%	8.6%	61.4%	21.5%	88.5%	20.6%	7.8%

Table E.4: γ+V subtraction systematic on the $E_{\mathrm{T}}^{\mathrm{miss}}$ estimate. The total unbinned error is calculated assuming uncorrelated bins.

Channel	$E_{\mathrm{T}}^{\mathrm{miss}}$ (GeV)						Total
	[90,100]	[100,120]	[120,140]	[140,160]	[160,180]	[180,200]	
ee	0.5%	0.6%	1.6%	1.8%	3.9%	3.1%	1.7%
$\mu\mu$	0.5%	0.6%	1.3%	1.7%	3.8%	3.1%	1.1%

Table E.5: Systematic error on the $E_{\mathrm{T}}^{\mathrm{miss}}$ estimate due to statistical fluctuations in the weights. The total unbinned error is calculated using all $E_{\mathrm{T}}^{\mathrm{miss}}$ bins.

Channel	$E_{\mathrm{T}}^{\mathrm{miss}}$ (GeV)						Total
	[90,100]	[100,120]	[120,140]	[140,160]	[160,180]	[180,200]	
ee	17.7%	17.5%	10.4%	13.5%	32.6%	19.7%	6.7%
$\mu\mu$	12.7%	18.6%	20.1%	20.9%	36.6%	21.1%	7.7%

Table E.6: Systematic error on the $E_{\mathrm{T}}^{\mathrm{miss}}$ estimate due to mis-modelling in the weights. The total unbinned error is calculated using all $E_{\mathrm{T}}^{\mathrm{miss}}$ bins.

Channel	$E_{\mathrm{T}}^{\mathrm{miss}}$ (GeV)						Total
	[90,100]	[100,120]	[120,140]	[140,160]	[160,180]	[180,200]	
ee	2.9%	1.1%	1.0%	3.9%	17.5%	24.1%	1.0%
$\mu\mu$	4.8%	2.7%	2.5%	2.8%	22.1%	11.4%	2.3%

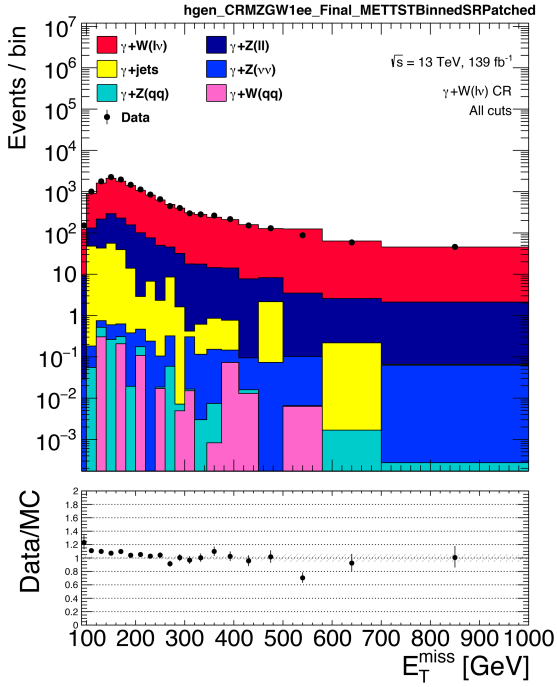

Figure E.5: $E_{\mathrm{T}}^{\mathrm{miss}}$ in the γ+$W(\ell\nu)$ control region.

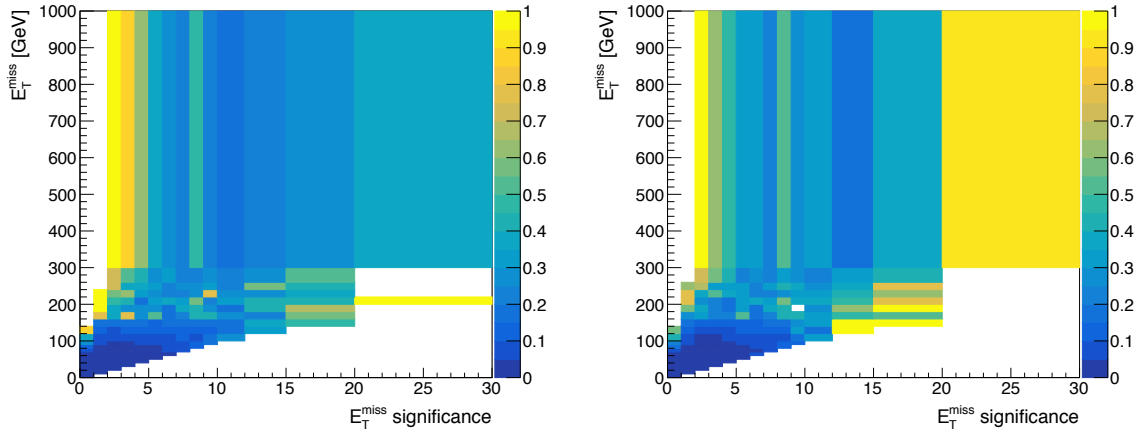

(a) (b)

Figure E.6: $w_2(E_{\mathrm{T}}^{\mathrm{miss}}, \mathcal{S})$ statistical errors for the (a) ee and (b) $\mu\mu$ channel. The z-axis is the error on each bin between 0-100%.

Table E.7: Systematic error on the $E_{\mathrm{T}}^{\mathrm{miss}}$ estimate due to experimental variations in the weights. The total unbinned error is calculated using all $E_{\mathrm{T}}^{\mathrm{miss}}$ bins.

Channel	$E_{\mathrm{T}}^{\mathrm{miss}}$ (GeV)						Total
	[90,100]	[100,120]	[120,140]	[140,160]	[160,180]	[180,200]	
ee	$^{+59.5}_{-47.3}\%$	$^{+55.4}_{-24.6}\%$	$^{+19.7}_{-30.1}\%$	$^{+37.3}_{-25.5}\%$	$^{+36.5}_{-45.5}\%$	$^{+76.4}_{-75.2}\%$	$^{+33.1}_{-16.2}\%$
$\mu\mu$	$^{+39.8}_{-39.5}\%$	$^{+62.4}_{-41.2}\%$	$^{+44.8}_{-71.9}\%$	$^{+52.8}_{-44.4}\%$	$^{+56.5}_{-46.7}\%$	$^{+42.2}_{-42.8}\%$	$^{+25.2}_{-27.1}\%$

Table E.8: Systematic error on the $E_{\mathrm{T}}^{\mathrm{miss}}$ estimate due to PDF and QCD scale variations in the weights. The total unbinned error is calculated using all $E_{\mathrm{T}}^{\mathrm{miss}}$ bins.

Channel	$E_{\mathrm{T}}^{\mathrm{miss}}$ (GeV)						Total
	[90,100]	[100,120]	[120,140]	[140,160]	[160,180]	[180,200]	
ee	$^{+10.9}_{-6.1}\%$	$^{+11.6}_{-11.6}\%$	$^{+6.0}_{-4.1}\%$	$^{+10.3}_{-2.8}\%$	$^{+9.0}_{-5.9}\%$	$^{+2.3}_{-6.6}\%$	$^{+5.6}_{-6.4}\%$
$\mu\mu$	$^{+8.3}_{-6.1}\%$	$^{+11.3}_{-11.4}\%$	$^{+3.0}_{-4.3}\%$	$^{+1.5}_{-4.7}\%$	$^{+6.9}_{-8.3}\%$	$^{+4.4}_{-5.6}\%$	$^{+3.6}_{-7.1}\%$

For the $E_{\mathrm{T}}^{\mathrm{miss}}$ discriminant, the final Z+jets estimates obtained from the γ+jets reweighting method are 327 $\pm$ 4 (stat) $^{+112}_{-62}$ (sys) for the ee channel, and 415 $\pm$ 5 (stat) $^{+121}_{-111}$ (sys) for the $\mu\mu$ channel. Table E.9 summarizes the reweighted estimate compared to the prediction from Z+jets simulation with theoretical and experimental systematics. Overall the results between $E_{\mathrm{T}}^{\mathrm{miss}}$ and m_{T}^{ZZ} estimates are very similar.

Table E.9: Comparison of γ+jets $E_{\mathrm{T}}^{\mathrm{miss}}$ estimate to Z+jets simulation for 139 fb^{-1}.

Channel	Source	Estimate	Statistical error	Systematic error
ee	γ+jets data	327	$\pm$1.1%	$^{+34.3}_{-18.8}\%$
	Z+jets MC	328	$\pm$7.6%	$^{+42.9}_{-28.4}\%$
$\mu\mu$	γ+jets data	415	$\pm$1.1%	$^{+29.2}_{-26.8}\%$
	Z+jets MC	410	$\pm$7.3%	$^{+37.5}_{-39.9}\%$

E.2 Non-closure systematic table

Table E.10 summarizes the systematic error for the first six relevant m_{T}^{ZZ} bins. Non-closure is only introduced for $m_{\mathrm{T}}^{ZZ} > 700$ GeV where coarse bins are used in the reweighting. There is one exception to this. In the $\mu\mu$ channel some non-closure is seen for the bin with [750,800] GeV. This bin has an artificially large drop in Z+jets MC due to an anomalous event weight, likely due to low statistics. When w_2 is calculated, this manifests as one 2D bin that has a very small value. Applying the weight as-is to γ+jets MC gives perfect closure, but applying the weight to data gives poor results for this bin; to avoid the issue, the w_2 problem bin is averaged using the neighbouring bins so that a reliable weight is calculated. This averaging subsequently produces some non-closure between Z+jets and γ+jets MC for this m_{T}^{ZZ} bin, but this effect has a negligible impact on the final result because the bin contains very few events in data.

Table E.10: Non-closure systematic on the Z+jets m_{T}^{ZZ} estimate for 139 fb^{-1} for the first six bins above 700 GeV. The total unbinned error is calculated using all m_{T}^{ZZ} bins.

Channel	m_{T}^{ZZ} (GeV)						Total
	[700,750]	[750,800]	[800,850]	[850,900]	[950,1000]	[1000,1100]	
ee	11.1%	29.1%	7.4%	14.4%	17.6%	23.7%	1.1%
$\mu\mu$	11.2%	731.3%	0.9%	1.5%	59.3%	44.3%	2.8%

E.3 Experimental systematic tables

This appendix provides experimental systematic tables relevant to the the γ+jets reweighting method. Table E.11 lists the top experimental systematics on γ+jets and Z+jets simulation that are larger than ∼3% (without reweighting). Table E.12 shows the impact of the top experimental systematics on the reweighted γ+jets estimate. The size of the total systematic is reduced by about 20-30% depending on the channel.

Systematic	γ+jets MC	$Z(ee)$+jets	$Z(\mu\mu)$+jets
JET_Flavor_Composition__1down	+7.9%	+25.0%	+16.2%
MET_SoftTrk_ScaleDown	+7.6%	+13.9%	+19.4%
JET_Pileup_RhoTopology__1down	+4.3%	+18.5%	+7.9%
JET_Flavor_Composition__1up	-8.0%	-13.4%	-17.2%
MET_SoftTrk_ScaleUp	-7.0%	-12.6%	-17.2%
MET_SoftTrk_ResoPerp	+7.0%	+11.9%	+16.4%
JET_Flavor_Response__1up	+4.3%	+13.2%	+6.7%
JET_EtaIntercalibration_Modelling__1down	+3.6%	+11.7%	+7.3%
JET_Pileup_RhoTopology__1up	-4.8%	-7.7%	-9.7%
JET_JvtEfficiency__1up	-9.5%	-3.6%	-4.6%
JET_Flavor_Response__1down	-4.6%	-5.4%	-8.6%
JET_EffectiveNP_1__1down	+2.2%	+8.6%	+5.0%
MET_SoftTrk_ResoPara	+5.6%	+3.7%	+8.4%
JET_Pileup_OffsetMu__1down	+1.4%	+6.5%	+7.4%
JET_EtaIntercalibration_Modelling__1up	-3.6%	-4.5%	-7.4%
JET_JvtEfficiency__1down	+7.0%	+2.3%	+3.1%
JET_Pileup_OffsetNPV__1down	+1.6%	+6.8%	+6.1%
JET_Pileup_OffsetMu__1up	-1.9%	-1.4%	-6.6%
JET_JER_EffectiveNP_4__1up	+0.1%	+2.4%	+5.6%
JET_JER_EffectiveNP_4__1down	-0.1%	-2.4%	-5.6%
JET_EffectiveNP_1__1up	-2.8%	-1.4%	-5.5%
JET_JER_EffectiveNP_2__1up	+0.5%	+4.3%	+4.1%
JET_JER_EffectiveNP_2__1down	-0.5%	-4.3%	-4.1%
JET_Pileup_OffsetNPV__1up	-1.8%	-1.5%	-4.3%
EG_SCALE_ALL__1down	-2.7%	-3.9%	0.0%
JET_JER_EffectiveNP_1__1up	+0.6%	+2.5%	+3.8%
JET_JER_EffectiveNP_1__1down	-0.6%	-2.5%	-3.8%
JET_JER_EffectiveNP_3__1up	+0.1%	0.0%	+3.4%
JET_JER_EffectiveNP_3__1down	-0.1%	0.0%	-3.4%
EG_SCALE_ALL__1up	+2.5%	+2.7%	0.0%
Total	$^{+17.8}_{-18.9}$%	$^{+43.1}_{-26.3}$%	$^{+37.0}_{-36.5}$%

Table E.11: Top experimental systematics on Z+jets and γ+jets samples (no reweighting) in the signal region and γ+jets control region. The systematics are ranked by their impact on the γ+jets MC. Only systematics with an impact larger than 3% (across all samples) are shown. The total asymmetric error is calculated by adding all of the largest positive and negative variations in quadrature, including all experimental systematics not shown in the table. If a systematic has two positive (negative) variations, the largest in magnitude is taken as the positive (negative) variation, and no negative (positive) variation is taken for that systematic.

Systematic	ee		$\mu\mu$	
	Up	Down	Up	Down
JET_Flavor_Composition	-8.8%	+19.5%	-14.8%	+12.3%
JET_Pileup_RhoTopology	-4.6%	+15.1%	-8.8%	+6.4%
MET_SoftTrk_Scale	-5.7%	+5.7%	-9.1%	+10.7%
MET_SoftTrk_ResoPerp	+4.9%	-4.9%	+9.7%	-9.7%
JET_Flavor_Response	+9.4%	-3.5%	+4.4%	-7.3%
JET_EtaIntercalibration_Modelling	-1.5%	+8.8%	-5.7%	+4.9%
JET_Pileup_OffsetMu	+0.7%	+7.5%	-5.7%	+8.5%
JET_EffectiveNP_1	+0.4%	+6.7%	-5.4%	+3.8%
JET_Pileup_OffsetNPV	-1.5%	+6.5%	-5.8%	+6.3%
JET_JvtEfficiency	+6.2%	-4.1%	+4.5%	-3.0%
JET_JER_EffectiveNP_2	+4.9%	-4.6%	+1.8%	-1.8%
JET_EtaIntercalibration_TotalStat	+2.4%	-0.3%	-3.7%	+1.0%
JET_JER_EffectiveNP_1	+3.6%	-3.6%	+2.7%	-2.7%
JET_Pileup_PtTerm	-2.0%	+2.2%	-3.6%	-0.1%
JET_JER_EffectiveNP_4	+2.2%	-2.2%	+3.5%	-3.5%
MET_SoftTrk_ResoPara	+3.3%	-3.3%	+1.2%	-1.2%
JET_JER_DataVsMC_MC16	+2.5%	-2.5%	+2.5%	-2.5%
JET_EffectiveNP_2	-0.5%	+2.4%	+1.0%	-1.2%
JET_JER_EffectiveNP_3	+0.7%	-0.7%	+2.2%	-2.2%
EG_SCALE_ALL	+1.2%	-2.2%	-1.7%	+2.1%
EG_RESOLUTION_ALL	-0.9%	-1.9%	-0.4%	+0.5%
JET_JER_EffectiveNP_5	+1.8%	-1.8%	+0.1%	-0.1%
MUON_MS	+0.1%	0.0%	-0.1%	+1.4%
MUON_SAGITTA_RHO	0.0%	0.0%	-1.1%	-1.1%
MUON_SCALE	0.0%	0.0%	-0.8%	+1.0%
MUON_SAGITTA_RESBIAS	0.0%	0.0%	0.0%	-1.0%
JET_JER_EffectiveNP_6	+0.7%	-0.7%	+0.8%	-0.8%
JET_JER_EffectiveNP_7restTerm	+0.6%	-0.6%	+0.1%	-0.1%
MUON_ID	0.0%	0.0%	+0.2%	+0.3%
Total	Positive	Negative	Positive	Negative
	+33.1%	-16.2%	+25.2%	-27.1%

Table E.12: Impact of experimental systematics on the reweighted γ+jets prediction. The total asymmetric error is calculated by adding all of the largest positive and negative variations in quadrature. If a systematic has two positive (negative) variations, the largest in magnitude is taken as the positive (negative) variation, and no negative (positive) variation is taken for that systematic.

Appendix F

Authorship Qualification Task on Jet Calibration Studies

The purpose of this work is to validate the jet calibration performance for $R = 0.4$ anti-k_t EM-scale jets in close-by environments. Previous studies [104] show that there is good agreement between data and simulation for close-by jets, but there is interest in understanding how well the jets are being calibrated and if improvements can be made to the calibration sequence. Figure F.1 gives an overview of the calibration scheme for jets at the EM scale. Each calibration, except for the origin correction, is applied to the four-momentum of the jet. The most relevant calibration for this work is the absolute MC-based (also known as the "η-JES") calibration. This calibration corrects the jet energy scale (JES) and jet η to the particle (truth) level. For the JES calibration, the energy difference between reconstructed and truth jets is quantified by the average energy response, $\langle E_{\text{reco}}/E_{\text{true}}\rangle$. In addition, the correction to E_{reco}

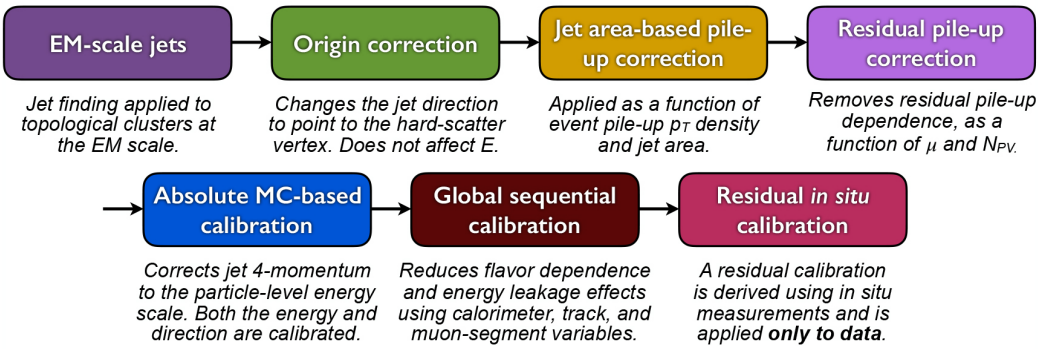

Figure F.1: Calibration sequence for EM-scale jets [103].

is derived from E_{true} using isolated jets only. The primary goal of this study is to validate how the calibrations perform on calibrated close-by jets by studying the energy response in simulation. The second goal is to determine a more robust truth matching definition in close-by environments from these response studies.

Three variables are used to assess how close a jet is to other jets. The first is ΔR, which is commonly used to measure how separated two jets are in terms of η and ϕ:

$$\Delta R = \sqrt{\Delta\eta^2 + \Delta\phi^2} \tag{F.1}$$

For these studies the interest is in ΔR_{min}, the minimum ΔR between the probe jet and the nearest jet. For $R = 0.4$ jets, a jet is considered close-by if $\Delta R_{\text{min}} < 0.8$. The second variable is the jet area, which can be normalized according to

$$\text{area} = A/\pi R^2, \tag{F.2}$$

where A is the active area of the jet, and $R = 0.4$ for small-R anti-k_t jets. Jets are typically expected to be circular in (η, ϕ). Isolated jets are typically circular and therefore the normalized area will be close to 1. However, for jets that are in close-by environments, it's possible that the area will be reduced. If a low p_{T} jet is overlapping with a high p_{T} jet, the area for the low p_{T} jet will be reduced, cut off by the circular, high p_{T} jet. This is due to the nature of the anti-k_t algorithm which clusters high p_{T} jets first. Close-by jets can also be identified by the amount of momentum activity nearby due to other jets. This can be quantified using f_{Closeby}:

$$f_{\text{Closeby}} = \sum_j \frac{\vec{p_j} \cdot \vec{p}}{|\vec{p}|^2} \tag{F.3}$$

This quantity is the momentum projection of nearby jets along the axis of the jet of interest. The surrounding jets have a minimum p_{T} requirement of 7 GeV and need to be within $\Delta R < 1.0$. While small ΔR_{min} and area indicate close-by jets, f_{Closeby} is potentially large for close-by jets. If the probe jet has high p_{T} and softer surrounding jets, its f_{Closeby} will be small. If the probe jet has a parallel, high p_{T} neighbouring jet, then f_{Closeby} will be large. The interest is in the latter case when the surrounding jets are more likely to affect the response of the probe jet.

The calibration performance is assessed by studying the jet response and resolution for fully calibrated close-by jets in Pythia 8 di-jet simulation as a function of ΔR_{min}, jet area, and f_{Closeby}. The jet p_{T} response is given by

$$\mathcal{R} = p_{\mathrm{T}}^{\mathrm{reco}}/p_{\mathrm{T}}^{\mathrm{true}}. \tag{F.4}$$

For perfectly calibrated jets the response should be 1.0. In reality the response histograms have a Gaussian distribution centred on 1.0, and a fit can be performed to get a measure of the average response. The average p_{T} response, $\langle\mathcal{R}\rangle = \langle p_{\mathrm{T}}^{\mathrm{reco}}/p_{\mathrm{T}}^{\mathrm{true}}\rangle$, is the mean of the fitted Gaussian, and the resolution,

$$\sigma_{\mathcal{R}} = \sigma(p_{\mathrm{T}}^{\mathrm{reco}})/p_{\mathrm{T}}^{\mathrm{reco}}, \tag{F.5}$$

is obtained from the RMS.

With minimal jet selections and standard $\Delta R < 0.3$ truth matching, a significant population of low response close-by jets is observed in simulation. Several categories of low response close-by jets are investigated. Of the categories investigated, the most important sources of low response are jets with a multi-matched truth jet (one truth jet matched to several jets), and jets with a bad truth matching (two close-by jets each matched to a wrong truth jet). An example is given in Figure F.2, where the response for all jets is compared to the response for jets that have a unique (singly matched) truth jet. This demonstrates that jets with multi-matched truth jets can have a significant proportion with low response.

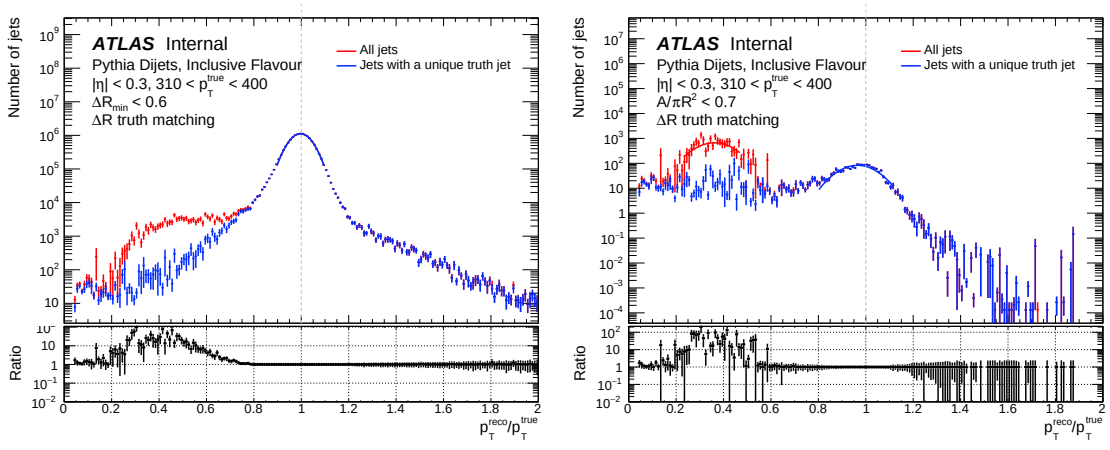

(a) Close-by jets with $\Delta R_{\mathrm{min}} < 0.6$.

(b) Close-by jets with area < 0.7.

Figure F.2: Response histograms comparing all jets (red) to jets with a unique truth jet (blue), with $310 < p_{\mathrm{T}}^{\mathrm{true}} < 400$ GeV.

Ghost truth association is studied as an alternative to ΔR truth matching. ΔR

matching can break down in very close-by environments, as illustrated in these studies, and does not take into account the amount of p_{T} overlap between a jet and a truth jet. Ghost truth association takes into account the four-momenta of the truth particles inside the truth jet, making it a more robust technique to use, especially in close-by environments. The procedure for matching via ghost truth association is as follows. The anti-k_t algorithm takes a list of topo-cluster four-momenta for reco jet finding, and a list of truth particle four-momenta for truth jet finding. For each truth particle, an identical "ghost" truth particle is created but with $p_{\mathrm{T}} \approx 0$ as to not affect the jet finding. This list of ghost truth particles is appended to the list of topo-clusters for the reco jet finding. After the anti-k_t algorithm is run, one then knows which (ghost) truth particles are inside a given reco jet, and one can then calculate the p_{T} fraction of the truth jet that overlaps with a given reco jet. In relevant derivations, reco jets are automatically linked with the truth jet that has the largest p_{T} fraction in that reco jet. The user can then perform the actual truth matching by requiring a minimum threshold on the ghost p_{T} fraction. A larger threshold means that the matched truth jet will have a larger p_{T} fraction overlapping with the reco jet. Figure F.3 shows how ΔR matching compares with ghost truth matching for p_{T} fraction thresholds of 0.5-0.8. There is clear improvement when using ghost truth matching compared to ΔR matching, especially when higher p_{T} fractions are used.

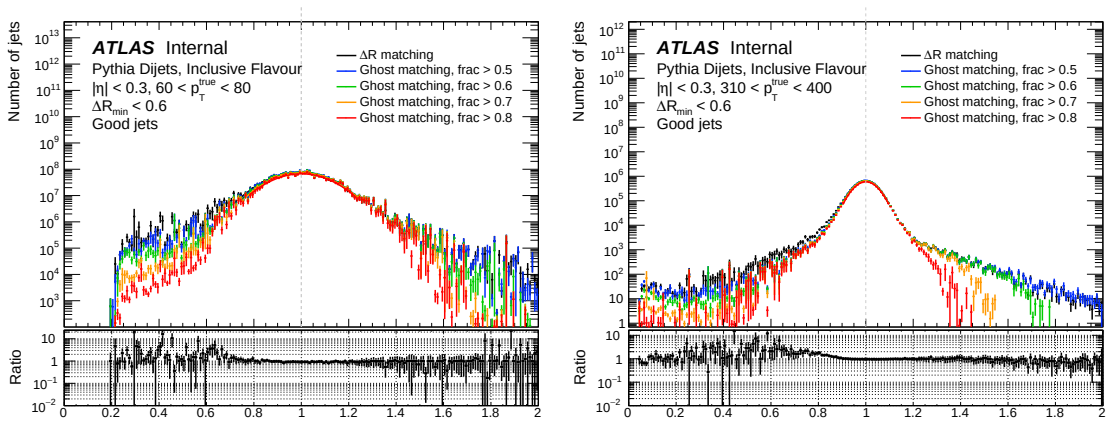

(a) Close-by jets with $60 < p_{\mathrm{T}}^{\mathrm{true}} < 80$ GeV. (b) Close-by jets with $310 < p_{\mathrm{T}}^{\mathrm{true}} < 400$ GeV.

Figure F.3: Response histograms comparing different truth matching methods for jets with $\Delta R_{\mathrm{min}} < 0.6$. Jets that fall into a known low response category are ignored. The black histogram represents jets matched using ΔR. The coloured histograms represent jets with ghost truth matching using various p_{T} fraction thresholds.

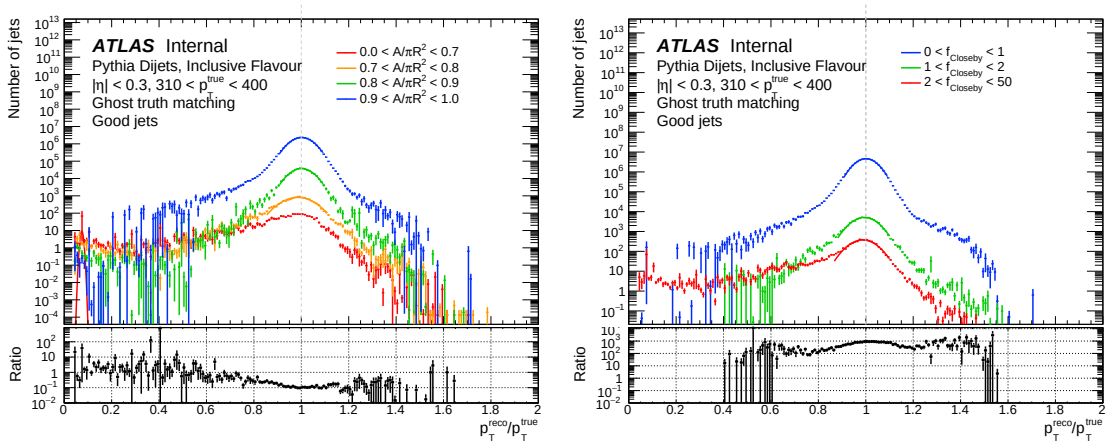

(a) Jets with varying area.

(b) Jets with varying f_{Closeby}.

Figure F.4: Response histograms comparing ghost matched jets for varying degrees of closeness with $310 < p_{\text{T}}^{\text{true}} < 400$ GeV. Jets that fall into a known low response category are ignored.

After removing the established sources of low response and switching to ghost truth matching, good agreement is seen in the response for close-by jets with small ΔR_{min} compared to more isolated jets. However some low response jets with small area and/or large f_{Closeby} remain, as illustrated in Figure F.4. Topology and global sequential calibration (GSC) dependence is investigated for these remaining jets. The GSC makes corrections to the jet four-vector to mitigate effects from the detector. These variables are: the number of tracks, n_{trk}, the track width, $width_{\text{trk}}$, and the fractions of the jet energy deposited in the Tile and LAr calorimeters, f_{Tile0} and f_{LAr3}. These variables are defined in Section 7.1 of the 2015 GSC document [105]. The low response fraction of close-by jets shows some dependence on the low statistics regions of $width_{\text{trk}}$ and possibly n_{trk}, and should be investigated further. Correlation studies on ΔR_{min}, area, and f_{Closeby} are also studied.

Further effort remains to understand the outstanding low response close-by jets. One promising outlook is that the implementation of ghost truth association has been improved in Release 21. The definition of the ghost truth association fraction in Release 20.7, as used in this work, is "the p_{T}-weighted fraction of associated truth particles that are constituents of a target truth jet (the one with the largest such fraction)." The new definition is "the p_{T}-weighted fraction of constituents from a target truth jet that are also ghost-matched to the jet holding the moment (for the jet with the highest such fraction)." The definition was improved because the Release

20.7 definition can lead to artificially high match fractions when the matched jet contains a very small fraction of high p_{T} constituents from one jet. This new definition takes the number of matched constituents into account, and is expected to improve almost all of the remaining bad match cases with the 20.7 definition. For this reason, similar close-by studies using the new definition in Release 21 would likely lead to further reduction in the low and high response tails, and hence further improvement in the average response and resolution for close-by jets.

Bibliography

[1] Planck Collaboration et al. Planck 2018 results. VI. Cosmological parameters. *A&A*, 641(A6):1–67, 2020. (Cited on pages 2 and 11.)

[2] H. Poincaré. La Voie lactée et la théorie des gaz. *Bulletin de la société astronomique de France*, 20:153–165, 1906. (Cited on page 2.)

[3] E. Aprile, J. Aalbers, F. Agostini, M. Alfonsi, L. Althueser, F. D. Amaro, M. Anthony, F. Arneodo, L. Baudis, B. Bauermeister, et al. Dark Matter Search Results from a One Ton-Year Exposure of XENON1T. *Phys. Rev. Lett.*, 121(11):111302, Sep 2018. (Cited on pages 2 and 124.)

[4] C. Amole, M. Ardid, I. J. Arnquist, D. M. Asner, D. Baxter, E. Behnke, M. Bressler, B. Broerman, G. Cao, C. J. Chen, et al. Dark matter search results from the complete exposure of the PICO-60 C_3F_8 bubble chamber. *Phys. Rev. D.*, 100(2):022001, Jul 2019. (Cited on pages 2, 124, and 127.)

[5] X. Cui, A. Abdukerim, W. Chen, X. Chen, Y. Chen, B. Dong, D. Fang, C. Fu, K. Giboni, F. Giuliani, et al. Dark Matter Results from 54-Ton-Day Exposure of PandaX-II Experiment. *Phys. Rev. Lett.*, 119(18):181302, Oct 2017. (Cited on pages 2 and 124.)

[6] P. Agnes, I. F. M. Albuquerque, T. Alexander, A. K. Alton, G. R. Araujo, D. M. Asner, M. Ave, H. O. Back, B. Baldin, G. Batignani, et al. Low-Mass Dark Matter Search with the DarkSide-50 Experiment. *Phys. Rev. Lett.*, 121(8):081307, Aug 2018. (Cited on pages 2 and 124.)

[7] M. Bañados and I. Reyes. A short review on Noether's theorems, gauge symmetries and boundary terms. *International Journal of Modern Physics D*, 25(10):1630021, Aug 2016. (Cited on page 4.)

[8] S. L. Glashow. Partial Symmetries of Weak Interactions. *Nucl. Phys.*, 22:579–588, Feb 1961. (Cited on page 5.)

[9] S. Weinberg. A Model of Leptons. *Phys. Rev. Lett.*, 19:1264–1266, Nov 1967. (Cited on page 5.)

[10] A. Salam. Weak and Electromagnetic Interactions. *Conf. Proc. C*, 680519:367–377, May 1968. (Cited on page 5.)

[11] M. Tanabashi et al. Review of Particle Physics. *Phys. Rev. D*, 98(3):030001, Aug 2018. (Cited on pages 5, 6, and 7.)

[12] A. Maas. Brout-Englert-Higgs physics: From foundations to phenomenology. *Progress in Particle and Nuclear Physics*, 106:132–209, May 2019. (Cited on page 6.)

[13] I. Aitchison and A. Hey. *Gauge Theories in Particle Physics: A Practical Introduction, Volume 1: From Relativistic Quantum Mechanics to QED*. Physics textbook. CRC Press, Boca Raton, FL, fourth edition, 2012. (Cited on pages 6 and 7.)

[14] D. J. Griffiths. *Introduction to Elementary Particles*. Physics textbook. Wiley, New York, NY, second revised edition, 2008. (Cited on page 8.)

[15] D. J. Gross and F. Wilczek. Ultraviolet behavior of non-abelian gauge theories. *Phys. Rev. Lett.*, 30(26):1343–1346, Jun 1973. (Cited on page 10.)

[16] H. D. Politzer. Reliable perturbative results for strong interactions? *Phys. Rev. Lett.*, 30(26):1346–1349, Jun 1973. (Cited on page 10.)

[17] L. A. Harland-Lang, A. D. Martin, P. Motylinski, and R. S. Thorne. Parton distributions in the LHC era: MMHT 2014 PDFs. *Eur. Phys. J. C*, 75(5):204, May 2015. (Cited on page 10.)

[18] Particle Data Group. Review of Particle Physics. *Progress of Theoretical and Experimental Physics*, 2020(8):083, Aug 2020. (Cited on pages 10 and 11.)

[19] G. Altarelli and G. Parisi. Asymptotic Freedom in Parton Language. *Nucl. Phys. B.*, 126:298–318, 1977. (Cited on page 11.)

[20] V. N. Gribov and L. N. Lipatov. Deep inelastic *ep* scattering in perturbation theory. *Sov. J. Nucl. Phys.*, 15:438–450, 1972. (Cited on page 11.)

[21] Y. L. Dokshitzer. Calculation of the Structure Functions for Deep Inelastic Scattering and e^+e^- Annihilation by Perturbation Theory in Quantum Chromodynamics. *Sov. Phys. JETP*, 46:641–653, 1977. (Cited on page 11.)

[22] J. L. Kuo, M. Lattanzi, K. Cheung, and J. W. F. Valle. Decaying warm dark matter and structure formation. *JCAP*, 2018:026, Dec 2018. (Cited on page 11.)

[23] T. D. Brandt. Contraints on MACHO dark matter from compact stellar systems in ultra-faint dwarf galaxies. *The Astrophysical Journal*, 824(2):L31, Jun 2016. (Cited on page 11.)

[24] R. D. Peccei and H. R. Quinn. CP conservation in the presence of pseudoparticles. *Phys. Rev. Lett.*, 38:1440–1443, Jun 1977. (Cited on page 11.)

[25] E. Kh. Akhmedov, G. C. Branco, and M. N. Rebelo. Seesaw mechanism and structure of neutrino mass matrix. *Phys. Lett. B.*, 478(1-3):215–223, Apr 2000. (Cited on page 11.)

[26] T. Hambye, M. H. G. Tytgat, J. Vandecasteele, and L. Vanderheyden. Dark matter from dark photons: A taxonomy of dark matter production. *Phys. Rev. D.*, 100(9):095018, Nov 2019. (Cited on page 12.)

[27] M. Kunz, S. Nesseris, and I. Sawicki. Constraints on dark-matter properties from large-scale structure. *Phys. Rev. D.*, 94(2):023510, Jul 2016. (Cited on page 12.)

[28] M. Viel, G. D. Becker, J. S. Bolton, and M. G. Haehnelt. Warm dark matter as a solution to the small scale crisis: New constraints from high redshift Lyman-α forest data. *Phys. Rev. D.*, 88(4):043502, Aug 2013. (Cited on page 12.)

[29] M. Markevitch, A. H. Gonzalez, D. Clowe, A. Vikhlinin, W. Forman, C. Jones, S. Murray, and W. Tucker. Direct Constraints on the Dark Matter Self-Interaction Cross Section from the Merging Galaxy Cluster 1E 0657-56. *The Astrophysical Journal*, 606(2):819–824, May 2004. (Cited on page 12.)

[30] G. Steigman, B. Dasgupta, and J. F. Beacom. Precise relic WIMP abundance and its impact on searches for dark matter annihilation. *Phys. Rev. D.*, 86(2):023506, Jul 2012. (Cited on page 12.)

[31] D. Abercrombie, N. Akchurin, E. Akilli, J. A. Maestre, B. Allen, B. Alvarez Gonzalez, J. Andrea, A. Arbey, G. Azuelos, P. Azzi, et al. Dark Matter benchmark models for early LHC Run-2 Searches: Report of the ATLAS/CMS Dark Matter Forum. *Phys. Dark Univ.*, 27:100371, Jan 2020. (Cited on pages 13 and 14.)

[32] N. F. Bell, A. J. Galea, J. B. Dent, T. D. Jacques, L. M. Krauss, and T. J. Weiler. Searching for dark matter at the LHC with a mono-Z. *Phys. Rev. D.*, 86(9):096011, Nov 2012. (Cited on pages 13 and 134.)

[33] F. Kahlhoefer, K. Schmidt-Hoberg, T. Schwetz, and S. Vogl. Implications of unitarity and gauge invariance for simplified dark matter models. *JHEP*, 2016(2):16, Feb 2016. (Cited on page 15.)

[34] E. Morgante. Simplified Dark Matter Models. *Adv. High Energy Phys.*, 2018:5012043, Apr 2018. (Cited on page 16.)

[35] A. Tomohiro et al. LHC Dark Matter Working Group: Next-generation spin-0 dark matter models. *Phys. Dark Univ.*, 27:100351, Jan 2020. (Cited on pages 16, 18, and 19.)

[36] L. Fromme, S. J. Huber, and M. Seniuch. Baryogenesis in the two-Higgs doublet model. *JHEP*, 11:038, Nov 2006. (Cited on page 16.)

[37] G. C. Dorsch, S. J. Huber, T. Konstandin, and J. M. No. A second Higgs doublet in the early universe: baryogenesis and gravitational waves. *JCAP*, 2017:052, May 2017. (Cited on page 16.)

[38] G. C. Branco, P. M. Ferreira, L. Lavoura, M. N. Rebelo, M. Sher, and J. P. Silva. Theory and phenomenology of two-Higgs-doublet models. *Physics Reports*, 516(1-2):1–102, Jul 2012. (Cited on page 17.)

[39] ATLAS Collaboration. Constraints on mediator-based dark matter and scalar dark energy models using $\sqrt{s} = 13\,\text{TeV}$ pp collision data collected by the ATLAS detector. *JHEP*, 05:142, Mar 2019. (Cited on pages 18, 32, 119, 120, 121, 122, and 127.)

[40] ATLAS Collaboration. Combination of Searches for Invisible Higgs Boson Decays with the ATLAS Experiment. *Phys. Rev. Lett.*, 122(23):231801, Jun 2019. (Cited on page 19.)

[41] E. Mobs. The CERN accelerator complex. General photo, available at `https://cds.cern.ch/record/2684277`, Jul 2019. (Cited on page 21.)

[42] J. Pequenao. Computer generated image of the whole ATLAS detector. Available at `https://cds.cern.ch/record/1095924`, Mar 2008. (Cited on page 22.)

[43] ATLAS Collaboration. The ATLAS Experiment at the CERN Large Hadron Collider. *JINST*, 3:S08003, Aug 2008. (Cited on pages 22, 24, 25, 26, and 28.)

[44] J. Pequenao. Computer generated image of the ATLAS inner detector. Available at `https://cds.cern.ch/record/1095926`, Mar 2008. (Cited on page 24.)

[45] ATLAS Collaboration. ATLAS Insertable B-Layer Technical Design Report. Technical Report CERN-LHCC-2010-013. ATLAS-TDR-19, Sep 2010. (Cited on page 25.)

[46] J. Pequenao. Computer Generated image of the ATLAS calorimeter. Available at `https://cds.cern.ch/record/1095927`, Mar 2008. (Cited on page 25.)

[47] J. Pequenao. Computer generated image of the ATLAS muon subsystem. Available at `https://cds.cern.ch/record/1095929`, Mar 2008. (Cited on pages 26 and 27.)

[48] ATLAS Collaboration. Performance of the ATLAS trigger system in 2015. *Eur. Phys. J. C*, 77(5):317, May 2017. (Cited on page 28.)

[49] ATLAS Collaboration. Muon reconstruction performance of the ATLAS detector in proton-proton collision data at $\sqrt{s}$ =13 TeV. *Eur. Phys. J.*, C76(5):292, Mar 2016. (Cited on pages 28 and 38.)

[50] ATLAS Collaboration. Electron and Photon Reconstruction with the ATLAS Detector. *Nucl. Part. Phys. Proc.*, 273-275:2539–2541, Apr-Jun 2016. (Cited on page 28.)

[51] ATLAS Collaboration. Reconstruction of hadronic decay products of tau leptons with the ATLAS experiment. *Eur. Phys. J. C*, 76(5):295, May 2016. (Cited on page 28.)

[52] ATLAS Collaboration. Jet reconstruction and performance using particle flow with the ATLAS Detector. *Eur. Phys. J. C*, 77(7):466, Jul 2017. (Cited on pages 28 and 39.)

[53] M. Cacciari, G. P. Salam, and G. Soyez. The anti-k_t jet clustering algorithm. *JHEP*, 04:063, Apr 2008. (Cited on page 28.)

[54] ATLAS Collaboration. Luminosity determination in pp collisions at $\sqrt{s} = 13$ TeV using the ATLAS detector at the LHC. Technical Report ATLAS-CONF-2019-021, CERN, Geneva, Jun 2019. (Cited on pages 29, 30, and 61.)

[55] ATLAS Collaboration. Number of Interactions per Crossing. ATLAS public result, available at `https://atlas.web.cern.ch/Atlas/GROUPS/DATAPREPARATION/PublicPlots/2018/DataSummary/figs/mu_2015_2018.pdf`, 2018. (Cited on page 30.)

[56] ATLAS Collaboration. Search for new phenomena in the $Z(\to \ell\ell) + E_{\mathrm{T}}^{\mathrm{miss}}$ final state at $\sqrt{s} = 13$ TeV with the ATLAS detector. Conf. Note. ATLAS-CONF-2016-056, CERN, Geneva, Aug 2016. (Cited on page 32.)

[57] ATLAS Collaboration. Search for an invisibly decaying Higgs boson or dark matter candidates produced in association with a Z boson in pp collisions at $\sqrt{s} = 13$ TeV with the ATLAS detector. *Phys. Lett. B*, 776:318–337, Jan 2018. (Cited on pages 32, 78, 80, 82, 84, 115, 116, and 134.)

[58] ATLAS Collaboration. Performance of missing transverse momentum reconstruction with the ATLAS detector using proton-proton collisions at $\sqrt{s} = 13$ TeV. *Eur. Phys. J. C*, 78(11):903, Nov 2018. (Cited on page 32.)

[59] S. Agostinelli et al. GEANT4 – a simulation toolkit. *Nucl. Instrum. Meth. A*, 506(3):250–303, Jul 2003. (Cited on page 34.)

[60] D. R. Tovey. Transformation properties of the transverse mass under transverse Lorentz boosts at hadron colliders. *Eur. Phys. J. C*, 79(4):294, Apr 2019. (Cited on page 35.)

[61] ATLAS Collaboration. Electron reconstruction and identification in the ATLAS experiment using the 2015 and 2016 LHC proton-proton collision data at $\sqrt{s} =$ 13 TeV. *Eur. Phys. J. C*, 79(8):639, Aug 2019. (Cited on pages 36 and 37.)

[62] ATLAS Collaboration. Electron and photon performance measurements with the ATLAS detector using the 2015-2017 LHC proton-proton collision data. *JINST*, 14(12):P12006, Dec 2019. (Cited on page 36.)

[63] ATLAS Collaboration. Recommendations of the Physics Objects and Analysis Harmonisation Study Groups 2014. Technical Report ATL-PHYS-INT-2014-018, CERN, Geneva, Jul 2014. (Cited on page 37.)

[64] ATLAS Collaboration. Determination of jet calibration and energy resolution in proton-proton collisions at $\sqrt{s} = 8$ TeV using the ATLAS detector. *Eur. Phys. J. C*, 80(12):1104, Oct 2020. (Cited on page 39.)

[65] ATLAS Collaboration. Tagging and suppression of pileup jets with the ATLAS detector. Technical Report ATLAS-CONF-2014-018, CERN, Geneva, May 2014. (Cited on page 40.)

[66] ATLAS Collaboration. Measurements of b-jet tagging efficiency with the ATLAS detector using $t\bar{t}$ events at $\sqrt{s} = 13$ TeV. *JHEP*, 08:089, Aug 2018. (Cited on page 41.)

[67] ATLAS Collaboration. Object-based missing transverse momentum significance in the ATLAS detector. Conf. Note. ATLAS-CONF-2018-038, CERN, Geneva, Jul 2018. (Cited on page 43.)

[68] ATLAS Collaboration. Formulae for Estimating Significance. Technical Report ATL-PHYS-PUB-2020-025, CERN, Geneva, Sep 2020. (Cited on page 44.)

[69] J. Alwall, R. Frederix, S. Frixione, V. Hirschi, F. Maltoni, O. Mattelaer, H. S. Shao, T. Stelzer, P. Torrielli, and M. Zaro. The automated computation of tree-level and next-to-leading order differential cross sections, and their matching to parton shower simulations. *JHEP*, 07:079, 2014. (Cited on page 46.)

[70] P. Nason. A new method for combining NLO QCD with shower Monte Carlo algorithms. *JHEP*, 11:040, 2004. (Cited on page 46.)

[71] E. Bothmann, G. Singh Chahal, S. Höche, J. Krause, F. Krauss, S. Kuttimalai, S. Liebschner, D. Napoletano, M. Schönherr, H. Schulz, et al. Event generation with Sherpa 2.2. *SciPost Physics*, 7(3), Sep 2019. (Cited on page 46.)

[72] T. Sjöstrand, S. Ask, J. R. Christiansen, R. Corke, N. Desai, P. Ilten, S. Mrenna, S. Prestel, C. O. Rasmussen, and P. Z. Skands. An introduction to PYTHIA 8.2. *Comput. Phys. Commun.*, 191:159, 2015. (Cited on page 46.)

[73] R. D. Ball, V. Bertone, S. Carrazza, C. S. Deans, L. Del Debbio, S. Forte, A. Guffanti, N. P. Hartland, J. I. Latorre, J. Rojo, et al. Parton distributions with LHC data. *Nuclear Physics B*, 867(2):244–289, Feb 2013. (Cited on page 48.)

[74] G. Avoni et al. The new LUCID-2 detector for luminosity measurement and monitoring in ATLAS. *JINST*, 13(07):P07017, 2018. (Cited on page 61.)

[75] J. C. Collins, D. E. Soper, and G. F. Sterman. Factorization of Hard Processes in QCD. *Adv. Ser. Direct. High Energy Phys.*, 5:1–91, 1989. (Cited on page 62.)

[76] S. Kallweit, J. M. Lindert, S. Pozzorini, and M. Schönherr. NLO QCD+EW predictions for $2\ell 2\nu$ diboson signatures at the LHC. *JHEP*, 11(11):120, Nov 2017. (Cited on page 77.)

[77] S. Heim. Private communication, 2020. (Cited on page 78.)

[78] S. Ask, M. A. Parker, T. Sandova, M. E. Shea, and W. J. Stirling. Using $\gamma+$ jets production to calibrate the Standard Model $Z\,(\to v\bar{v})$ + jets background to new physics processes at the LHC. *JHEP*, 10:058, Oct 2011. (Cited on page 85.)

[79] ATLAS Collaboration. Search for new phenomena in events containing a same-flavour opposite-sign dilepton pair, jets, and large missing transverse momentum in $\sqrt{s} = 13$ tev pp collisions with the ATLAS detector. *Eur. Phys. J. C*, 77(3):144, Mar 2017. (Cited on page 89.)

[80] M. Baak, G. J. Besjes, D. Côté, A. Koutsman, J. Lorenz, and D. Short. HistFitter software framework for statistical data analysis. *Eur. Phys. J. C*, 75(4):153, Apr 2015. (Cited on pages 107 and 110.)

[81] G. Cowan, K. Cranmer, E. Gross, and O. Vitells. Asymptotic formulae for likelihood-based tests of new physics. *Eur. Phys. J. C*, 71:1554, Feb 2011. (Cited on pages 108, 109, and 110.)

[82] S. S. Wilks. The Large-Sample Distribution of the Likelihood Ratio for Testing Composite Hypotheses. *The Annals of Mathematical Statistics*, 9(1):60–62, Mar 1938. (Cited on page 109.)

[83] A. Wald. Tests of Statistical Hypotheses Concerning Several Parameters When the Number of Observations is Large. *Transactions of the American Mathematical Society*, 54(3):426–482, Nov 1943. (Cited on page 109.)

[84] T. Junk. Confidence level computation for combining searches with small statistics. *Nuclear Instruments and Methods in Physics Research Section A: Accelerators, Spectrometers, Detectors and Associated Equipment*, 434:435–443, Sep 1999. (Cited on page 109.)

[85] A. Boveia et al. Recommendations on presenting LHC searches for missing transverse energy signals using simplified *s*-channel models of dark matter. *Phys. Dark Univ.*, 27:100365, 2020. (Cited on pages 115, 116, 123, and 132.)

[86] D. S. Akerib, S. Alsum, H. M. Araújo, X. Bai, A. J. Bailey, J. Balajthy, P. Beltrame, E. P. Bernard, A. Bernstein, T. P. Biesiadzinski, et al. Limits on Spin-Dependent WIMP-Nucleon Cross Section Obtained from the Complete LUX Exposure. *Phys. Rev. Lett.*, 118(25):251302, Jun 2017. (Cited on page 124.)

[87] E. Aprile, J. Aalbers, F. Agostini, M. Alfonsi, L. Althueser, F. D. Amaro, M. Anthony, V. C. Antochi, F. Arneodo, L. Baudis, et al. Constraining the Spin-Dependent WIMP-Nucleon Cross Sections with XENON1T. *Phys. Rev. Lett.*, 122(14):141301, Apr 2019. (Cited on page 124.)

[88] E. Aprile, J. Aalbers, F. Agostini, M. Alfonsi, L. Althueser, F. D. Amaro, V. C. Antochi, E. Angelino, F. Arneodo, D. Barge, et al. Search for Light Dark Matter Interactions Enhanced by the Migdal Effect or Bremsstrahlung in XENON1T. *Phys. Rev. Lett.*, 123(24):241803, Dec 2019. (Cited on pages 124 and 125.)

[89] ATLAS Collaboration. Dark matter summary plots for *s*-channel mediators. Technical Report ATL-PHYS-PUB-2020-021, CERN, Geneva, Jul 2020. (Cited on pages 125 and 126.)

[90] CMS Collaboration. Search for dark matter produced in association with a leptonically decaying Z boson in proton-proton collisions at $\sqrt{s} = 13$ TeV. *Eur. Phys. J. C*, 81(1):13, 2021. (Cited on pages 128 and 129.)

[91] ATLAS Collaboration. Technical Design Report for the ATLAS Inner Tracker Pixel Detector. Technical Report CERN-LHCC-2017-021. ATLAS-TDR-030, CERN, Geneva, Sep 2017. (Cited on page 131.)

[92] T. Kawamoto, S. Vlachos, L. Pontecorvo, J. Dubbert, G. Mikenberg, P. Iengo, C. Dallapiccola, C. Amelung, L. Levinson, R. Richter, and D. Lellouch. New Small Wheel Technical Design Report. Technical Report CERN-LHCC-2013-006. ATLAS-TDR-020, CERN, Geneva, Jun 2013. (Cited on page 131.)

[93] ATLAS Collaboration. Technical Design Report: A High-Granularity Timing Detector for the ATLAS Phase-II Upgrade. Technical Report CERN-LHCC-2020-007. ATLAS-TDR-031, CERN, Geneva, Jun 2020. (Cited on page 131.)

[94] ATLAS Collaboration. Technical Design Report for the Phase-I Upgrade of the ATLAS TDAQ System. Technical Report CERN-LHCC-2013-018. ATLAS-TDR-023, CERN, Geneva, Sep 2013. (Cited on page 131.)

[95] P. Baldi, K. Cranmer, T. Faucett, P. Sadowski, and D. Whiteson. Parameterized neural networks for high-energy physics. *Eur. Phys. J. C*, 76(5):235, Apr 2016. (Cited on page 132.)

[96] T. Kozynets, S. Fallows, and C. B. Krauss. Sensitivity of the PICO-500 bubble chamber to supernova neutrinos through coherent nuclear elastic scattering. *Astroparticle Physics*, 105:25–30, Feb 2019. (Cited on page 132.)

[97] E. V. Jauregui. PICO-500L: Simulations for a 500L Bubble Chamber for Dark Matter Search. Talk at TAUP 2017. Available at `https://indico.cern.ch/event/606690/contributions/2591726/attachments/1498457/2332757/Eric_Vazquez_Jauregui_TAUP_2017.pdf`, Sudbury ON, Jul 2017. (Cited on page 132.)

[98] D. S. Akerib, C. W. Akerlof, S. K. Alsum, H. M. Araújo, M. Arthurs, X. Bai, A. J. Bailey, J. Balajthy, S. Balashov, D. Bauer, et al. Projected WIMP sensitivity of the LUX-ZEPLIN dark matter experiment. *Phys. Rev. D.*, 101(5):052002, Mar 2020. (Cited on page 132.)

[99] E. Aprile, J. Aalbers, F. Agostini, M. Alfonsi, L. Althueser, F. D. Amaro, V. C. Antochi, E. Angelino, J. R. Angevaare, F. Arneodo, et al. Excess electronic recoil events in XENON1T. *Phys. Rev. D.*, 102(7):072004, Oct 2020. (Cited on page 133.)

[100] The Fermi-LAT Collaboration. The Fermi Galactic Center GeV Excess and Implications for Dark Matter. *The Astrophysical Journal*, 840(1):43, May 2017. (Cited on page 133.)

[101] R. K. Leane and T. R. Slatyer. Revival of the Dark Matter Hypothesis for the Galactic Center Gamma-Ray Excess. *Phys. Rev. Lett.*, 123(24):241101, Dec 2019. (Cited on page 133.)

[102] ATLAS Collaboration. Search for dark matter and other new phenomena in events with an energetic jet and large missing transverse momentum using the ATLAS detector. *JHEP*, 01:126, Jan 2018. (Cited on page 135.)

[103] ATLAS Collaboration. Jet energy scale measurements and their systematic uncertainties in proton-proton collisions at $\sqrt{s} = 13$ TeV with the ATLAS detector. *Phys. Rev. D.*, 96(7):072002, Oct 2017. (Cited on page 162.)

[104] ATLAS Collaboration. Jet reclustering and close-by effects in ATLAS run II. Technical Report ATLAS-CONF-2017-062, CERN, Geneva, Jul 2017. (Cited on page 162.)

[105] ATLAS Collaboration. Jet global sequential corrections with the ATLAS detector in proton-proton collisions at $\sqrt{s} = 8$ TeV. Technical Report ATLAS-CONF-2015-002, CERN, Geneva, Mar 2015. (Cited on page 166.)